Photohadronic emission of VHE gamma rays in blazars and the CTA neutrino target of opportunity program

Alberto Rosales de León

A thesis presented for the degree of

Doctor of Philosophy

Centre for Advanced Instrumentation

The University of Durham

United Kingdom

August 2022

Photohadronic emission of VHE gamma rays in blazars and the CTA neutrino target of opportunity program

Alberto Rosales de León

Abstract

Blazars are an extremely luminous and highly variable type of Active Galactic Nucleus (AGN), which possess a relativistic jet with a small viewing angle towards the observer. Recent results, such as the $\sim 3\sigma$ spatial and temporal coincidence of TXS 0506+056 with the IceCube neutrino alert IC-170922A, have motivated an ongoing discussion of how these astrophysical sources can produce high-energy neutrinos during a flaring state and which scenario can successfully describe the observed gamma-ray behaviour.

In this thesis, the possibility of a hadronic contribution to the very high energy (VHE) gamma-ray emission of blazars, as well as the possible detection of neutrino events, are explored by considering photohadronic ($p\gamma$) interactions in a lepto-hadronic scenario. The model is applied to fit the flaring period of Markarian 421 in 2010, for which a dedicated analysis of *Fermi*-LAT data from the source was performed in the MeV range (100 MeV - 1 GeV). The fit results were compared with two leptonic models using the Akaike Information Criterion (AIC) test. In all cases the photohadronic model was favoured as a better fit description in comparison to the one-zone leptonic model.

The photohadronic model was also applied to the blazar 4FGL J0658.6+0636, which was found within the 90% localisation region of the IceCube neutrino alert IC-201114A. By analysing $\sim$ 12.3-years of *Fermi*-LAT data, the periods in which the blazar was detected significantly were identified and studied. For one of these periods, it was found that the photohadronic flaring model results are consistent with the observed gamma-ray behaviour of 4FGL J0658.6+0636 and the IC-201114A is discussed under the photohadronic scenario. These results show the potential of a photohadronic contribution to a lepto-hadronic origin of gamma-ray flux of blazars.

The final part of this thesis describes the neutrino and gamma-ray simulations performed for the Neutrino Target of Opportunity (NToO) program for the Cherenkov Telescope Array (CTA). The detection probability with CTA of the gamma-ray flux associated with the simulated IceCube hot-spots for steady neutrino source populations is investigated, and the performance of the CTA Omega configuration array is analysed to predict the potential science reach of the NToO program.

Supervisors: Paula M. Chadwick and Anthony M. Brown

Acknowledgements

First I would like to thank my supervisors, Prof. Paula M. Chadwick and Prof. Anthony M. Brown, for giving me the opportunity to work with them and helping me throughout all the steps of the PhD process. Thanks for your dedication, patience, guidance and professionalism.

I also want to thank the rest of my colleagues from the gamma-ray group, which have been always present in the daily routine of doing science, Dr. Cameron Rulten, Dr. Sheridan Lloyd, Dr. Patrick Stowell, Dr. Atreya Acharyya, Dr. Jamie Graham, Max Harvey, and Amrit Nayak. It has been my pleasure to work around this wonderful group and share countless conversations with all of you. I also have learned from you in many different ways, and you definitely have enhanced my PhD experience for good.

Thanks to the wonderful people that I have the privilege to work with and meet within the CTA Consortium, especially to the Neutrino Target of Opportunity team: Dr. Konstancja Satalecka, Dr. Olga Sergijenko, Prof. Ignacio Taboada, Dr. Chris Tung, and Dr. Damiano Fiorillo. It was a great pleasure to work with all of you during my PhD, and I hope to keep collaborating with you in the near future.

Thanks to the Physics department people that have helped me during my PhD, including professors, staff, postdocs, fellow PhD and master postgrads.

A million thanks to my parents for all their love and support. For letting me go to the other side of the world to accomplish my life dream and always being there for me. You are a big inspiration and a reason to never give up.

Thanks to my siblings, Humberto, Rafael, and Maria de los Ángeles. I am as proud of you as you are proud of me. Your presence always gives me confidence for the future and your help and advice have been invaluable.

I am also thankful with life to give me the opportunity of making so many friends during this journey: Giorgio, Christos, Vera, Kevin, Sam, Trishla, Victor, Thomas, Emir, Eduardo, Daniel, Abraham, Caterina, Mina, Erandi, Mónica, Cedrik, Shaf, Tarneem, Safiya, and many more. Thanks for your friendship, I am grateful for all the time we spent together.

Thanks to the Ustinov College staff and administration team. Ustinov was my home for 3 years in Durham and I always going to remember my time there. Living in such a vibrant international community, working alongside other fellow postgrads in the Global Citizenship Programme, and winning a Basketball Championship as couch and captain in 2020. I will keep all the memories fondly.

Finally, but not less important, I would like to thank CONACyT for funding me for over 3+ years, which allowed me to pursue a PhD degree in Astrophysics.

Contents

Declaration

The work in this thesis is based on research carried out at the Centre for Advanced Instrumentation, Department of Physics, University of Durham, England. No part of this thesis has been submitted elsewhere for any other degree or qualification, and it is the sole work of the author unless referenced to the contrary in the text.

The results presented in Chapters 5 and 6 are part of a collaboration work done within the Neutrino Target of Opportunity (NToO) program for CTA. I share credits with my collaborators: Dr. Konstancja Satalecka, Dr. Olga Sergijenko, Prof. Anthony M. Brown, Dr. Damiano Fiorillo, Prof. Ignacio Taboada and Dr. Chris Tung. My contribution to this project included the set-up and test of a pipeline for gamma-ray simulations, computing 1/3 of them using `Ctools`, helping to integrate the results to predict CTA performance, analysing the redshift distributions and the differences between the simulated CTA sources.

Some of the work presented in this thesis has been published in journals and conference proceedings - the relevant publications are listed below.

Publications

A. Rosales de León, A. M. Brown and P. M. Chadwick. Photohadronic modelling of the 2010 gamma-ray flare from Mrk 421. *MNRAS*, 501 (2):2198–2208, Feb. 2021. doi:10.1093/mnras/staa3839.

A. Rosales de León, A. M. Brown and P. M. Chadwick. Possible photohadronic origin of the IC-201114A alert, In *Proceedings of the 37th International Cosmic Ray Conference*, page 1001, March 2022.

K. Satalecka, A. M. Brown, A. Rosales de León, et al. Neutrino Target of Opportunity program of the Cherenkov Telescope Array, In *Proceedings of the 36th International Cosmic Ray Conference*, page 784, July 2019.

O. Sergijenko, A. M. Brown, D. Fiorillo, et al. Sensitivity of the Cherenkov Telescope Array to emission from the gamma-ray counterparts of neutrino events, In *Proceedings of the 37th International Cosmic Ray Conference*, page 975, March 2022.

List of Figures

List of Tables

Nomenclature

AEGIS All-wavelength Extended Groth Strip International Survey

AGILE Astro-rivelatore Gamma a Immagini Leggero

AGN Active Galactic Nucleus

AGNs Active Galactic Nuclei

AIC Akaike Information Criterion

AMANDA Antarctic Muon and Neutrino Detector Array

AMEGO All-sky Medium Energy Gamma-ray Observatory

AMON Astrophysical Multi-messenger Observatory Network

ANTARES Astronomy with a Neutrino Telescope and Abyss Environmental Research

ARCA Astroparticle Research with Cosmics in the Abyss

AU Astronomical Units

Baikal-GVD Baikal Gigaton Volume Detector

BAT Burst Alert Telescope

BATSE Burst And Transient Source Experiment

BE Backward Evolution

BL Lac BL Lacerate object

BLR Broad-Line Region

BLRGs Broad-Line Radio Galaxies

CANGAROO Collaboration of Australia and Nippon for a Gamma Ray Observatory in the Outback

CAT Cherenkov Array at Themis

CC Charged Current

CDF Cumulative Distribution Function

CGRO Compton Gamma-ray Observatory

CIB Cosmic Infrared Background

CL Confidence Level

COB Cosmic Optical Background

CMB Cosmic Microwave Background

COMPTEL Compton Telescope

CTA Cherenkov Telescope Array

DM Dark Matter

DUMAND Deep Underwater Muon and Neutrino Detector

DOMs Digital Optical Modules

EAS Extensive Air Shower

EBL Extragalactic Background Light

EDF Empirical Distribution Function

EGRET Energetic Gamma-ray Experiment Telescope

EHE Extremely-High Energy

ESA European Espace Agency

FAR False-Alarm Rate

FE Forward Evolution

FIRESONG First Extragalactic Simulation of Neutrinos and Gamma-rays

FLWO Fred Lawrence Whipple Observatory

FoV Field of View

FSRQ Flat Spectrum Radio Quasars

FWHM Full Width Half Maximum

GBM Gamma-ray Burst Monitor

GCN Gamma-ray Coordinates Network

GRB Gamma-ray Burst

GRID Gamma-ray Imaging Detector

GTI Good Time Intervals

GW Gravitational Wave

GZK Greisen–Zatsepin–Kuzmin

HAWC High-Altitude Water Cherenkov

HBL High-peaked BL Lac

HE High energy

HEGRA High-Energy Gamma-ray Astronomy

HESE High-Energy Starting Events

H.E.S.S. High Energy Stereoscopic System

IACTs Imaging Atmospheric Cherenkov Telescopes

IBL Intermediate-peaked BL Lac

IC Inverse Compton

ICRC International Cosmic-Ray Conference

IGMF InterGalactic Magnetic Field

IDGRB Isotropic Diffuse Gamma-ray Background

IR Infrared

IRFs Instrument Response Functions

ISM Interstellar Medium

LAT Large Area Telescope

LBL Low-peaked BL Lac

LE Low Energy

LIGO Laser Interferometer Gravitational-Wave Observatory

LP Log-Parabola

LST Large-Sized Telescope

LF Luminosity Function

MAGIC Major Atmospheric Gamma-ray Imaging Cherenkov

ME Middle Energy

MJD Modified Julian Date

MLM Maximum Likelihood Method

MST Medium-Sized Telescope

MWL multi-wavelength

NASA National Aeronautics and Space Administration

NC Neutral Current

NLR Narrow-Line Region

NLRGs Narrow-Line Radio Galaxies

NToO Neutrino Target of Opportunity

NSB Night Sky Background

NSF National Science Foundation

ORCA Oscillation Research with Cosmics in the Abyss

OSO Orbiting Solar Observatory

OSSE Oriented Scintillation Spectrometer Experiment

P-ONE Pacific Ocean Neutrino Experiment

PL Power-Law

PMNS Pontecorvo–Maki–Nakagawa–Sakata

PMT Photomultiplier tube

PWN Pulsar Wind Nebulae

PSF Point Spread Function

RoI Region of Interest

QSO Radio Quiet Quasars

SAA South Atlantic Anomaly

SBGs Starburst galaxies

SCT Schwarzschild-Couder Telescope

SED spectral energy distribution

SFR Star Formation Rate

SFH Star Formation History

SiPM Silicon Photomultiplier

SMBH Supermassive Blackhole

SNRs Supernova Remnants

SSC synchrotron self-Compton

SSRQs Steep Spectrum Radio Quasars

SST Small-Sized Telescope

TS Test Statistic

UHE Ultra High Energy

UHECRs Ultra High Energy Cosmic Rays

UTC Universal Time Coordinated

UV Ultra-Violet

UVOT Ultra-Violet Optical Telescope

VERITAS Very Energetic Radiation Imaging Telescope Array System

VHE Very High energy

VLBI Very-Long-Baseline Interferometry

WIMPs Weakly Interacting Massive Particles

XRT X-Ray Telescope

Chapter 1

Introduction

1.1 Gamma-ray Astronomy

The sky can be categorised according to the different frequencies in which it is observed. The electromagnetic spectrum can be subdivided into radio, microwaves, IR, optical, UV, X-ray and gamma-ray wave bands. This is exemplified in Figure 1.1, in which the different wavebands that constitute the electromagnetic spectrum are shown. The low energy part of the spectrum is non-ionising radiation; this means that it has not enough energy to remove electrons from atoms, creating ions in the process. This category includes near UV light, visible light, IR radiation, microwaves and radio waves. The ionising radiation includes far UV light, X-rays and gamma-rays.

Gamma-ray astronomy is dedicated to the study of the highest energy photons in the universe; the low energy boundary starts around 0.5 MeV and the most energetic astrophysical photons detected up to date exceed 1 PeV in energy.

Within gamma-ray astronomy, we can also refer to different energy sub-ranges:

- Low energy (Low Energy (LE); $E < 1$ MeV) range.
- Middle energy (Middle Energy (ME); 1 MeV $< E <$ 100 MeV) range.
- The High Energy (High energy (HE); 100 MeV $< E <$ 100 GeV) range.

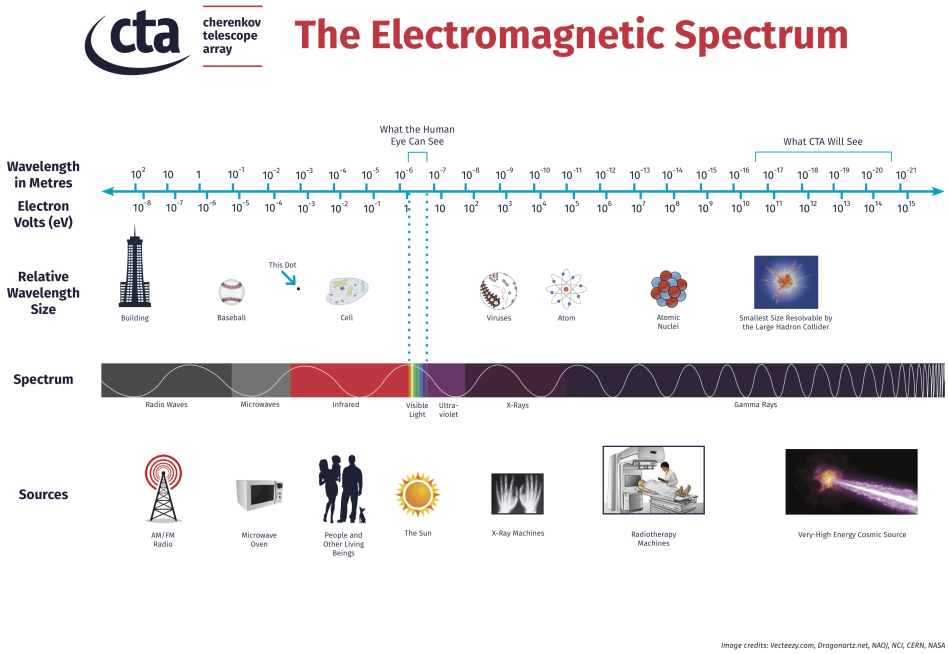

Figure 1.1: The electromagnetic spectrum. The gamma-ray domain starts on the far left of the spectrum, with a frequency of $\sim 10^{20}$ Hz. Image credits: Vecteezy.com, Dragonartz.net, NAOJ, NCI, CERN, NASA.

- Very High Energy (VHE; 100 GeV $<$ E $<$ 10 TeV) range.
- Ultra-high energy (Ultra High Energy (UHE); E $>$ 10 TeV) range.

This work was developed with a focus on the HE and VHE bands, particularly the gamma-ray emission from astrophysical sources and the possible VHE neutrinos coming from them.

The upgrades and development of the observation technology in the last decades have allowed gamma-ray astronomy to collect important information about extragalactic objects. The VHE gamma-ray sky counts with more than 270 identified extragalactic sources (according to the TevCat online gamma-ray catalogue Wakely and Horan (2008)). Many of the detected point-sources correspond to AGNs, luminous galaxies powered by a SMBH at their centre. Within the VHE gamma-ray sky, BL Lacerate object (BL Lac) objects, a branch of AGNs, form the most numer-

ous class of extragalactic sources seen at VHE gamma-rays with about 70 detected, with another brand, FSRQs representing a minor proportion, with only 8 identified objects. A wider description of these astrophysical sources, their classification and characteristics is given in Chapter 2.

The journey throughout the decades of research and discoveries in gamma-ray astronomy is given in this chapter, including a description of the technology used in modern Cherenkov detectors and gamma-ray satellites such as NASA's *Fermi* mission. A summary of the most important developments in the last 60 years is shown in Figure 1.2 as a time line. The history of gamma-ray astronomy is presented below, for space-based instruments see Section 1.2.1 and for ground-based gamma-ray observatories see Section 1.3.6.

1.2 Space-based Gamma-ray Astronomy

1.2.1 Early history

During the 1960s, the first efforts to detect gamma-rays from space were made, including balloon experiments and detectors on board satellites.

Explorer-11 was the starting point of gamma-ray astronomy research from Earth-orbiting satellites (See Figure 1.3). Designed to detect gamma-rays of energy > 50 MeV, it was launched on April 27th, 1961 (Kraushaar and Clark, 1962). *Explorer-11* detected the first hints of gamma-ray emission from our Galaxy at 100 MeV (Kraushaar et al., 1965).

Between 1962 and 1978, the Orbiting Solar Observatory (OSO) programme from NASA launched and operated a series of satellites focused on the study of the Sun's radiation in the UV, X-ray and gamma ray bands, although some non-solar experiments were also included. The *OSO-3* satellite (1967-1969) was equipped with a multi-layer scintillation detector, build of layers of CsI and plastic. It also contained a Cherenkov counter sensitive to gamma-rays above 50 MeV (Kraushaar

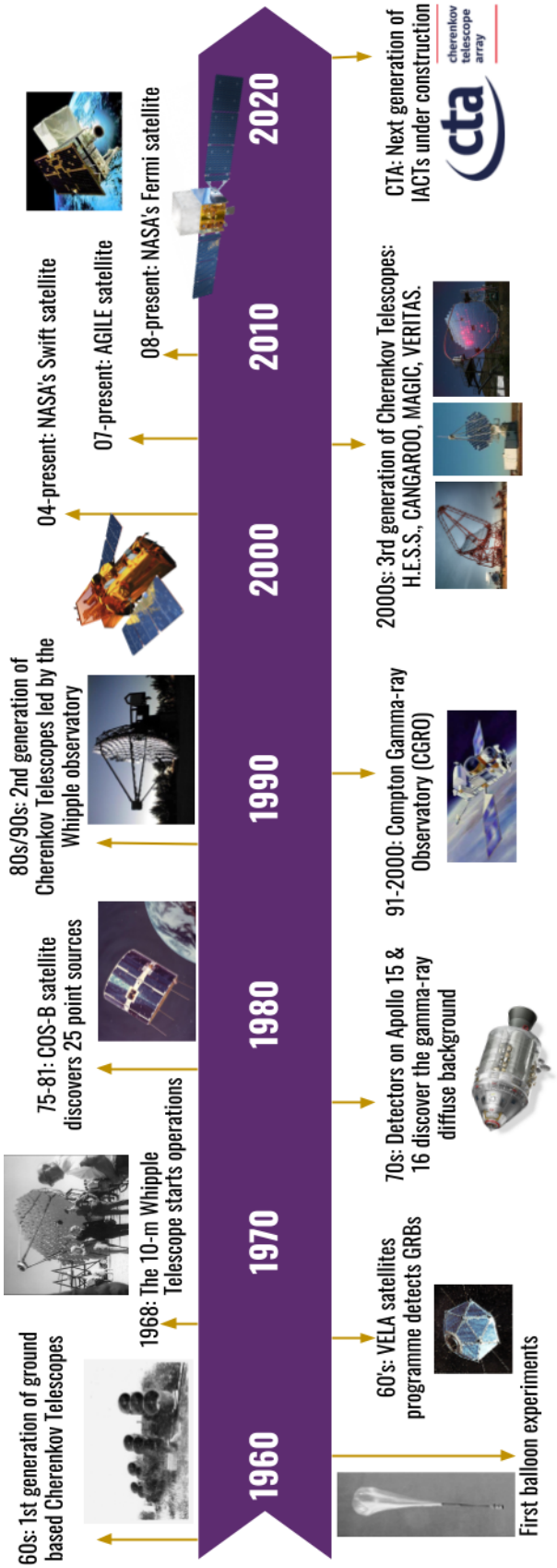

Figure 1.2: The evolution of gamma-ray astronomy (space-based and ground-based) over the last 60 years. Info credit: Robert Naeye and David Thompson, NASA; `https://www.nasa.gov/mission_pages/GLAST/main/timeline.html`, last accessed on 01/08/22.

Figure 1.3: Archive photo of *Explorer-11*; this satellite marked the beginning of space-based gamma-ray astronomy. *Explorer-11* detected the first extraterrestrial gamma-rays in a seven-month mission during 1961. Image Credit: NASA, `https://nssdc.gsfc.nasa.gov/nmc/spacecraft/display.action?id=1961-013A`, last accessed on 01/08/22.

et al., 1972). The *OSO-3* satellite confirmed the existence of Galactic emission from cosmic-ray interactions, and discovered the diffuse gamma-ray background (Kraushaar et al., 1972).

The *Vela* project started as a military project for the U.S. Department of Defense in 1959 to monitor gamma-ray pulses emitted by nuclear weapon tests in space and the Earth's atmosphere (Singer, 1965). A series of satellites were deployed during the 60's and 70's (see Figure 1.4), and serendipitously detected the first ever recorded Gamma-ray Burst (GRB) event on July 2, 1967 (Klebesadel et al., 1973). In total, the *Vela* series detected 16 other GRB events (Klebesadel et al., 1973). Since then, much research has been done to explain the origin of these mysterious events (Kumar and Zhang, 2015), including the catalogues from several dedicated instruments on board space missions.

During the early 1970s, gamma-ray spectrometers mounted on board *Apollo-15* and *Apollo-16* measured the cosmic gamma-ray diffuse background in the 300 keV to

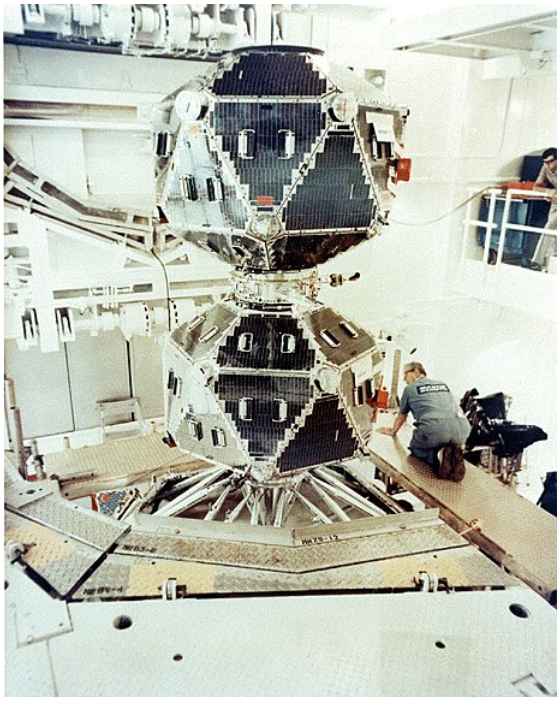

Figure 1.4: *Vela-5A* and *Vela-5B* satellites getting ready before their mission. The two satellites were separated after launch. The *Vela* series were deployed during the 60's and 70's. *Vela-5A/B* and *Vela-6A/B* recorded 16 GRB events between July 1969, and July 1972 (Klebesadel et al., 1973). Image Credit: Los Alamos National Laboratory, `https://heasarc.gsfc.nasa.gov/docs/vela5b/vela5b_images.html`, last accessed on 01/08/22.

27.5 MeV band (Trombka et al., 1973), while the *Apollo-16* spectrometer detected a gamma ray burst during its transit to the moon (Trombka et al., 1974). The *Vela-6A* satellite detected the same burst, which was thus the first example of a burst seen by two separate spacecrafts (Klebesadel et al., 1973). These same instruments helped to map the gamma-ray spectrum emitted from radioactive elements on the lunar surface (Adler et al., 1973).

On another front, during a 6 year span (1975-1981), the ESA satellite *COS-B* (Bignami et al., 1975) mapped the gamma-ray sky (See Figure 1.5). This pioneer initiative was the first ESA mission dedicated to a single experiment, the study of gamma-ray emission sources. During its first 3 years of operation, the *COS-B* satellite also completed a gamma-ray map of the Milky Way disc (Mayer-Haselwander et al., 1980), shown in Figure 1.6. The data recorded by the *COS-B* satellite was

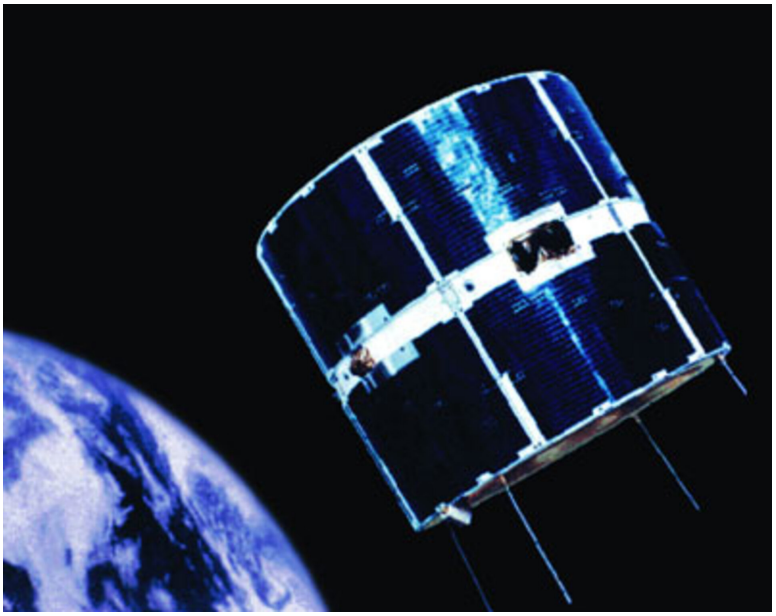

Figure 1.5: Artist's impression of the *COS-B* satellite orbiting the earth. *COS-B* was operating between 1975 and 1981, performing a survey of the gamma-ray sky and providing the first gamma-ray map of the Milky Way. Image Credit: Photo Archive ESA, `https://www.esa.int/ESA_Multimedia/Images/1998/01/Cos-B_in_orbit`, last accessed on 01/08/22.

used to create a catalogue of around 25 new gamma-ray point-sources (Swanenburg et al., 1981), including some extragalactic sources, like the first AGN of the blazar type, 3C 273 (Hermsen et al., 1981), and pulsars (Buccheri et al., 1983).

At the end of the decade some gamma-ray instruments to study GRBs were included on board space missions, like the Soviet-French experiment SIGNE-2MS on the *Venera 11*, *Venera 12*, and *PROGNOZ-7* spacecrafts (Barat et al., 1981). The *Venera* missions travelled to Venus with a separation of 0.5 Astronomical Units (AU) between September 1978 and April 1980. This was the first time that an experiment used identical detectors simultaneously on separate spacecrafts over interplanetary distances. During these missions, the SIGNE-2MS experiment confirmed 49 GRBs, resulting in a catalogue of such events recorded between September 1978 and January 1980 (Diyachkov et al., 1983; Atteia et al., 1987). The KONUS detectors were also mounted on the *Venera 11* and *Venera 12* spacecrafts. These instruments recorded the duration, intensity and distribution of 143

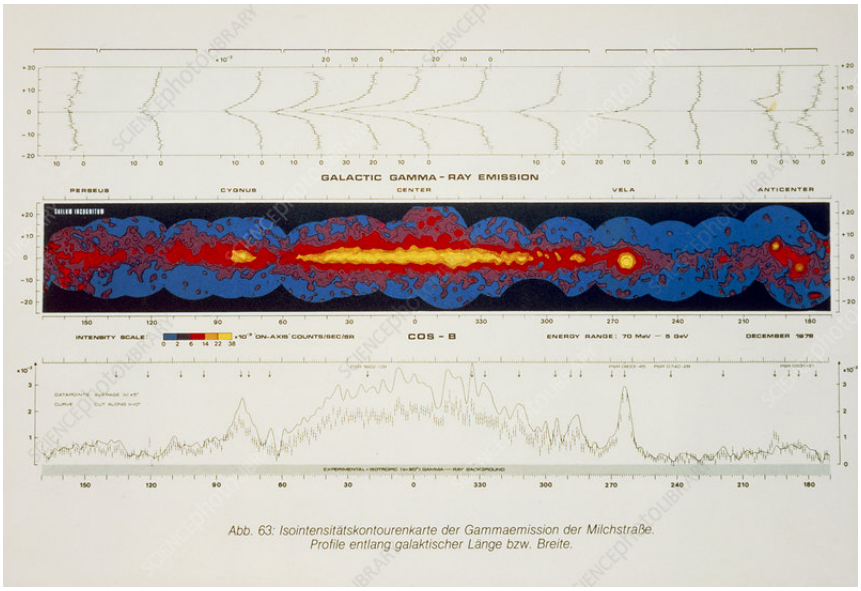

Figure 1.6: Gamma-ray sky map of the Milky Way based on data recorded by the *COS-B* satellite. The colours represent the intensity of the gamma ray emission from blue (faintest) through purple and red to yellow (brightest). Image Credit: Science Photo Library ESA, `www.sciencephoto.com/media/332270/view/cos-b-gamma-ray-map-of-the-band-of-the-milky-way`, last accessed on 01/08/22.

bursts during a span of 384 days (Mazets et al., 1981). The locations of 58 sources were determined with the KONUS data and helped to imposed new restrictions for theoretical models on the origin and nature of GRBs (Mazets and Golenetskii, 1981).

Launched in May 1978, the *Pioneer Venus* spacecraft is another good example of on board detectors in space missions. It carried twelve instruments in total, most of them dedicated to investigating the Venusian atmosphere. However, a gamma-ray burst detector was added with the intention of recording the temporal and spectral characteristics of cosmic gamma-ray bursts (Klebesadel et al., 1980). Most of the instruments, including the gamma ray burst detector, were still operating when the spacecraft entered the atmosphere of Venus on October 8, 1992. A total of 225 GRBs were detected between September 1978 and July 1988; a catalogue was published by Chuang (1990).

The data from the early space missions and satellites confirmed the existence of a

Figure 1.7: Archive photo of the *Venera* satellite series. The SIGNE-2MS and the KONUS detectors were mounted on the Soviet satellites to search for gamma-ray bursts at the end of the 1970s. Image Credit: NASA, `https://heasarc.gsfc.nasa.gov/docs/heasarc/missions/venera1112.html`, last accessed on 01/08/22.

gamma-ray background, produced the first gamma-ray sky map and resulted in the detection of a small number of point-sources. However, the poor resolution of the instruments made it impossible to identify many of the detected point-sources and for this the world had to wait for the next generation of gamma-ray observatories.

Entering the 1990s, NASA's *CGRO* mission was essential to take a step further in gamma-ray astronomy. Launched on April 5th, 1991, *CGRO* was in orbit and collecting data for 9 years (Gehrels and Shrader, 2000). Equipped with 4 multi-purpose instruments: BATSE, EGRET, COMPTEL, and OSSE; this mission covered 6 orders of magnitude in energy, from 30 keV to 30 GeV. A diagram of the *CGRO* satellite with its 4 instruments is shown in Figure 1.9.

BATSE (Pendleton et al., 1992) was an all sky monitor sensitive from about 20-600 keV. BATSE detected more than 2,700 GRBs (Kaneko et al., 2006) showing that these events can occur all over the sky with no sign of an underlying structure in the distribution, which supported the idea of an extragalactic origin. It also helped to classify the GRB events in two broad categories: long bursts (lasting more than 2 seconds) and short bursts (staying below the 2 second limit in duration).

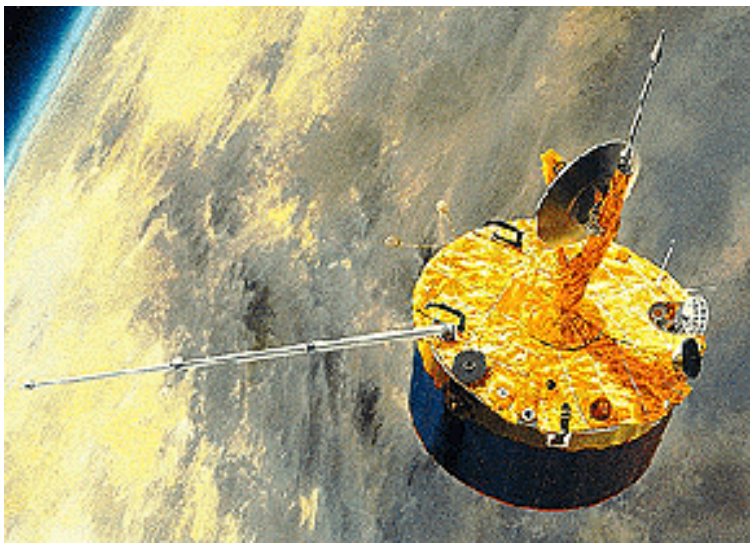

Figure 1.8: Artist's impression of the *Pioneer Venus Orbiter*. A a gamma-ray burst detector incorporated to the spacecraft registered 225 gamma-ray burst events between September 1978 and July 1988. Image Credit: NASA, `https://heasarc.gsfc.nasa.gov/docs/heasarc/missions/pvo.html`, last accessed on 01/08/22.

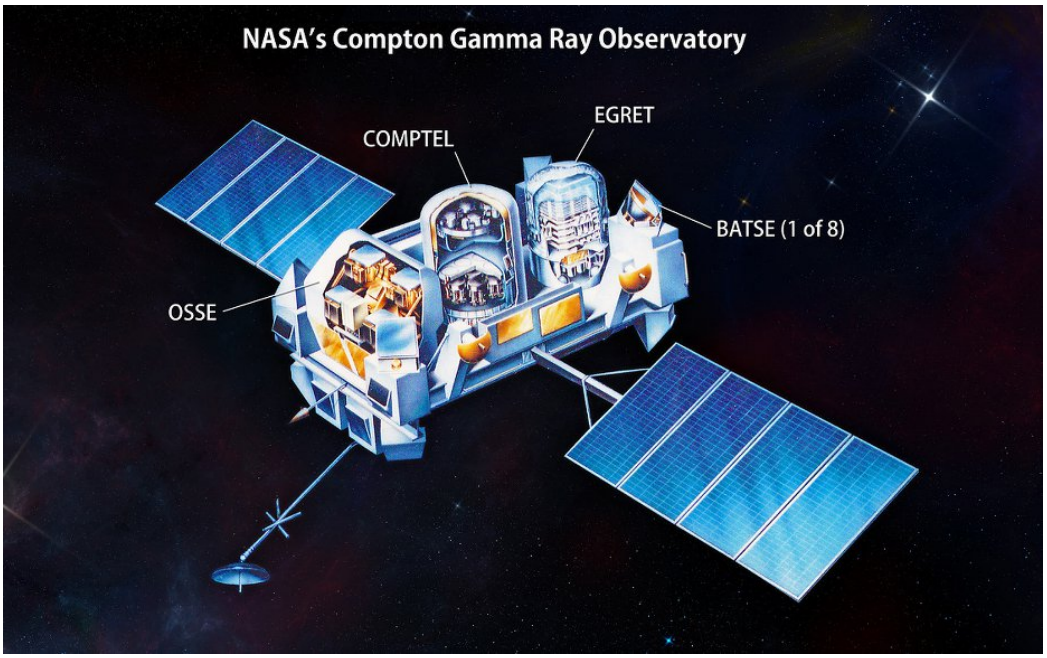

Figure 1.9: The CGRO satellite carried 4 instruments to study the gamma-ray sky: BATSE, EGRET, COMPTEL and OSSE. The *CGRO* satellite was in orbit for 9 years and represented a step further in gamma-ray astronomy research. Image credit: NASA, `https://astrobiology.nasa.gov/missions/cgro/`, last accessed on 01/08/22.

In addition, the EGRET instrument (Kanbach et al., 1989), was designed to detect gamma-rays in the 30 MeV to 20 GeV energy range and mapped the entire HE gamma-ray sky in the search for new sources. At the end of its mission, the 3rd EGRET catalogue was released, listing 271 detected point-sources (EGRET Collaboration, 1999), of which 66 were identified as blazars; there were also 5 pulsars, 1 radio galaxy, 27 potential blazars and 170 unidentified sources found. A revised version of the catalogue using reprocessed data at energies above 100 MeV was released in 2008 (Casandjian and Grenier, 2008), with a total of 188 sources. Among the potential counterparts, 53 were spatially coincident and catalogued as blazars, 13 as radio pulsars, 13 as Supernova Remnants (SNRs), 9 as Pulsar Wind Nebulae (PWN), and 19 as other radio sources. For the revised version of this catalogue, the usage of an improved interstellar background model, alongside two Galactic cosmic-ray density distribution models, removed of 107 sources listed in the 3rd EGRET catalogue. The vast majority of the apparent sources from the 3rd EGRET catalogue were unidentified and marked as possibly extended or confused.

During its operation time, EGRET measured the flux of dozens of blazars and found them to be quite variable, recording flares on time scales of days to hours. EGRET also obtained the first sensitive map of the diffuse gamma-ray emission of the Milky Way (EGRET Collaboration, 1997), and made a reliable measurement of the isotropic, extragalactic diffuse emission (EGRET Collaboration, 1998).

The COMPTEL instrument (COMPTEL Collaboration, 1993a) was designed to detect gamma-rays in an energy range between 1 and 30 MeV, and was the first telescope to perform a complete survey of the sky at 1-3 MeV, 3-10 MeV and 10-30 MeV energies (Schoenfelder et al., 1996). The COMPTEL instrument also observed the Crab and Vela pulsars, and performed gamma-ray spectroscopy studies of the Galactic distribution of Aluminum-26, which showed that stars are forming in the Milky Way. (COMPTEL Collaboration, 1993b).

Finally, the OSSE instrument (OSSE Collaboration, 1992) was included on the *CGRO* satellite to undertake observations of astrophysical sources between 0.05

and 10 MeV. The OSSE instrument mapped the electron-positron annihilation radiation from the centre of the Galaxy, and detected gamma-ray emission signals from X-ray binaries, blazars and Seyfert galaxies, among other highlights. More information about the discoveries and highlights of the OSSE instrument can be found in OSSE Collaboration (1993).

The *Swift*, *AGILE* and *Fermi* satellites represent the current generation of spaced-based telescopes. They have been operational over the last 10+ years, providing constant updates and catalogues from the gamma-ray sky, redefining our ideas about the high energy astrophysical processes and continue to search for the most energetic phenomena in the Universe.

1.2.2 *Swift*

At the beginning of the 21st century, the NASA launched the *Swift* satellite on November 2004, a first-of-its-kind mission dedicated to study, locate and follow-up GRBs. The Neil Gehrels *Swift* observatory (Swift Collaboration, 2004) was designed to cover an energy range between 0.2-150 keV, with three on board instruments that work together to record the information in multiple wavebands: gamma-ray, X-ray, optical, and UV. The BAT, XRT, and UVOT instruments on board the *Swift* satellite are shown in Figure 1.10.

The BAT is a large Field of View (FoV) detector (1.4 sr) with an energy range of 15–150 keV. The BAT operates in two different modes: survey mode and burst mode. In survey mode, it collects hard X-ray count rate data in 5-min time intervals for 18 energy bins. When a burst occurs and the count rate goes above the expected background and constant sources, BAT switches into burst mode and searches for the position using a photon-by-photon detection. Within the first 10 seconds of detecting a burst, the BAT can calculate an initial position for the GRB event to an accuracy of about 3 arcmin. The BAT FoV always includes the XRT and UVOT FoV, which allows data to be collected simultaneously in X-rays and UV/Optical

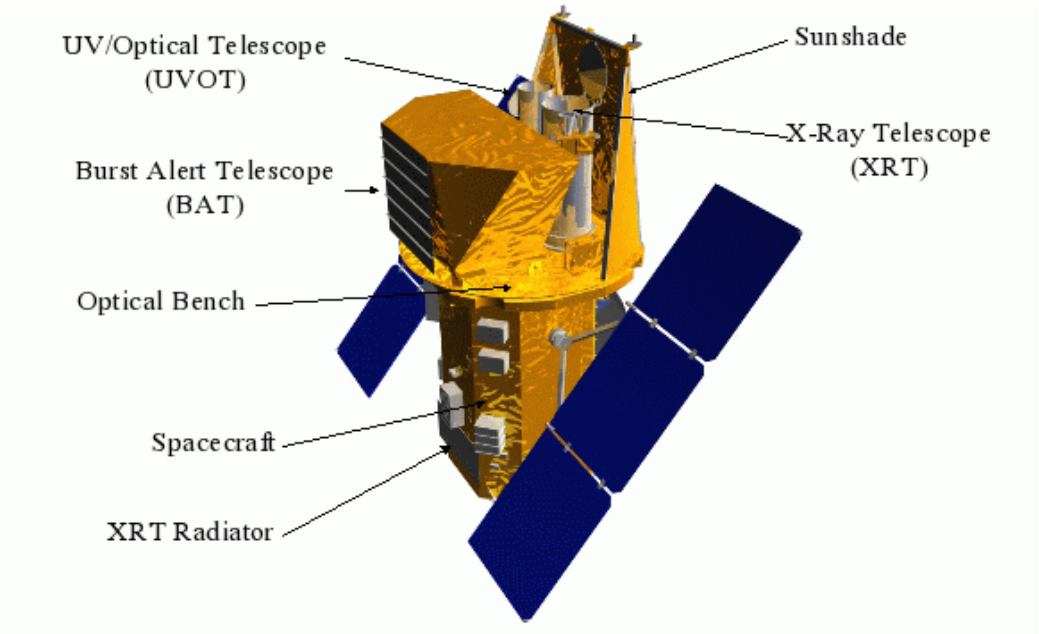

Figure 1.10: The Neil Gehrels *Swift* observatory with its 3 instruments on board: BAT, XRT, and UVOT. This first-of-its-kind mission is dedicated to study GRB phenomena in multiple wavebands: gamma-ray, X-ray, optical, and UV. Image credit: Swift Collaboration (2004).

emission for long duration GRBs. If a burst is detected, the location and intensity of the event are immediately sent to the Gamma-ray Coordinates Network (GCN) to be distributed worldwide. Further technical information about the BAT instrument is given in Swift Collaboration (2005a).

The second instrument on board the *Swift* satellite is the XRT (Swift Collaboration, 2005c), an X-ray imaging spectrometer, which can operate completely autonomously from the other 2 instruments. XRT was designed to measure the fluxes over 7 orders of magnitude, record the GRBs detected by the BAT instrument and follow the afterglow emission over days or weeks. The XRT instrument enables *Swift* to determine GRB positions with an accuracy of 5 arcseconds and is designed to provide an automated source detection and position within 100 seconds after a burst alert from the BAT instrument. XRT can also measure the redshift of GRBs using the Fe line emission or other spectral features. The XRT instrument possesses a broad-band energy range of 0.2-10 keV, a FoV of 23.6×23.6 arcmin^2, and

an angular resolution of 18 arcsec.

Finally the UVOT (Swift Collaboration, 2005b) is the third instrument on board the *Swift* satellite. With an aperture of 30-cm diameter, a wavelength range of 170-600 nm and a FoV of 17×17 arcmin^2, the UVOT was designed to capture the UV and optical photons from the afterglow of gamma-ray bursts, in short (35 to 70 seconds after the burst) and long term (days after the burst) observations. The UVOT is also able to detect and measure the GRBs redshift using the optical and UV grisms in a range of $1.5 < z < 4.5$.

Since its launch, *Swift* has been detecting about 100 GRB events per year. This mission has revealed burst properties never seen before and shed light on the nature of short-duration bursts. Its list of discoveries include: the validation of theoretical models suggesting that short GRBs (< 2 seconds) come from neutron star mergers (Swift Collaboration, 2017), high-redshift GRB detections (z > 6) (Swift Collaboration, 2006, 2009a,b), including GRB 090429 (Swift Collaboration, 2011), the most distant event measured at $z \sim 9.2$, the discovery of a new ultra-long class of events, whose high-energy emissions endure for hours (Levan, 2015); among others. An extensive review about the scientific highlights and the impact of *Swift* can be found in Castro-Tirado and Gorosabel (2021); Gehrels et al. (2009).

1.2.3 *AGILE*

The *AGILE* satellite is a high-energy astrophysics Italian Space Agency mission launched in April, 2007. *AGILE*'s main scientific goal is to provide a powerful and cost-effective mission to study AGNs, GRBs, pulsars, Galactic compact objects, SNRs, TeV sources, unidentified gamma-ray sources, diffuse Galactic gamma-ray emission, and high-precision timing studies. *AGILE* combines a sensitive (30 MeV to 50 GeV) Gamma-ray Imaging Detector (GRID) made out of Silicon-Tungsten trackers, a Cesium Iodide mini-calorimeter (sensitive in the range 350 keV–100 MeV), and an anti-coincidence system (AGILE Collaboration, 2009). In addition,

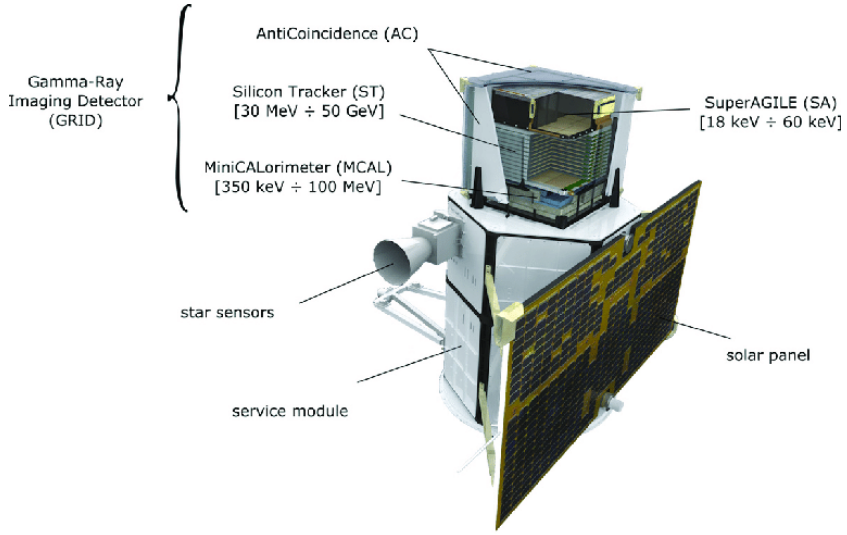

Figure 1.11: Schematic view of the *AGILE* satellite and its scientific instruments: a sensitive gamma-ray detector, a mini-calorimeter, a hard X-ray imager and an anticoincidence module. *AGILE* was launched in April, 2007 and is still in operation. Image credit: AGILE Collaboration (2019).

a hard X-ray detector named Super-*AGILE* was included to observe the energy range between 18–60 keV. The Super-*AGILE* detector consists of an additional plane of four Silicon square units positioned on top of the GRID Tracker and provides simultaneous observations from astrophysical sources in the hard X-ray domain. A schematic view of the *AGILE* satellite is shown in Figure 1.11.

AGILE was provided with a very large FoV for both the gamma-ray imaging detector (2.5 sr, i.e., $\sim$ 5 times larger than EGRET) and the hard X-ray imager (1 sr); an excellent imaging capability in the energy range of 100 MeV to 50 GeV (improving EGRET's angular resolution by a factor of 2); and excellent timing capabilities, with very short deadtimes for gamma-ray detections (< 200 μs).

During its first 10 years of operations *AGILE* has surveyed the gamma-ray sky detecting many bright active galaxies, discovered several new gamma-ray pulsars, discovered gamma-ray emission from the microquasar Cygnus X-3, surveyed the Galactic plane with simultaneous hard X-ray/gamma-ray capability, and discovered emission up to 100 MeV from Terrestrial Gamma-Ray Flashes (Tavani, 2019).

Quantity	LAT	GBM
Instrument	Pair conversion detector	NaI and BGO scintillators
Energy range	20 MeV to >300 GeV	8 keV to 40 MeV
Field of view (FoV)	> 2 sr	> 8 sr
Angular resolution	$< 3.5°$ (at 100 MeV) $< 0.15°$ (for E>10 GeV)	typically 1°
Energy resolution	$< 10\%$ (1σ, on-axis)	<10% (1σ, 0.1-1 MeV)
Source location	< 0.5' (1σ radius, >100 MeV)	$\sim 3°$ (Final GRB) $\sim 15°$ (Alert GRB)
Timing accuracy	1 μs	2 μs
Average deadtime per event	< 100 μs/event	<10 ms/count
Sensitivity	$< 6 \times 10^{-9}$ cm^{-2} s^{-1}	< 0.5 cm^{-2} s^{-1}

Table 1.1: LAT and GBM performance specifications. Info credits: NASA; `https://fermi.gsfc.nasa.gov/science/instruments/table1-2.html`, `https://fermi.gsfc.nasa.gov/science/instruments/table1-1.html`, last accessed on 01/08/22.

1.2.4 The *Fermi* Gamma-ray Space Telescope

Fermi gamma-ray observatory is equipped with two experiments on board (see Figure 1.12). The first one is the LAT, a pair conversion detector that provides several improvements in angular resolution, FoV, energy resolution, collecting area, and a sensitivity factor > 30 in comparison to its predecessor, the EGRET instrument on board the CGRO mission. The *Fermi* satellite also contains the GBM, which was designed to detect transient gamma-ray outbursts at energies between 8 keV and up to 40 MeV. The *Fermi*-GBM is the descendant of the BATSE instrument on board the CGRO satellite. Both instruments are reviewed in more detail in the following subsections, with special interest in the *Fermi*-LAT, as it is one of the tools used all along this work and a key part in the methodology to model blazar gamma-ray emissions (see Section 3.3 and Section 4.2).

1.2.4.1 The Large Area Telescope (LAT)

The *Fermi*-LAT is the primary instrument on board the *Fermi* satellite, and is a gamma-ray detector operating from an energy range of 20 MeV and over 300 GeV. The primary interaction of photons above 20 MeV with matter is pair conversion. A unique signature for gamma-rays can be detected via the reconstruction of the

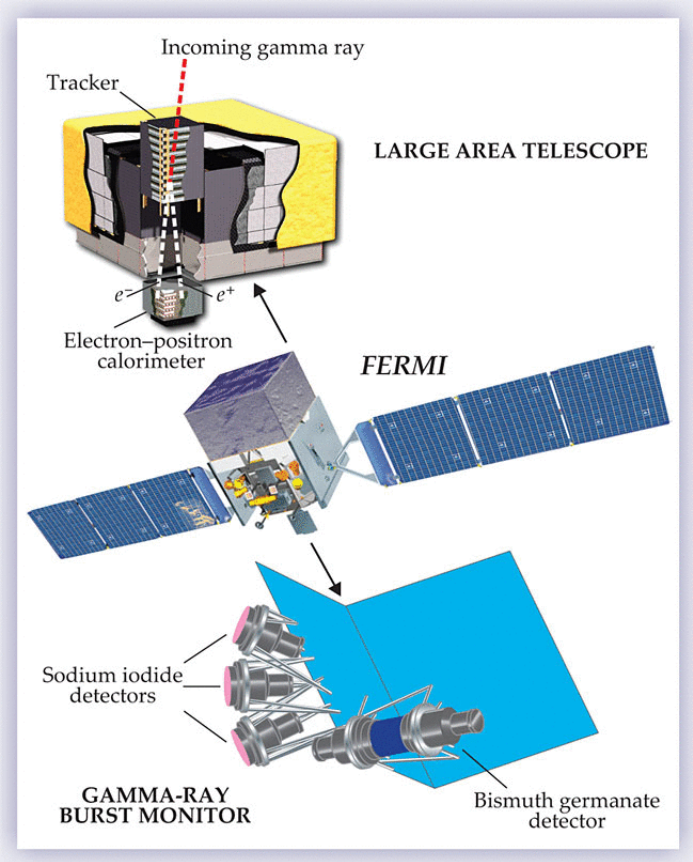

Figure 1.12: Diagram of the two experiments on board the *Fermi* Gamma-Ray Space Telescope. The LAT measures arrival directions and energies of photons with energies from about 20 MeV and above 300 GeV. The GBM is designed to detect low-energy transient gamma-ray outbursts at energies from 8 keV and up to 40 MeV. Image credit: Michelson et al. (2010).

trajectories of the resulting e^+e^- pairs, allowing a determination of the incident photon direction. To accomplish this, the LAT comprises a tracker system that consists of a 4×4 matrix of towers, with 18 silicon strip detector modules, with interleaved tungsten foils for converting gamma-ray photons to electron-positron pairs, initiating electromagnetic showers within the detector. The charged particles ionise the silicon as they pass through the layers, providing measurable tracks. A calorimeter detector subsystem provides an estimation of the gamma-ray photon energy. The LAT is surrounded by an anti-coincidence detector, consisting of scintillator tiles, which detect charged particles and issue a veto signal. The LAT has a FoV of about 2.4 sr with an angular resolution of less than 1° for energies

above 1 GeV. Table 1.1 summarises the LAT's main performance characteristics. Further details on the *Fermi*-LAT mission are given in Fermi-LAT Collaboration (2009) and Fermi-LAT Collaboration (2012).

The LAT performance is described by a set of Instrument Response Functions (IRFs), which take into account the photon's energy, arrival direction and the conversion point within the instrument, among other important parameters for the LAT's event reconstruction. The IRFs version used for the gamma-ray data analysis within this thesis are Pass8 (Fermi-LAT Collaboration, 2013c). The Pass8 IRFs provide a full reprocessing of the entire mission dataset, including improved event reconstruction, a wider energy range, better energy measurements, and significantly increased effective area in comparison to previous versions (Fermi-LAT Collaboration, 2018b).

The IRFs are obtained through dedicated Monte Carlo simulations. A large number of gamma-ray events are simulated covering all possible combinations in the photon incidence angle and energy range. LAT's IRFs include three terms: the detector's effective area, the angular resolution given by the PSF, and the energy dispersion. The IRFs are internally partitioned into FRONT and BACK conversion types. Starting from the front of the instrument, the LAT tracker has 12 layers of 3% radiation length tungsten converters (FRONT section), followed by 4 layers of 18% radiation length tungsten converters (BACK section). These sections have intrinsically different PSFs, the thicker BACK section maximises the conversion efficiency at the cost of additional particle scattering and worse angular resolution. The PSF for FRONT events is $\sim \times 2$ better than the PSF for BACK events (See Figure 1.13).

The Pass8 IRFs performance plots are presented below:

- Point Spread Function (PSF).- The LAT PSF as a function of energy is shown in Figure 1.13. The curves are derived entirely from Monte Carlo simulations. The PSF improves with energy, reaching a 68% containment angle of $< 1^{\circ}$

above 1 GeV. For energies $> 10^5$ MeV the function is bounded by the spatial resolution of the LAT's Silicon Tracker. The difference between FRONT, BACK and TOTAL=FRONT+BACK conversion type events is shown in Figure 1.13.

- Effective Area.- The LAT's effective area for normal incidence gamma-ray photons is given in Figure 1.14. The key parameters that influence efficiency are the inclination angle of the incident photon and its energy. Above 1 GeV the effective area reaches maximum values. The plot shows the curves for FRONT (in red), BACK (in blue) and TOTAL=FRONT+BACK (in black) conversion types.

- Energy Resolution.- The energy dispersion of the LAT is defined in terms of the fractional difference between the reconstructed energy the true energy of the events: $\Delta E/E$. The LAT's energy resolution is defined the minimum 68% containment interval of the energy dispersion. The energy resolution for the Pass8 IRFs is shown in Figure 1.15. As in the previous plots, curves are shown for the 3 types of event conversion. Multiple scattering of the electron-positron pair by the LAT's components when the conversion happens in the FRONT section results in a worse energy resolution. The deflection and energy dispersion scales with the material thickness, which limits the FRONT energy resolution at low energies.

Since the start of regular observations in August 2008 the LAT has continuously scanned the sky, providing all-sky coverage every two orbits (around 3 hours). The LAT data have been used for rapid notification of gamma-ray transient events, monitoring of variable sources, constructing a full catalogue of celestial gamma-ray sources, measuring the diffuse gamma-ray background, indirect searches for Dark Matter (DM) signals, GRBs, EBL studies, SFH studies, Lorentz invariance tests, solar physics, terrestrial gamma-rays, and many other interesting scientific projects. Unfortunately, the large number of results and publications makes it

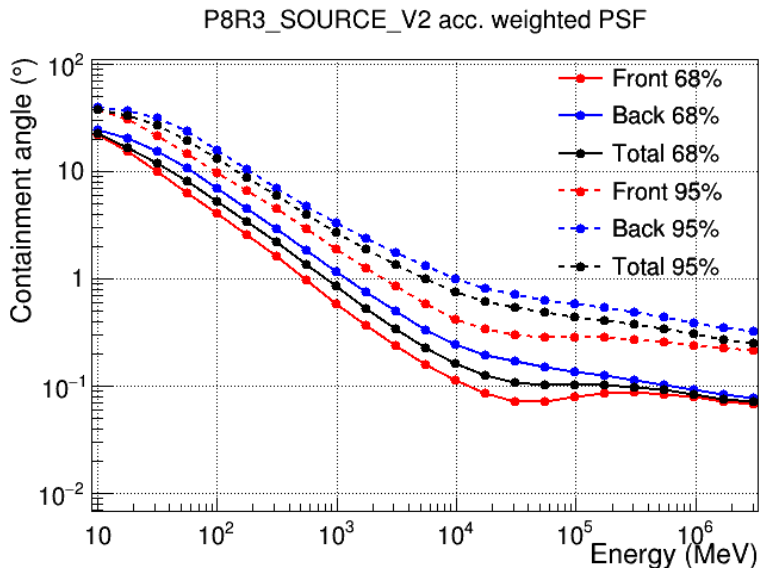

Figure 1.13: Point spread function (PSF) for the LAT as a function of energy. The 68% (solid lines) and 95% (dotted lines) containment angle are plotted for the FRONT (red), BACK (blue) and TOTAL (black) conversion types. Image credit: Fermi-LAT Collaboration; `www.slac.stanford.edu/exp/glast/groups/canda/lat_Performance.htm`, last accessed on 01/08/22.

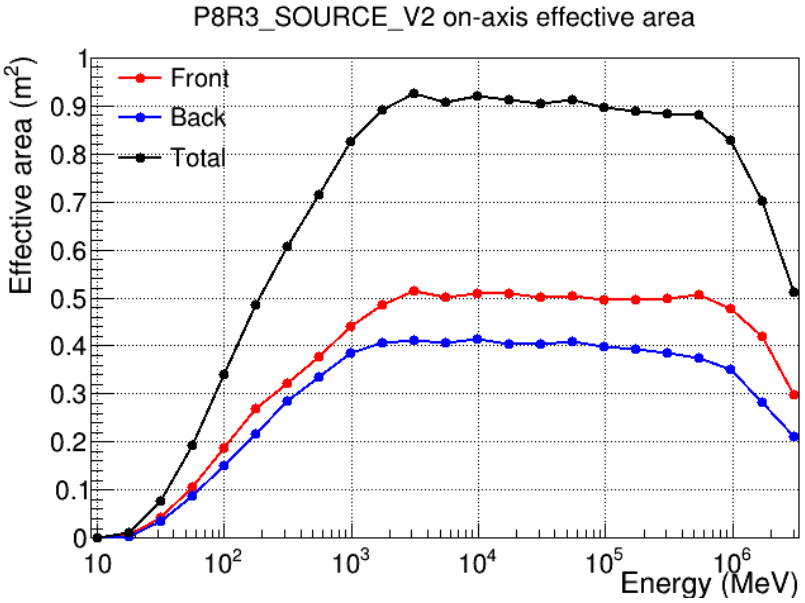

Figure 1.14: LAT effective area as a function of energy for normal incidence photons. The colours represent the three different options of conversion event types: FRONT conversion (in red), BACK conversion (in blue) and TOTAL (Front+Back in black). Image credit: *Fermi*-LAT Collaboration; `www.slac.stanford.edu/exp/glast/groups/canda/lat_Performance.htm`, last accessed on 01/08/22.

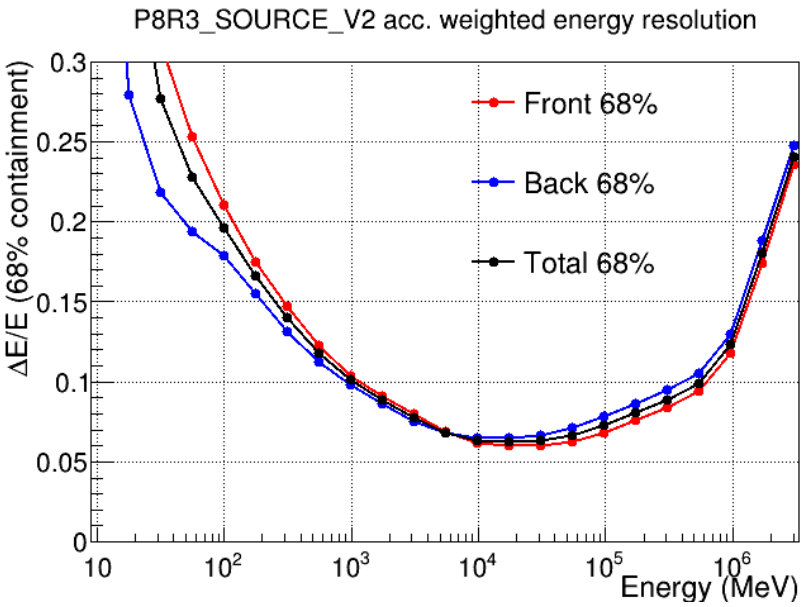

Figure 1.15: Energy resolution as a function of energy for the *Fermi*-LAT Pass8 IRFs. The 68% containment (half width of the reconstructed incoming photon energy) curves are shown for: FRONT (in red), BACK (in blue) and TOTAL (in black) event type conversion. The energy dispersion effect through the layers of the LAT limits the FRONT energy resolution at low energies. Image credit: *Fermi*-LAT Collaboration; `www.slac.stanford.edu/exp/glast/groups/canda/lat_Performance.htm`, last accessed on 01/08/22.

extremely difficult to explore and cite them all here. Some of the main science highlights achieved by the *Fermi*-LAT are:

- The *Fermi*-LAT catalogue.- The LAT has observed more than 5,000 individual gamma-ray sources and elaborated catalogues with periodic versions and updates. The 4FGL-DR2 catalogue (Fermi-LAT Collaboration, 2020a) contains a list of the gamma-ray sources detected in the first 10 years of operations of *Fermi*-LAT (August 4, 2008, to August 2, 2018). The analysis was performed in the energy range from 50 MeV to 1 TeV. The catalogue contains 5,787 sources and can be downloaded in the official *Fermi*-LAT website: `https://fermi.gsfc.nasa.gov/ssc/data/access/lat/10yr_catalog/`, last accessed on 01/08/22.

  The 4FGL-DR2 catalogue has been used in this thesis as part of the analysis of selected gamma-ray sources (flaring blazars) in Sections 3.3 and 4.2.

- The LAT detected a flaring of gamma-ray emission from the blazar TXS 0506+056 (Tanaka et al., 2017), which was associated at the $\sim 3\sigma$ significance level with the detection of a HE neutrino event by the IceCube neutrino alert system (IceCube Collaboration et al., 2018). This joint detection marked the first plausible association of combined neutrino and gamma-ray emission from a flaring blazar. Further information from this event is given in Section 1.5.2.

- Other catalogues of AGN sources.- (Fermi-LAT Collaboration, 2015, 2020b), and transient sources (Fermi-LAT Collaboration, 2021) have also been compiled with LAT data. Numerous flaring blazar episodes have been reported, and multi-wavelength studies have been performed in collaboration with LAT.

- Gamma-rays from neutron star merger.- The *Fermi*-LAT Collaboration participated in the historic gamma-ray detection of the GRB 170817A on August 2017. This event was associated with a binary neutron star merger (GW 170817; LIGO Scientific Collaboration and Virgo Collaboration (2017)), representing the first joint detection of gravitational and electromagnetic radiation from a single source.

- Crab Nebula studies.- *Fermi*-LAT data revealed the Crab Nebula as a variable source in gamma-rays. Flares with sub-hourly variability indicated inner acceleration sites where electrons reach VHE energies (Mayer et al., 2013).

- Confirmation of SNRs as cosmic-ray accelerators.- The LAT detected a distinctive gamma-ray signature of neutral pion decay, confirming the hypothesis that protons can be accelerated to cosmic-ray energies in young SNRs (Fermi-LAT Collaboration, 2013b).

- Galactic gamma-rays.- On the Galactic plane, the *Fermi*-LAT has provided the most detailed view to date of the Galactic centre gamma-ray emission (Fermi-LAT Collaboration, 2016a), a study performed in the energy range

between 1-100 GeV, including a point-source catalogue of the region. Studies of the diffuse Galactic gamma-ray emission (Fermi-LAT Collaboration, 2010b), Galactic pulsars (Fermi-LAT Collaboration, 2017a), PWN (Fermi-LAT Collaboration, 2013a), and SNRs (Fermi-LAT Collaboration, 2016b), have also been conducted with LAT gamma-ray observations.

- The discovery of the *Fermi* Bubbles.- The *Fermi*-LAT Collaboration announced the discovery of two large, extended gamma-ray and X-ray emitting zones above and below the Galactic centre, also called *Fermi* bubbles (Dobler et al., 2010; Su et al., 2010). Their formation, structure, particle acceleration and gamma-ray emission mechanisms have been studied in several publications since then, for example: Fermi-LAT Collaboration (2014), Yang et al. (2018), Herold and Malyshev (2019).

1.2.4.2 The Gamma-ray Burst Monitor (GBM)

The *Fermi* mission has on board a second instrument in addition to the LAT: the GBM, designed to detect and locate GRB transient events. The GBM includes two sets of detectors: twelve sodium iodide (NaI) scintillators, and two cylindrical bismuth germanate (BGO, $Bi_4Ge_3O_{12}$) scintillators. The NaI detectors are sensitive in the lower end of the energy range, from a few keV to about 1 MeV, while the BGO detectors cover an energy range of $\sim$ 150 keV to $\sim$ 40 MeV, providing an energy range overlap with the NaI scintillators (at the lower energy end), and with the LAT (at the high energy end).

The GBM uses counting rates in the different detectors to measure the energy spectra and celestial locations of bright gamma sources, particularly brief transients such as GRBs. The characteristic sensitivity of the GBM are comparable with the LAT, which enables it to detect GRB events at LE and HE simultaneously with similar statistical significance. Furthermore, the GBM provides GRB locations over a wide FoV, that can be used to re-point the LAT at particularly interesting bursts.

When the GBM detects a GRB event, it will calculate a preliminary position and spectral information for telemetry to the ground and inform the LAT for with a prompt notification.

A summary of the instrument performance characteristics is given in Table 1.1 and further information about the GBM can be found in Fermi-GBM Collaboration (2009) and Paciesas (2011). The combination of the GBM and the LAT instruments represent a powerful tool to study the GRB spectra among the whole gamma-ray sky.

Since its launch in 2008, the GBM has recorded almost 2 transient events per day, and identified 2,356 as cosmic GRBs.

- *Fermi*-GBM Gamma-Ray Burst Catalogue.- The GBM science team periodically releases source catalogues listing the information about source detections compiled over the years. The latest release is the 4th GBM GRB catalogue (Fermi-GBM Collaboration, 2020), which contains observations from the first 10 years of operations. During this period, 176 GRBs were jointly detected by the LAT and the GBM instruments.

- GRB 170817A.- One of the most important GRB detections, is the well known GRB 170817A (Fermi-GBM Collaboration, 2017), which is associated with a Gravitational Wave (GW) signal from a neutron star merger (GW 170817, LIGO Scientific Collaboration and Virgo Collaboration (2017)). The GBM detected the burst less than 2 seconds after the Laser Interferometer Gravitational-Wave Observatory (LIGO) experiment detected the signal from GW 170817. The near simultaneous detection of the electromagnetic emissions and GW signal from this event confirmed the hypothesis that neutron star mergers can produce short GRBs. The follow-up observations revealed a bright optical transient and delayed X-ray and radio emissions in the following days. A search of 10 years of GBM data identified 13 GRB candidates with similar characteristics (Fermi-GBM Collaboration, 2019), from

which it is predicted there would be one triggered event of this type per year in LIGO.

- GBM Pulsar Monitoring. – Although the GBM is not a pointed or imaging instrument, it can be used as a monitor for known sources, such as pulsars. The history of pulse frequency and pulsed flux measured with the GBM are available in the webpage: `https://gammaray.nsstc.nasa.gov/gbm/science/pulsars.html`, last accessed on 01/08/22.

After more than a decade of fruitful operations, the LAT and GBM instruments have contributed to improve our understanding of HE and VHE astrophysical phenomena. The *Fermi* satellite remains in good operating condition, and both on board instruments are expected to prolong their operation for the upcoming years, acting as key players for major advances in multi-messenger studies.

1.3 Ground-based Gamma-ray Astronomy

The gamma-ray signals coming from space-based instruments correspond mainly to an energy range below 100 GeV in energy, up to which they become statistics-limited. The complementary detectors sited on Earth expand this range up to TeV energies using the imaging atmospheric Cherenkov technique, combining large optical telescopes and modern electronics to capture the Cherenkov radiation from atmospheric air showers initiated by VHE gamma-rays (E $>$ 100 GeV). In the following pages the physics of air showers, the detection techniques, the early years of ground-based gamma-ray astronomy and the current telescopes are quickly reviewed.

1.3.1 Cherenkov radiation

Cherenkov radiation is a phenomenon that occurs when a charged particle travels faster than the phase velocity of light in a dielectric medium. It was first discovered

by Marie Curie in 1910 (Curie, 1959), who observed a blue glow in her experiments with concentrated radium, although this was not reported until 1941. Some years after the discovery, Pavel Alexeevich Cherenkov and Sergei Vavilov studied this phenomenon experimentally and described it (Cherenkov, 1934). Later on, a theoretical framework was developed by Igor Tamm and Ilya Frank (Tamm and Frank, 1937). For the discovery and the interpretation of this effect, Frank, Tamm and Cherenkov were awarded the Nobel prize in 1958. A brief description of Cherenkov radiation follows.

When a charged particle travels through a medium, it attracts opposite charges in its path, such that the surrounding space is polarised. Then, as the particle moves forward, at each point of its path in the material is quickly neutralised (depolarised) and emits radiation as the electron moves away. If the particle's speed is slower than the electromagnetic radiation in the medium, the wave fronts interfere destructively. If the particle moves faster than the radiation emitted along its trajectory, then the wave fronts of the emitted radiation interfere constructively producing a characteristic blue glow that can be observed in a transparent medium. Frank-Tamm's formula predicts that Cherenkov radiation is not emitted in all directions but only in the direction of electron movement.

By constructing the envelope of the coherent wave fronts, the phenomenon can be seen as a cone of light (Figure 1.16). If n is the refractive index of the medium, $\beta = \frac{v}{c}$ the quotient between the velocity of the particle v and the speed of light c, then it is possible to describe the angle generated by the Cherenkov cone as:

$$\cos(\theta) = \frac{\frac{ct}{n}}{\beta ct} = \frac{1}{n\beta} \tag{1.1}$$

The threshold condition for observing the Cherenkov effect is obtained when $\theta = 0$

$$\beta \geq \frac{1}{n} \tag{1.2}$$

If the particle is relativistic ($\beta \sim 1$) the so-called Cherenkov angle can be roughly

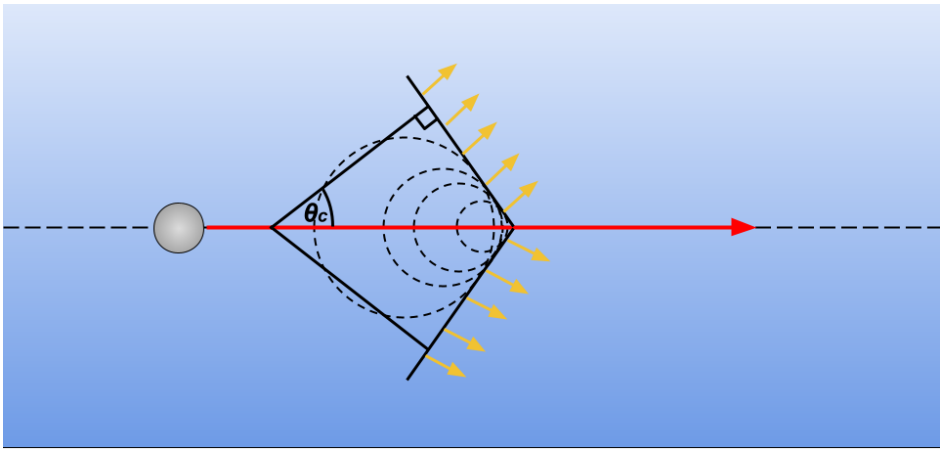

Figure 1.16: Schematic of the Cherenkov angle produced by a charged particle (grey circle) moving in a transparent medium. The red arrow represents the direction of the charged particle and the yellow arrows are the direction of the emitted Cherenkov photons.

approximated as:

$$\theta_C = \arccos\left(\frac{1}{n}\right) \tag{1.3}$$

For example, pure water has a refractive index of $n = 1.33$ which corresponds to a Cherenkov angle of $\theta_{C,\text{water}} = 41.4\ ^\circ$. For pure ice the refractive index is n =1.31, which gives a Cherenkov angle of $\theta_{C,\text{ice}}$ =40.2 °. Meanwhile, for air the refractive index changes with the density, but in general $\theta_{C,\text{air}} \leq 1.5\ ^\circ$. The refractive index of air can be expressed as a function of the pressure (P) and temperature (T):

$$(n_{\text{air}} - 1) = 2.92 \times 10^{-4} \times \frac{P}{P_0} \times \frac{288.15\text{K}}{T} \tag{1.4}$$

where P_0 is the atmospheric pressure at sea level. Due to the evolution of the atmospheric density with altitude, the Cherenkov angle increases from $\sim 0.2^\circ$ at an altitude of 30 km to $\sim 1.5^\circ$ at sea level.

Frank and Tamm deduced the Cherenkov effect from electromagnetic theory, which considers that part of the particle's energy is transformed into visible light. In this way the Frank-Tamm formula allows the calculation of the number of emitted photons (Engelfried, 2011, 2006):

$$\frac{d^2N(x,\lambda)}{dxd\lambda} = 4\pi^2\frac{(Ze)^2}{hc^2\lambda^2}\left(1 - \frac{1}{n^2\beta^2}\right) \tag{1.5}$$

where $N(x, \lambda)$ is the number of photons generated in a given wavelength range, λ is the wavelength, Z is an integer that describes the number of electric charges e and h =6.62607×10^{-34} kg m^2 s^{-1} is Planck's constant.

Using the trigonometric relation $\sin^2(\theta)+\cos^2(\theta) = 1$ and fixing $Z = 1$ (for example an electron, or a muon) we can change Eq. 1.5 into:

$$\frac{d^2N(x,\lambda)}{dxd\lambda} = \frac{2\pi}{\lambda^2}\alpha \sin^2(\theta_c) \tag{1.6}$$

where $\alpha = \frac{2\pi e^2}{hc} \approx 1/137$ and $hc = 1.239 \times 10^{-4}$ eV cm^{-1} .

It is possible to integrate the expression between the wavelength limits (λ_1, λ_2) of a detector to calculate the number of photons emitted per length unit:

$$\frac{dN(x)}{dx} = 2\pi\alpha \sin^2(\theta_c) \int_{\lambda_1}^{\lambda_2} \frac{d\lambda}{\lambda^2} = 2\pi\alpha \sin^2(\theta_c)(\frac{1}{\lambda_1} - \frac{1}{\lambda_2}) \tag{1.7}$$

On the other hand we have that

$$E = h\nu = \frac{hc}{\lambda} = \frac{2\pi\hbar c}{\lambda} \tag{1.8}$$

So we can use the following expression to change the λ dependence into an energy dependence

$$\frac{d^2N(x,E)}{dxdE} = \frac{d^2N(x,\lambda)}{dxd\lambda}\frac{d\lambda}{dE} = \frac{\lambda^2}{2\pi\hbar c}\frac{d^2N(x,E)}{dxdE} \tag{1.9}$$

Then the Eq. 1.6 is written as:

$$\frac{d^2N}{dxdE} = \frac{\alpha}{\hbar c}\sin^2(\theta_c) \tag{1.10}$$

Which can be used to calculate the energy loss of the charged particle by each photon emitted per unit length (Engelfried, 2006).

Physicists realised that these equations could be used to determine the velocity, direction and deposited energy of a charged particle in a transparent medium by measuring the produced Cherenkov radiation. This idea revolutionised experimental particle physics and astrophysics; today Cherenkov radiation is a critical element in numerous applications, including the ground-based gamma-ray telescopes and neutrino detectors used to this day.

1.3.2 Detecting air showers

In 1912, Victor Hess discovered the first evidence that extraterrestrial ionising radiation (cosmic-rays) constantly impinges on the Earth's atmosphere (Hess, 1912), and in 1939 Pierre Auger discovered Extensive Air Shower (EAS) initiated by cosmic-rays hitting the atmosphere (Auger et al., 1939). Ever since then, different techniques have been developed to detect and study the origin of this cosmic ray flux. When a HE cosmic-ray or importantly VHE gamma-ray photon arrives at the Earth's upper atmosphere, it triggers an EAS, a cascade of relativistic charged particles travelling through the air. These secondary charged particles produce the characteristic Cherenkov radiation that can be observed with IACTs.

The electromagnetic showers initiated by VHE gamma-ray photons are governed by two elementary processes: pair production of $e^{\pm}$ by the conversion of high energy photons, and Bremsstrahlung radiation of the $e^{\pm}$ particles. A simplified model to describe the electromagnetic shower development is given by a repeated symmetrical branching process of electrons, positrons and gamma-rays, with the charged particles radiating gamma-rays, and the gamma-ray converting into electron-positron pairs subsequently. Both processes have a characteristic radiation length, defined as (de Naurois and Mazin, 2015):

$$X_0 = \left[4\alpha r_e^2 \frac{N_A Z^2}{A} \ln\left(183 Z^{-1/3}\right) \right]^{-1} \text{ g cm}^{-2} \tag{1.11}$$

where A is the atomic mass and Z the atomic number of the material, while N_A is Avogadro's number, $\alpha = 1/137$ is the fine structure constant and r_e the classical electron radius. For air, the radiation length is $X_0 \approx 36.5$ g cm^{-2}.

The characteristic splitting length d_{split} over which an electron loses half its energy is related to the radiation length X_0 as $d_{\text{split}} = X_0 \ln 2$. After splitting n times, the total number of particles in the shower is 2^n, and the energy per particle is $E_0/2^n$, where E_0 is the primary gamma-ray energy. The shower continues to develop until the average electron energy drops to $E_c = 84$ MeV, the critical energy below which ionisation losses dominate.

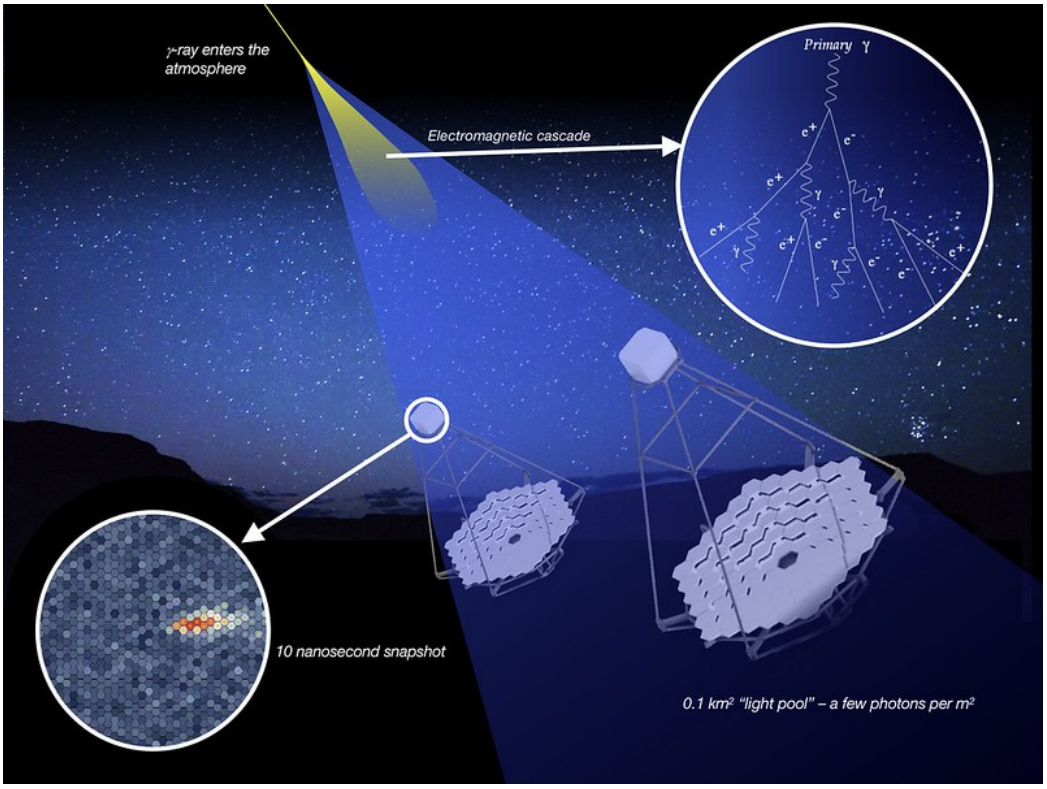

Figure 1.17: Schematic of a gamma-ray shower in the atmosphere being detected by a modern ground-based telescope using the imaging atmospheric Cherenkov technique. Image credit: CTA Consortium; `https://www.flickr.com/photos/cta_observatory/`, last accessed on 01/08/22.

For an altitude of 10 km, a gamma-ray photon in the energy range of 100 GeV to 1 TeV can produce a Cherenkov light cone that extends all the way down to the surface with a radius of 120 m (See Figure 1.17). The light pool is defined as the area on the ground with nearly constant density of Cherenkov photons. The typical photon density expected from 1 TeV gamma-rays is $\sim$ 100 photons/m^2, with a wavelength that peaks around $\lambda \sim 300 - 350$ nm. The Cherenkov photons arrive in short pulses that last $\sim$ 10 nanoseconds.

HE cosmic-rays (protons and charged energetic nuclei) also generate EAS when they hit the atmosphere. The produced secondary charged particles also initiate electromagnetic sub-showers as they propagate. Hadronic showers are more complicated to describe than electromagnetic showers; they comprise several components that depend on different characteristic lengths: hadronic components resulting

from the collision of cosmic-rays with atmospheric nuclei, electromagnetic components resulting from the decay of neutral pions into gamma-rays, and HE muons and atmospheric neutrinos resulting from the decay of charged mesons. The cosmic-ray events are predominant by a factor of 10^3 in comparison to the gamma-ray events. This implies a large background that must be separated from the gamma-ray signals; the fundamental physics of the shower development provides a way to do this.

1.3.3 Air shower parameterisation and discrimination

As a result of the large transverse momentum transfer in hadronic interactions, the shower development is broad and irregular, therefore the Cherenkov images coming from a cosmic-ray origin are wider, with no preferred orientation, and less regular than the images captured for the electromagnetic gamma-ray showers. Figure 1.18 shows the difference between a gamma-ray induced electromagnetic shower and a hadronic shower with a cosmic-ray origin.

The electromagnetic shower image has an elliptical shape with the shower direction aligned with its major axis, which makes possible to discriminate the gamma-ray originated cascades from the cosmic-ray background. The distortion effects produced by the Earth's magnetic field also affect the gamma/hadron separation analysis, because these can make gamma-ray showers look more hadron-like.

Most of the data analysis techniques that modern IACTs (see Section 1.3.8) use to discriminate between gamma-ray or cosmic-ray induced showers are based on the parameterisation of the shower images. In 1985, based on pioneering Monte Carlo simulations, A.M. Hillas proposed to reduce the recorded images to a few parameters, corresponding to the modelling of the induced gamma-ray shower by a two-dimensional ellipse (Hillas, 1985). The parameters used are: the length L and width w of the recorded ellipse, the image centre of gravity, the nominal distance d (angular distance between the centre of the camera and the image centre of

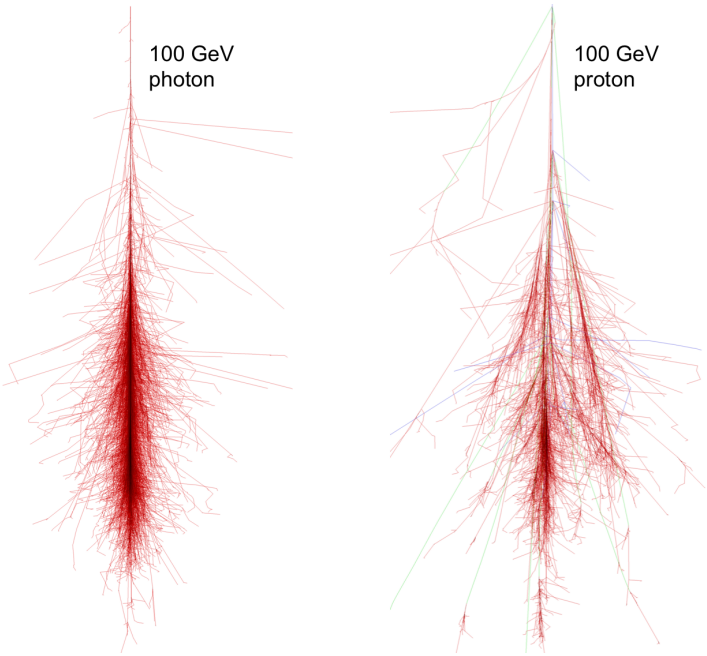

Figure 1.18: Difference between an electromagnetic shower induced by a 100 GeV gamma-ray photon (left) and a hadronic shower induced by a 100 GeV proton (right). The gamma-ray shower is narrow and axially symmetric, while the hadronic shower is broader, irregular and contains electromagnetic sub-showers. The images were produced using Monte Carlo simulations in CORSIKA. Image credit: Holder (2021).

gravity), the image size (total charge of photo-electrons), the azimuth angle ϕ and the orientation angle α of the ellipse main axis. These parameters are illustrated in Figure 1.20.

A shower moving along the axis of the telescope will produce an image concentrated at the centre of the camera's focal plane. A shower moving parallel to the telescope's axis but displaced from the telescope by some distance on the ground produces approximately elliptical images in the focal plane with the major axis of the ellipse pointing towards the centre of the camera. On the other hand, showers arriving with a tilted angle relative to the telescopes's axis will be an ellipse whose major axis does not point towards the centre of the camera. The isotropic cosmic-ray background can be rejected based on the reconstructed arrival directions and shapes of the hadronic showers.

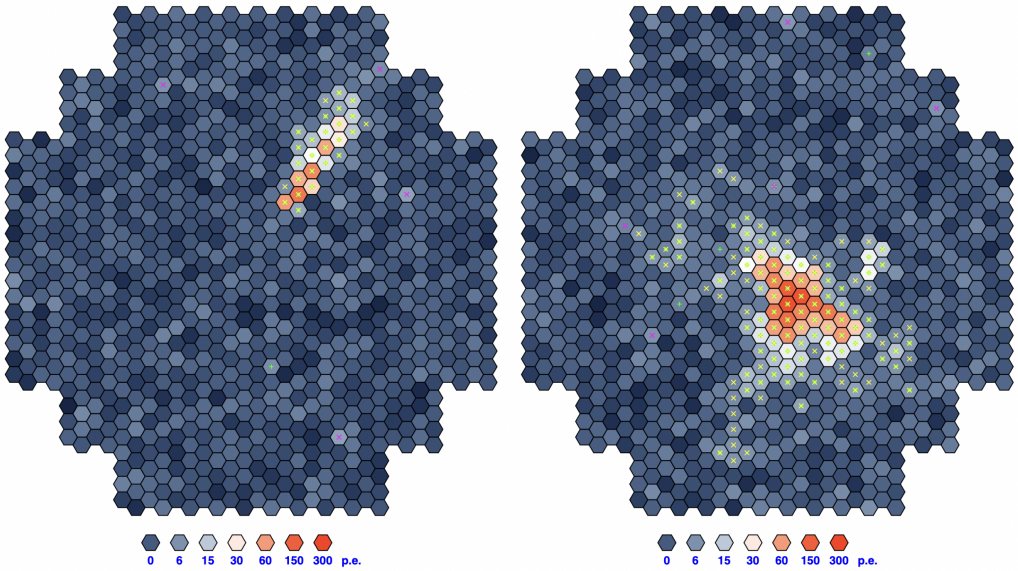

Figure 1.19: Example images of a detection from a 1 TeV gamma-ray induced electromagnetic shower (left) and a hadronic shower from a 2.6 TeV proton (right). The electromagnetic shower image has an elliptical shape with the shower direction aligned with its major axis. The hadronic shower image has a broader, irregular shape and no preferred direction. Image credit: Völk and Bernlöhr (2009).

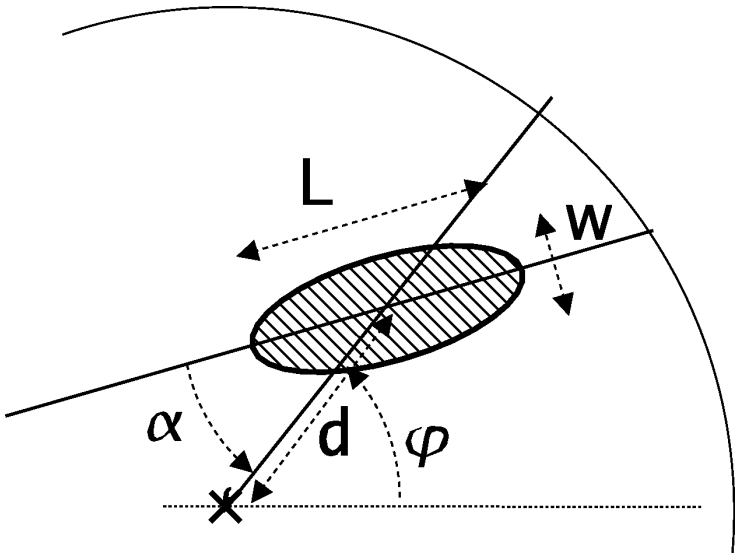

Figure 1.20: Diagram of an electromagnetic shower as seen by an IACT. The image shower shape and orientation is described by a set of few parameters: L and w are the length and width of the recorded ellipse respectively, d is the angular distance between the centre of the camera and the image centre, ϕ represents the azimuth angle and α is the orientation angle of ellipse main axis. Image credit: de Naurois and Mazin (2015).

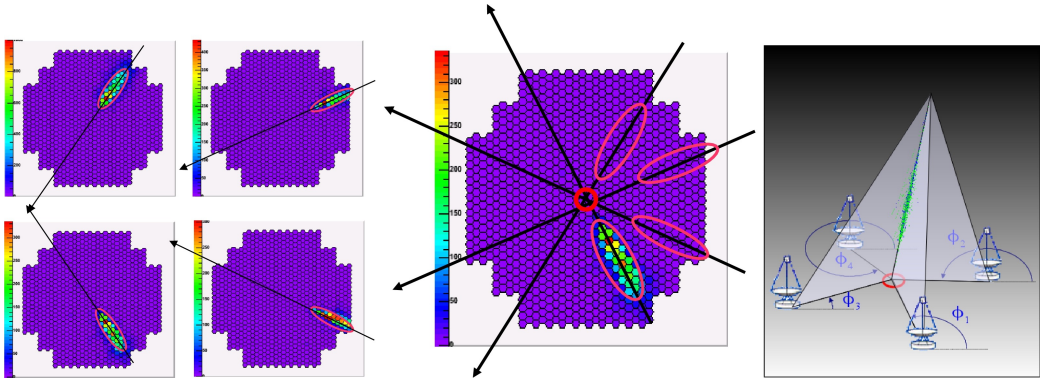

Figure 1.21: Stereoscopic observation of an extensive air shower with an hypothetical array of 4 telescopes (left). The geometric reconstruction of the shower provides the direction of the incoming particle (red circle at the centre) by projecting the main axis of the images recorded by the different telescopes (middle). The intersection of the planes containing the shower tracks and the telescopes provides the shower impact on the ground (right). Image credit: de Naurois and Mazin (2015).

1.3.4 Stereoscopic observations

Stereoscopic observations use several telescopes to observe the same shower in coincidence. Observing an EAS in stereoscopic mode allows a unique determination of the shower direction by performing the geometrical reconstruction of the images recorded in all triggered telescopes and projecting them into a single plane. The intersection point of the images' main axes provides the shower direction. The shower impact point is obtained by using a geometrical intersection of the planes containing the telescopes and the shower axes. This is shown in Figure 1.21, where a simulated air shower is observed at the same time by multiple telescopes. The shower's energy can be estimated from a weighted average of each single telescope energy reconstruction. In addition, the shower's parameters also provide a discrimination criterion based on the extension (width and length) of the recorded images.

Stereoscopic observations allowed a better assessment of the shower geometry, and yielding an increase in sensitivity of a factor of $\sim \times 10$ in comparison to a single telescope of the same size. The angular and energy resolution were also improved

with this technique as well as the background rejection. The stereoscopic technique has become the standard for current and future gamma-ray observatories.

Another advantage of the stereoscopic technique is the suppression of atmospheric muon background events created in the cosmic-ray interactions. The atmospheric muons leave an image only in a single telescope from the array, but not in the rest. A stereo trigger condition enables muon-induced images to be eliminated almost completely. The telescopes can thus operate with a good background rejection even close to the threshold energy limit.

1.3.5 Magnetic field effects

The Earth's magnetic field affects the measurements of the Cherenkov light from EAS. The Lorentz forces generated over the charged particles bend their trajectories, producing a lateral spread over the shower development and stretching the Cherenkov light pool, which in consequence decreases the photon density and reduces the chances of triggering the observations, specially for low energy showers.

The magnetic force depends on the angle formed between the trajectory of the charged particle and the Geomagnetic field. The Lorentz force on the particles deflects their trajectories, according to:

$$F_L = q(\vec{v} \times \vec{B}) \propto qB_p \tag{1.12}$$

where q is the charge of the particle, $\vec{v} = (v_x, v_y, v_z)$ is the particle's velocity vector, $\vec{B} = (B_x, B_y, B_z)$ is the magnetic field vector, and B_p is the magnetic field component perpendicular to the observation direction.

The perpendicular magnetic field component B_p can be calculated in terms of the zenith angle θ and an azimuth angle ϕ as:

$$B_p = (B_x^2(cos^2\theta + sin^2\theta sin^2\phi) - B_x B_z sin2\theta cos\phi + B_z^2 sin^2\theta)^{1/2} \tag{1.13}$$

where B_x and B_z are the horizontal and vertical components of the Geomagnetic field respectively. The B_x component is pointing to the local magnetic north, while

B_z is oriented downwards. Higher magnetic field intensities increase the energy thresholds and degrade the precision of the angular and energy resolution of the telescopes.

Because of the lateral spread on the air showers caused by the magnetic field, the recorded images appear distorted, which produces additional uncertainties on the reconstruction of the cascade, the estimated energy and arrival direction. As a result, it is more difficult to discriminate between electromagnetic and hadronic showers. Studies of the magnetic field strength and its influence are taken into account before the construction of major gamma-ray observatories.

1.3.6 Early history

The starting point of ground-based gamma-ray astronomy can be placed at the end of 1940's, when the British physicist, P. M. S. Blackett was conducting his research on the detection of high energy particles. He was the first person to propose the use of Cherenkov telescopes to detect extensive air showers produced by VHE particles hitting the upper atmosphere (Blackett, 1948).

In 1952, Galbraith and Jelley detected short light pulses from the night sky using a 25-cm parabolic mirror with a PMT attached at the focus (see Figure 1.22), proving that part of the night-sky background comes from the Cherenkov radiation produced by cosmic rays (Galbraith and Jelley, 1953). In follow-up experiments, Galbraith and Jelley looked for possible point-sources of cosmic radiation and pointed in the direction of Cygnus A, Cas A and the Crab Nebula for few nights, but without detecting any excess of Cherenkov photons (Galbraith and Jelley, 1955; Jelley and Galbraith, 1955).

In 1959 a major research programme started to develop in the Lebedev Institute of Moscow, lead by A.E. Chudakov and N.M. Nesterova. They were the first research team to confirm the existence of the night-sky Cherenkov pulses (Chudakov and Nesterova, 1955). Soon after, Chudakov set up an array of 4 detectors in

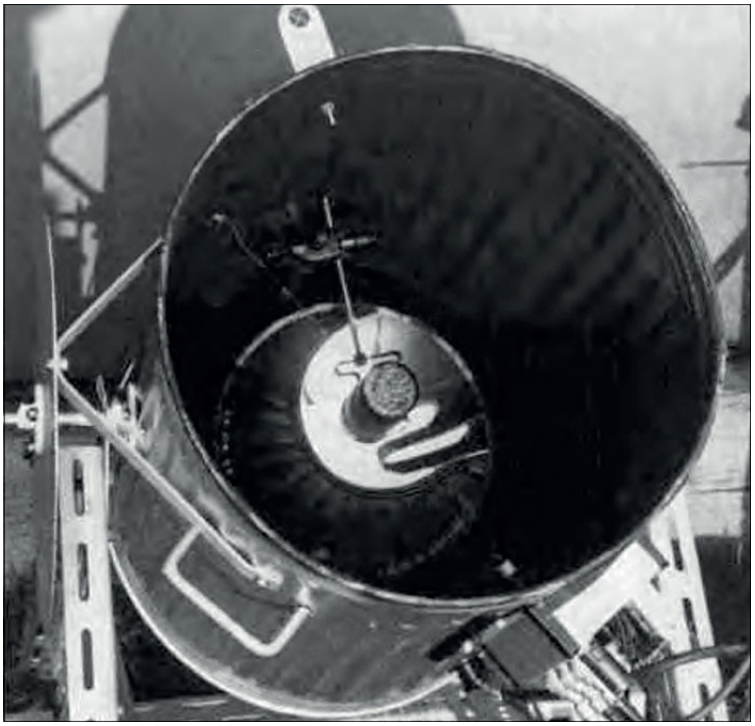

Figure 1.22: The first Cherenkov detector used by B. Galbraith and J. V. Jelley in 1953. A 25-cm parabolic mirror with a PMT attached at the focus inside a garbage can. Image credit: Jelley (1987).

Katsiveli, Crimea in collaboration with G.T. Zatsepin (Zatsepin and Chudakov, 1961). Each 1.5-m diameter telescope was arranged in a close pack to increase the photon collecting area. The array was then expanded to 12 detectors and were used in an observation campaign to search for prominent gamma-ray sources (see Figure 1.23). This array was the first instrument specially designed for VHE gamma-ray observations. In 1964, after 4 years of observations during the winter nights, no excess was found during the all sky search (Chudakov et al., 1963; Chudakov et al., 1965). The cosmic-ray background was too large for this first generation of telescopes and they could not discriminate between electromagnetic and hadronic showers.

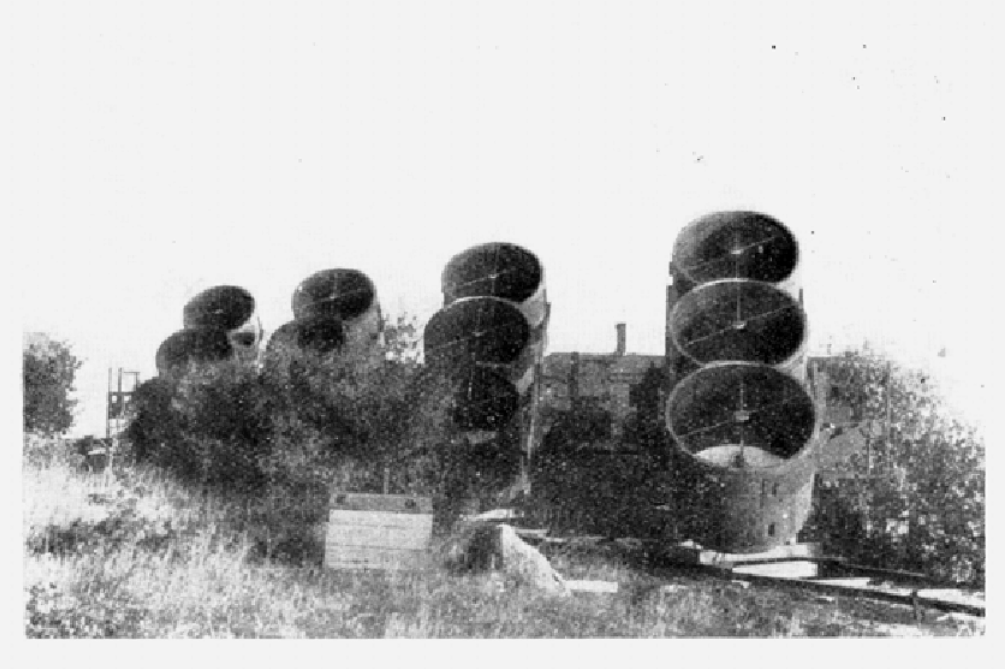

Figure 1.23: Gamma-ray telescope array built by Chudakov and Zatsepin in Katsiveli, Crimea. The site was in operation during 4 years (1960-1964) and it was the first instrument specially designed for VHE gamma-ray observations of cosmic origin, it had 12 mirrors with a diameter of 1.5 m each one. Image credit: Lidvansky (2006) .

1.3.7 First imaging telescopes

In 1968, a 10-m telescope (with a total reflecting area of 75 m^2) was completed at the Fred Lawrence Whipple Observatory in Mount Hopkins Arizona, USA. Figure 1.24 shows a photo of the opening day. During its first operational phase only a single PMT was used as a camera, and although the light collecting mirror was large, no source could be detected. The design transitioned from a single PMT camera, to a set of 2 PMTs in coincidence in 1972, and then a set of 3 PMTs with a guard ring of seven additional tubes in 1976. In 1977 T. C. Weekes and K. E. Turver proposed a multi-PMT camera design for the Whipple telescope (Weekes and Turver, 1977). Completed in 1983, the 37-pixel imaging camera covered a FoV of 3.5° and allowed images to be recorded from extensive air showers (Weekes, 1981). A methodology to discriminate between the gamma-ray induced electromagnetic showers from the cosmic-ray background (gamma/hadron separation)

Figure 1.24: Fred Whipple at Mount Hopkins Observatory's opening day in 1968. Image credit: F.L. Whipple Observatory, `https://ecuip.lib.uchicago.edu/multiwavelength-astronomy/infrared/tools/02.html`, last accessed on 01/08/22.

was also implemented during this time. The method was based on the combination of the shower image orientation (Weekes, 1981) and an analysis to evaluate the difference in images between gamma-ray and hadron showers (Stepanian et al., 1983).

In 1989, the Whipple Collaboration published the first successful detection (5σ significance) of VHE gamma-ray emission from the Crab nebula (Whipple Collaboration, 1989), 37 years after the initial observation of Cherenkov light pulses by Galbraith and Jelley. A series of upgrades in the following years provided the Whipple 10-m telescope with a 109-pixel camera and a 3.5° FoV that allowed the detection of the first TeV extragalactic gamma-ray source, the blazar Markarian 421 (Whipple Collaboration, 1995). The upgrades continued to increase the number of PMTs in the camera reaching 151 pixels and a FoV of 3.5° in 1996, then 331

pixels with a FoV of 4.8° in 1997 and finally a small-pixel, high-resolution camera of 490 pixels with FoV of 4.8° in 1999. The objective of the upgrades was to obtain an improvement in sensitivity, enhanced gamma/hadron separation and to lower the energy threshold. The improved Whipple telescope operated in an energy range of 300 GeV to 20 TeV with the last camera configuration.

Since the mid 2000's the telescope's primary concern was long-term blazar monitoring, including: Mrk421, Mrk 501, 1ES2344+514, 1ES1959+650, 1ES0229+200 and H 1426+428 (Pichel, 2009). The lessons learned during the operation of the Whipple telescope were incorporated into the design and construction of VERITAS (VERITAS Collaboration, 2006). Further information on the Whipple telescope can be found in Whipple Collaboration (2007).

After the successful detection of the Crab Nebula with the Whipple telescope in 1989 (Whipple Collaboration, 1989), gamma-ray telescopes were developed following the same design philosophy: the mirror diameters were increased up to the natural limitation, which helped to reduce the energy threshold of the telescopes; the number of PMTs and FoV in the camera designs were also increased for the imaging technique, which helped to improve the background rejection; and finally an array of telescopes working simultaneously in stereoscopic mode was implemented. Modern gamma-ray observatories have these 3 characteristics in common.

During the 80's and first years of the 90's there were different efforts to build Cherenkov telescopes around the world, this second generation of observatories were arrays with multiple individual reflectors on a single mount or a small array of single-reflector telescopes with few meters in diameter. There was an array with 6 reflectors built in Haleakala, Hawaii (Resvanis et al., 1987); 3 more telescopes (with 3 reflectors each one) at Potchefstroom in South Africa (Brink et al., 1991; Raubenheimer, 1995); a set of 18 individual telescopes in Pachmarhi India (Bhat et al., 1990), the ASGAT (ASGAT Collaboration, 1990) and THEMISTOCLE (THEMISTOCLE Collaboration, 1993) projects in Themis, France, that ended up merging into the Cherenkov Array at Themis (CAT) project (Degrange and

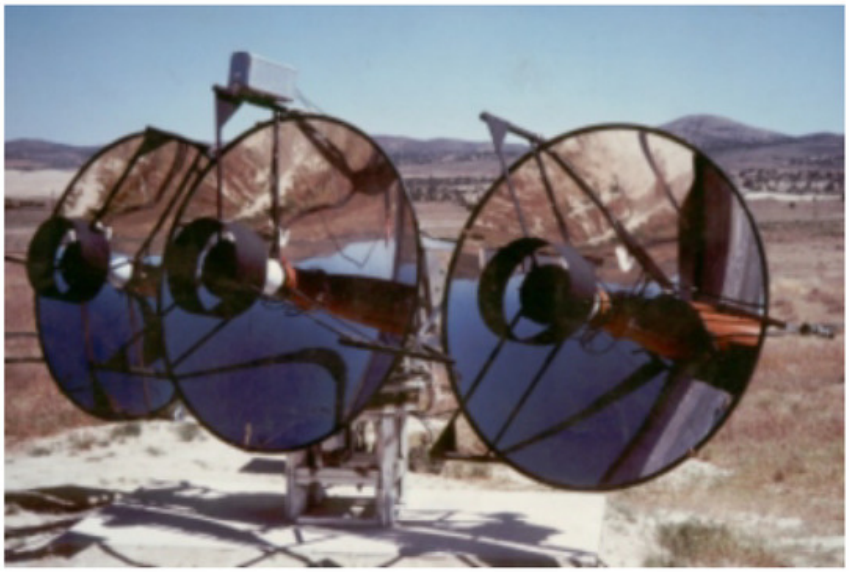

Figure 1.25: Mark I gamma-ray telescope at Dugway Proving Ground, Utah, USA. This was the first VHE gamma-ray telescope designed and built by the Durham group among the Mark series. Image credit: (Chadwick, 2021).

Paré, 1998; CAT Collaboration, 1998b) in 1996; and a triple-reflector telescope in Woomera, Australia (Clay et al., 1989).

Durham University experimented with the Mark I and Mark II telescope series located in Dugway, Utah, USA between 1981 and 1984. The Mark I telescope design had three 1.5-m diameter mirrors on a single mount operated in coincidence (see Figure 1.25), each mirror contained a 12.5-cm PMT with a FoV of $\sim 1.7^\circ$ as camera (Gibson, 1981). Four of these Mark I telescopes were built and deployed at Dugway. The Mark II telescope design also had three reflectors, but employed a matrix of small custom-built mirrors and used a 7.5-cm PMT with a FoV of $\sim 1.3^\circ$ in as a camera (Dowthwaite, 1987). The experience gained in the manufacturing process and during the operation of the Dugway telescopes provided the necessary empirical background for the upcoming Mark telescope series operated in Narrabri and La Palma on the following years.

The Mark III telescope was located in Narrabri, New South Wales, Australia starting operations in 1986 (see Figure 1.26). The site was recognised as a good spot for an observatory in the southern hemisphere, and the hunt for VHE gamma-ray sig-

Figure 1.26: Mark III gamma-ray telescope located in Narrabri, New South Wales, Australia. The Mark III consisted of a single mount with three 11-m^2 reflectors formed from 40+ smaller spherical mirrors made out of anodised aluminium supported by an aluminium honeycomb structure. Image credit: Durham University, Gamma-ray Group, `https://www.dur.ac.uk/cfai/vhegammaraygroup/grouphistory/australia/`, last accessed on 01/08/22.

nals from X-ray binary systems containing pulsars (Chadwick, 1987). The Mark III designed consisted of three 11-m^2 reflectors on a single mount, with each reflector formed by 43 (44 for the central dish) smaller spherical mirrors made out of anodised aluminium and provided with 4 7.5-cm diameter PMTs as camera (Brazier et al., 1989). The use of a reflective surface made out of anodised aluminium, supported by an aluminium honeycomb material structure, improved the reflectivity, endurance and lightweight of the mirrors for the Mark III observations (Chadwick et al., 1987) and upcoming telescopes. During its operation, Mark III observations found evidence for VHE gamma-ray emission from a number selected sources, including the X-ray binary systems Cen X-3 (Chadwick, 1987; Brazier et al., 1990b), Vela X-1 (Carraminana et al., 1989) and Sco X-1 (Brazier et al., 1990c), though these were not confirmed by later imaging telescopes.

Soon after, the Mark IV instrument was designed as a portable telescope suitable for short observing campaigns. It had similar specifications as the Mark III

Figure 1.27: Mark IV telescope at La Palma, Canary islands, Spain. The Mark IV was a portable telescope designed for short observing campaigns, it was operated in La Palma during June-October 1988. Image credit: Durham University, Gamma-ray Group, `https://www.dur.ac.uk/cfai/vhegammaraygroup/grouphistory/australia/`, last accessed on 01/08/22.

telescope, but with three samller (6-m^2) reflectors (Brazier et al., 1989). It was operated during a short time (June-October 1988) in Roque de los Muchachos, at La Palma, Spain, and provided evidence for VHE gamma-ray emission from: Cygnus X-3 (Brazier et al., 1990b), 4U 0115 +63 (Carraminana, 1992) and 1E 2259+586 (Brazier et al., 1990a). A photo of the Mark IV telescope at La Palma site is shown in Figure 1.27.

After the success of the imaging technique used in the Whipple telescope, the Durham group designed and tested the Mark 5 (Bowden et al., 1991) telescope in 1992, a prototype equipped with three 9.2-m^2 parabolic reflectors a 31-pixel camera at the focus of its central reflector. Eventually, this led to the construction of a bigger telescope using this technology and design. The Mark 6 (Armstrong et al., 1999) consisted of three 42-m^2 parabolic reflectors on a single mount, with a 109 element PMT camera on the central mirror and 19 PMT cameras for the side reflectors, operating in a triple coincidence system (See Figure 1.28). The 3-fold

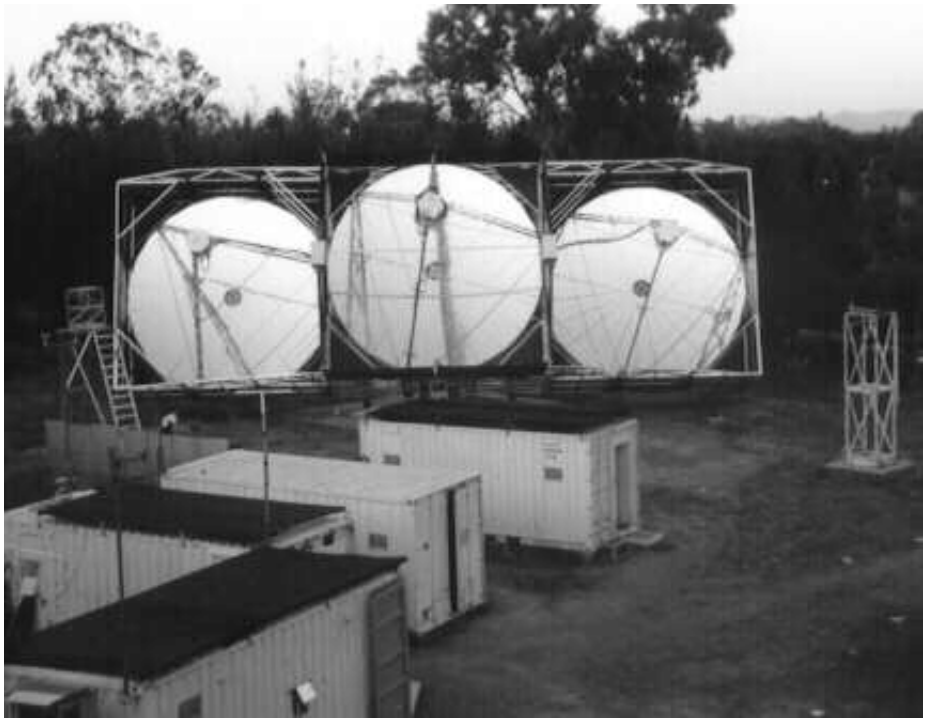

Figure 1.28: Mark 6 gamma-ray telescope deployed at Narrabri, Australia in 1994. Three 42-m^2 parabolic reflectors on a single mount working in 3-fold coincidence to trigger data recording. The central mirror was provided with a 109 PMT camera and the side mirrors with a 19 PMT camera. Image credit: Armstrong et al. (1999).

coincidence technique developed by the Durham group recorded a Cherenkov event only when all three mirrors show a signal from the same area of sky; this coincidence system allowed the energy threshold of the instrument to be lowered by reducing the effects of the noise produced from night sky brightness. The Mark 6 telescope was installed in Narrabri in 1994 and started operations in 1995. The Mark 6 telescope was able to provide effective gamma/hadron separation for gamma-ray energies above 300 GeV, and active until March, 2000. Amongst its highlights are the discovery of VHE gamma-rays from the blazar PKS 2155-304 (Chadwick et al., 1999), and observations performed of other 10 AGNs (Chadwick et al., 2001), X-ray binary systems (Chadwick et al., 2000b), pulsars and SNRs (Chadwick et al., 2000a).

The effective usage of multiple telescopes in stereoscopic mode was proved by the HEGRA Collaboration, which operated an array of 5 IACTs in La Palma, Spain

from 1996 to 2002. Each telescope was provided with a 271-pixel camera with a FoV of 4.6° in the focal plane of a 3.4-m diameter mirror (HEGRA Collaboration, 2003b) (See Figure 1.29). Four telescopes were arranged in the corners of a square of roughly 100-m side length; the fifth telescope was located in the centre of the square.

Stereoscopic observations of air showers with an array of telescopes provide several advantages in comparison to single telescope observations. It allows a better assessment of the shower geometry, with an unambiguous spatial reconstruction of the shower axis, and yields an improved resolution of the angular and spectral reconstruction of the primary particle. Hadron rejection and muon background suppression improves the sensitivity to very weak gamma-ray sources, and the triggering condition in multiple telescopes allows the energy threshold of the observations to be lowered.

The HEGRA array was able to detect several blazars (like the previously discovered Markarian 421 (HEGRA Collaboration, 1996) and Markarian 501 (HEGRA Collaboration, 1997a)), and measured them with improved quality. HEGRA also observed the gamma-ray emission of the young SNR Cassiopeia A (HEGRA Collaboration, 2001) and the radio galaxy M87 (HEGRA Collaboration, 2003a). In 2002 HEGRA discovered the first unidentified TeV source J2032+4130 (HEGRA Collaboration, 2002, 2005), showing that some astrophysical objects are not detectable in any other waveband. After years of faithful operation, the HEGRA telescope system was shut down in September 2002.

Another important IACT operated at the time was the CAT imaging telescope (CAT Collaboration, 1998b), which used a very high definition camera associated with a sophisticated method for shower-image analysis. The CAT imaging telescope was active between 1996 and 2002 in Themis, France. Using a single telescope with a $\sim$ 18-m^2 reflecting area and a 546-pixel camera with 4.8° FoV, the CAT telescope provided a very high image definition with excellent energy resolution, and was effectively using imaging analysis to improve background rejection and

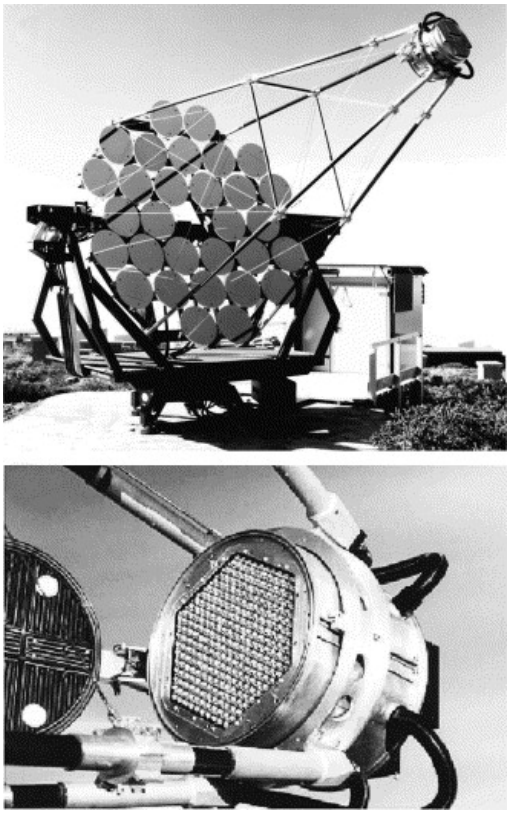

Figure 1.29: One of the HEGRA telescopes built in La Palma, at Roque de los Muchachos observatory (up) and the front view of the mounted hexagonal camera (down), a pixel matrix conformed of 271 PMTs. The HEGRA IACT system was operational from 1996 to 2002. Image credit: HEGRA Collaboration (2003b).

gamma/hadron discrimination (CAT Collaboration, 1998a). The image analysis included a detailed evaluation of the shower asymmetry, its lateral extension, and the employment of a maximum likelihood method in which shower images were compared to a realistic pre-calculated model to discriminate between gamma-ray and cosmic-ray showers. With this method, even with a single $\sim$ 18-m^2 telescope, the CAT Collaboration was able to make detailed gamma-ray shower reconstructions and achieve an energy threshold of about 250 GeV, which is comparable to the value reached by the Whipple telescope (75-m^2).

The CAT, HEGRA and Whipple Collaborations were able to detect a flaring episode from the Markarian 501 blazar in April 1997 (HEGRA Collaboration, 1997b; Whipple Collaboration, 1997; CAT Collaboration, 1999). This was the first simultaneous detection of a flaring source and the first time a coherent light curve was

Figure 1.30: Evolution of the CANGAROO project throughout the years. On the left, the 3.8-m CANGAROO-I telescope, in the central image the CANGAROO-II 7-m telescope, and on the right image one of the 10-m telescopes from the CANGAROO-III array. Image credits: CANGAROO Collaboration (2000) and Mori (2003).

obtained by using data from 3 different experiments.

In the Southern hemisphere, the Collaboration of Australia and Nippon for a Gamma Ray Observatory in the Outback (CANGAROO) (CANGAROO Collaboration, 1991, 2001) operated a Cherenkov telescope from 1992 to 1999 in Woomera, Australia. The first CANGAROO telescope had a 3.8-m diameter mirror and a 220-pixel camera with a 3° FoV. After the successful operation of the 3.8-m CANGAROO-I telescope, which included evidence for gamma-rays from the pulsar PSR1706-44 (CANGAROO Collaboration, 1995), the Crab Nebula (CANGAROO Collaboration, 1998a) and the SNR SN1006 (CANGAROO Collaboration, 1998b); the collaboration later built the CANGAROO-II telescope (CANGAROO Collaboration, 2000), a 7-m segmented reflector provided with a fine resolution 512-pixel imaging camera with a 3° FoV, which was in operation during 1999-2003.

The project finally evolved into a 4 telescope array for the CANGAROO-III phase (CANGAROO Collaboration, 2002, 2003). Each telescope was provided with a 10-m diameter mirror and was equipped with a 552-pixel camera with a FoV of about 3°. The CANGAROO-III array was in operation from 2003 to 2011, during which reported the detection of several objects (Mori, 2003), such as: SNR (SN1006, RX J1713.7–3946), pulsar nebulae (Vela, PSR B1706–44, PSR B1509–58), micro-

quasars , blazars (Markarian 421, PKS2005–489, PKS2155–304), the Galactic centre and other extragalactic sources (NGC 253, 3EG J1234–1318).

Due to various factors, including the technical choices for PMTs and the mirror technology being vulnerable to damage in the outdoor environment, CANGAROO-III's was quickly outperformed by other IACT systems (VERITAS, H.E.S.S., MAGIC).

A great advantage of ground-based observatories over spaced-based detectors is their very large collection area. The effective area of an IACT can exceed that of space-based instruments by 4 or 5 orders of magnitude. This advantage results in much greater source sensitivity, which is required since gamma-ray sources have falling power law-spectra. IACTs are also able to reach multi-TeV energies, which are not possible to reach with space-based detectors due to the background and low statistics. On the other hand, space-based observatories, like *Fermi* and *AGILE*, have the advantage of an extended duty cycle that allows them to monitor the whole sky in few hours, as avoiding the effects of the Earth's atmosphere. Both approaches are complementary and have worked together to obtain a wider picture.

1.3.8 Current and future IACTs

The current generation of IACTs are the three major gamma-ray observatories: H.E.S.S., MAGIC and VERITAS. The technology and methods developed during the last 60 years of ground-based gamma-ray astronomy have been applied to the present telescopes' design and operation. All of them share three main characteristics: large reflectors to lower the energy threshold of the observations, fast and fine-grained cameras to obtain high definition images of the air showers, and stereoscopic observation capabilities to provide effective gamma/hadron separation as well as improved energy and angular resolution.

These gamma-ray observatories are presented in more detail in this Section, including their main discoveries and scientific highlights. The characteristics and

Observatory	VERITAS	H.E.S.S.	MAGIC
Location	Arizona, USA	Namibia	La Palma, Canary Islands
Latitude	+32°	-23°	+29°
Altitude (a.s.l.)	1,250 m	1,800 m	2,200 m
Number of Telescopes	4	5	2
Telescope Diameter	12 m	4×12 m + 1×28 m	2×17 m
Mirror Area	$4{\times}110$ m^2	$4{\times}108$ m^2 + $1{\times}614$ m^2	$2{\times}236$m^2
FoV	3.5°	5° + 3.6°	3.5°
# PMTs per camera	4×499	$4 \times 960 + 1 \times 2048$	2×1039
Energy Range	100 GeV - 30 TeV	30 GeV - 100 TeV	50 GeV - 50 TeV
Sensitivity (in 50-h obs. time)	>1% Crab	0.7% Crab	0.6% Crab

Table 1.2: Summary table with the location characteristics and technical specifications for the current operating generation of IACTs): VERITAS, MAGIC and H.E.S.S.

Figure 1.31: Locations of the current operating (blue spots) and future (green spots) gamma-ray observatories around the world, including SGSO (yellow ellipse). While VERITAS, H.E.S.S., MAGIC and CTA are IACTs; HAWC, TIBET, TAIGA, LHAASO and the proposed SGSO are based on particle detector arrays. Image credit: W. Hofmann (Talk at TeVPA2018); `https://indico.desy.de/event/18204/contributions/29702/`, last accessed on 01/08/22.

technical information from these three experiments are summarised in Table 1.2 and a map showing their locations is presented in Figure 1.31.

Figure 1.32: View of the FLWO basecamp and the 4 telescope VERITAS array at the base of Mount Hopkins in southern Arizona, USA. Designed to detect gamma-rays in an approximately energy range of 50 GeV to 30 TeV, the full array configuration started operations in September 2007 and it was upgraded in 2009. Image credit: VERITAS Collaboration; `https://veritas.sao.arizona.edu/`, last accessed on 01/08/22.

1.3.8.1 VERITAS

The Very Energetic Radiation Imaging Telescope Array System (VERITAS) is a major ground-based gamma-ray detector located on the Fred Lawrence Whipple Observatory basecamp, in southern Arizona, USA. The experience from the previous 10-m Whipple telescope was used in the design, construction and operation of the VERITAS array. The first telescope started operations in February 2005, the array was fully operational in September 2007 and a series of upgrades were implemented between 2009 and 2012. To provide a more uniform array spacing and a better point-source sensitivity, one of the telescopes was moved in 2009. In subsequent years, upgrades to the telescope included a new trigger system and the replacement of all PMTs in the VERITAS cameras by higher quantum efficiency versions (Ong, 2014). Designed to detect gamma-rays in an energy range of 100 GeV to 30 TeV, the current configuration consists of a 4 IACT array. Each telescope possesses a 12 m diameter segmented reflector and a camera of 499 PMTs, providing a FoV of 3.5° (See Figure 1.32).

VERITAS typically collects around 70-100 hours of data per month over 10 months, excluding July and August when observations are not possible due to monsoon

conditions (Staszak and VERITAS Collaboration, 2015). VERITAS has developed non-standard techniques to actively pursue observations into bright moonlight conditions and extend the duty cycle of the telescopes (Griffin and VERITAS Collaboration, 2015). Around 165 hours of the total annual observation time corresponds to low moonlight observations.

VERITAS is a mature scientific project with more than 15 years of operation. Its scientific focus has evolved from source discovery to collecting deep exposures on known objects. It has achieved various scientific highlights during its operation time, some of which are:

- The VERITAS VHE gamma-ray catalogue has evolved from 21 detected sources in 2009, to its current 57 sources (VERITAS Collaboration, 2022). The VERITAS Data catalogue (VTSCat) includes five different VHE source classes: AGNs (like blazars), binary systems, PWNs, starburst galaxies, SNRs, and a bunch of unidentified sources. The current catalogue is available for public access at: `https://github.com/VERITAS-Observatory/VERITAS-VTSCat/releases`, last accessed on 01/08/22.

- There is regular monitoring campaign of active AGNs (mostly blazars) (Benbow and VERITAS Collaboration, 2015), as well as frequent multi-wavelength observation campaigns in collaboration with other observatories to detect flares from known objects. Approximately 160 AGNs have been monitored with the VERITAS observation programme, from which much VHE blazar activity has been detected throughout the years: Markarian 421 in February 2010 (VERITAS Collaboration et al., 2020), PKS 1424+240 in 2009 (VERITAS Collaboration and Fermi-LAT Collaboration, 2010) and 2013 (VERITAS Collaboration and Fermi-LAT Collaboration, 2014), 1ES 0229+200 observed between 2009-2012 (VERITAS Collaboration, 2014b), 1ES 1727+502 in 2013 (VERITAS Collaboration, 2015), RGB J2243+203 in 2014 (VERITAS Collaboration, 2017a), PKS 1441+25 in 2015 (VERITAS Collaboration et al.,

2015), S3 1227+25 2015 (Mukherjee, 2015), amongst others. The VERITAS observations of VHE gamma-ray blazars have allowed us to probe indirectly the InterGalactic Magnetic Field (IGMF) (VERITAS Collaboration, 2017c). The best sources for this are hard-spectrum, distant blazars that are strongly detected at VHE energies. The VERITAS Collaboration also derived upper limits for more than 100 AGNs (Benbow and VERITAS Collaboration, 2015).

- VERITAS is responsible for the first detection of a starburst galaxy M82 (VERITAS Collaboration, 2009b), and the two radio galaxies M87 and NGC 1275. These last objects provide strong evidence of the correlation between a high Star Formation Rate (SFR) and VHE emission.

- The follow-up of transient events is also included in the VERITAS observational programme. GRBs are given the highest priority among all sources, as an example we have the follow-up of the GRB 130427A event from which VHE emission upper limits were derived (VERITAS Collaboration, 2014a).

- HE neutrino event alerts are also followed-up by VERITAS. For steady neutrino sources, VERITAS has performed studies observing the positions around muon neutrino track events from IceCube (VERITAS Collaboration and Icecube Collaboration, 2015).

- VERITAS has also performed extensive observations of Galactic sources (detecting SNRs, PWN, X-ray binary systems, and pulsars), as well as a sky survey in the Cygnus OB1 region (Ong, 2014).

- Additionally, VERITAS has a DM search programme (VERITAS Collaboration, 2017b), focusing in the detection of gamma-ray signals from an hypothetical decay of Weakly Interacting Massive Particles (WIMPs) that may be present in a variety of object classes. The targets include the Galactic centre, the Galactic halo, galaxy clusters, and dwarf spheroidal galaxies.

Further details on the VERITAS array are reported in VERITAS Collaboration (2009a), and the official website for the VERITAS Collaboration *. The VTSCat compiles experimental data from all of the high-level science results published in 112 papers using VERITAS (VERITAS Collaboration, 2022).

1.3.8.2 H.E.S.S.

Located in the Khomas Highlands of Namibia at 1,800 m above sea level, the H.E.S.S. observatory was designed as a general purpose detector for observing the southern sky with an unprecedented sensitivity. It consists of 5 IACTs operating in the energy range from 30 GeV to 100 TeV. The first phase of the project started observations in 2004 with 4 telescopes arranged on a square of 120-m side, with the diagonal of the square oriented in the direction North to South (See Figure 1.33). Each telescope has a 12-m diameter reflector with a 960 PMT camera of 5° FoV. The square array was complemented in 2012 by a parabolic 28-m diameter telescope located at the centre. With the installation of the fifth telescope the energy threshold of the array was lowered from 100 GeV down to 30 GeV. A summary of technical information about the H.E.S.S. telescopes is given in Table 1.2. A detailed overview of the H.E.S.S. telescopes and more information about the observatory can be found in HESS Collaboration (2004) and de Naurois (2019).

H.E.S.S. employs a stereoscopic reconstruction system and only air showers which generate images in at least two telescopes are recorded. With its large central telescope, H.E.S.S. is the only hybrid array operating at the moment, and has paved the way for the upcoming CTA which combines 3 different telescope sizes in the planned array configuration (see Section 1.3.8.4 for an overview of the CTA project). An automatic repositioning system for the telescopes was implemented to obtain a quick response to targets of opportunity; as a result half of the sky is reachable in less than 60 seconds.

*`https://veritas.sao.arizona.edu/about-veritas/veritas-specifications`, last accessed on 01/08/22.

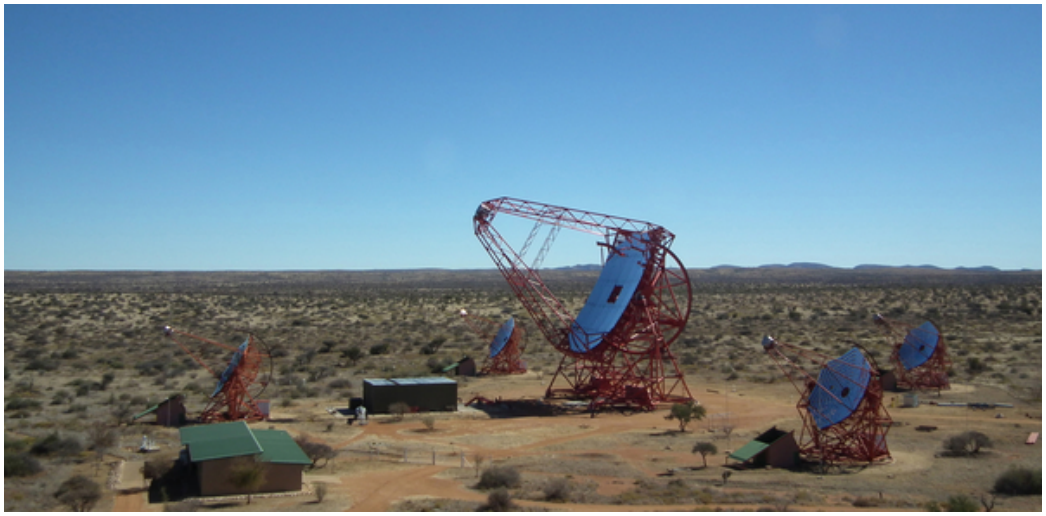

Figure 1.33: H.E.S.S. gamma-ray observatory in Namibia. The final array consists of four 12 m diameter telescopes arranged on a square of side 120 m and a parabolic 28 m diameter telescope located at the centre. H.E.S.S. is the only operating hybrid IACT array and its energy range covers from 30 GeV to 100 TeV. Image credit: H.E.S.S. Collaboration; `https://www.mpi-hd.mpg.de/hfm/HESS/pages/about/telescopes/`, last accessed on 01/08/22.

In more than 15 years of operations, the H.E.S.S. observatory has discovered more than 100 gamma-ray sources, conducted a 10 year long Galactic plane survey and population studies, performed multi-wavelength and observation campaigns for selected sources (H.E.S.S. Collaboration, 2005a), and follow-up of multi-messenger alerts (H.E.S.S. Collaboration, 2017a) (including high-energy neutrino alerts and GWs), amongst other discoveries. A short summary of the more important H.E.S.S. results is given below:

- A Galactic plane survey was carried out using 2700 hours of high-quality observations taken between 2004-2013. The project results included a public release of the Galactic sky map, a catalogue of 78 cosmic accelerators, and the discovery of 16 new VHE gamma-ray sources (H. E. S. S. Collaboration, 2018).

- The Galactic centre region was also observed and reviewed in detail during the survey. The H.E.S.S. Collaboration analysed 250 hours of data to perform a detailed morphological study of the diffuse VHE gamma-ray emission ob-

served from the Galactic centre and reconstruct its total spectrum (H.E.S.S. Collaboration, 2018a).

- The H.E.S.S. Collaboration also conducted population studies on PWN (H.E.S.S. Collaboration, 2018c), SNRs (H.E.S.S. Collaboration, 2018e) and obtained the first evidence of gamma-ray emission from the outer edge of the shell region in the SNR RX J1713.7-3946 (H.E.S.S. Collaboration, 2018d).

- H.E.S.S. has detected several blazars, and recorded flaring episodes for PKS 0736+017 in February 2015 (H.E.S.S. Collaboration, 2020), PKS 1510-089 in May 2016 (H.E.S.S. Collaboration and MAGIC Collaboration, 2021), 3C 279 in April 2014 and July 2015 (H.E.S.S. Collaboration, 2019a), and Markarian 501 in June 2014 (H.E.S.S. Collaboration, 2019c), amongst others.

- H.E.S.S. has performed observation campaigns to search for steady gamma-ray emitters from regions around the High-Energy Starting Events (HESE) detected by IceCube (VERITAS Collaboration et al., 2017). No significant steady gamma-ray counterparts have been identified for the neutrino events observed so far.

- In the case of transient phenomena, the H.E.S.S. observatory is part of an active multi-messenger programme (H.E.S.S. Collaboration, 2017a) and can rapidly react to incoming alerts and analyse the data in real-time. The system has already performed follow-up of neutrino alerts from IceCube (IC-200926A, IC-201007A and IC-201114A) and ANTARES (ANT170130A) (Satalecka et al., 2021). In both cases, the differential upper limits on the gamma-ray flux were derived as no significant gamma-ray emission could be found.

- The telescopes also responded to the GW alert associated to GW170817 (H.E.S.S. Collaboration, 2017b). H.E.S.S. telescopes were on target 5.3 hours after the GW alert was distributed. A monitoring campaign extended over

several days covering an energy range between 270 GeV to 8.55 TeV. No significant gamma-ray emission was found.

- H.E.S.S. also observed the afterglow emission of the GRB 180720B 10 hours after the end of the prompt emission phase (H.E.S.S. Collaboration, 2019b). This discovery placed constraints on the GRB emission mechanisms.

The highlighted results in the previous paragraphs represents only a small fraction of the long list of H.E.S.S. discoveries. More detailed information about H.E.S.S. and its publications can be found in the official website *, and in a special volume edition of *Astronomy & Astrophysics* (de Naurois, 2019) in which the H.E.S.S. Collaboration released a bundle of 14 publications focusing on the Galactic plane studies.

1.3.8.3 MAGIC

The Magic Atmospheric Gamma-ray Imaging Cherenkov (MAGIC) telescope system consists of two 17-m diameter telescopes located at Roque de los Muchachos, on the Canary Island of La Palma, Spain, at an altitude of 2200 m above the sea level (see Figure 1.34). The first MAGIC telescope (MAGIC-I) has been operating since 2004, an upgrade to include a second telescope (MAGIC-II) was completed in autumn 2009. A summary of technical information about the MAGIC telescope system is given in Table 1.2 and further details of the project are reported in MAGIC Collaboration (2012a) and MAGIC Collaboration (2016a).

The major goal of the MAGIC telescope system was to obtain the lowest possible energy threshold through fine-grained cameras, fast sampling electronics and a large mirror area. Since the major upgrades made to harmonise the specifications of the telescopes in 2011-2012, the energy range of the stereoscopic system goes from 50 GeV to 50 TeV with an angular resolution between 0.07°–0.14° at energies 0.1–1 TeV (MAGIC Collaboration, 2016a). The array operates in stereoscopic

*`www.mpi-hd.mpg.de/hfm/HESS/pages/publications/`, last accessed on 01/08/22.

Figure 1.34: The 17 m diameter MAGIC telescopes located at Roque de los Muchachos, La Palma. MAGIC is optimised to perform gamma-ray observations from 50 GeV and up to 50 TeV, and to follow fast transient phenomena with its rapid rapid repositioning system. Image credit: Daniel Lopez; `https://magic.mpp.mpg.de/`, last accessed on 01/08/22.

mode, with only events triggering both telescopes recorded and analysed. The parameters from both telescopes are combined to reconstruct the arrival directions and energies of the gamma-ray events recorded.

The MAGIC telescopes were designed and optimised to observe low energy transient phenomena. Both telescopes employ a light mechanical structure (<70 tons) built for rapid repositioning, which is necessary for observations of short transient phenomena, such that the MAGIC array can reach any position in the sky within 30 seconds. Due to its good performance around the low energy threshold, the high sensitivities reached within hour timescales (see Table 1.2) and the fast repositioning system, MAGIC became an ideal instrument to follow-up and study GRBs.

MAGIC has discovered new VHE gamma-ray sources, performed observations to numerous objects for multi-wavelength studies, recorded flaring states from blazars, and performed follow-up observations for both the GRB and multi-messenger

programmes that have obtained outstanding results. A short summary is presented here:

- The radio quasar 3C 279, at a redshift of $z = 0.536$, was the first extragalactic source identified by MAGIC and enabled the transparency of the universe to gamma rays to be tested (MAGIC Collaboration, 2008a). Other extragalactic sources discovered by MAGIC in the VHE gamma-ray domain include: PKS 1222+21 (FSRQ MAGIC Collaboration (2011a)), 1ES 0033+595 (BL Lac MAGIC Collaboration (2015)), PKS 1222+216 (FSRQ MAGIC Collaboration (2011b), 1ES 1727+502 (BL Lac MAGIC Collaboration (2014b)) and 1ES 1215+303 (BL Lac MAGIC Collaboration (2012b)).

- MAGIC has observed numerous AGN flaring episodes: Mrk 501 in July 2005 (MAGIC Collaboration, 2007), Mrk 421 in March 2010 (MAGIC Collaboration and VERITAS Collaboration, 2015a), PKS 1222+216 in June 2010 (MAGIC Collaboration, 2011b), PKS 1441+25 in April 2015 (MAGIC Collaboration and Fermi-LAT Collaboration, 2015) and 1ES 1959+650 in 2016 (MAGIC Collaboration and Fermi-LAT Collaboration, 2020), just to mention a few. MAGIC has also detected extremely fast variability from different classes of extragalactic objects: radio galaxies, FSRQs, BL Lacs, etc.

- MAGIC also performed follow-up observations to the flaring blazar TXS 0506+056 after the emission of an IceCube neutrino alert on September 22nd, 2017. This event and the possible correlation between gamma-ray activity and neutrino signals from blazars are explored in Chapter 4.

- The MAGIC Collaboration has made follow-up observations of 101 GRBs since 2005 by following the alerts received through the GCN. 22 of these events were followed-up with a delay smaller than 100 seconds. On January 14, 2019, MAGIC observations of GRB 190114C, resulted in the detection of gamma-ray emission at TeV energies (the first ever detected from a GRB).

Real-time analysis of the burst gave $> 20\sigma$ significance in the first 20 minutes of observations for energies >300 GeV.

- MAGIC has also performed observations and studies of Galactic sources such as pulsars (MAGIC Collaboration, 2016c), SNRs (MAGIC Collaboration, 2017) and X-ray binaries (MAGIC Collaboration, 2006b).

Other studies in which MAGIC has been involved are:

- The measurement of the EBL in combination with *Fermi*-LAT using the spectra of 12 blazars with redshift up to $z = 1$ (MAGIC Collaboration, 2019).
- Indirect DM searches by looking at the possible gamma-ray emission due to annihilations or decays of Weakly-Interacting Massive Particles (WIMPs) in clusters of galaxies (MAGIC Collaboration, 2018), the Galactic centre (Doro, 2017) and dwarf galaxies (MAGIC Collaboration, 2016d).
- Follow-up of the GW events detected with LIGO/VIRGO: GW 170817 (MAGIC Collaboration, 2022)

All the contributions from MAGIC, VERITAS and H.E.S.S. have impacted significantly our understanding of the VHE astrophysical phenomena. The current generation of IACTs have proven the effectiveness of the imaging Cherenkov technique and paved the way to more ambitious projects for the future generation of gamma-ray observatories.

1.3.8.4 The Cherenkov Telescope Array

The Cherenkov Telescope Array (CTA) will provide gamma-ray observations from around 20 GeV and up to 300 TeV with an unprecedented angular resolution and sensitivity. 3 different telescope sizes will be used to cover the full CTA energy range: The Large-Sized Telescopes (LSTs) will be sensitive to the faint low-energy showers (below 200 GeV). The Medium-Sized Telescopes (MSTs) will operate in

the core energy range of the array (100 GeV and 10 TeV) and increase the effective area by operating a large number of telescopes simultaneously. As an alternative option to the MSTs, a Schwarzschild-Couder Telescope (SCT) design is also being developed. The SCT is planned to work in the same energy range as the MST and use a two-mirror optical system to focus the light with greater imaging detail and improved detection of faint sources. Finally the Small-Sized Telescopes SSTs are planned to be spread out over a km^2 in the southern hemisphere array only, and cover the highest part of CTA energy range (between a few TeVs and 300 TeV) also using a two-mirror optical system. The LST and MST cameras will be equipped with PMT detectors, while the SCT and SST cameras will use Silicon Photomultiplier (SiPM) technology. The technical specifications of the telescopes are given in Table 1.3 and the schematics for the expected design are shown in Figure 1.35.

CTA observatory will consist of 2 observation sites. In the northern hemisphere the selected location is the Roque de los Muchachos observatory, on the island of La Palma, at 2,200 m above the sea level. The site is already used by the MAGIC Collaboration, and has proven to be a good observation spot. In the southern hemisphere, the CTA site will be located at the Paranal Observatory in the Atacama desert in Chile. While the northern hemisphere array will operate in an energy range of 20 GeV to 50 TeV, the southern hemisphere array will concentrate on southern Galactic targets and will operate in an energy range of 20 GeV to 300 TeV. The ultimate full-scope configuration array for CTA) (also known as the Omega configuration array CTA Consortium (2016)) is projected to have 4 LSTs and 15 MSTs located over a 0.6 km^2 for CTA-N site, while for CTA-S, an array of 4 LSTs, 25 MSTs and 70 SSTs is expected in a 4 km^2 array. For the early years of CTA Science Operation, the Alpha configuration array will be operational with a lower number of operational telescopes, consisting of 4 LSTs and 5 MSTs for CTA-N and 15 MSTs and 50 SSTs for CTA-S.

With full-sky coverage, a wide FoV, unprecedent sensitivity, enhanced energy and angular resolution and a rapid repositioning system, able to point anywhere in the

	LSTs	MSTs/SCTs	SSTs
Energy range	20 GeV - 3 TeV	80 GeV - 50 TeV	1 TeV - 300 TeV
Reflector diameter	23.0 m	11.5/9.7 m	4.3 m
Effective area	370 m^2	88/41 m^2	8 m^2
Focal length	28 m	16/5.6 m	2.15 m
Field of view (FoV)	4.3°	7.5/7.7/7.6°	10.5°
Photodetector type	PMT	PMT/SiPM	SiPM
Pixels per camera	1855	1754/1855/11328	2368
Pixel size (imaging)	0.1°	0.17/0.17/0.07°	0.19°
Repositioning time (any point in the sky)	50 s	90 s	90 s
# of telescopes for CTA-N	4	15	-
# of telescopes for CTA-S	4	25	70

Table 1.3: Techincal specifications for the 3 different CTA telescope sizes. For the midle-sized telescopes, two designs are being built and tested: MST and SCT. The reflector diameter and effective are given are referred to the primary reflectors of the telescopes. The expected number of telescopes for the CTA Omega configuration is listed. See `www.cta-observatory.org/project/technology/` for further details about the telescopes design (last accessed on 01/08/22).

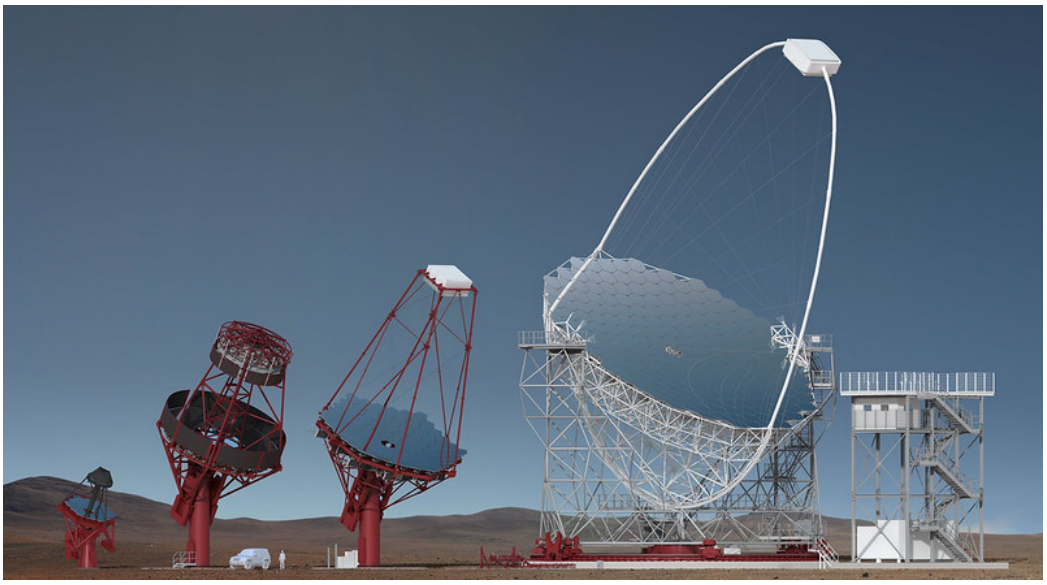

Figure 1.35: Schematics of the 3 different telescope sizes developed for CTA. From left to right: Small-Sized Telescopes (SSTs), Medium-Sized Telescopes (MSTs), and Large-Sized Telescopes (LSTs). For the MSTs, 2 designs are being built and tested. Image credit: CTA Consortium and Gabriel Pérez Diaz; `https://www.cta-observatory.org/project/technology/`, last accessed on 01/08/22.

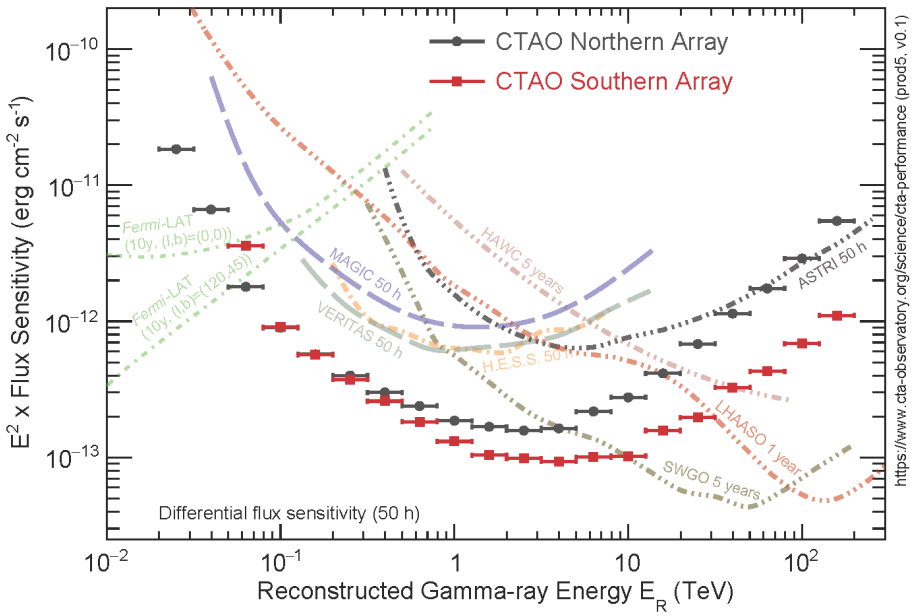

Figure 1.36: Differential sensitivity of CTA Northern and Southern arrays. The curves show the minimum flux to obtain a 5σ detection of a point-like source. The curves for other major gamma-ray observatories are shown for comparison. Image credit: CTA Consortium; `https://www.cta-observatory.org/science/ctao-performance/`, last accessed on 01/08/22.

observable sky in less than 50 seconds for the LSTs and 90 seconds for the MSTs and SSTs (CTA Consortium, 2019a), CTA will have exceptional discovery potential. Figure 1.36 shows the expected differential sensitivity for 50 hours observations with CTA northern and southern arrays in comparison to other major gamma-ray observatories. CTA's angular resolution along the full energy range is shown in Figure 1.37. The curves present the 68% containment angle.

The CTA consortium has a broad range of science objectives and research goals. Some of the projects within CTA include: Galactic centre and plane surveys, DM programme, extragalactic survey, transient sources, cosmic-ray PeVatrons, and AGNs. To efficiently address the broad-range of scientific questions, and describe the potential of the CTA experiment, the Collaboration prepared a book entitled 'Science with the Cherenkov Telescope Array' (CTA Consortium, 2019a).

For transient sources, CTA has optimal characteristics to follow-up multi-wavelength

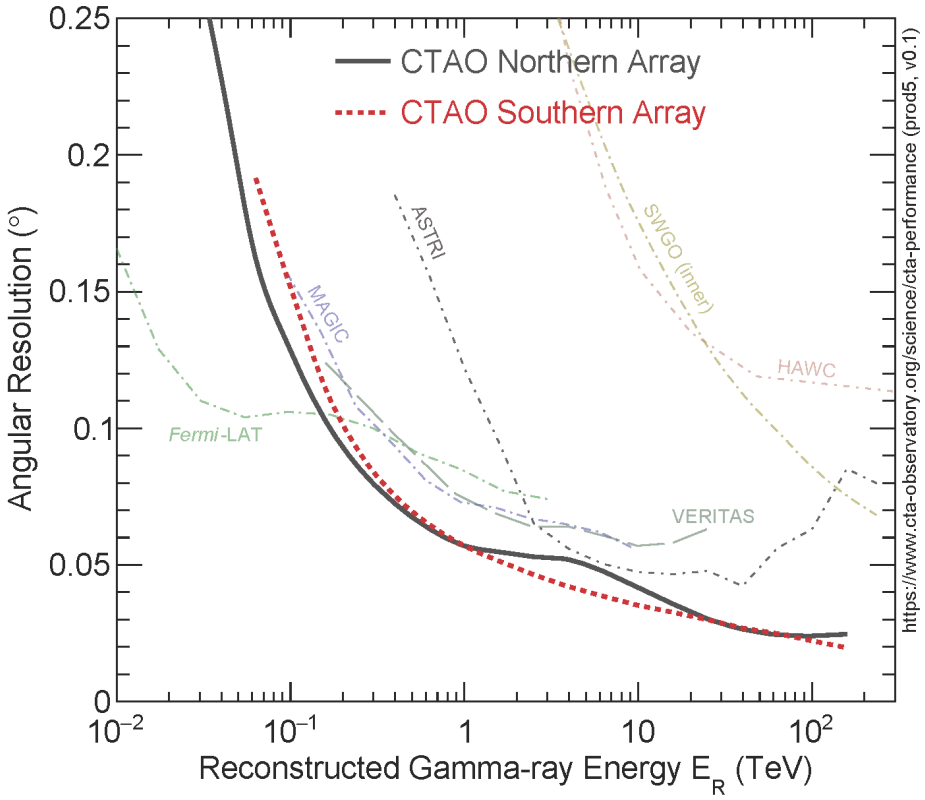

Figure 1.37: Angular resolution of CTA Northern and Southern arrays as a function of the reconstructed energy. The curves show the 68% containment angle along the full energy range of the arrays. Image credit: CTA Consortium; `https://www.cta-observatory.org/science/ctao-performance/`, last accessed on 01/08/22.

and multi-messenger alerts, including GRBs, GWs and HE neutrinos. In Chapter 5 this possibility is explored and the Neutrino Target of Opportunity NToO program for CTA is introduced. My contribution to this project is described and the highlights obtained are presented. In this Chapter, I introduce neutrino astronomy to put the work described in Chapter 5 in context.

1.4 Neutrino Astronomy

The Universe is opaque to VHE photons, limiting the reach of gamma-ray astronomy observations. Neutrinos on the other hand, can be thought of as ideal cosmic messengers, because they only interact via the nuclear weak force and have a very

small interaction cross-section, they are able to escape dense astrophysical environments and enables them to travel long distances. Neutrinos are also electrically neutral, which makes them unaffected by IGMFs, therefore pointing back to their original direction.

The small interaction cross-section, however, also makes neutrinos hard to detect. To identify astrophysical neutrinos large volume detectors (in the order of $\sim 1\ \mathrm{km}^3$) are required to increase the probability of detection.

The idea of a neutrino telescope was first formulated in the 1960s by M. Markov (Markov and Zheleznykh, 1961). Using a large three-dimensional array of PMTs modules installed in a transparent medium, like ice or water, they realised it is possible to capture the Cherenkov radiation emitted by the secondary charged particles generated in neutrino interactions. The incoming direction and energy of the neutrino is then reconstructed using the arrival time of the photons and the Cherenkov light intensity.

1.4.1 DUMAND, Baikal and AMANDA

The first attempt to use this technique in deep ocean water was tested by the DUMAND Collaboration, a project developed between 1973 and 1995 near the island of Hawaii (Roberts, 1992). After discarding the original idea of a cubic-kilometre design due to financial and technical challenges (see Figure 1.38), an 8-string configuration with 216 PMTs was planned for the DUMAND-II project (DUMAND Collaboration, 1988). The Collaboration was able to deploy a test string with 7 PMTs in 1987 and the first string of the DUMAND-II array in 1993, before the eventual cancellation of the project in 1995.

During the 80s, small experiments were constructed and deployed in Lake Baikal, Russia, with the aim of constructing an underwater neutrino detector. Consisting of an array with 192 optical modules in 8 strings of 21.5-m length each (see Figure 1.39), the NT200 detector was completed in 1998 and was operational for over

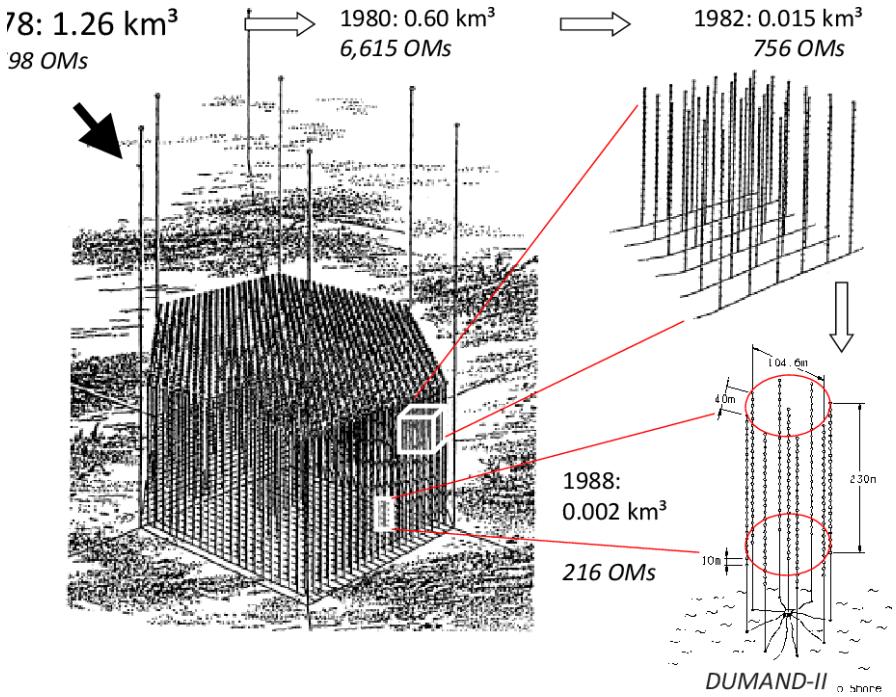

Figure 1.38: The originally conceived DUMAND underwater cubic-kilometer detector and the different downgrading versions over the years, leading to the DUMAND-II array design. Image Credits: DUMAND Collaboration; Spiering (2012).

a decade during which $\sim$ 400 upward-going muon events (produced by neutrinos transversing the Earth from the opposite hemisphere) were collected (see Figure 1.39).

In 2005 the experiment was updated to NT-200+, with the deployment of 3 additional strings with 12-PMT modules each (Aynutdinov et al., 2005), and in 2015 the Baikal Gigaton Volume Detector (Baikal-GVD) project started its construction phase (Baikal-GVD Collaboration, 2017). With a total of 2,304 PMTs already deployed, the Baikal-GVD is aimed to reach its final cubic-kilometre configuration in the next few years and provide a picture of the TeV-PeV neutrino sky with a sensitivity similar to IceCube. A description of the status of the Baikal-GVD experiment can be found in Baikal-GVD Collaboration (2022).

Between 1993-1996, the AMANDA array was deployed at depths between 1.5 km and 2.0 km below the Antarctic ice (AMANDA Collaboration, 2001), which proved

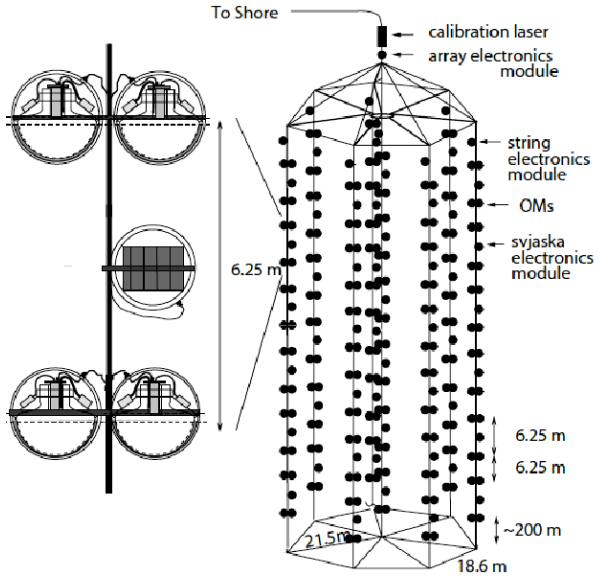

Figure 1.39: Schematic view of the Baikal NT200 neutrino telescope. The underwater detector operated for nearly a decade at Lake Baikal, Russia, and was able to detect $\sim$ 400 upward-going muon events. Image Credit: Kuzmichev (1999).

the feasibility of the project and established the necessary technology to build a kilometre-scale neutrino observatory like IceCube. After an upgrading period from 1997 to 1999, the final AMANDA-II configuration was finished, consisting of 19 strings with a total of 667 optical modules over a volume of $\sim 10^{-2}$ km^3. AMANDA-II detected 6,959 astrophysical neutrino events until the end of its operational period in 2009. No statistically significant point-like excess was detected, therefore only upper limits on point-source fluxes could be derived (AMANDA Collaboration, 2009), but a neutrino sky map was created and the measured spectrum of atmospheric neutrinos was extended up to 200 TeV.

1.4.2 ANTARES

With a construction phase lasting from 2002 to 2008, the ANTARES Collaboration deployed an underwater neutrino detector, located at a depth of 2,475 m in the Mediterranean Sea, near the southern coast of France (ANTARES Collaboration, 2009, 2011). An schematic view of the array is shown in Figure 1.41, with nearly 900 PMTs installed on 12 detection lines in about 10^{-2} km^3, ANTARES

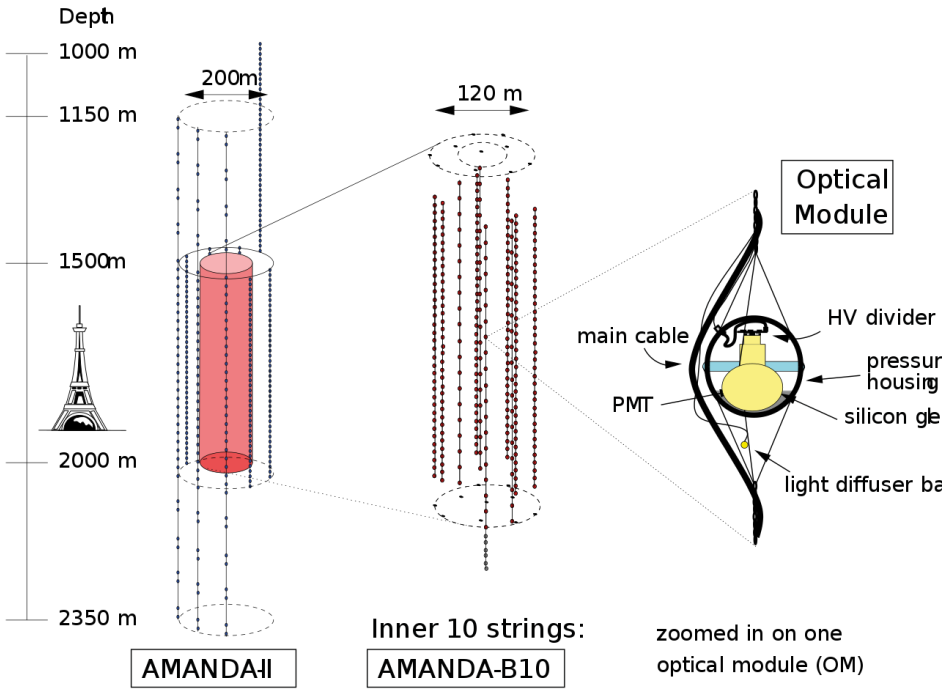

Figure 1.40: AMANDA neutrino telescope array. Deployed at a depth of 1.5–2.0 Km under the Antarctic ice. The final AMANDA-II array consisted of 667 optical modules distributed in 19 strings. AMANDA was the first-generation of detectors under deep ice and direct predecessor of the IceCube neutrino telescope. Image Credits: AMANDA Collaboration; AMANDA Collaboration (1999).

In the most comprehensive analysis by ANTARES to date, an all-sky unbinned blind search was performed using nearly $\sim 8,000$ neutrino events collected between 2007 and 2015 (ANTARES Collaboration, 2017). The study included specific searches in the direction of known astrophysical objects, HE IceCube events, the Galactic centre, and Sagittarius A, but ANTARES did not find any significant excess over the background expectations. An overview on the latest results from ANTARES is compiled in ANTARES Collaboration and KM3NeT Collaboration (2020).

Based on the successful experience with ANTARES, the next generation of underwater neutrino telescopes, KM3NeT, is under construction in the deep waters of Mediterranean sea: the Astroparticle Research with Cosmics in the Abyss (ARCA) facility in the coast of Sicily, designed for HE neutrino astronomy, which will improve in size and performance (sensitivity) the ANTARES experiment (KM3NeT

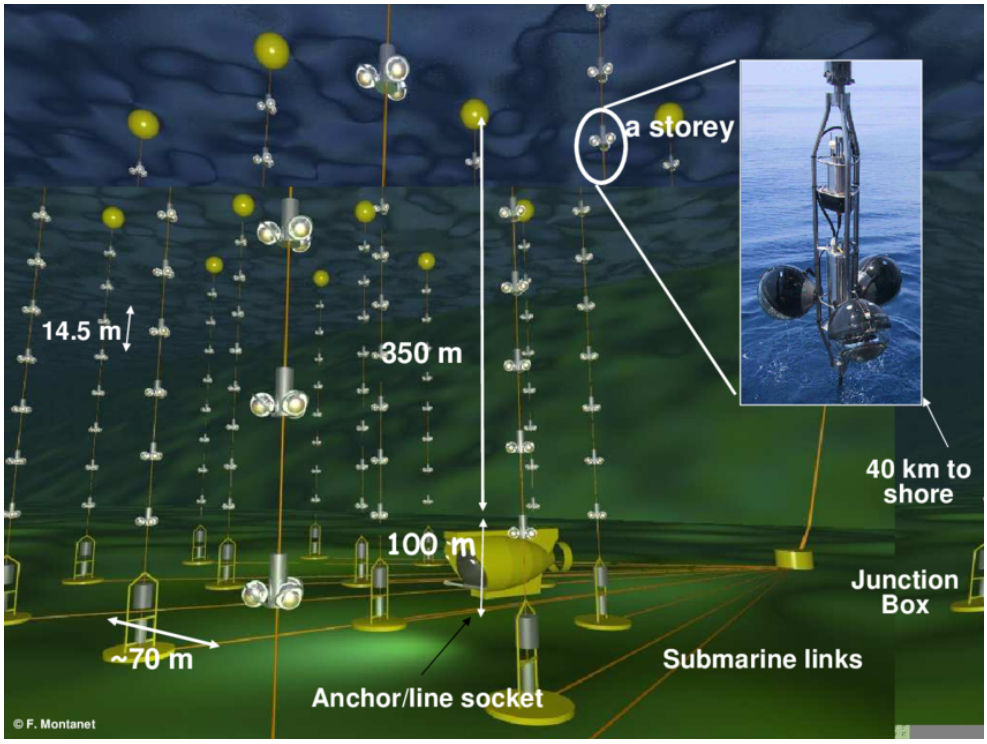

Figure 1.41: Schematic view of the ANTARES detector. The full array consisted of 12 strings and nearly 900 optical modules and was completed in 2008. Image Credits: ANTARES Collaboration; ANTARES Collaboration (2011).

Collaboration, 2019). On the other hand, the Oscillation Research with Cosmics in the Abyss (ORCA) facility is being deployed off the French coast near the ANTARES location, and will be dedicated to studying fundamental neutrino physics, such as the precise measurement of atmospheric neutrino oscillations, the determination of the neutrino mass hierarchy, non-standard interactions and sterile neutrinos, amongst other topics (Kalaczyński and KM3NeT Collaboration, 2021).

1.4.3 The IceCube Neutrino Observatory

Consisting of a cubic-kilometre of instrumented ice, the IceCube Neutrino Observatory is composed of 5,160 Digital Optical Modules (DOMs) arranged in 86 strings between 1,450 m and 2,450 m below the surface of Antartica (IceCube Collaboration, 2017d). An schematic view of IceCube is shown in Figure 1.42. Completed in 2011, it is the largest neutrino detector built to date and in 2013 discovered the

existence of a diffuse flux of high energy astrophysical neutrinos (IceCube Collaboration, 2013b, 2014b), which points at contributions from extragalactic sources, although there are no point-sources yet identified solely on the basis of neutrino emission. IceCube also comprises an air shower array at the surface called IceTop, with the main purpose being to detect cosmic rays in an energy range between 10^{15} eV and 10^{18} eV (IceCube Collaboration, 2013d). Discoveries made by IceCube are the most important for the work described later in this thesis.

The detection of neutrinos from IceCube depends on the Cherenkov light emission from secondary charged particles produced in neutrino-nucleon interactions deep in the Antarctic ice. The direction and energy of the neutrino can be inferred by reconstructing the tracks of the secondary particles from the data collected by the DOMs. The majority of the detected neutrino events fall into two categories: track and cascade (shower) events. The track-like events are characterised by a kilometre long trace left by a HE muon (μ) created during a Charged Current (CC) muon-neutrino (ν_μ) interaction with a nucleon N:

$$\nu_\mu + N \rightarrow \mu + X \tag{1.14}$$

where X represents the cascade sub-products. In most of the cases, the interaction occurs outside of the volume detector. Track events allow a more accurate reconstructed direction, the angular uncertainty of these events is usually below 1°, but they present a large uncertainty (factor of ~ 2) on the reconstructed energy (IceCube Collaboration, 2014a). Cascade events show a spherical topology when the interaction occurs inside the instrumented ice volume. Cascade-like events are produced by electron neutrinos ν_e with a nucleon via CC interactions:

$$\nu_e + N \rightarrow e + X \tag{1.15}$$

and Neutral Current (NC) interactions from all neutrino flavors:

$$\nu_l + N \rightarrow \nu_l + X \tag{1.16}$$

where $l = e, \mu, \tau$ is the electric charged particle companion that designates the flavour of the neutrino $\nu_l = \nu_e, \nu_\mu, \nu_\tau$. The angular uncertainty for cascade events

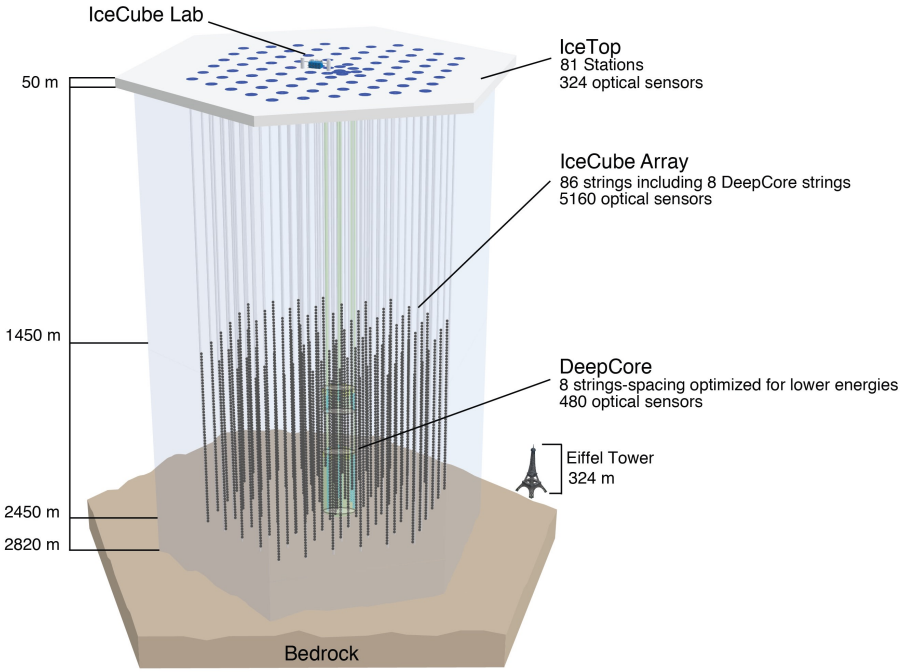

Figure 1.42: Schematic view of the IceCube neutrino observatory, consisting of 5,160 DOMs arranged in 86 strings between 1,450 m and 2,450 m below the surface of Antartica. The IceTop surface array and the DeepCore array are indicated in the diagram. Image Credits: IceCube/NSF; IceCube Collaboration (2013d).

is usually between 10° and 15°, but it can be larger. The energy reconstruction of cascade events, in contrast to track events, is better, with ±30% at 100 GeV and ±8% at 100 TeV (IceCube Collaboration, 2014a).

There is a large neutrino background produced by the decay of pions and kaons generated in cosmic-ray interactions: $\pi^{\pm}, K^{\pm}$; where:

$$K^{\pm} \rightarrow \pi^{\pm} + \pi^{0};\ K^{\pm} \rightarrow \mu^{\pm} + \nu_{\mu}(\bar{\nu_{\mu}});\ K^{-} \rightarrow \pi^{0} + \mu^{-} + \nu_{\mu} \tag{1.17}$$

and

$$\pi^{\pm} \rightarrow \mu^{\pm} + \nu_{\mu}(\bar{\nu_{\mu}});\ \mu^{\pm} \rightarrow e^{\pm} + \nu_{e}(\bar{\nu_{e}}) + \bar{\nu_{\mu}}(\nu_{\mu}) \tag{1.18}$$

The conventional neutrino flux (from ν_e and ν_μ) generates a spectrum described by a power-law (PL) dependency of $E_{\nu}^{-3.7}$ IceCube Collaboration (2015a)). The ν_e flux is lower than the ν_μ flux and the ratio ν_μ/ν_e increases with energy, until reaching a factor of ~ 20 at 1 TeV.

At energies above 1 TeV there is also a prompt neutrino flux produced from the decay of charmed particles generated in the early phase of the air shower development. These charmed particles have short lifetimes and decay without interaction, producing a spectrum with the original spectral slope of the primary cosmic-rays: $E_{\nu}^{-2.7}$ (IceCube Collaboration, 2011b; Mascaretti and Vissani, 2019). Prompt neutrinos are uniformly produced in the atmosphere, with equal fluxes of ν_{μ} and ν_{e} (IceCube Collaboration, 2015a).

Due to the high rate of downward-going cosmic rays, it is difficult to separate the muon neutrino events from the atmospheric background, but with the entire Earth as a shield, atmospheric muon background events can be discriminated from upward-going muon events, as in the latter case we are looking through the Earth towards the opposite hemisphere.

The atmospheric background events also become less frequent when moving to higher energies ($>$ 100 TeV and into PeV), where the astrophysical neutrinos from cosmic-ray sources can be identified. As the atmospheric neutrino background exceeds the number of astrophysical neutrino events by several orders of magnitude, a detailed event selection and a maximum likelihood statistical analysis needs to be performed to search for a significant excess from a specific direction of the sky and further identification of the possible source.

In 2020, the IceCube Collaboration released a 10-year data sample of track-like neutrino candidates, which showed evidence at the 3.3σ significance level with respect to the atmospheric neutrino background. A cumulative excess of events coming principally from the Seyfert II galaxy NGC 1068, and 3 blazars: TXS 0506+056, PKS 1424+240 and GB6 J1542+6129 (IceCube Collaboration, 2020b). Nevertheless, none of these known sources reached a 5σ significance level with respect to the neutrino background. This may point to a large population of faint, steady sources or flaring objects as origin of this flux; in both scenarios, blazars remain as an intriguing possibility as the sources of the extragalactic neutrino flux.

The tight link between HE neutrinos and gamma-ray photons from hadronic scenarios is the prime motivation in the search for correlated neutrino and gamma-ray. The hunt for more neutrino events associated with flaring blazars is being explored using coordinated alerts that are distributed worldwide, including via the IceCube real-time neutrino alert system, which is described in the next Section.

1.5 Multi-messenger Astronomy

The developments made in the last 60 years in space and ground-based gamma-ray astronomy (See Chapter 1, Section 1.2.1 and 1.3.6) have allowed the current generation of observatories to make quasi-simultaneous observations of some transient events, in which gamma-ray photons are detected alongside other cosmic messengers: neutrinos, GWs, and photons from other wavelengths (radio to X-ray). This approach is known as multi-messenger astronomy, and represents a powerful tool to decipher some of the most energetic phenomena in the universe, by extrapolating valuable information from joint observations, that could not be obtained otherwise.

Discoveries from the last 5 years have propelled multi-messenger astronomy to the forefront of astrophysics (IceCube Collaboration et al., 2018; LIGO Scientific Collaboration et al., 2017; Mészáros et al., 2019). One of the most significant multi-messenger detections, came out of the improved neutrino alert system operated by the IceCube Collaboration (Blaufuss et al., 2019). As mentioned in Section 1.4, the $\sim 3\sigma$ correlation found between the IceCube neutrino alert IC-170922A and a flaring episode from the blazar TXS 0506+056 (IceCube Collaboration et al., 2018), represents the first plausible association of a VHE neutrino with an astrophysical point-source.

Blazars have been proposed as possible cosmic-ray accelerators, where hadronic interactions with radiation fields or matter clouds can produce HE cosmic rays, neutrinos and gamma-rays. In a multi-messenger picture (see Figure 1.43), HE neutrinos will serve as a probe of cosmic particle acceleration and correlated follow-up

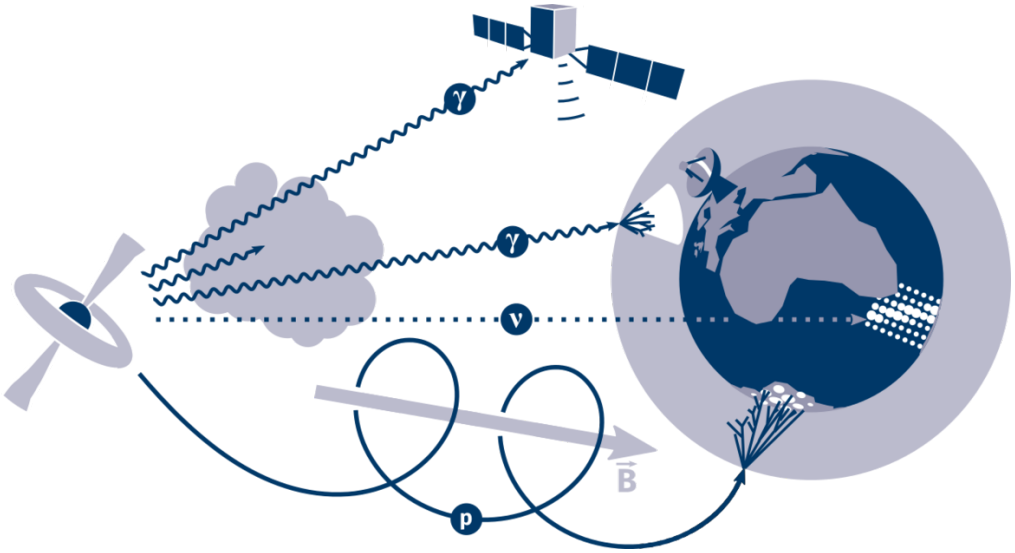

Figure 1.43: Multi-messenger picture of an astrophysical object. Image Credits: Inter-University Institute For High Energies; `www.iihe.ac.be/icecube`, last accessed on 01/08/22.

gamma-ray observations will be able to confirm hadronic scenarios. The hadronic production mechanisms are explored in Section 2.7 of Chapter 2.

There are other examples in which multi-messenger astronomy has marked a breakthrough in modern astrophysics, like the GW signal detected on 17th August, 2017 by the LIGO and Virgo detectors (LIGO Scientific Collaboration et al., 2017; LIGO Scientific Collaboration and Virgo Collaboration, 2017). The registered event of two neutron stars spiralling towards each other and finally merging, was also detected by the *Fermi*-GBM, seconds after the GW signal (GRB 170817A Fermi-GBM Collaboration (2017)). The follow-up observations revealed a bright optical transient with delayed X-ray and radio emission revealed in the following days. The near simultaneous detection of the electromagnetic emission and a GW signal from this event, confirmed the hypothesis that neutron star mergers can produce short GRBs.

Public alerts are distributed amongst the observational community using Astrophysical Multi-messenger Observatory Network (AMON) and the Gamma-ray Coordinates

Network* (GCN).

AMON has been created to facilitate the interaction between different observatories. It provides a common framework to analyse data across multiple experiments, and the astrophysical community is notified of any interesting events worthy of follow-up (Ayala Solares et al., 2020). The AMON system also receives sub-threshold data from the High-Altitude Water Cherenkov (HAWC) and IceCube observatories, and combines them in real time to perform a multi-messenger search for sources that emit in both gamma-rays and cosmic neutrinos (HAWC Collaboration and IceCube Collaboration, 2021).

On the other hand, the GCN provides a system that continuously reports transient events and follow-up alerts. GCN notices are detected by spacecraft and provide the location of GRBs and other transient events, while GCN circulars are reports of follow-up observations made by ground-based and space-based optical, radio, X-ray, TeV gamma-rays, and other particle observatories.

1.5.1 IceCube real-time neutrino alert system

In 2016, IceCube initiated a system of public real-time alerts relating to neutrino candidate events likely to be of astrophysical origin (IceCube Collaboration, 2017c). These alerts are focused on track events, due to their more precise angular resolution. The median angular uncertainty for track-like events in IceCube is considered to be $< 1^{\circ}$. These type of events are the best option to identify point-like steady sources.

The reconstruction accuracy of track-like events depends on geometrical factors, such as the incoming angle of the track to the instrumented volume, as well as the energy of the event (muons have stochastic energy losses above 1 TeV via bremsstrahlung, pair production, and nuclear interactions (Bradascio and Gluesenkamp, 2019). IceCube's reconstruction technique follows a maximum likelihood

*`https://gcn.gsfc.nasa.gov`, last accessed on 01/08/22.

algorithm to estimate the best-fit parameters of the incoming muon track (time of arrival, deposited energy, trajectory, etc) and is described in AMANDA Collaboration (2004). The reconstructed directions of these events can be used to perform follow-up observations (in radio, IR, visible, UV, X-ray, gamma-ray) and identify possible electromagnetic counterparts.

Initially, there were two alert streams: the Extremely-High Energy (EHE) alerts and the HESE alerts. EHE alerts announced the detection of a single extremely HE neutrino coming from the Northern Hemisphere, i.e., one that reaches IceCube after passing through Earth, thus filtering out all background, while IceCube HESE alerts were issued when a single HE neutrino event was registered inside the instrumented volume of ice.

An update to the alert stream system was introduced in 2019 (Blaufuss et al., 2019). Two new categories replaced the original channels, so that all alerts are classified depending on the likelihood of the events as: Gold alerts, with events that are at least 50% likely to be of astrophysical origin and have an expected rate of 10 alerts per year, and Bronze alerts, with a lower threshold of 30% chance of being from astrophysical origin and a higher rate of 20 alerts per year. The likelihood estimate of an event having an astrophysical origin is also called "signalness". Each alert contains information about the discovery time and date, the reconstructed direction with 50% and 90% error uncertainties, the likely neutrino energy, signalness, and a False-Alarm Rate (FAR). The contour size for the 90% and 50% error uncertainties depends on IceCube's reconstruction algorithm, which has been changed and improved over the years (see Bradascio and Gluesenkamp (2019)). The IceCube neutrino alerts are distributed amongst the observational community using AMON and GCN. These are candidates for follow-up multi-wavelength observations.

Apart from the IC-170922A alert, which was associated with the blazar TXS 0506+056 and is reviewed in Section 1.5.2; other blazars that were found in spatial coincidence with a neutrino alert are FSRQ PKS 1502+106, located within the 50% uncertainty region of IC-190730A (IceCube Collaboration, 2019b), and 4FGL J0658.6+0636,

observed within the 90% uncertainty region of IC-201114A (IceCube Collaboration, 2020a). A lepto-hadronic scenario has been used to explain the multi-wavelength emission from PKS 1502+106 in Rodrigues et al. (2021), while the possibility of 4FGL J0658.6+0636 being a neutrino emitter is explored in Chapter 4. Other possible associations have also been studied in Franckowiak et al. (2020).

1.5.2 TXS 0506+056 & IC-170922A

The gamma-ray flare observed from TXS 0506+056 on September 2017 in coincidence with the neutrino alert IC-170922A, is the highlight of the IceCube neutrino alert system so far. On September 22nd 2017 at 20:54:30.43 UTC (58018 MJD), a high-energy neutrino-induced muon track was detected and an extensive multi-wavelength campaign was triggered right after this event. The best fit reconstructed position was RA=77.43 (+0.95, −0.65) and Dec=5.72 (+0.50, −0.30), and an estimated neutrino energy of 290 TeV, with a 90% CL lower limit of 183 TeV. In less than 1 min, an automated alert was distributed worldwide.

The blazar TXS 0506+056, located at just 0.1° from the best fitting neutrino direction was reported to be in a flaring state by the *Fermi*-LAT Collaboration (Tanaka et al., 2017) and had considerably brightened in the GeV band since April 2017. The enhanced electromagnetic emission from TXS 0506+056 was found in spatial and temporal coincidence at a statistical significance of $\sim 3\sigma$ (IceCube Collaboration et al., 2018). This case represents the first plausible association of a high energy neutrino alert with an astrophysical point-source, a flaring blazar.

In addition to this event, a time-dependent analysis done by the IceCube Collaboration found an excess of 13 ± 5 high energy neutrino events coming from the direction of this source between September 2014 and March 2015 (IceCube Collaboration, 2018). This represents a $\sim 3.5\sigma$ significance level evidence for neutrino emission from the direction of TXS 0506+056, and stands as an independent result from the 2017 observations. A detailed analysis of *Fermi*-LAT data did not

reveal any remarkable activity along this time period: no excess of gamma-rays or a significant gamma-ray spectral change with respect to the average was detected (Fermi-LAT Collaboration et al., 2019). This neutrino detection without an evident electromagnetic counterpart presents also an interesting scenario within hadronic models, in which the opacity of the emission region or a mechanism of internal absorption affects the detected gamma-ray flux. Such scenarios are explained in Chapter 2, where hadronic interactions are presented as an alternative to explain the gamma-ray and neutrino emissions from blazars. Then, in Chapter 4 a hadronic scenario is proposed to explain the behaviour of the blazar 4FGL J0658.6+0636, a suspected counterpart of the IceCube neutrino alert IC-201114A.

Chapter 2

Theoretical Framework and Methods

In this chapter, an overview of AGN sources and blazars is given. I describe the Fermi acceleration mechanism, often used to explain proton acceleration in astrophysical sources, and the effect of the EBL on the gamma-ray propagation. A quick review of the leptonic and hadronic scenarios and their differences is also included in this chapter, and in particular the photohadronic flaring model used in the research work presented in Chapters 3 and 4. Finally, the photohadronic flaring model caveats are discussed and the Akaike Information Criterion (AIC), a statistical tool for model comparison, is presented.

2.1 Gamma-ray sources

In the study of VHE gamma-ray astronomical sources, two broad categories emerge depending on the location of the source. They can be catalogued as either:

Galactic sources.- This category refers to sources located in our Galaxy, and includes (among other subcategories):

- Pulsars (Grenier and Harding, 2015).- The first gamma-ray pulsars were detected by space-based instruments like the *COS-B* satellite in the early 1970's,

the EGRET instrument on board the CGRO mission (See Section 1.2.1 for further information), and since 2007-2008 AGILE and *Fermi*-LAT. IACTs have also detected the pulsed gamma-ray emission from a few objects: Crab pulsar (MAGIC Collaboration, 2008b), Vela pulsar (H.E.S.S. Collaboration, 2018f) and the Geminga pulsar (MAGIC Collaboration, 2020b).

- Pulsar Wind Nebulae (PWN; Hewitt and Lemoine-Goumard (2015)).- The most famous example of a PWN environment is the Crab nebula, which has been extensively studied in all wavelengths, from radio to gamma-rays. In the Galactic plane survey carried out by H.E.S.S., the Galactic population of PWN was studied (H.E.S.S. Collaboration, 2018c).

- Supernova Remnants (SNRs; Hewitt and Lemoine-Goumard (2015)).- For a long time SNRs have been considered sources of Galactic cosmic-rays, reaching multi-TeV energies via 1st order Fermi acceleration (diffusive shock acceleration, see Section 2.4). The latest generation of ground-based Cherenkov telescopes and the *Fermi*-LAT are sensitive enough to resolve SNRs at their respective energy range.

- X-ray binary systems (Dubus, 2015).- Only small fraction of X-ray binaries emit VHE gamma-rays. Some of the few detected binary systems in gamma-rays are: LS 5039 (H.E.S.S. Collaboration, 2005b), LS I+61 303 (MAGIC Collaboration, 2006a), PSR B1259-63 (Johnston et al., 1992), and PSR J2032+4127 (VERITAS Collaboration and MAGIC Collaboration, 2018).

- The Galactic centre (Su and van Eldik, 2015).- The Galactic centre hosts a concentration of star forming regions, PWN, SNRs, and the central supermassive black hole Sgr A*. The region has been observed at HE (between 10 MeV and 100 GeV) and VHE (>100 GeV) energies. Gamma-ray diffuse emission, which is assumed to be generated from cosmic-ray interactions with the molecular clouds has also been detected (EGRET Collaboration, 1997; Fermi-LAT Collaboration, 2010b; MAGIC Collaboration, 2020a).

Extragalactic sources.- These are objects located outside our Galaxy, with typical redshifts of up to ~ 2, but which are still bright enough for detection with the 3rd generation of gamma-ray IACTs and space-based observatories. This category includes:

- Active Galactic Nuclei (AGNs; Dermer and Giebels (2016)).- AGNs are extremely luminous galaxies ($> 10^{40}$ erg s^{-1}) powered by a SMBH and are considered astrophysical laboratories for particle acceleration and extreme physics. There is a wide AGN classification depending on their properties, which is explored in Section 2.1.1. The jetted AGNs with small viewing angles with respect to the line of sight are part of a subcategory within AGNs named blazars. These astrophysical objects, known for their unpredictable behaviour and variability, are described in more detail in Section 2.2, as they are the object of study of this thesis.

- Gamma-ray Bursts (GRBs; Piron (2016)).- Described as the most violent explosions in our Universe, releasing energies up to 10^{51} - 10^{54} erg in a short time period. The GRB events are characterised by their rapid and irregular variability on timescales of milliseconds to thousands of seconds. GRBs show prompt emission followed by a long duration afterglow emission across the entire electromagnetic spectrum. If the prompt emission lasts for less than 2 seconds, the event is classified as a short GRB; on the other hand, if it lasts longer than 2 seconds, then is classified as a long GRB event.

  The detection of the GRB 170817A (LIGO Collaboration et al., 2017) event associated with a GW signal GW 170817 (LIGO Scientific Collaboration and Virgo Collaboration, 2017) has proved that short GRBs can be produced by the merger of compact objects, neutron stars in this case. Long GRBs are thought to be associated with the death of massive stars or core-collapse supernova (Piran et al., 2013).

- Starburst galaxies (SBGs).- Galaxies where massive stars are forming at a very high rate are designated SBGs. These galaxies contain a high concentration of gas, radiation, and young massive stars with relatively short lifetimes that can explode as supernovae. SBGs contain ideal environments for cosmic-ray acceleration, with the possibility of VHE gamma-ray and neutrino emission being produced from proton-proton (*pp*) interactions. The 3rd generation IACTs (H.E.S.S., MAGIC and VERITAS) have detected and studied SBGs (Ohm, 2012; H.E.S.S. Collaboration, 2018b).

In the present work, the main focus is the study of gamma-ray photons and possible neutrino emission coming from a sub-class of AGN: blazars. The following sections present a description of the main AGN characteristics and the resulting classification. Blazars are described in Section 2.2, including their properties, typical spectrum and classification.

2.1.1 Active Galactic Nuclei (AGNs)

AGNs are distant galaxies with a very bright nuclei powered by a SMBH ($M_{BH} > 10^6 M_\odot$). Accreting matter, spiralling around and towards the black hole, forms an accretion disc, which is surrounded by a dusty torus. Figure 2.1 shows a diagram of a typical AGN. As matter spirals towards the black hole, it heats up, producing large amounts of energy. Near the accretion disc, there are rapidly moving gas clouds forming the Broad-Line Region (BLR), which produces strong optical and UV emission lines. The optical and UV radiation is obscured along some lines of sight by the dusty torus. Slower moving clouds of gas farther away from the central black hole create the Narrow-Line Region (NLR), which produces narrower emission lines in the observed optical spectrum. At the same time, high speed beams of gas and plasma may be ejected perpendicular to the accretion disc, forming the relativistic jets seen in some of these objects. Magnetic fields generated in the disc

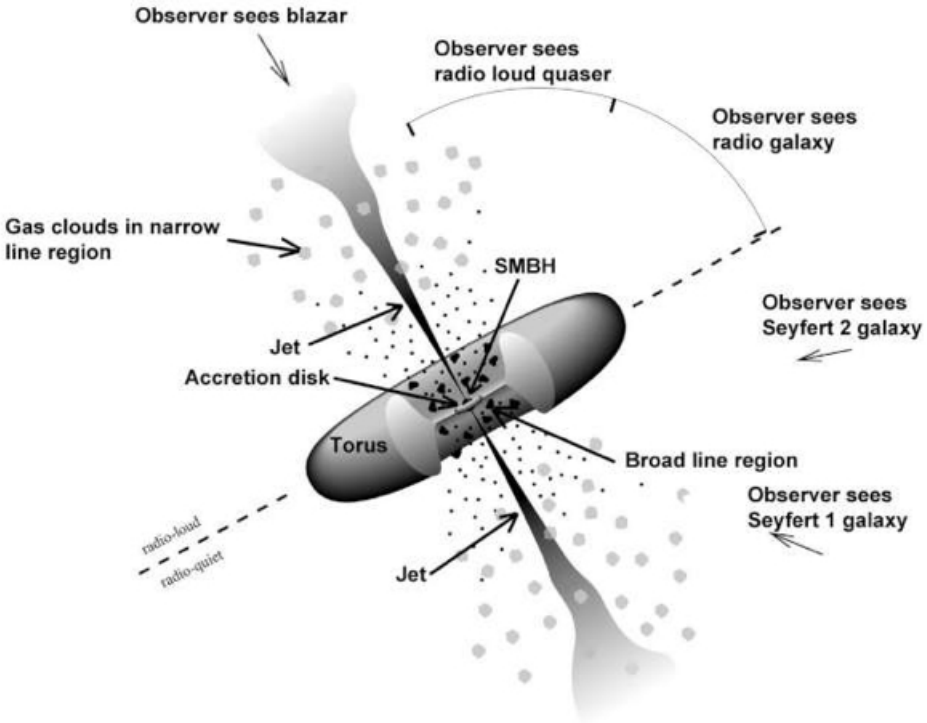

Figure 2.1: Diagram of a typical AGN. Powered by a SMBH at its centre, matter spiralling around and towards the black hole forms an accretion disc, which is surrounded by a dusty torus. Rapidly moving gas clouds form the BLR which emits strong optical and UV emission lines, obscured along some lines of sight by the dusty torus. Slower moving clouds of gas, farther away from the central region conforms the NLR. Some AGNs have relativistic jets, perpendicular to the accretion disc. AGNs are classified depending on their orientation (viewing angle). Image Credits: NASA; `https://fermi.gsfc.nasa.gov/science/eteu/agn/`, last accessed on 01/08/22.

are carried by the jets out to the radio lobes, where they play a crucial role in producing the observed radiation.

Some general properties of an AGN are:

- High luminosities.- AGN can be found over a very wide range of luminosities, from 10^{40} erg s^{-1} and above 10^{48} erg s^{-1}, where the central nucleus outshines the rest of the galaxy.

- Non thermal spectrum.- The radiation is not described by a black body curve (non-thermal). The emission is observed across entire electromagnetic spec-

trum, from the radio to the gamma-ray band, over almost 20 orders of magnitude in frequency.

- Strong variability.- Their energy output can be highly variable, which is consistent with the picture of a small central nucleus (less than a parsec across) producing the emission. For blazars, less than hour-scale variability in gamma-rays has been observed.

- Broad emission lines.- Optical and UV emission lines are produced by the recombination of ions of various elements (H, He, C, N, O, Ne, Mg, Fe). Their width varies due to the Doppler effect associated with the motion of the emission region around the central SMBH. Some AGNs exhibit broad emission lines, which is indicative of rapid internal motion within the emission region.

- Radio-loud sources.- Some AGN types have relativistic jets with superluminal motion. Using Very-Long-Baseline Interferometry (VLBI) radio imaging, it has been possible to track how the jet evolves (Boccardi et al., 2017). Blobs have been observed, as they are emitted and move downstream in the jet, as well as shocks and knots (Marscher et al., 2008).

In the unified AGN classification scheme (Antonucci, 1993; Urry and Padovani, 1995), AGNs are classified depending on their orientation (viewing angle). The perception of the characteristics from the accretion disc, the jet's emission, and the BLR/NLR zones determine its nomenclature. The unified AGN classification scheme is shown in Figure 2.2 and in Table 2.1. On a basic level, AGNs can be classified as either radio-loud or radio-quiet sources. Then, depending on the characteristics observed in the optical and UV spectrum emission lines, AGNs can also be divided into Type 1 (broad-lined) and Type 2 (narrow-lined) objects. The broad emission lines observed in AGNs have a Full Width Half Maximum (FWHM) which is typically in the range of 5,000 to 10,000 km s^{-1} (Stirpe, 1991), while the narrow-line emission is typically described by FWHM $<$ 2,000 km s^{-1} (Goodrich,

1989). Blazars have unusual emission line properties (and are often described as Type 0), as they present very weak emission lines with typical equivalent widths < 5 Å. Narrow emission lines mean that either the zones producing the emission have low velocities, or that the line of sight is obscured by a thick wall of absorbing material in the dusty torus.

- **Radio-loud galaxies**

  Only about 10% to 15% of AGNs are described as 'radio-loud'. In the radio-loud branch, Type 2 AGN are also called Narrow-Line Radio Galaxies (NLRGs). In this category we have two AGN sub-types named according to their radio morphology as Fanaroff-Riley I and II (FR I and II). The low-luminosity objects with weaker, diffuse, and approximately symmetric jets are classified as FR-I, while the ones with high luminosity ($2 - 5 \times 10^{26}$ W), sharp-edged lobes are classified as FR-II.

  Broad-Line Radio Galaxies (BLRGs) are radio-loud Type 1 AGNs with low luminosities. BLRGs show a continuum optical and UV spectrum with emission lines similar to those of luminous Seyfert galaxies. Jets in BLRGs are not pointing directly toward the observer, which reduces the effects of the relativistic beaming and the jet emission dominance.

  Radio quasars are generally divided into Steep Spectrum Radio Quasars (SSRQs) and Flat Spectrum Radio Quasars (FSRQs), according to their spectral shape at the radio waveband, objects with a spectral index > 0.5 measured at a few GHz are defined as SSRQs. The characteristic flat spectrum from FSRQs is an indication of a core-dominated emission, while the SSRQs indicate an extended emission, generally associated with the radio-lobes. The properties of SSRQs are intermediate between FSRQs and radio quiet quasars.

  Blazars are extremely luminous (in the range of 10^{45} to 10^{49} erg s^{-1}), radio-loud AGN. They have a relativistic jet pointing directly towards the observer

Radio Loudness	Optical Emission Line Properties		
	Type 2 (Narrow-Line)	Type 1 (Broad-Line)	Type 0 (Unusual)
Radio-quiet:	Seyfert 2	Seyfert 1 QSO	
Radio-loud:	NLRG: FR-I FR-II	BLRG SSRQ	Bl Lac FSRQ
	decreasing angle to the line of sight →		

Table 2.1: AGN classification according to their orientation (viewing angle), and the observed spectrum characteristics. Type 2 AGN have weak continua and only narrow emission lines, while Type 1 AGN also presents bright continua and broad emission lines. The different AGN types are also specified in Figure 2.2.

(small viewing angle), which results in Doppler boosted emission. Blazar jets can be collimated over distances in the order of 100 kpc, but their spectrum is dominated by non-thermal emission from the core, rather than the radio lobes. The sub-categories are FSRQs and BL Lac objects. FSRQs have strong, broad emission lines, while BL Lacs have weak or absent emission lines. The possible emission mechanisms of blazars are still under discussion. A more detailed description of these objects is given in Section 2.2.

- **Radio-quiet galaxies**

  In the radio-quiet branch, Seyfert 1 galaxies will show broad and narrow emission lines with no jets, while Seyfert 2 galaxies are similar but without the presence of broad lines. Seyfert galaxies can be classified somewhere between 1 and 2 based on the width of the observed emission lines (Peterson, 1997).

  Seyfert 1 galaxies have relatively low luminosities (in comparison to other type 1 galaxies) and therefore are seen only nearby, where the host galaxy can be resolved.

  Objects which present optically strong luminosities and broad emission lines are classified as Radio Quiet Quasars (QSO)s.

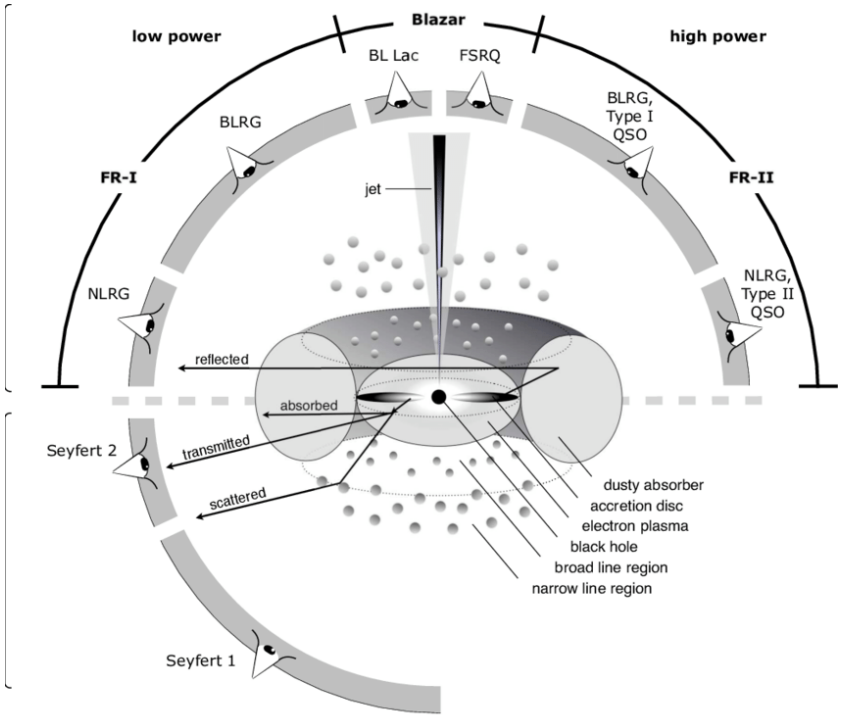

Figure 2.2: AGN classification in the unified scheme. The labels around the central image show the AGN type according to the viewing angle. The AGN classification is divided in two, radio-loud AGNs appear on the top part of the image, while radio-quiet AGNs are on the bottom part. Image credits: Beckmann and Shrader (2012) & Marie-Luise Menzel.

2.2 Blazars

Blazars are a sub-class of radio-loud AGNs with a relativistic jet pointing very close to our line of sight. There are more than 1,500 known blazars detected at GeV energies, and more than 60 at TeV energies (Dermer and Giebels, 2016). These objects have a highly variable spectrum and flaring states, with periods of enhanced activity on time scales that can go from minutes to months. This variability makes it extremely difficult to model the broad-band SED of these sources. Blazars are known to show variability in all wavebands, if we add the lack of a complete understanding of the physical processes inside the jet and the knowledge of the AGN components that contribute to the SED, we face a complex problem in modelling blazar emission.

The bulk motion of the plasma inside a blazar's jet is close to the speed of light, which means relativistic effects play an important role in the observed emission and physical processes. Blazars jets show apparent superluminal motion (Rees, 1966); this phenomenon occurs when a emitting region moves at a relativistic speed relative to the observer and there is a small viewing angle ($< 15°$) respect to the line of sight. The strength of the beaming is parameterised by the Doppler factor, which is described by:

$$D = \frac{1}{\Gamma(1 - \beta \cos\theta)} \tag{2.1}$$

where $\Gamma = (1 - \beta^2)^{-1/2}$ is the Lorentz factor, with $\beta = v/c$ the beamed particle's velocity in units of light speed, and θ the observer's viewing angle.

The observed frequency $\nu_{\rm obs}$ is related to the emitted frequency ν' through:

$$\nu_{\rm obs} = \frac{D\nu'}{(1 + z)} \tag{2.2}$$

An observer sees a more intense emission (energy flux) than if the plasma were at rest. The observed emission, $F_{\rm obs}$ is:

$$F_{\rm obs} = F'[\Gamma(1 - \beta \cos\theta)]^{-3} = F'D^3 \tag{2.3}$$

where F' is the emission in the blob's reference frame*.

The relativistic effects also impact the observed variability $t_{\rm obs}$ as:

$$t_{\rm obs} = t'\frac{(1 + z)}{D} \tag{2.4}$$

where t' is the intrinsic time variability of the source.

Blazars can be classified, based on the presence of emission lines in their optical spectra, into two types:

- BL Lacerate objects (BL Lacs).- BL Lac objects tend to have weak or absent emission lines in their spectra. Based on the location of the synchrotron peak ($\nu_{\rm sync}$) in the SED, the BL Lacs can be sub-divided into three sub-classes:

*The prime notation is adopted to refer the blob's reference frame.

Low frequency peaked BL Lacs (LBLs) with $\nu_{\rm sync} < 10^{14}$ Hz, Intermediate frequency peaked BL Lacs (IBLs) with $10^{14} < \nu_{\rm sync} < 10^{15}$ Hz, High frequency peaked BL Lacs (HBLs) which presents $\nu_{\rm sync} > 10^{15}$ Hz. This sub-classification is shown in Figure 2.3 and its known as the blazar sequence (Fossati et al., 1998).

- Flat Spectrum Radio Quasars (FSRQs).- FSRQs display strong optical emission lines coming from the BLR, which indicates the presence of a prominent and dense external radiation field. FSRQs also have higher bolometric luminosities and the broad emission lines are intrinsically brighter than BL Lacs (Padovani, 1992; Padovani et al., 2019).

  In the blazar sequence (Figure 2.3), the SEDs are shifted from higher to lower frequencies as the source gamma-ray luminosity increases, i.e. there is an anti-correlation between the location of synchrotron peak and the source luminosity (Fossati et al., 1998) . Going from higher to lower frequencies, we move from HBLs to IBLs, then LBLs and finally to FSRQs.

- Masquerading BL Lacs.- Proposed by (Giommi et al., 2013), this category refers to misclassified FSRQs. Objects could exhibit weak emission lines either because they have intrinsically weak lines in the spectrum (BL Lacs), or because they present heavily diluted broad-lines that are swamped by non-thermal emission (Masquerading BL Lacs). As BL Lacs are classified based on their observed emission lines, a misclassification can occur if FSRQs exhibit weak, or undetectable, emission lines.

2.2.1 Spectral Energy Distribution

The broadband Spectral Energy Distribution (SED) of a blazar typically consists of two peaks of non-thermal radiation, as shown in Figure 2.3. The SED νF_ν is normally plotted in a log-log scale vs the frequency (ν), but can also be expressed as $\nu F_\nu = E^2 dN/dE$ vs the energy, where dN/dE is the differential energy spectrum.

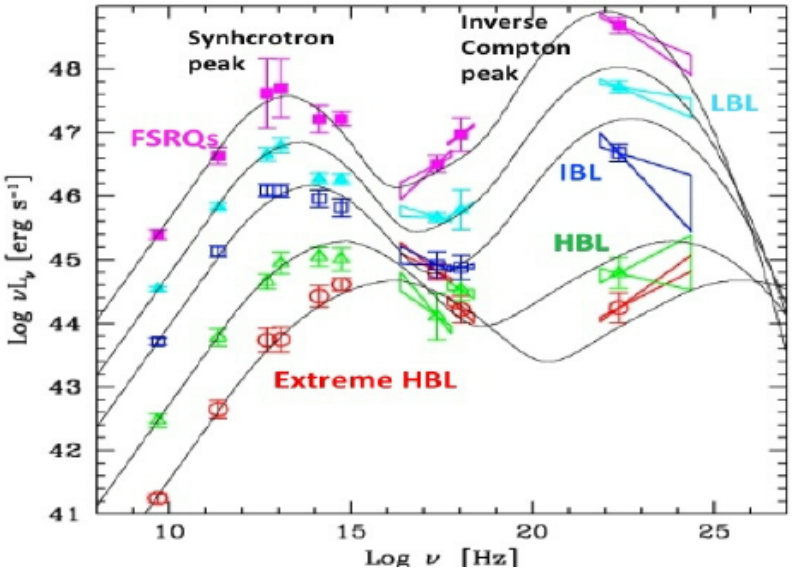

Figure 2.3: Blazar sequence. The SED blazar sub-classification is determined by the location of the synchrotron peak. The types of blazars are shown in ascending order by frequency: FSRQs (magenta), LBLs (light blue), IBLs (blue), HBLs (green) and extreme HBLs (red). Image credit: Fossati et al. (1998)

The low-energy peak lying between the radio and X-ray energy range is attributed to synchrotron emission from a population of relativistic electrons. The emission region (blob) is believed to be located in the base of the jet, close to the SMBH engine.

The origin of the second peak, which may lie in the gamma-ray part of the spectrum, is still a matter of debate, with both the emission mechanism and the location of the emission region still unclear. There are two main scenarios that could explain the typical blazar SED emission:

- **Leptonic scenarios**.- When electrons (and/or positrons) are accelerated to ultra-relativistic energies, the typical SED can be explained by two main processes: electron-synchrotron radiation and Inverse Compton (IC) radiation coming from up-scattered synchrotron photons (SSC) or up-scattered photons from external fields (BLR, accretion disk, obscuring torus, etc). This scenario is further discussed in Section 2.6

- **Hadronic scenarios**.- If the conditions enable protons to be accelerated up

to relativistic energies into a photon field or a matter target, then gamma-ray photons and neutrinos will be produced as sub-products of the proton interactions. These scenarios are explored in Section 2.7.

The main difference between the two proposed scenarios is that in leptonic models the gamma-ray emission responsible for the second peak in the SED is due to IC scattering, while hadronic scenarios predict that the gamma-ray component in the SED may result from proton-synchrotron radiation, photo-pion production, synchrotron emission from the sub-product charged particles in the decay chain, or a combination of these. Importantly, in hadronic models a neutrino flux is expected from the sources, which will enable their identification as cosmic-ray accelerators.

2.3 Cosmic-ray and gamma-ray production

Gamma-ray production is intimately related to the production of cosmic rays. Several possible sources have been studied in order to find the acceleration sites of cosmic-ray particles, however as cosmic-rays are deflected by intergalactic magnetic fields, they do not necessarily point back to their places of origin. Gamma-ray photons, on the other hand, are not deflected and can be traced back to identify the progenitor sources. Objects that can accelerate cosmic rays up to PeV energies are often called PeVatrons.

The cosmic-ray spectrum is approximately described by a power-law that covers almost 14 orders of magnitude in energy, $dN/dE \propto E^{-\alpha}$, where α is an spectral index that changes over the energy range of the spectrum (See Figure 2.4). This variation indicates a change in the properties of the cosmic rays, such as their chemical composition and whether their sources are Galactic or extragalactic. The cosmic-ray spectrum has been measured by many experiments over the years; extragalactic sources are expected to be more abundant as energy increases, and these are the only type of cosmic accelerators able to produce Ultra High Energy Cosmic Rays (UHECRs), charged particles with energies that exceed 10^{18} eV.

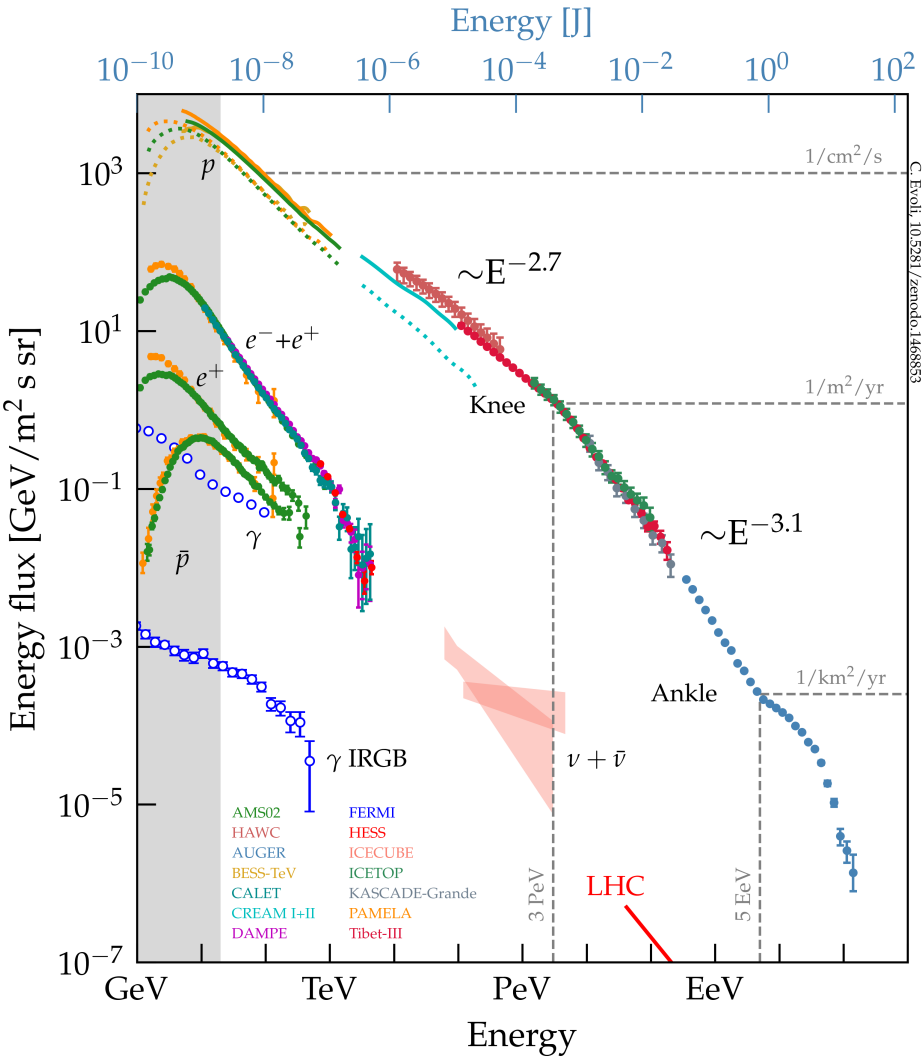

Figure 2.4: Cosmic-ray energy spectrum as measured by several experiments. Image credit: Carmelo Evoli, `https://doi.org/10.5281/zenodo.2360277`, last accessed on 01/08/22.

For energies between 10^9 eV and 4×10^{15} eV the power-law index that describes the cosmic-ray spectrum best is $\alpha \sim 2.7$. For energies above 4×10^{15} eV, the flux starts to decrease more steeply; α changes from ~ 2.7 to about ~ 3.1. This feature is called 'the knee', and is supposed to indicate the maximum acceleration energy of Galactic sources (Blümer et al., 2009). There is another pivotal point in the cosmic-ray spectrum slope around 10^{17} eV, where the spectral index becomes ~ 3.3. This feature is also referred as the 'second knee' (Bergman and Belz, 2007).

For energies above 5×10^{18} eV the spectrum flattens and α returns to a value of

~ 2.6. The corresponding feature for this third pivotal point is called 'the ankle'.

Above 5×10^{19} eV sees a strong suppression of the cosmic-ray flux observed (Pierre Auger Collaboration, 2008). This is referred to as the Greisen–Zatsepin–Kuzmin (GZK) limit (Greisen, 1966; Zatsepin and Kuzmin, 1966) and can be explained either by the energy losses occurring due to interaction with the CMB radiation during propagation, or by an intrinsic limit of sources, i.e. that they are not able to accelerate particles beyond a certain energy.

According to the bottom-up scenario (i.e. cosmic rays accelerated by astrophysical sources), gamma-ray photons can be produced by the radiation from charged particles (cosmic rays) crossing through a magnetic field.

In addition, for hadronic scenarios (see Section 2.7) gamma-rays and neutrinos can be produced from the interaction of relativistic protons with photon fields ($p\gamma$ interactions) or nuclear targets (pp interactions), such as molecular clouds or dust. Therefore, gamma-rays and neutrinos can be used as probes for revealing the sites of cosmic-ray acceleration.

A clear identification of extragalactic neutrino sources and their significant association with gamma-ray counterparts would be conclusive evidence for hadronic scenarios in astrophysical sources and a step forward into the long-standing problem of the enigmatic neutrino sources. This idea is explored in Chapter 4 and Chapter 5, where a hadronic scenario is applied to explain the emission from a blazar, and the potential of a multi-messenger collaboration programme between IceCube and CTA is investigated.

2.4 Fermi acceleration

Proposed by Enrico Fermi (Fermi, 1949), the Fermi acceleration model is one in which particles can gain energy through collisions with interstellar clouds. This mechanism can be present in many astrophysical environments, like AGNs, stellar

winds, SNRs, GRBs, X-ray binaries, etc.

In the second-order Fermi acceleration mechanism, acceleration occurs by particles having random elastic collisions with interstellar clouds. The particles will gain energy as they scatter among the clouds, which are moving at a typical velocity V_{clouds}. Under relativistic conditions, the average increase in energy during a collision is:

$$\langle \frac{\Delta E}{E} \rangle = \frac{8}{3} \left(\frac{V_{\text{clouds}}}{c} \right)^2 \tag{2.5}$$

Since the gain in energy is proportional to $(V_{\text{clouds}}/c)^2$, this process is called second-order Fermi acceleration. This result leads to an exponential increase in the the particle's energy.

If the mean free path between clouds along a direction is L_{free}, and ϕ the pitch angle, then the time between collisions can be averaged to $2L_{\text{free}}/c$, and the average rate of energy increase would be (Longair, 2011):

$$\frac{dE}{dt} = \frac{4}{3} \left(\frac{V_{\text{clouds}}^2}{cL_{\text{free}}} \right) E = \zeta E \tag{2.6}$$

where

$$\zeta = \frac{4}{3} \left(\frac{V_{\text{clouds}}^2}{cL_{\text{free}}} \right) . \tag{2.7}$$

The particles are assumed to remain gaining energy via collisions for a characteristic time τ_{esc}, after which they will escape the acceleration region. A power-law distribution of particle energies is obtained from the second-order Fermi acceleration process:

$$\frac{dN}{dE} = -\left(1 + \frac{1}{\zeta \tau_{\text{esc}}} \right) \frac{N(E)}{E} \tag{2.8}$$

and the

$$N(E) \propto E^{-(1+(\zeta\tau_{\text{esc}})^{-1})}, \tag{2.9}$$

First-order Fermi acceleration occurs when a charged particle crosses a plasma magnetic turbulence. The particle receives a small increase in energy when crossing the shock from the downstream to the upstream flow and in travelling from

upstream to downstream. The process is repeated back and forth across the shock leading to a transfer of energy and momentum to the charged particle, increasing its speed. After many acceleration cycles, the particle can reach relativistic velocities. This process is also known as the diffusive shock acceleration mechanism, and was discovered independently by a number of authors in the late 70's (Axford et al., 1977; Krymskii, 1977; Bell, 1978; Blandford and Ostriker, 1978).

Assuming V_s is the typical velocity of the shock front, then the average energy gained by the particle when crossing a shock front is given by:

$$\langle \frac{\Delta E}{E} \rangle = \frac{2}{3} \left(\frac{V_s}{c} \right) \tag{2.10}$$

The first-order Fermi acceleration model provides an efficient way to accelerate particles (cosmic rays). A key feature of this process is that the particle's acceleration is first order in the shock velocity and automatically results in a power-law spectrum with an energy spectral index of ≈ 2:

$$N(E)dE \propto E^{-2}dE \tag{2.11}$$

In this work, the diffusive shock acceleration mechanism is assumed to take place in blazars to explain the existence of a relativistic particle population that would be responsible for the gamma-ray emission. The nature (leptonic or hadronic) of this particle population is explored and discussed in Sections 2.6 and 2.7.

The diffusive shock acceleration mechanism requires a particle to be confined within a region (of size L) where magnetic field shocks are present (with a magnetic field strength B). Once the particle reaches its maximum energy, the magnetic field is not able to keep the particle confined within the acceleration region and the particle escapes. Assuming a population of charged particles accelerated in an astrophysical source through the first-order Fermi mechanism, the maximum energy to which a particle can be accelerated is (Hillas, 1985):

$$E_{\max} = ZeBV_sL \tag{2.12}$$

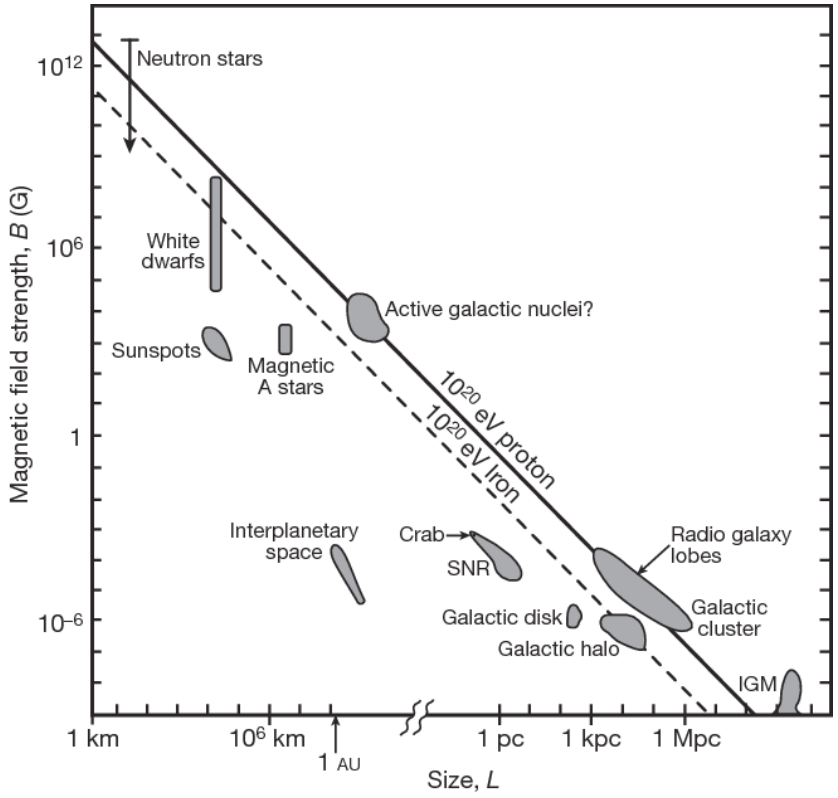

Figure 2.5: Hillas diagram showing possible cosmic-ray astrophysical sources. An approximate value for the combinations of size and magnetic field strength necessary to accelerate cosmic rays are shown as grey areas for a variety of sources. Above the solid (dashed) line, protons (iron nuclei) can be confined to energies above 10^{20} eV. Image credit: (Bauelo and Rodriguez Martino, 2009)

where Ze represents the electric charge of the accelerated particle and $\beta_s = V_s/c$ is the speed of the shock in units of light speed. This expression is known as the Hillas criterion (Hillas, 1985), and enables us to predict the most likely sources that might be able to accelerate protons to energies $\sim 10^{20}$ eV given the right combination of the size of the accelerator and the magnetic field strength. (See Figure 2.5).

2.5 Gamma-ray propagation

VHE particle propagation across cosmological distances involves interaction with photon fields from different wavelengths. In the UV and optical bands, the universe is populated by the light of stars, galaxies and its formation processes, that have

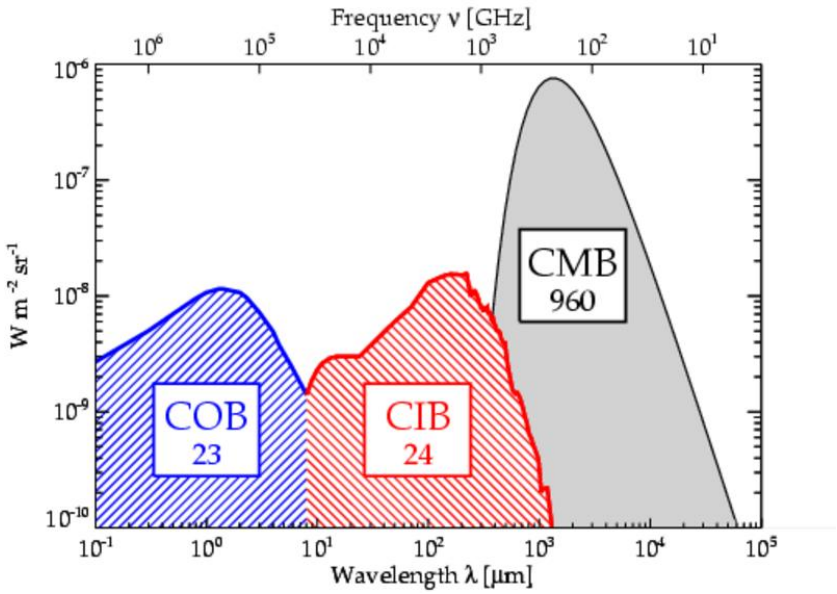

Figure 2.6: The Cosmic Infrared Background CIB, and the Cosmic Optical Background COB conforms the Extragalactic Background Light EBL. The EBL wavelength range extends from the IR band, through the optical and into the UV band. The CMB is also shown in the plot. Image credits: H. Dole et al.; `www.ias.u-psud.fr/irgalaxies/SpitzerPR2006/`, last accessed on 01/08/22.

been emitting since the epoch of reionisation ($z < 10$). This light is known as the Cosmic Optical Background (COB), which extends between 0.1 to 8 μm. The dusty environments in the Interstellar Medium (ISM) and around AGNs absorbs part of the visible light to be subsequently radiated in the IR band, forming the Cosmic Infrared Background (CIB), which extends in a wavelength between 8 and 1000 μm. The radiation accumulated by the COB and the CIB integrated over redshifts over all the cosmic Star Formation History (SFH) is known as the diffuse Extragalactic Background Light (EBL). Figure 2.6 shows the EBL components (CIB+COB) and their wavelength range.

As mentioned before, the EBL range extends from the IR through the optical and into the UV band. The EBL constitutes a fundamental source of opacity for the propagation of high energy cosmic ray particles and photons throughout space. The detection of extragalactic gamma-ray sources is limited by the absorption effect of the EBL.

The underlying process governing EBL absorption was described by Nikishov (1961) and later on by Gould and Schréder (1967). VHE gamma-rays from extragalactic sources suffer from attenuation effects by the creation of electron–positron pairs when photon-photon interactions occur with the EBL background: $\gamma\gamma \rightarrow e^{+}e^{-}$. This process takes place if the following kinematic condition is satisfied:

$$E'_{\gamma}\epsilon' > \frac{2(m_e c^2)^2}{1 - cos\theta'} \tag{2.13}$$

where E'_{γ} and ϵ' are the energies of the gamma-ray and background photons respectively in the comoving frame in which the interaction occurs, m_e is the mass of the electron, and θ' is the angle between the momenta of the two photons. If the collision is frontal, the kinematic condition dictates a lower energy threshold for the interaction: $2(m_e c^2)^2$.

The effective absorption observed at a given energy E'_{γ} from a gamma-ray source at a redshift z_0 is quantified by the optical depth $\tau_{\gamma,\gamma}(E_{\gamma}, z)$ (Dwek and Krennrich, 2005):

$$\tau_{\gamma,\gamma}(E_{\gamma}, z) = \int_0^{z_0} \frac{\partial D(z)}{\partial z} dz \int_0^{\infty} \frac{\partial n'(\epsilon', z)}{\partial \epsilon'} d\epsilon' \int_{-1}^{1} \frac{1 - cos\theta'}{2} dcos\theta' \sigma_{\gamma,\gamma}(E'_{\gamma}, \epsilon', cos\theta') \tag{2.14}$$

where $\partial D(z)/\partial z$ is the distance element in the Λ-cold dark matter (Λ-CDM) cosmology model, $\partial n'/\partial \epsilon'$ is the differential number density of the EBL photons, θ' the angle between the gamma-ray and the target photons in the comoving frame and $\sigma_{\gamma,\gamma}$ the differential cross-section for pair production process, which is given by (Jauch and Rohrlich, 1976):

$$\sigma_{\gamma,\gamma}(E'_{\gamma}, \epsilon', cos\theta') = \frac{3\sigma_T}{16}(1 - \beta^2) \times \left[2\beta(\beta^2 - 2) + (3 - \beta^4) \ln\left(\frac{1 + \beta}{1 - \beta}\right)\right] \tag{2.15}$$

where $\sigma_T = 6.65 \times 10^{-25}$ cm^2 is the Thomson cross-section and β is defined as:

$$\beta = \sqrt{1 - \frac{2(m_e c^2)^2}{E'_{\gamma}\epsilon'(1 - cos\theta')}} \tag{2.16}$$

The EBL intensity per unit solid angle is given by (Dwek and Krennrich, 2013):

$$I_{EBL}(\lambda, z) = \frac{c}{4\pi} \int_0^\infty \mathcal{L}(\lambda, z) \frac{dt}{dz} \frac{dz}{(1+z)} \tag{2.17}$$

where $\mathcal{L}(\lambda, z)$ is the luminosity density in a comoving volume element at redshift z and wavelength λ. The EBL intensity is usually presented in units of W m^{-2} sr^{-1} and provies an integral constraint on all the radiative energy releases over cosmic time. The comoving luminosity density is dominated by the radiation from stars, which means that most of the EBL is generated by these sources. AGNs can dominate the optical to IR output of a galaxy; however, in total AGNs make only a small contribution to the total energy release in the universe.

Several approaches have been used to model the EBL intensity. A direct measurement is a difficult task due to the high uncertainties and contamination coming from bright foregrounds from the Milky Way and the solar system, such as the zodiacal light (Hauser and Dwek, 2001). The derivation of the EBL intensity can also be done by studying the CIB fluctuations in the IR measurements (Kashlinsky, 2005; Pénin et al., 2012; Shang et al., 2012), however this method requires a detailed knowledge of the galaxy source counts, their luminosity function, and their clustering properties as a function of redshift.

There are also 'Backward' and 'Forward' evolution models to calculate the EBL intensity. Backward Evolution (BE) models (Franceschini et al., 2008; Domínguez et al., 2011) start from the determination of the local luminosity density $\mathcal{L}(\lambda, z)$, to evolve it with redshift using observed galaxy number counts at different wavelengths. Having determined the evolution of the spectral luminosity density with redshift, the EBL is obtained by integrating $\mathcal{L}(\lambda, z)$ over redshift. Forward Evolution (FE) models (Finke et al., 2010; Kneiske and Dole, 2010; Gilmore et al., 2012) use the fact that the total luminosity density is a direct measure of the Cosmic SFR. $\mathcal{L}(\lambda, z)$ is inferred from a variety of wavebands observations (Madau and Dickinson, 2014), then population synthesis and radiative transfer models are used to determine the distribution of the energy over the different wavelengths.

Another option is to determine the EBL from gamma-ray observations, but this requires knowledge of the sources' intrinsic spectra. The detection of the first distant gamma-ray sources led to the first observational constraints on gamma-ray absorption (e.g. 3C 279 Stecker et al. (1992)). Due to the energy relations between the interacting photons (Equation 2.13), a VHE gamma-ray photon will interact with an EBL photon in a narrow wavelength range. Given that blazars have a gamma-ray spectrum extending up to TeV energies, and BL Lacs do not present strong UV, Optical or IR photon fields, these objects are ideal cosmological probes for the EBL. The observations of blazar's spectra at GeV-TeV energies over a large redshift range allow the EBL intensity to be studied. The main challenge in constraining the EBL from gamma-ray observations of BL Lacs lies in the uncertainties coming from the complexity in understanding the emission process with internal absorption and dealing with possible curvatures in the intrinsic spectrum of the source. A more comprehensive review on the different methods to determine the EBL intensity can be found in Hauser and Dwek (2001) and Dwek and Krennrich (2013).

In Figure 2.7 the approximated EBL intensity at $z = 0$ is shown for different models: Franceschini et al. (2008), Domínguez et al. (2011), Finke et al. (2010), (Kneiske and Dole, 2010) and Gilmore et al. (2012). In general, all models agree on the shape and tendencies of the EBL intensity and provide an adequate fit to the EBL observational limits.

In this work, the EBL model of Domínguez et al. (2011) is used to calculate the observed gamma-ray spectrum of the blazars: Markarian 421 in Chapter 3 and 4FGL J0658.6+0636 in Chapter 4. It is also used as part of the modelling in simulations for hypothetical populations of steady neutrino and gamma-ray sources in Chapter 5. Domínguez et al. (2011) is a BE model based on measurements from the rest-frame K-band galaxy Luminosity Function (LF) up to $z = 4$ (Cirasuolo et al., 2010) and on multi-wavelength galaxy data from All-wavelength Extended Groth Strip International Survey (AEGIS) (AEGIS Collaboration, 2007) of about

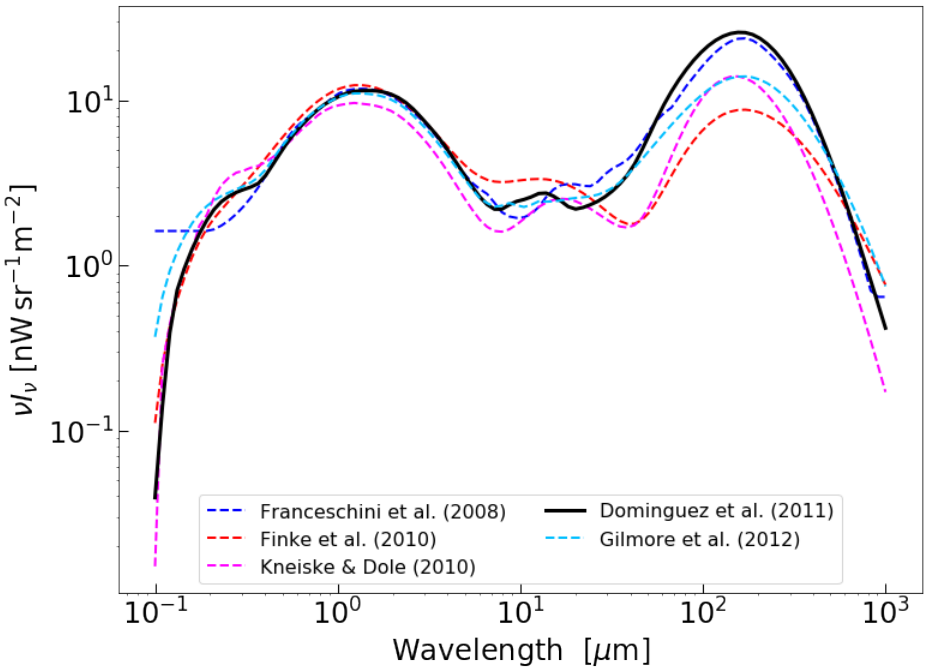

Figure 2.7: EBL intensity comparison for different models: Franceschini et al. (2008) (blue), Domínguez et al. (2011) (black), Finke et al. (2010) (red), (Kneiske and Dole, 2010) (magenta) and Gilmore et al. (2012) (light blue).

6,000 galaxies in the redshift range of $z = 0.2$ to $z = 1.0$. The luminosity densities at all wavelengths were calculated in three different bins according to the absolute rest-frame K-band magnitude (faint, middle and bright). Within every bin, an SED type was attached to each galaxy in the LF assuming SED-type fractions that are a function of redshift within those magnitude bins. Finally the light given at all redshifts is added up by to get the overall EBL spectrum. For further details see Domínguez et al. (2011).

The gamma-ray absorption effect for astrophysical sources is characterised by an exponential attenuation: $e^{-\tau_{\gamma\gamma}(E_\gamma,z)}$; where $\tau_{\gamma\gamma}$ is the optical depth, which depends on the redshift (z) of the source and the energy of the gamma-ray photons (E_γ). In Figure 2.8 the optical depth is plotted as a function of energy for the EBL model of Domínguez et al. (2011). The colour curves represent the redshift range considered. In Figure 2.9 the corresponding attenuation factor is given at different redshifts between 100 GeV and 100 TeV. The redshift dependency of the Domínguez

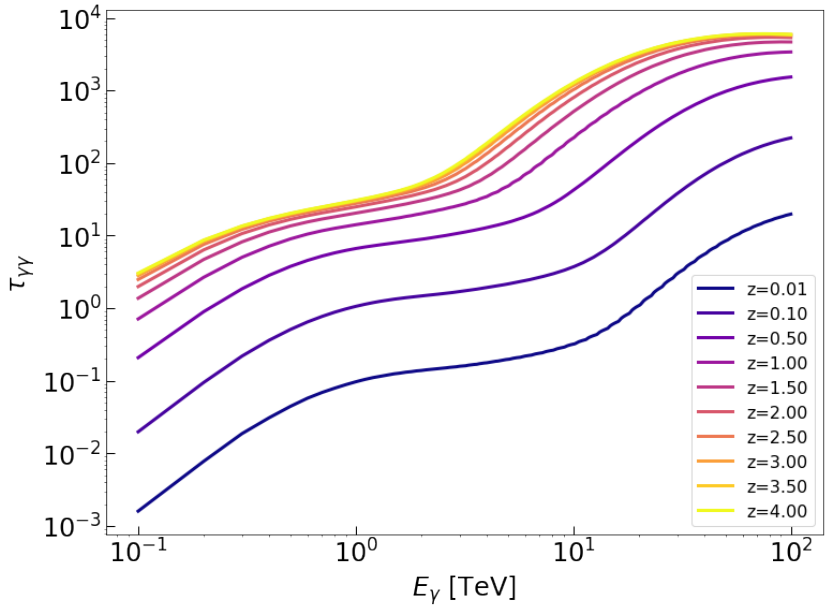

Figure 2.8: Optical depth (τ) for the EBL model of Domínguez et al. (2011) as a function of redshift over an energy range between 100 GeV and 100 TeV. The colour curves show the value for τ at different redshifts $0.1 \leq z \leq 4.0$.

et al. (2011) EBL model is shown in Figure 2.10.

GeV photons interact mainly with UV/optical photons, whereas TeV photons interact mainly with photons in the near-IR region of the EBL. The measured intensity of the EBL is lower at UV energies, which suggests a universe essentially transparent to gamma-rays with energies below 10 GeV (See Figure 2.10), and becoming gradually opaque for TeV sources at redshifts of $z > 0.5$ (See Figure 2.9).

2.6 Leptonic scenarios

In a leptonic scenario, the radiative output responsible for the typical blazar SED shape is completely explained by the electron/positron population. The X-ray and gamma-ray emission (often correlated in observed blazar emissions) is naturally explained by the SSC radiation.

It is assumed that electrons are accelerated following a power-law distribution: $\phi_e = dN/dE_e = K_e E_e^{-p}$, where p is the spectral index, K_e a normalisation constant

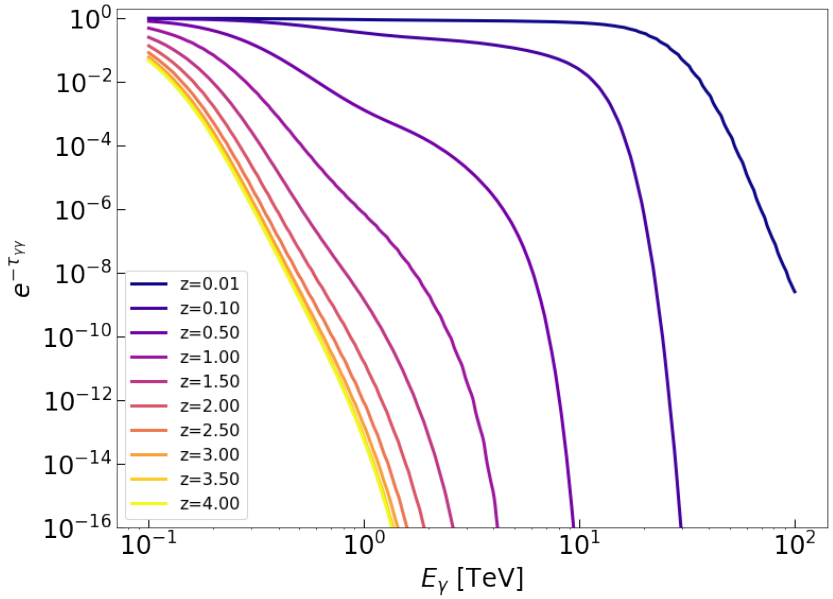

Figure 2.9: Attenuation factor given by the EBL model of Domínguez et al. (2011) at different redshifts ($0.1 \leq z \leq 4.0$) over an energy range between 100 GeV and 10 TeV. The flux of the astrophysical sources at higher redshifts is drastically attenuated, specially at the TeV energy range.

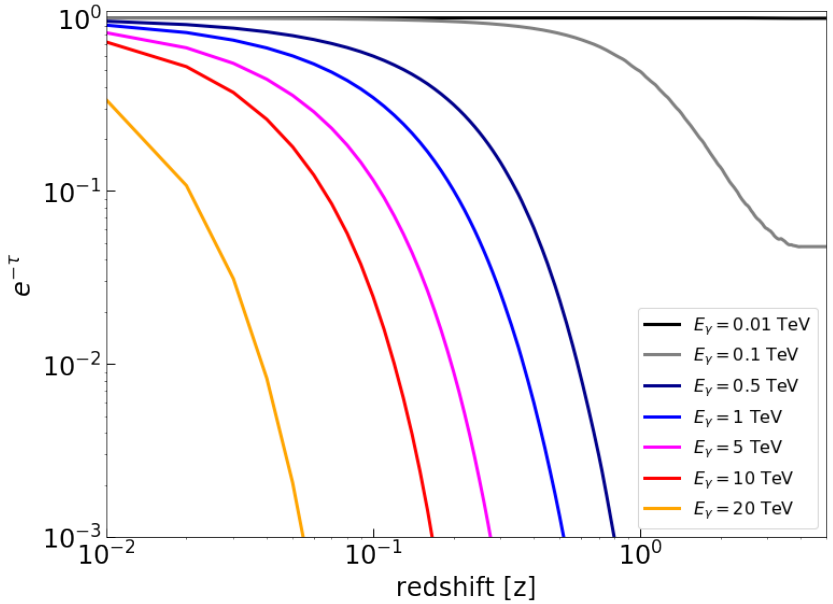

Figure 2.10: Attenuation factor $e^{-\tau_{\gamma\gamma}}$ for the EBL model of Domínguez et al. (2011) as a function of redshift (z). The curves plotted show the attenuation effect over an energy range of 0.01-20 TeV. The universe is considered transparent to gamma-rays below 10 GeV.

and E_e the electron's energy. Given a uniform magnetic field B, the associated magnetic energy density is:

$$U_B = \frac{B^2}{8\pi} \,, \tag{2.18}$$

and the power loss of an electron by synchrotron radiation can be expressed as:

$$P_{\text{sync}} = \frac{dE_e}{dt} = 2\sigma_T c\beta^2\gamma^2 \sin^2 U_B\psi \tag{2.19}$$

where ψ is known as the pitch angle between the electron velocity v_e and the magnetic field B, γ is the Lorentz factor as defined in Section 2.2, $\beta = v_e/c$ is the velocity of the particle in light speed units, and $\sigma_T = 6.65 \times 10^{-25}$ cm^2 is the Thomson cross-section of an electron.

The accelerated electron populations in radio sources can have lifetimes of 10^3 to 10^6 years, timescales in which the particles are scattered repeatedly, making the pitch angle distribution isotropic. Given that $\langle \sin^2 \psi \rangle = 2/3$, the average synchrotron power per electron is:

$$\langle P_{\text{sync}} \rangle = \frac{4}{3}\sigma_T c U_B \beta^2 \gamma^2 \tag{2.20}$$

Considering that the synchrotron energy radiated by an ensemble of electrons in a frequency range ν to $\nu + d\nu$ can be attributed to the electrons with energies between E_e and $E_e + dE_e$, the emissivity will be:

$$J(\nu)d\nu = -\frac{dE_e}{dt} N(E_e) dE_e \tag{2.21}$$

if the electron energy distribution follows a power-law description $dN(E_e)/dE_e = K_e E_e^{-p}$; the emissivity can be expressed as (Longair, 2011):

$$J(\nu)d\nu \propto K_e B^{(p+1)/2} \nu^{-(p-1)/2} = K_e B^{a+1} \nu^{-a} \tag{2.22}$$

where $a = (p-1)/2$ is the spectral index of the synchrotron emission, and is determined by the electron distribution power index p.

The second mechanism involved in the SED emission associated with the production of gamma-ray photons is IC scattering. In this mechanism the photons can gain energy by interacting with the relativistic electrons.

The average frequency $\langle\nu\rangle$ of an up-scattered photon in the observer's reference frame is:

$$\langle\nu\rangle = \frac{4}{3}\gamma^2\nu_0 \tag{2.23}$$

where ν_0 is the initial frequency of the photon and γ the associated Lorentz factor. Under the IC mechanism, low-energy photons (such as radio photons) can scatter to higher energies in the X-ray and gamma-ray band while draining energy from the population of relativistic electrons. The IC spectrum is sharply peaked near the value of the average photon frequency (Blumenthal and Gould, 1970).

The radiated power of the IC up-scattered photons is given by

$$P_{\rm IC} = \frac{4}{3}\sigma_T c\beta^2\gamma^2 U_{\rm rad} \tag{2.24}$$

where σ_T is the Thomson cross-section $U_{\rm rad} = n_\gamma h\nu$ is the energy density of the incident radiation, n_γ the photon number density, and h the Planck constant. If the emitted synchrotron photons are up-scattered by the parent electron population, then the process is called Synchrotron Self-Compton (SSC).

An interesting feature is that the ratio of the IC radiation power and the synchrotron radiation power is:

$$\frac{P_{\rm IC}}{P_{\rm Sync}} = \frac{U_{\rm rad}}{U_B} \tag{2.25}$$

The similarity between the synchrotron and IC scattering processes is also reflected in the power-law description for the IC spectrum. The spectral index of the IC radiation process will be also given by $a = (p-1)/2$, just like in the synchrotron case, where p is the power-index of the electron energy distribution.

The standard interpretation of the leptonic scenario (one-zone SSC model; Maraschi et al. (1992), Dermer and Schlickeiser (1993), Bloom and Marscher (1996), Tavecchio et al. (1998)) assumes a population of relativistic electrons which are accelerated into a spherical region inside the jet (a blob). Due to the strong magnetic field associated with the jet, electrons emit synchrotron radiation. When a synchrotron photon collides with an electron, the photon gets up-scattered by the

IC effect, reaching higher energies in the X-ray and gamma-ray domain. This picture allows us to explain the typical SED of a blazar with a single emission zone; the observed variability is interpreted by postulating a small and compact region of emission resulting in the X-ray and gamma-ray emission being correlated naturally.

2.6.1 Two-zone leptonic models

The rapid variability observed in gamma-ray data (with timescales down to minutes) represents a challenge to modelling the whole SED with a one-zone SSC model, as the low-frequency radio emission, or data in the IR, optical or UV region would not be reproducible with the same model parameters. A possibility within the leptonic scenario to solve this problem is adding an extra emission region (two-zone SSC). The two regions are assumed to be independent of each other, which will increase the number of free parameters in the model but might produce a more realistic approximation of the SED.

To extend the typical one-zone SSC model, two-zone models where external photon fields serve as targets for IC emission have been used to model blazars. The external radiation fields can be optical-UV photons from the BLR (Sikora et al., 1994; Finke, 2016), photon fields from the accretion disk emission (Dermer et al., 1992; Dermer and Schlickeiser, 1994, 2002; Böttcher et al., 2009), IR radiation from the obscuring torus (Błażejowski et al., 2000) or synchrotron emission from faster regions inside the blazar's jet (Georganopoulos and Kazanas, 2003, 2004). More than two-zones can also be considered to model blazar emissions, this approach is referred in literature as multi-zone emission models (Graff et al., 2008; Marscher, 2014).

2.7 Hadronic scenarios

There have been different motivations to consider hadronic interactions in blazars. An important example is the possible correlation between the emission from the

flaring blazar TXS 0506+056 and the IceCube neutrino alert IC-170922A (IceCube Collaboration et al., 2018), which was found in spatial and temporal coincidence at a significance level of $\sim 3\sigma$. An independent IceCube analysis found an excess of high energy neutrino events (13 ± 5 equivalent to $\sim 3.5\sigma$ significance level) coming from the direction of TXS 0506+056 between September 2014 and March 2015 (IceCube Collaboration, 2018), establishing TXS 0506+056 as one of the most promising neutrino candidates. This possible neutrino association is reviewed in detail on Section 1.5.2. Hadronic acceleration would also explain other possible reported associations of blazars with HE astrophysical neutrinos (Kadler et al., 2016; Giommi et al., 2020), there are also several studies searching for gamma-ray counterparts and predicting consistent limits within the IceCube neutrino flux so far (Krauß et al., 2014; TANAMI Collaboration and Fermi-LAT Collaboration, 2015; Brown et al., 2015; Padovani et al., 2016; Glüsenkamp, 2016).

Hadronic scenarios propose the existence of protons that can be co-accelerated alongside electrons to relativistic energies ($E_p > 10^{17}$ eV). Confining protons of this energy within a small emission region (inferred from the observed rapid variability), typically requires magnetic fields of $10 < B < 100$ G. Due to the strong magnetic field, electron-synchrotron and proton-synchrotron radiation are expected. Depending on the model, these scenarios could have a dominant proton synchrotron contribution (Aharonian, 2000; Mücke and Protheroe, 2001; Mücke et al., 2003; Zech et al., 2017), while other groups of models invoke photohadronic ($p\gamma$) interactions, in which the relativistic high-energy protons collide with internal photon fields (typically electron-synchrotron) producing VHE gamma-rays and neutrinos from photo-meson decay (Mannheim and Biermann, 1992; Mannheim, 1993; Böttcher, 2005; Böttcher et al., 2013; Dimitrakoudis et al., 2012; Mastichiadis et al., 2013; Diltz and Böttcher, 2016; Keivani et al., 2018; Cerruti et al., 2019; Gao et al., 2019; Rodrigues et al., 2019; Petropoulou et al., 2020). As these models include both leptonic and hadronic contributions, they are also named lepto-hadronic models.

Other hadronic models are based on hadronuclear (pp) interactions. These interactions can occur if the high energy protons accelerated along the jet reach a matter target, for example the gas clouds in the BLR (Dar and Laor, 1997; Araudo et al., 2010; Liu et al., 2019) or the interaction of a massive star with the base of the jet structure (Barkov et al., 2010; Bosch-Ramon et al., 2012). The (pp) interaction has a lower cross-section compared to the $p\gamma$ interaction process, so a high density target is required to improve the efficiency of the process.

Hadronic models have also been used to explain the spectral hardening at TeV energies, behaviour which has been observed in some blazars, such as W Comae, 3C 66A (Böttcher et al., 2013), 1ES 0229+200 (Tavecchio et al., 2009), 1ES 1101-232 and H 2356-309 (Aharonian et al., 2006)). From these studies, it is clear that a pure leptonic component was not able to provide a good SED representation, and the addition of hadronic components were required. Succesful SED modelling of flaring episodes with hadronic models include: Mrk 501 (Aharonian, 2000), Markarian 421 (Fermi-LAT Collaboration et al., 2011; Zech et al., 2017; Mastichiadis et al., 2013; Sahu et al., 2016, 2018), RXJ0648.7+1516 (VERITAS Collaboration, 2011), RBS 0413 (VERITAS Collaboration, 2012), 1ES 0414+009 (VERITAS Collaboration et al., 2012), 1ES 1011+496 (Sahu et al., 2017), 3C 454.3 (Diltz and Böttcher, 2016), 1ES2344+514 (MAGIC Collaboration et al., 2020), amongst others.

According to the standard SSC model, a strict correlation between the gamma-ray and X-ray band should be observed during a flaring state, since the high-energy peak is produced by the self-Compton interactions of an electron particle population. However, there are some exceptions in which gamma-ray flaring activity is not accompanied by X-ray variations; these are called “orphan” flares and have been detected on different occasions from: 1ES 1959+650 during 2002 (Whipple Collaboration, 2003; Krawczynski et al., 2004), Mrk 421 in 2004 (VERITAS Collaboration, 2005), PKS 1510-089 in 2008 (Marscher et al., 2010), 3C 273 during 2009-2010 (Rani et al., 2013), 3C 279 in 2011 (MAGIC Collaboration, 2014a), amongst others. Orphan flares challenge the traditional leptonic SED explanation

and have proven difficult to reproduce using a one-zone SSC model. The notion of uncorrelated gamma-ray emission can be explained by introducing a hadronic component.

2.7.1 Photohadronic interactions

Photohadronic models require protons to be accelerated to energies above 10^{17} eV to reach the threshold energy of $p\gamma$ interactions. It is also required magnetic fields with $B > 10$ G to constrain the size of the emission region within $R < 10^{16}$ cm, which corresponds to the typical values inferred from the observed variability in blazars. The target photon field is typically assumed to be the synchrotron photons from the co-accelerated electron population, but it also can be IC radiation or external Compton photon fields.

Photo-pion production can be described by the the Δ^+-resonance approximation; a simplified approach to compute the gamma-ray emission from $p\gamma$ interactions. The subsequent decay products include gamma rays and neutrinos in the following way:

$$p + \gamma \rightarrow \Delta^+ \rightarrow \begin{cases} p\pi^0,\ \pi^0 \rightarrow \gamma\gamma \\ n\pi^+,\ \pi^+ \rightarrow \mu^+\nu_\mu,\ \mu^+ \rightarrow e^+ + \nu_e + \bar{\nu_\mu}\,. \end{cases} \tag{2.26}$$

The Δ^+ particle decays into $(p + \pi^0)$ in 2/3 of all cases while it goes to $(n + \pi^+)$ in 1/3 of all cases due to iso-spin conservation (Longair, 2011). There are other barionic resonances that can occur in photohadronic interactions (see Rachen (1996)), however the Δ^+-resonance is the one that has the lowest energy threshold and the most prominent cross-section, which is why is used as an approximation for phenomenological and semi-analytical models.

VHE gamma-ray emission from blazars is dominated by photo-pion production, although synchrotron radiation from the charged particles in the decay chain, such as protons, $\pi^\pm$, $\mu^\pm$, can contribute to the emission.

Photo-pair production via the Bethe-Heitler process is another type of $p\gamma$ interaction that could contribute at lower gamma-ray energies:

$$p + \gamma \rightarrow p + e^- + e^+ \tag{2.27}$$

The threshold energy for this process is ~ 1 MeV in the rest frame of the proton (Romero et al., 2017). When the proton energy exceeds the threshold energy for photo-meson production, the photohadronic interactions dominate over the photo-pair production (Kelner and Aharonian, 2008).

It is also worth mentioning that hadronic processes are accompanied by the production of neutrinos. The expected neutrino flux is discussed in Section 2.7.4.

2.7.2 Delta-resonance approximation

The Δ^+ particle has a mass of $m_{\Delta^+} = 1.232$ GeV; this is the threshold for interaction and corresponds to the production of the particle at rest. Above this energy threshold, the cross-section of the process is enhanced and this decay channel becomes dominant over other components. At its peak, the cross-section of the Δ^+-resonance reaches a value of $\sigma_{\rm peak} \sim 500$ μbarn, which is $\sim 5 \times 10^{-28}{\rm cm}^2$, being bigger by a factor of ~ 5 than the direct channel cross-section production (Hümmer et al., 2010). There are other baryon resonances (see red dashed line in Figure 2.11), which have smaller cross-sections at higher energies and are not considered in the Δ^+-resonance approximation. Multi-pion production becomes the dominant production channel at higher energies, where the total photohadronic cross-section becomes roughly constant at $\sim 125\mu$barn.

The threshold of the interaction dictates an energy relation between the proton energy E'_p and seed photon ϵ'_γ in the emission region reference frame:

$$E'_p = \frac{m^2_{\Delta^+} - m^2_p}{2\epsilon'_\gamma(1 - cos\phi)}\,, \tag{2.28}$$

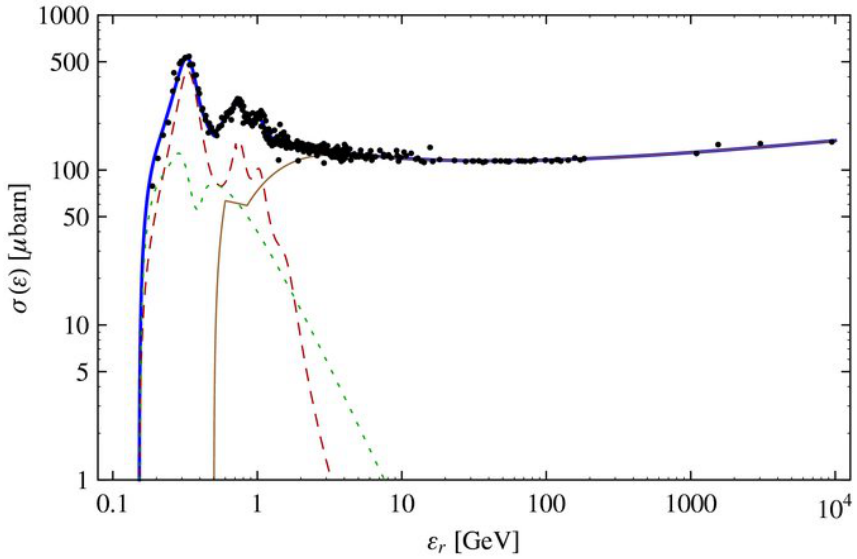

Figure 2.11: $p\gamma$ photo-meson cross-section as a function of the photon's energy (ϵ_γ) in the proton rest frame. The contributions of baryon resonances (red dashed), the direct channel (green dotted), and multi-pion production (brown) are shown separately. Data from Particle Data Group (2020) are shown as dots. This image was taken from Hümmer et al. (2010).

where m_p is the proton mass and ϕ is the angle formed between the interacting particles. Since the proton will collide with the target photons from all directions there is not a preferred angle of interaction and $1 - cos(\phi) \sim 1$.

Near the energy threshold of the process the Δ^+-resonance has been used as an approximation, which gives a pion production cross-section as:

$$\sigma_{\Delta^+} = 500\ \mu\text{barns}\ \Theta(\sqrt{s} - m_{\Delta^+} + \Gamma_{\Delta^+}/2) \cdot \Theta(m_{\Delta^+} + \Gamma_{\Delta^+}/2 - \sqrt{s}) \qquad (2.29)$$

where $m_{\Delta^+} = 1.232$ GeV is the mass and $\Gamma_{\Delta^+} = 0.115$ GeV is the width of the Δ^+-resonance, Θ is the Heaviside step function (Stecker, 1973; Gaisser et al., 1995). A more detailed discussion of the Δ^+-resonance can be found in Mücke et al. (1999); Gaisser et al. (1995).

Hadronic interactions in astrophysical sources can also be computed using Monte Carlo simulation methods (Mücke et al., 2000; Mücke and Protheroe, 2001). Monte Carlo simulations provide a more sophisticated description of the hadronic interactions given a set of parameters, but the simulations require long computational

times and efficient implementation within lepto-hadronic codes. As an alternative, semi-analytical and phenomenological models have been used in simplified scenarios. The photohadronic flaring model, presented in the next Section, uses the Δ^+-resonance approximation to estimate the photo-pion production of gamma-rays and neutrinos in blazars, and in Chapter 5 the model given by Ahlers and Halzen (2018) is discussed and used to calculate the gamma-ray flux from hypothetical neutrino sources.

2.7.3 Photohadronic Flaring Model

In the photohadronic scenario a one-zone leptonic model is assumed to contribute to the SED via electron synchrotron and SSC radiation; this is a standard leptonic interpretation. The low-energy peak from the SED comes from the synchrotron component which is of leptonic origin, while the synchrotron and SSC components can provide a target photon field in the MeV range. For the photohadronic contribution to arise, it is hypothesised that protons are accelerated into the single spherical emission region of radius R'_f * (flaring blob), with a tangled magnetic field B, propagating along the jet with a velocity β_Γ (in light speed units) and an associated bulk Lorentz factor Γ. The jet forms a small angle θ with respect to the line of sight, which results in a Doppler boosting characterised by the Doppler factor D.

The size of the emission region can be constrained using the minimum variability time scale (Dondi and Ghisellini, 1995):

$$R'_f \leq cDt_{\rm obs}(1+z)^{-1}\,, \tag{2.30}$$

where $t_{\rm obs}$ is the observed time variability (obtained with Equation 2.4), c is the speed of light and z the source's redshift.

It is proposed that during the flaring episode, the blazar possesses a dense, compact inner jet structure (Ghisellini et al., 2005; Marscher et al., 2008, 2010; MacDonald

*The prime notation is adopted to refer the jet comoving reference frame.

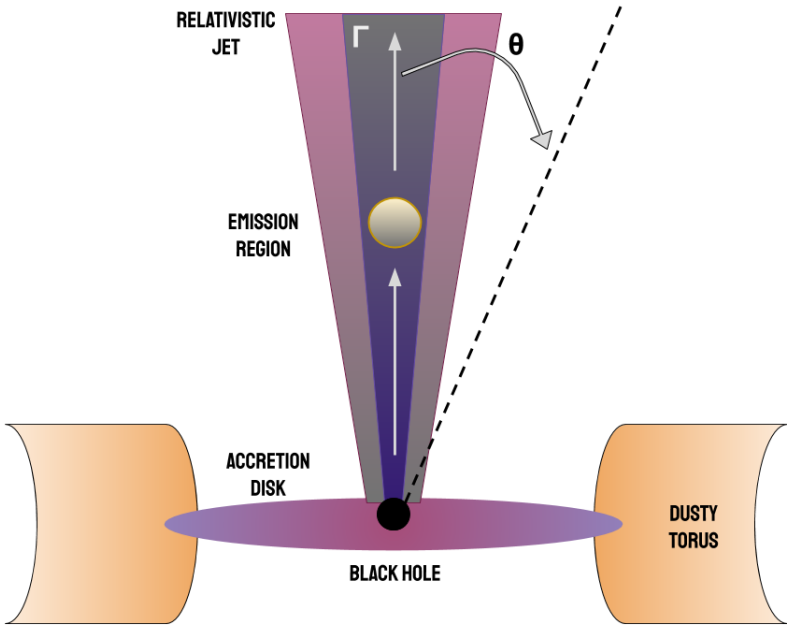

Figure 2.12: Schematic representation of a one-zone emission region in a flaring blazar. A blob is propagating inside the relativistic jet boosted by a Lorentz factor Γ. The photohadronic interaction will take place inside the emission region, producing neutrinos and gamma-rays through pion-decay.

et al., 2015; Homan et al., 2015; Walker et al., 2016). Geometrically this represents a double conical shape, with a compact and smaller region enclosed by the jet along its axis (see Figure 2.12). The inner compact region has a photon density $n'_{\gamma,f}$, which is much higher than the outer region n'_{γ}; this helps to increase the efficiency of the photohadronic interactions. Inside the emission region an electron population will produce synchrotron and SSC radiation following the usual one-zone leptonic scenario. $p\gamma$ interactions can emerge from the collisions between high energy protons and the internal photon field, the SSC photons in the MeV range will serve as targets for the interaction, resulting in a TeV energy gamma-ray from the photo-pion production.

In the observer's frame, due to the Doppler boosting effect from the jet, the photon energy will be enhanced as:

$$\epsilon_{\gamma} = \frac{D}{1+z}\epsilon'_{\gamma}\,. \tag{2.31}$$

Considering that each pion carries $\sim 20\%$ of the proton energy (Hümmer et al., 2010) and in the photo-pion production 2 gamma rays are produced from the π^0-decay, we have the following relation between the gamma-ray photon energy E_γ produced with a proton energy E_p in the observer's frame:

$$E_\gamma = \frac{1}{10}\frac{D}{1+z}E'_p = \frac{D}{10\Gamma}E_p\,. \tag{2.32}$$

In this scenario, high energy protons can be injected into a confined region (a spherical blob) of radius R'_f inside the blazar's jet. For simplicity, it is assumed that the internal jet region and the external jet are moving with almost the same bulk Lorentz factor Γ. For blazars, we consider that the Doppler factor and the Lorentz factor are approximately of the same magnitude $D \sim \Gamma$ (Oikonomou et al., 2019).

From the energy threshold condition to produce the Δ^+-resonance, an energy relation between the target photons ϵ_γ and the gamma-ray photons E_γ in the observer's frame can be expressed as:

$$E_\gamma \epsilon_\gamma \simeq 0.032\frac{D^2}{(1+z)^2}\ \mathrm{GeV}^2\,. \tag{2.33}$$

The central region of an AGN possesses shocks that are able to accelerate electrons and ions through the Fermi mechanism; when one of these relativistic particles crosses the shock from downstream to upstream or vice versa, it gains energy (Baring, 1997). A PL injected spectrum for the protons is considered: $dN(E_p)/dE_p \propto E_p^{-\alpha}$, where the spectral index α is treated as a free parameter in the model.

The high energy protons will interact in the inner jet region where the seed photon density is $n'_{\gamma,f}$. The gamma-ray spectrum obtained at VHE will depend proportionally on the photon background and the injected proton spectrum (Sahu et al., 2012, 2013):

$$F_{int}(E_\gamma) \propto n'_{\gamma,f}E_p^2\frac{dN_p}{dE_p}\,. \tag{2.34}$$

The seed photon density will impact on the efficiency of the $p\gamma$ process; a low value reduces the chances of interaction and therefore the gamma-ray photon emission

obtained by this method. This photon density in the inner region of the jet is unknown, but we can set a very rough upper limit by assuming that the Eddington luminosity (L_{Edd}) of the source should not be exceeded and that it is equally shared by the jet and the counter jet. An upper limit on the seed photon density can be placed using:

$$n'_{\gamma,f} \ll \frac{L_{Edd}}{8\pi R'^2_f \epsilon'_\gamma}\,, \tag{2.35}$$

The photon density $n'_{\gamma,f}$ is proportional to the luminosity $L_\gamma(\epsilon_\gamma)$, and inversely proportional to the seed photon energy ϵ_γ. The luminosity at a certain energy is proportional to the observed flux $\Phi_{input}(\epsilon_\gamma)$, so we have that:

$$n'_{\gamma,f} \propto \Phi_{input}(\epsilon_\gamma)\epsilon_\gamma^{-1}\,. \tag{2.36}$$

This means the intrinsic gamma-ray flux will follow:

$$F_{int}(E_\gamma) \propto \Phi_{input}(\epsilon_\gamma)\epsilon_\gamma^{-1}E_p^2\frac{dN_p}{dE_p}\,, \tag{2.37}$$

considering a PL injected proton spectrum and using the energy relations between the proton energy (E_p), the seed photon energy (ϵ_γ) and the energy of the gamma-ray photon (E_γ), the intrinsic gamma-ray flux F_{int} coming from the π^0-decay can be expressed as:

$$F_{int}(E_\gamma) = A_\gamma \Phi_{input}(\epsilon_\gamma)\left(\frac{E_\gamma}{\mathrm{TeV}}\right)^{-\alpha+3}\,, \tag{2.38}$$

where A_γ is a dimensionless normalisation constant that absorbs the information from the various proportional relations given above, and α is the power index from the assumed proton spectrum.

When calculating the gamma-ray spectra, we must account for the attenuation of the high energy gamma rays due to the pair production effect with the EBL. The EBL provides an attenuation factor of the form $e^{-\tau_{\gamma\gamma}}$, where $\tau_{\gamma\gamma}$ is the optical depth, which increases at higher energies.

Including this attenuation factor in the expression for the gamma-ray flux (Equation 2.38), we get:

$$F_\gamma(E_\gamma) = A_\gamma \Phi_{input}(\epsilon_\gamma)\left(\frac{E_\gamma}{\mathrm{TeV}}\right)^{-\alpha+3} e^{-\tau_{\gamma\gamma}(E_\gamma,z)}\,. \tag{2.39}$$

2.7.4 Neutrino flux

A distinctive feature of hadronic models over the leptonic scenario is the the production of high-energy neutrinos. The identification of blazars as neutrino sources would unambiguously prove the presence of hadronic acceleration.

Neutrino production is expected from the subsequent pion decay in the $p\gamma$ scenario. From the kinematics of the decay chain, each neutrino will carry 1/4 of the π^+, therefore taking 3/4 of the total π^+, while the π^0 decays only into photons. On average, 20% of the proton's energy is transferred to the pion, which means the neutrino energy is roughly $E_\nu \sim E_p/20$ (Mücke et al., 1999). From these kinematic relations, the ratio between photon and neutrino luminosities corresponds to:

$$\frac{L_\nu}{L_\gamma} = 3/8 \tag{2.40}$$

The neutrino spectrum is assumed to mimic the proton spectrum and therefore a PL:

$$\frac{dN}{dE_\nu} = A_\nu E_\nu^{-\beta}\,, \tag{2.41}$$

where A_ν is the neutrino flux normalisation constant and β the neutrino spectrum index. A power index of $\beta = 2$ is assumed for the following calculations.

The gamma-ray flux and the neutrino flux have a common origin and can be related as (Alvarez-Muñiz and Halzen, 2002; Halzen and Hooper, 2005):

$$\int_{E_{\gamma,\min}}^{E_{\gamma,\max}} E_\gamma \frac{dN}{dE_\gamma} dE_\gamma = K \int_{E_{\nu,\min}}^{E_{\nu,\max}} E_\nu \frac{dN}{dE_\nu} dE_\nu \tag{2.42}$$

where K is a factor that depends on the type of hadronic interaction; for $p\gamma$ collisions $K = 4$, and for pp interactions $K = 1$. $E_{\gamma,\min}$ ($E_{\gamma,\max}$) is the minimum (maximum) energy of the produced gamma-ray photons and $E_{\nu,\min}$ ($E_{\nu,\max}$) is the minimum (maximum) energy for the related neutrino flux in the observer's reference frame. Both normalisation constants are then related via:

$$A_\nu \approx A_\gamma \frac{E_{\gamma,\min}^{-\alpha+2}}{(\alpha-2)Kln(E_{\nu,\max}/E_{\nu,\min})} E_\nu^{-2}\,. \tag{2.43}$$

The expected number of neutrino muon events can be approximated using the effective area from the neutrino detector considered:

$$N_{\text{events}} = T \int_{E_{\nu,\min}}^{E_{\nu,\max}} \frac{dN}{dE_\nu} A_{\text{eff}}(E_\nu, \delta) dE_\nu \ , \tag{2.44}$$

In this thesis, different IceCube string configurations (IC40, IC59, IC79, IC86) were used to calculate the expected number of neutrino events. Therefore A_{eff} corresponds to the effective area of the IceCube configuration under consideration, and T is the observation length period of time. The minimum neutrino energy $E_{\nu,\min}$ used in this step will depend in the lower limit given by the IceCube array configuration used, and the maximum neutrino energy $E_{\nu,\max}$ will be given by the imposed limit from the Hillas criterion (see Section 2.4). The effective area of the detector is declination (δ) and energy (E_ν) dependent; the numerical values used for the different IceCube configurations are available from the IceCube data releases web-page * (IceCube Collaboration, 2011a, 2013a, 2020b).

Most of the events detected with IceCube come from the atmospheric background, muons or neutrinos that are created when cosmic-rays interact with the atmosphere. The detection rates of these backgrounds within the IceCube detector are energy and zenith angle dependent, as well as being dependent upon the number of DOMs populating IceCube as it was constructed. The average atmospheric neutrino rate for the whole IC40 array was ~ 40 neutrino events per day (IceCube Collaboration, 2011a), for IC59 it was ~ 120 (IceCube Collaboration, 2013a), and for the IC86 configuration, the average atmospheric neutrino rate detection for the whole array is $\sim 200/$ events per day (IceCube Collaboration, 2020b).

To identify any object as an astrophysical neutrino point-source, a significant excess of neutrino events above the average background would be needed; this detection is energy and declination dependent, based on the effective areas and reconstruction response functions for each IceCube configuration. According to the IceCube Collaboration et al. (2018), a high-significance point-source detection can require

*See `https://icecube.wisc.edu/science/data-releases/`, last accessed on 01/08/22.

as few as two or three, or as many as 30, signal events to stand out from the background, depending on the energy spectrum and the clustering of events in time. Following this statement, if at least two neutrino events above the background level are required for a high-significance point-source detection, the concept of a Minimum Detection Time (MDT) can be defined as the estimated time elapsed for IceCube to detect this minimum quota during an active state of the source, but it is worth mentioning that a higher number of events might be needed for a positive detection. The concept of a MDT will be used in Chapter 4.

2.7.5 Model caveats

The photohadronic model assumes that the high energy protons are accelerated through a second order Fermi acceleration (diffusice shock acceleration) and that the seed photons for the $p\gamma$ interactions are coming from the standard leptonic mechanisms: electron synchrotron and SSC radiation.

The $p\gamma$ contribution calculated for the VHE part of the SED is highly dependent on the seed photon input considered Φ_{input}; which impacts the calculation of the estimated gamma-ray flux and therefore the normalisation constant for the predicted neutrino flux.

In the present work it is assumed a power-law (PL) description to fit the input (target) photon spectrum as:

$$\Phi_{input} = N_{PL}\epsilon_{\gamma}^{-\kappa+2} \tag{2.45}$$

The input photon spectrum can be derived using *Fermi*-LAT data and extended to energies below 100 MeV, where the $p\gamma$ interactions would occur. Therefore, reliable data in the MeV energy range that enable a more complex input model might improve the final fits, but at the expense of adding a larger number of free parameters.

The results obtained with the photohadronic model fit are concentrated on predictions for a dominant component at VHE gamma-rays under a one-zone emission

scenario, and it relies on the leptonic scenario interpretation. The feasibility of $p\gamma$ interactions is based on the high cross-section of the photo-pion production process through the Δ^+-resonance, and the gamma-ray flux is calculated adopting a phenomenological approach. It is noted that other contributions might be relevant at the GeV energy band, either from leptonic processes (e.g. SSC radiation), or from other hadronic processes such as proton-synchrotron cooling or synchrotron radiation emitted by the secondary charged particles produced in the $p\gamma$ decay chain. These multiple scenarios are beyond the scope of this thesis, and represent future improvements to the photohadronic flaring model.

2.7.6 Hadronuclear interactions

Proton-proton interactions (pp) represent another option to produce high energy neutrinos along with gamma-ray photons.

$$p + p \rightarrow \begin{cases} \pi^0 \rightarrow \gamma\gamma \\ \pi^+ \rightarrow \mu^+\nu_\mu \rightarrow e^+ + \nu_e + \nu_\mu + \bar{\nu_\mu} \\ \pi^- \rightarrow \mu^-\bar{\nu_\mu} \rightarrow e^- + \bar{\nu_e} + \nu_\mu + \bar{\nu_\mu} \end{cases} \tag{2.46}$$

This process has an energy threshold of:

$$E_{th} = m_p + m_\pi \frac{m_\pi + 4m_p}{2m_p} \approx 1.2 \text{ GeV} \tag{2.47}$$

The cross-section for the pp interactions is almost energy independent and lower than the expected for the $p\gamma$, $\sigma_{pp} \approx 4 \times 10^{-26}$ cm^2. For environments where the radiation density is low (few photons) pp can dominate over $p\gamma$ interactions.

Some studies assume pp interactions to avoid the high energy threshold limit of the $p\gamma$ interactions, which involves a dominance of the proton power in the jet and sometimes it is explained by super Eddington luminosities. On the other hand a pp interaction has a lower cross-section compared with the prominent Δ^+-resonance, so a high density target is required to improve the efficiency of the hadronic interactions. Hadronuclear interaction scenarios are not addressed in this work.

2.8 The Akaike Information Criterion (AIC)

As mentioned in the previous sections, there is a variety of models, both leptonic and hadronic, that could be used to fit the VHE gamma-ray data from blazars during flaring periods. These models are not homogeneous in complexity, i.e. the number of components and parameters used differs, as well as their fitting methods. To answer the question 'which model is better?', there is a methodology based on information theory widely used to assess the goodness of the fit, the AIC, which enables us to compare and rank different models for a given dataset.

Developed during the Second World War by Solomon Kullback and Richard Leibler (Kullback and Leibler, 1951), information theory is a compendium of methods and fundamental discoveries that provided a basis for model selection and inference. It has been applied to physics, medicine, ecology, economics, computer science and many other disciplines with huge success (Hipel, 1981; Burnham and Anderson, 2001; Glatting et al., 2007; Snipes and Taylor, 2014).

Information is defined as data that decrease our uncertainty about the state of a system. This cannot be measured with instruments but thanks to information theory it can be defined as a fundamental quantity in science, in terms of probability distributions. It is particularly useful to define the loss of information using the definition from Kullback and Leibler (K-L, Burnham and Anderson (2001); Burnham and Anderson (2002)): when a model g with certain parameters θ is used to approximate reality, represented by f, there is going to be a divergence between them. This is the loss of information and can be expressed as the integral

$$I(f,g) = \int f(x) log \frac{f(x)}{g(x|\theta)} dx \,, \tag{2.48}$$

where f and g are probability distributions. This can also be interpreted as a distance between the approximating model g to reality f. The best given model will minimise the integral, providing the smallest loss of information possible.

The link between information theory and statistics was found and explained by Hirotugu Akaike. He used the K–L information as a starting point to make a connection with the concept of maximum likelihood through his work. The Akaike Information Criterion (AIC) (Akaike, 1974), is a test that can be used to determine if a model fit is significantly better than another (Harris et al., 2014; Bozdogan, 1987; Forster, 2000). The AIC takes into account both the goodness of the fit and the simplicity of the model. This is done by assessing the likelihood and the number of free parameters adopted. For a given model s, AIC is defined as:

$$AIC_s = -2ln(L_s) + 2k_{fs}\,, \tag{2.49}$$

where L_s is the likelihood of the model used and k_{fs} is the number of free parameters in the model.

The AIC is based on a theoretical framework within information theory and provides a way to evaluate both the simplicity and accuracy of the model fits. The difference between the AIC of two models p,q is expressed as:

$$\Delta AIC_{p,q} = AIC_p - AIC_q\,. \tag{2.50}$$

The AIC difference enables the models considered to be compared and ranked. The model with the lowest AIC represents the best description of the empirical data available. Any model comparison with a $\Delta AIC_{p,q} > 2$ above the minimal AIC value is considered significantly worse (Burnham and Anderson, 2001; Lewis et al., 2011). The larger the difference, the less plausible is that a given model from a candidate set represents the best approximation.

In Chapter 3, the photohadronic model is applied alongside a one-zone and a two-zone pure leptonic scenario during a flaring period of the blazar Markarian 421. Using the AIC it was possible to compare and select the best fitting model for the daily datasets available.

Chapter 3

Possible Photohadronic Interactions in Markarian 421

The photohadronic scenario can be used to model the VHE emission from blazars during a flaring state. To test its potential, the near blazar Markarian 421 was selected during a high activity 14-day period in March 2010, during which ground-based telescopes (MAGIC, VERITAS and Whipple) recorded the flare in VHE gamma-rays. A tailored *Fermi*-LAT analysis was done on the source, focusing on the MeV range (100 MeV - 1 GeV) to describe the target photon spectrum, and the VHE data modelled on time scales of a couple of days. The final fit results were compared with a one-zone and a two-zone leptonic models using the Akaike Information Criterion (AIC) test. The results show how it is possible to explain the VHE emission with a dominant photohadronic contribution using a lepto-hadronic origin scenario. This chapter is based on the results and work published in (Rosales de León et al., 2021).

3.1 Markarian 421

Markarian 421 (Mrk 421; RA=66.114°, Dec=38.209°, z=0.031), a blazar catalogued as a HBL type (Fermi-LAT Collaboration, 2010a), is also one of the closest and

brightest objects in the extragalactic VHE sky. This blazar has been observed at radio, optical, X-ray and gamma-ray frequencies. It was the first extragalactic source detected using IACTs: between 24th March and 2nd June 1992 the 10m Whipple Observatory made a total of 15 hours of observations and found a signal with statistical significance of 6σ above the background which corresponded to an average flux of 1.5×10^{-11} photons cm^{-2} s^{-1} above 0.5 TeV, equivalent to 0.3 times that of the Crab Nebula (Punch et al., 1992).

Mrk 421 has been regularly monitored since its discovery, and is one of the few sources that can be detected at VHE energies nearly all the time with ground-based instruments, including flaring states on several occasions (Fermi-LAT Collaboration et al., 2011; MAGIC Collaboration and VERITAS Collaboration, 2015b,a). The highly variable nature of blazars makes MWL campaigns an important part of the process to understand their behaviour and define their limits. The results from each campaign provide further clues to decipher the possible emission mechanisms and set constraints on the modelling parameters, such as the size and possible location of the emission region. For Mrk 421, long MWL campaigns have been coordinated in the last couple of decades: March 2001 (Fossati et al., 2008), February 2003 to June 2004 VERITAS Collaboration (2005), November 2005 to June 2006 (Horan et al., 2009), March 2007 to June 2009 (MAGIC Collaboration, 2016b), January to June 2009 (MAGIC Collaboration and VERITAS Collaboration, 2015b), February (VERITAS Collaboration et al., 2020) and March 2010 (MAGIC Collaboration and VERITAS Collaboration, 2015a), November 2015 to June 2016 (MAGIC Collaboration et al., 2021), amongst others.

In some of these studies a correlation has been reported between VHE gamma-rays and X-rays during enhanced activity periods (Fossati et al., 2008; Katarzyński and Walczewska, 2010; MAGIC Collaboration et al., 2021). This is an indication that a common electron distribution, in a single physical region, can be responsible for the emission in both energy bands, supporting the idea of a one-zone SSC leptonic model to explain the blazar's MWL emission.

During a flaring state, Mrk 421's TeV emission can vary on sub-hour timescales. In May 1996, for example, the Whipple telescope recorded a dramatic flare of about 1-hour long that reached a flux level greater than the quiescent state by a factor of 50 (Gaidos et al., 1996). During a second outburst a week later, which lasted approximately 30 minutes, the flux increased by a factor of 20-25. In February 2010, an observation campaign also recorded two bursts in less than 140-minutes, on this occasion the VERITAS collaboration was able to bin light curves on 2-minute and 5-minute timescales during a flare that reached a level of 27 Crab Units above 1 TeV (VERITAS Collaboration et al., 2020). The short time variability of a few minutes presents difficulties for single-zone SSC leptonic models to reproduce the flaring data, implying that hadronic contributions or multiple zones might be needed to provide a better description.

Despite multiple studies and publications, the underlying physical processes that lead to VHE blazar emission are still under discussion. The SED of Mrk 421 has been successfully modelled during flaring states with one-zone leptonic models (VERITAS Collaboration, 2005; Fermi-LAT Collaboration et al., 2011; MAGIC Collaboration and VERITAS Collaboration, 2015a) and lepto-hadronic models (Fermi-LAT Collaboration et al., 2011; Zech et al., 2017; Mastichiadis et al., 2013; Sahu et al., 2016, 2018).

In 2010, a remarkable flare was recorded during a MWL campaign, with a rich dataset including VHE gamma-ray observations. This episode represents an ideal scenario to evaluate the possibility of a hadronic production mechanism and its evolution during a flare.

3.2 Flaring activity in 2010

Mrk 421 exhibited flaring activity over a 14-day period in 2010 from March 9th to March 23rd (MJD 55264-55278). At the time, a multi-instrument campaign was performed which included the gamma-ray space telescope *Fermi*-LAT and three

IACTs: MAGIC, VERITAS and the Whipple gamma-ray telescope. Extensive data were collected also in other wavebands; the MWL observations are shown in Figure 3.1.

In the VHE gamma-ray part of the spectrum, MAGIC took 11 observations in stereoscopic mode with exposure times ranging from 10 to 80 min each, which led to 4.7 h of good-quality data with a zenith angle range of $5° - 30°$. The data collected were taken in dark conditions and were not affected by moonlight, but the data recorded on MJD 55272 and 55275 suffered from bad weather and were therefore removed from the MWL observations (MAGIC Collaboration and VERITAS Collaboration, 2015a).

VERITAS monitored the source on MJD 55260, 55265, and 55267-55274 with a 10 min run per day (VERITAS Collaboration et al., 2020). The observations were performed at zenith angles $18° - 23°$ to benefit from the lowest possible energy threshold.

The Whipple telescope performed 10 observations in ON/OFF and TRK (tracking) modes (Pichel, 2009), lasting from one to six hours each on MJD 55267-55271 and MJD 55273-55277. The dataset collected for this flaring period amounts to 36 h.

The VHE gamma-ray data gathered from ground-based IACTs during the 14-day flaring period was published by MAGIC Collaboration and VERITAS Collaboration (2015a), and lies in an energy range between 80 GeV to 5 TeV. This VHE dataset is used to test a possible dominant contribution from photohadronic interactions. In this chapter, I focus on the modelling of the VHE gamma-ray observations. The energy ranges for the target photons and the accelerated protons are derived using the photohadronic flaring model with the Δ^+-resonance approximation in Section 3.6. The *Fermi*-LAT analysis and the IACT data were two key elements needed, and data from other wavelengths were not critical for the calculations (see MAGIC Collaboration and VERITAS Collaboration (2015a) for a full description of the MWL observations). The light curves from MAGIC, VERITAS

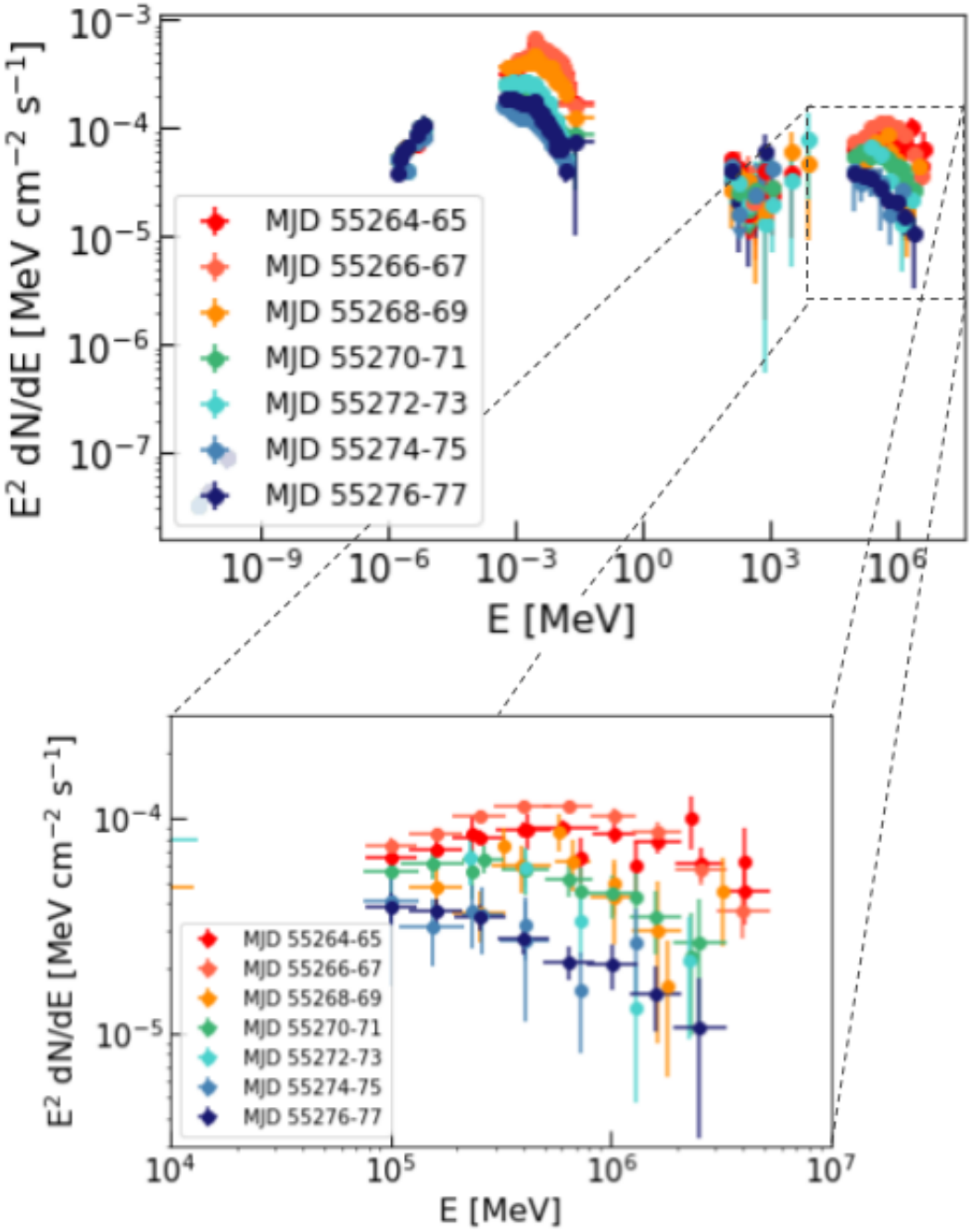

Figure 3.1: MWL data during the 14-day flaring period of Mrk 421 in March 2010 (MJD 55264-55278). A zoom-in to the VHE gamma-ray data recorded with IACTs during a flaring period is shown. The multi-instrument data are taken from MAGIC Collaboration and VERITAS Collaboration (2015a)

and Whipple above 200 GeV are shown in Figure 3.9. In terms of simultaneity of the data, the shorter observation times of the IACTs define the 2-day bins used for the *Fermi*-LAT analysis, noting that there is a 7-h time difference between the VERITAS/Whipple and MAGIC observations due to their different longitudes. The variability reported in the gamma-ray data corresponds to daily changes in the VHE emission; no intra-night variability was reported on the days studied.

Mrk 421 was highly active during other periods in 2010, and the VERITAS Collaboration reported another flare in February 2010 (MJD 55234-55240), the brightest ever observed from this object in VHE gamma rays (VERITAS Collaboration et al., 2020). They concluded that the time variability of the source was difficult to explain using a single-zone SSC model. This result provides another motivation to go beyond leptonic models and look for hadronic contributions.

3.3 *Fermi*-LAT data analysis

The following section describes the steps followed to perform a baseline analysis of Mrk 421 using *Fermi*-LAT data. The workflow showing the steps of the process, describing the tools used in the analysis and listing the output files is given in Figure 3.2. A similar analysis technique was used for 4FGL J0658.6+0636, described in Chapter 4.

The data analyses carried out throughout this thesis were performed with the Pass8v6 version of the IRFs and the v11r5p3 Science Tools software with `Fermipy` (Fermi-LAT Collaboration, 2017b). Taking advantage of the improved Pass8 IRFs (See section 1.2.4 for further details), data analysis can be extended into lower energies than previously possible, resulting in a more comprehensive spectrum of the source during flaring periods.

`Fermipy` is a `Python` package that facilitates analysis of data from the LAT with the *Fermi* Science Tools. It provides a set of high-level tools to perform the data preparation, modelling, statistics and analysis tasks.

3.3.1 Data extraction

All the data used for analysis are publicly-available and can be downloaded from the *Fermi*-LAT data server system: `https://fermi.gsfc.nasa.gov/cgi-bin/ssc/LAT/LATDataQuery.cgi` (last accessed on 01/08/22). The data are split into photon event files (evfiles) containing a list of recorded events by the LAT and a spacecraft file (scfile) containing the location and orientation of the satellite necessary for data analysis.

To exemplify the analysis steps, a dataset is used consisting of a list of events in a 15° radius RoI around Mrk 421's location (RA=66.114°, Dec=38.209°), with an energy range of 100 MeV to 300 GeV, from 2008 August 4th to 2022 June 14th (MJD 54682 - 59744), corresponding to the whole mission elapsed time (at the time of writing). The RoI size chosen allows a point-source analysis to be performed, considering a region of the sky in which the gamma-ray contributions from nearby sources and the background will be modelled. The energy range selection varies according to the purpose and specifics of each analysis. For a point-source analysis it is not recommended to go below 100 MeV as the containment angle described by the PSF worsens at low energies (see Figure 1.13), while at energies above 300 GeV the rate of recorded events will decrease significantly.

3.3.2 Data reduction

The downloaded raw files need to go through some cuts and filters before running any analysis; some complementary files required to model and fit the gamma-ray data are generated in the process. The data reduction steps made use of `gt-tools`, included in the *Fermi* Science Tools.

- `gtselect`.- For a point-source analysis, the process starts by selecting all 'SOURCE' class events (evclass=128) within the RoI, which are converted from the FRONT and BACK sections of the LAT detector (evtype=3). A

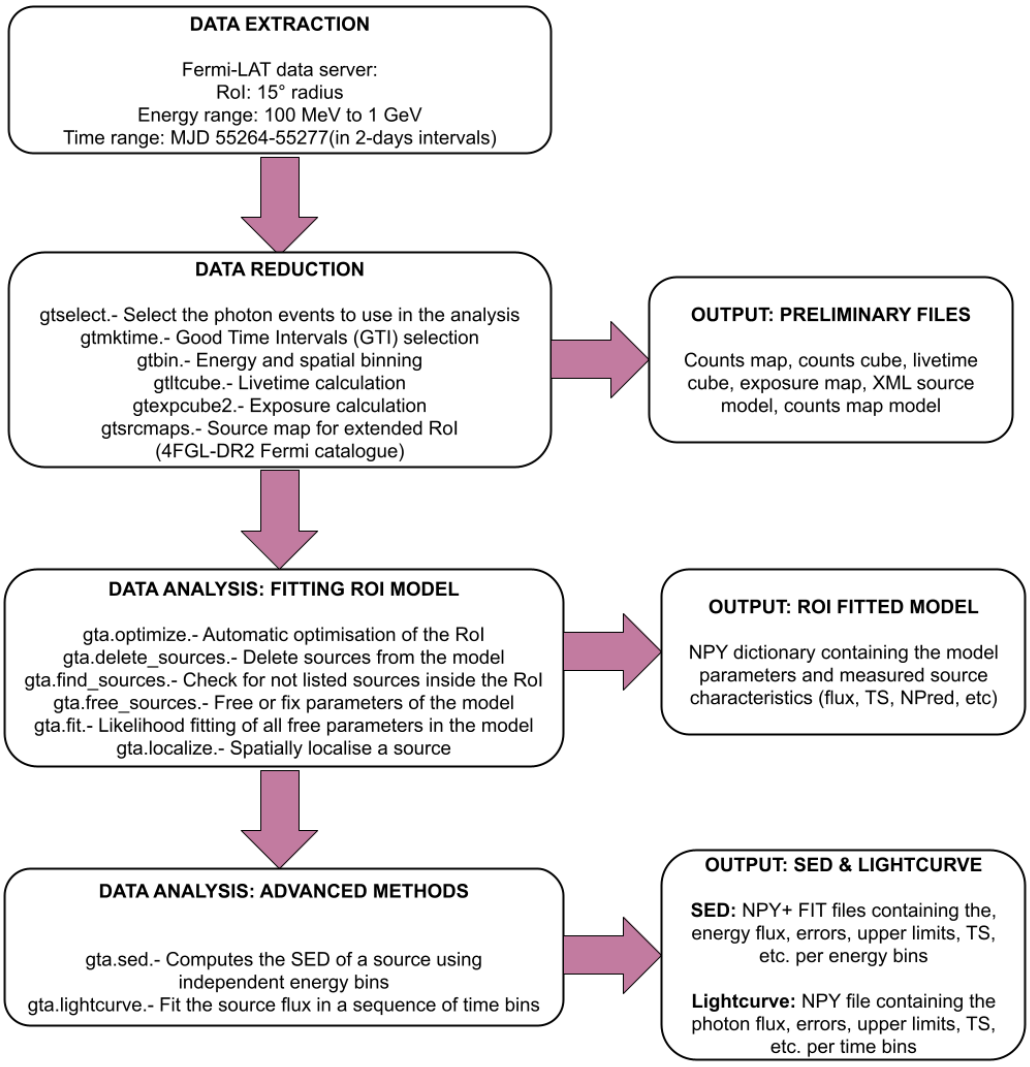

Figure 3.2: Workflow showing the data reduction steps and methods used to analyse *Fermi*-LAT data. The output files containing the results of each step of the process are shown on the right.

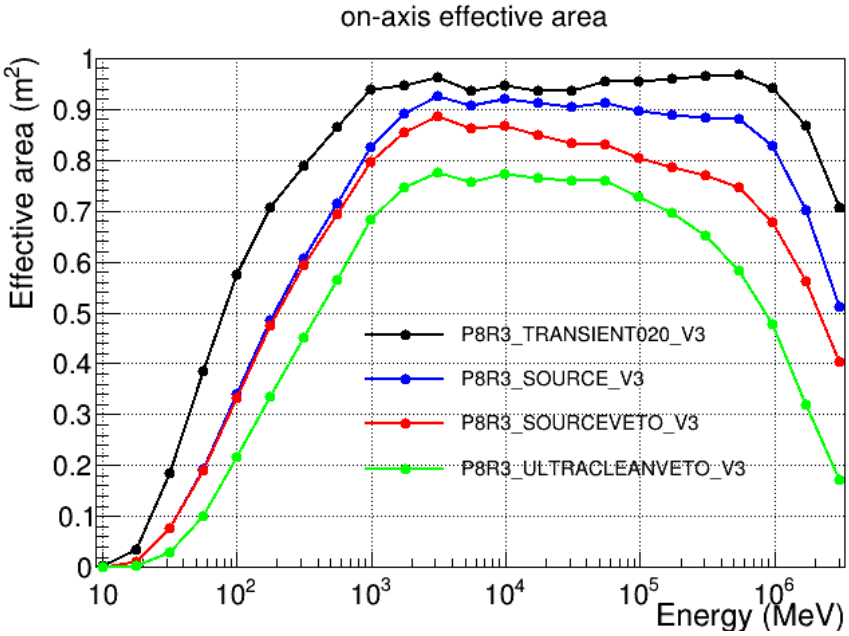

Figure 3.3: Comparison of the effective area as a function of the energy for different event classes included in the Pass8 IRFs of *Fermi*-LAT.Image credit: *Fermi*-LAT collaboration; `www.slac.stanford.edu/exp/glast/groups/canda/lat_Performance.htm`, last accessed on 01/08/22.

90° zenith cut angle was applied to avoid background gamma-ray photons coming from Earth's atmosphere.

Event classes (shown in Table 3.1) and are determined by how likely a given event is to be a recorded gamma-ray photon; higher probability photon selections (such as SOURCE, ULTRACLEANVETO and SOURCEVETO) provide lower background contamination of events from the Isotropic Diffuse Gamma-ray Background (IDGRB) at the expense of having smaller effective areas. The 'SOURCE' class provides good sensitivity for analysis of point-sources while keeping a low background contamination, making it the recommended class for most purposes. A comparison of the effective area for some of the LAT event classes is shown in Figure 3.3.

Events within a class are subdivided into event types depending on the location of the tracker layer in which the photon-to-pair conversion occurred: FRONT (evtype=1), BACK (evtype=2) and TOTAL=FRONT+BACK (ev-

type=3). The effective area, Point Spread Function (PSF), and energy resolution for these conversion types are described in Section 1.2.4.

- `gtmktime`.- To remove sub-optimal data, only the events within Good Time Intervals (GTI) were analysed. These are defined as the time range during which the data can be considered valid, i.e. when the LAT is working in the 'science data-taking mode'. The LAT does not collect data when the spacecraft traverses the South Atlantic Anomaly (SAA), a region with a high density of charged particles that are trapped by the configuration of the Earth's magnetic field, which requires to lower the voltage on instruments. The data-taking mode is also turned off during rare events, such as software updates or spacecraft manoeuvres.

  By applying the filters '(DATA_QUAL>0) && (LAT_CONFIG==1)' with the `gtmktime` tool the good quality of the data is ensured and only GTIs are selected. A cut in the rocking angle (the angle between the Earth zenith and the *Fermi*-LAT boresight) at 52° is also specified as '(ROCK_ANGLE <52)' to ensure the spacecraft was within the range of rocking angles used during nominal sky-survey observations.

- `gtbin`.- The gamma-ray data are then binned and a counts map of the RoI is created using the binning data summed over the photon energy range. For this example, 4 bins per decade in energy were used and the spatial bin size was 0.1° (see Figure 3.4).

  To perform a likelihood analysis, a three-dimensional counts map with an energy axis is needed, called a counts cube. The `gtbin` tool will create this file using the binning specifications. The likelihood analysis may lose accuracy if the energy bins are not sufficiently narrow.

- `gtltcube` (livetime calculation).- The number of photons registered by the LAT depends on the amount of time that the target source spent at a given inclination angle during an observation. This livetime quantity depends only

Event Class	evclass	Description
TRANSIENT020	16	Event class designed for short duration events, such as GRBs. It provides a high photon statistics while tolerating a broader PSF and ×2 the background rate of TRANSIENT010 class.
TRANSIENT010	64	Transient event class with the background rate of the reference spectrum of the IDGRB measurement from Fermi-LAT Collaboration (2010b).
SOURCE	128	This event class is the recommended class for most analyses and provides good sensitivity for analysis of point-sources and moderately extended sources.
CLEAN	256	This class is identical to the SOURCE class below 3 GeV. Above 3 GeV it has a 1.3 to 2 times lower background rate and is slightly more sensitive to hard spectrum sources at high galactic latitudes.
ULTRACLEAN	512	This class has a background rate very similar to ULTRACLEANVETO. It has the lowest particle contamination and is recommended for diffuse sources analysis.
ULTRACLEANVETO	1024	This is the cleanest Pass8 event class. Its background rate is 15-20% lower than the background rate of SOURCE class below 10 GeV, and 50% lower at 200 GeV. This class is recommended to check for CR-induced systematics as well as for studies of diffuse emission that require low levels of CR contamination.
SOURCEVETO	2048	This class has the same background rate than the SOURCE class background rate up to 10 GeV but, above 50 GeV, its background rate is the same as the ULTRACLEANVETO.

Table 3.1: Description of the different Fermi-LAT event classes. The second column indicates the parameter value that is associated with the event class selection when using `gtselect` tool. Info credits: NASA; `https://fermi.gsfc.nasa.gov/ssc/data/analysis/documentation/Cicerone/Cicerone_Data/LAT_DP.html`, last accessed on 01/08/22.

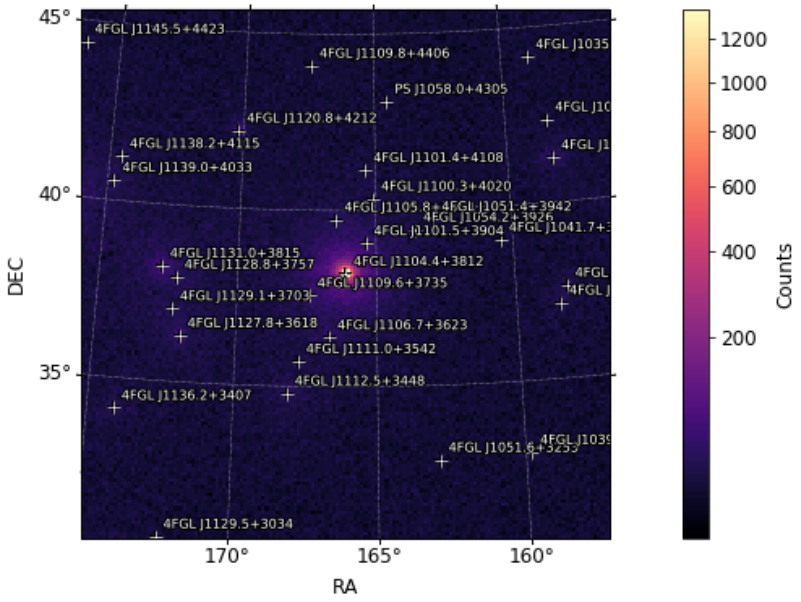

Figure 3.4: Counts map of the of gamma-ray photons in a 15° RoI around Mrk 421 obtained with LAT data from 2008 August 4th to 2022 June 14th. The photons lies in an energy range between 100 MeV and 300 GeV. The gamma-ray data were binned using 4 bins per decade in energy, and 0.1° spatial bin size.

on the history of the LAT's orientation during the observation and not on the source model. The array of these livetimes at all points on the sky is called the livetime cube (ltcube). `gtltcube` creates the ltcube as a HealPix table, covering the entire sky, with the integrated livetime covered by the spacecraft file (scfile) as a function of inclination with respect to the LAT z-axis.

- `gtexpcube2` (exposure calculation).- This tool generates a binned exposure map, which is a required input for the likelihood analysis. The exposure map is obtained by integrating the total response of the instrument over the entire RoI data-space. Generating and combining the exposure maps is computationally intensive task, `gtexpcube2` calculates the exposure map for the RoI and combines it with the livetime spent at each inclination angle for every point in the RoI, which is taken from the previously generated ltcube.

  The counts produced by a source at a given position on the sky is the integral

of the source flux and the exposure map (as a function of energy) at that position. There is a chance that at low energies, due to the large PSF of the LAT (see Figure 1.13), sources from outside the RoI could affect the counts cube, and therefore contaminate the analysis of sources inside the RoI. To compensate for this effect, the exposure map includes sources up to 5 degrees outside the RoI.

- `gtsrcmaps`.- This tool creates a model counts map that will be used during the binned likelihood analysis. For each source in the model, it multiplies the spectrum by the exposure at the source position, and convolves that exposure with the effective PSF.

  The model counts map consists of gamma-ray sources and a background with a Galactic diffuse and an extragalactic component (see Figure 3.5). The 4FGL-DR2 catalogue (Fermi-LAT Collaboration, 2020a), containing the spatial and spectral information of the known gamma-ray sources based on 10 years of *Fermi*-LAT data (in the 50 MeV to 1 TeV energy range), is used to create the model. All the sources listed in the 4FGL catalogue inside a 20° radius from the centre of the RoI were included; this was to account for the possible contributions of sources outside but near the edge of our RoI. The spectral and spatial information of the sources is saved in a XML file (source model) that can be modified during the analysis steps.

  The Galactic diffuse background is dominated by the emission from interstellar processes in the Milky Way. The gamma-ray sources studied must be detected and characterised taking into account this background component. The LAT collaboration has developed templates that describe the Galactic diffuse emission, for the current analysis the model used was 'gll_iem_v06.fit'. The *Fermi*-LAT data are also affected by background contributions from extragalactic diffuse gamma-rays, unresolved extragalactic sources, and residual (misclassified) cosmic-ray emission; these were included in the analysis by using the isotropic spectral template 'iso_P8R2_SOURCE_V6_v06.txt'.

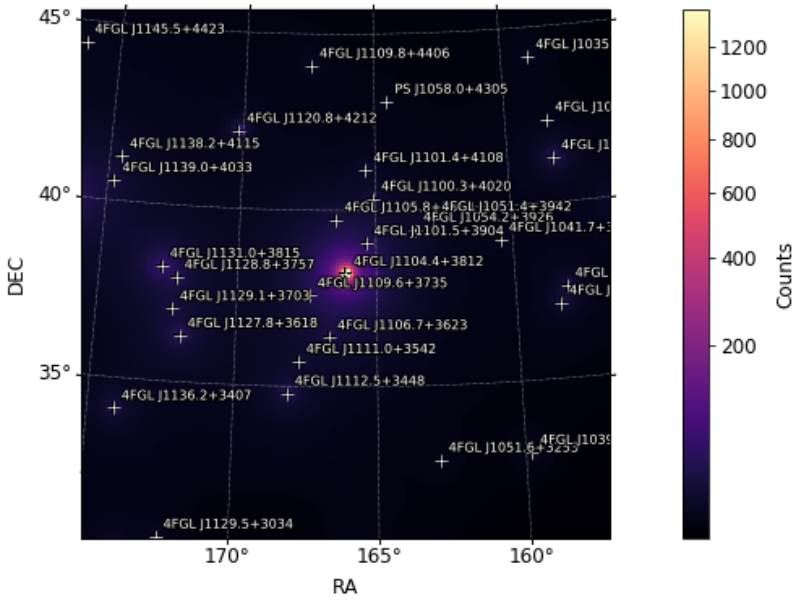

Figure 3.5: Model counts map created for a 15° radius RoI around Mrk 421 to fit LAT from 2008 August 4th to 2022 June 14th.. The colour scales indicates the expected number of photons at each pixel in an energy range of 100 MeV to 300 GeV.

> Further information and about the background templates can be found in: `https://fermi.gsfc.nasa.gov/ssc/data/access/lat/BackgroundModels.html`, last accessed on 01/08/22.

All the analysis parameters for the data reduction steps were specified in a YAML format configuration file, including the data selection cuts, the size and centre coordinates of the RoI, the spatial and energy bin sizes and other model specifications. A quick set-up can be done with `Fermipy` using the configuration file, which will go through the data reduction steps and create all the required files (counts map, counts cube, ltcube, exposure map and XML model) for the likelihood analysis.

3.3.3 Data analysis: Likelihood fitting

Using the `GTAnalysis` tools the gamma-ray model can be fit and optimised with a Maximum Likelihood Method (MLM) to find the best fit values for all the free parameters in the model. The likelihood is defined as the probability of obtaining the observed data given an input model, which specifies the distribution of gamma-ray sources on the sky, and includes their intensity and spectra. For each source, the significance of its emission is evaluated using a TS, which is defined as (Fermi-LAT Collaboration, 2018a):

$$\mathrm{TS} = -2\ln\left(\frac{L_{\mathrm{max},0}}{L_{\mathrm{max},1}}\right) , \tag{3.1}$$

where $L_{\mathrm{max},0}$ is the maximum likelihood value for a model without an additional source (null hypothesis) and $L_{\mathrm{max},1}$ is the maximum likelihood value for a model with an additional source at a specified location. The TS calculates the likelihood ratio between the best fit model with and without the source, a larger TS value would indicate that the null hypothesis is incorrect.

The detection significance (σ) of a source, is given by:

$$\sigma = \sqrt{2}\mathrm{erf}^{-1}\left(\chi^2_n(\mathrm{TS})\right) \tag{3.2}$$

where the TS follows a χ^2_n distribution which depends on the number of free parameters (n) in the source model, and erf^{-1} is the inverse of the error function, defined as:

$$\mathrm{erf}(x) = \frac{2}{\sqrt{\pi}}\int_0^x e^{-t^2}dt \tag{3.3}$$

As a rule of thumb, the square root of the TS value is approximately equal to the detection significance for a given source ($\sqrt{\mathrm{TS}} \sim \sigma$). A source is considered significantly detected if $\mathrm{TS} > 25$, i.e. when the significance is above $\sim 5\sigma$.

During the analysis, the spectral parameters from a number of sources must be fitted simultaneously. The fitting requires repeatedly calculating the likelihood for the varying sets of free parameters until the maximum value is found. In the

process, the properties (flux, TS, predicted number of counts ($N_{\rm pred}$), etc.) for each source are calculated and updated in the RoI model.

The typical analysis steps to fit the gamma-ray model are the following:

- `gta.optimize()`.- The analysis starts with an initial optimisation of the RoI by a maximum likelihood algorithm. This tool will loop over all model components in the RoI and fit their normalisation and spectral shape parameters. With this step, the initial values for the model parameters are approximated. This method also computes the TS value of all listed sources in the RoI. Depending on the TS value, insignificant sources can be identified and removed from the model, reducing the number of parameters used.

- `gta.delete_sources()`.- The sources that were considered insignificant (TS $<$ 9) can be discarded from the RoI gamma-ray model. The list of undetected sources that can be discarded will not affect the gamma-ray model, as their contribution only introduces noise in the calculations. By ignoring these weak sources, the total number of model parameters is reduced and the gamma-ray model is improved.

- `gta.find_sources()`.- This tool is used to check for any additional point-sources inside the RoI which are not listed in the 4FGL catalogue. It computes a TS map for a test source model and identifies peaks above a certain threshold; a point-source with TS $>$ 25 would be considered significant. If any other bright source that could contribute significantly is found, the spatial and spectral description is added to the counts map model and the RoI is re-optimised.

- `gta.free_sources()`.- Before performing the likelihood fitting, the spectral shape parameters of the nearby sources, typically in a 5° radius around the RoI's centre, are left free to vary. This is done to describe accurately the zone around the source of interest. It is also recommended to free any other

bright source in the RoI. The normalisation factor of the two background components (isotropic and Galactic diffuse emission) are also left free to vary during the maximum likelihood fitting.

- `gta.fit()`.- This tool is used to adjust all the free parameters of the model, by calculating and maximising the likelihood of the fitting. The set of parameters has to converge to consider the fit successful. The variation of the likelihood in the vicinity of the maximum value achieved can be used to estimate the uncertainties on the source parameters.

  A `Numpy` dictionary (NPY file) containing the the model parameters and measured source characteristics (flux, TS, NPred, etc) is returned by the fit method. A variety of diagnostic information about the fit is also produced to assess the quality of the fit, including a residual map and a TS map of the RoI. The residual map is the left over counts after subtracting all the modelled sources from the RoI, while the TS map is created by putting a tentative source at every location and calculating the likelihood of it existing. The RoI status after the fitting can be saved using the `gta.write_roi()` command.

3.3.4 Analysis methods: residuals, light curve and SED

The data reduction steps described in the previous section were followed to prepare, optimise and fit the RoI; this process is usually referred as a baseline analysis. There are advanced methods within `Fermipy` that can be applied afterwards to assess the model fit, like `gta.residmap` and `gta.tsmap`, as well as `gta.lightcurve` to study the gamma-ray flux temporal behaviour of the source and `gta.sed()` to extract the source spectrum.

- `gta.residmap()`.- A residual map of the RoI can be calculated by subtracting all of the modelled sources contributions from the photon counts map. The residual maps showing the excess in counts and significance for the analysis example are shown in Figure 3.6. Whereas a TS map is only sensitive to

positive deviations with respect to the model, a residual map is sensitive to positive and negative deviations and therefore can be used to evaluate the fitted RoI and check the regions where the model is not matching the data.

- `gta.tsmap()`.- A TS map can be generated with this routine by assuming a tentative source centred at each spatial bin in the RoI and calculating the likelihood of it existing. This method returns a map with the calculated TS value and the predicted number of counts of the best fit test source at each position. If there is a significant excesses in the data that can be associated with an unknown source, the residual plots and TS map will be helpful to identify it.

- `gta.lightcurve()`.- This tool fits the characteristics of a source in a sequence of time bins using the same data selection criterion and model as the baseline analysis. To fit each temporal bin, the spectral parameters of the source and the normalisation factors of the background components were left free to vary. As an output, a `Numpy` dictionary containing the results (flux, energy flux, TS, best fit parameters, etc.) with their respective uncertainties per time bin is obtained.

- `gta.sed()`.- This tool performs an independent maximum likelihood fit per energy bin for the flux normalisation. The binning size used by default is the one specified for the baseline analysis. An example plot of the Mrk 421 SED is shown in Figure 3.8. The energy range (100 MeV to 300 GeV) was split into 4 evenly spaced log-energy bins per decade. The return value of `gta.sed` is a FITS file and a `Numpy` dictionary containing the results (energy flux, errors, upper limits, TS, etc.) per energy.

  The spectral shape of Mrk 421 is described by a Log-Parabola (LP) function:

$$\frac{dN}{dE} = N_0 \left(\frac{E}{E_0}\right)^{-\alpha-\beta\ln(E/E_0)} \tag{3.4}$$

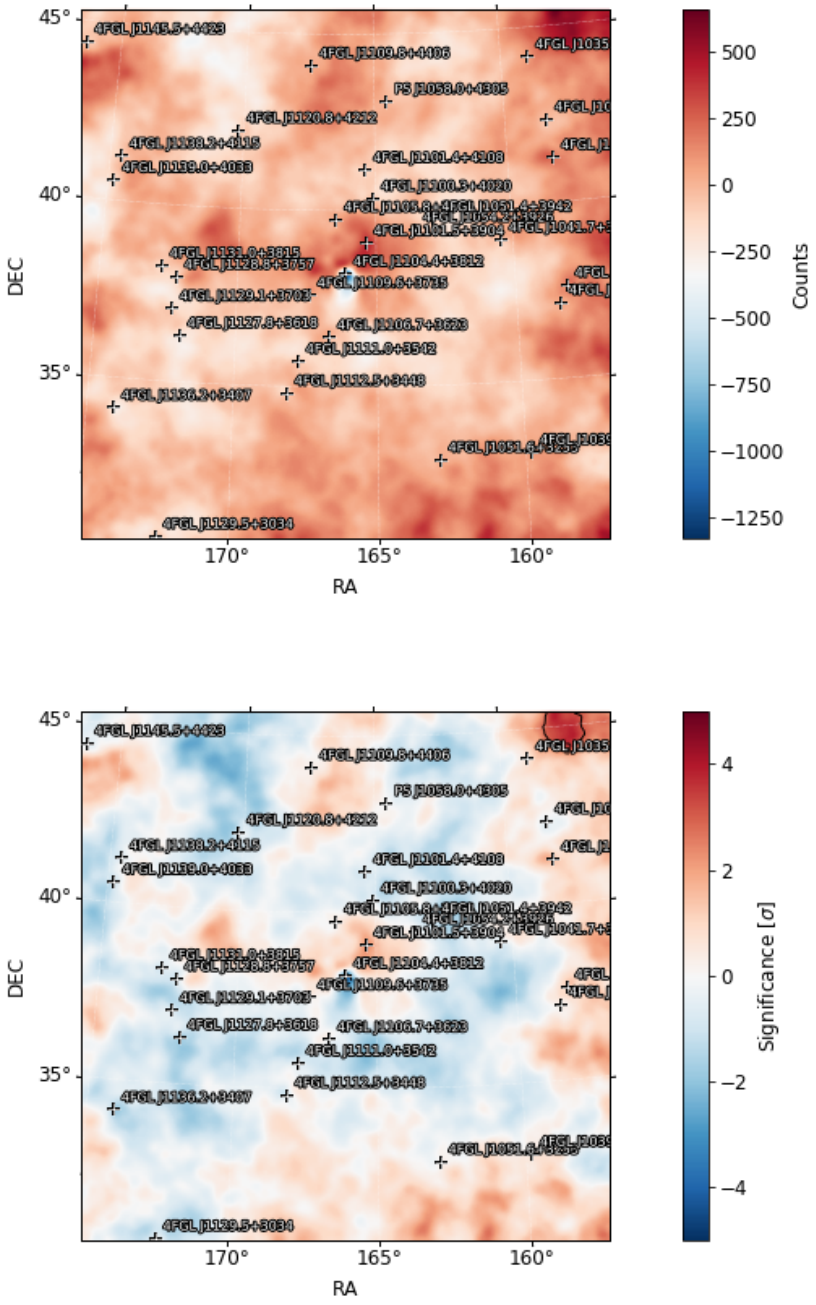

Figure 3.6: Residual maps showing the residual counts map (top) and the residual significance map (bottom) calculated for the example RoI. The colour scales indicates eithr the positive (red) or negative (blue) photon excess (top) and the significance excess in Gaussian σ (bottom).

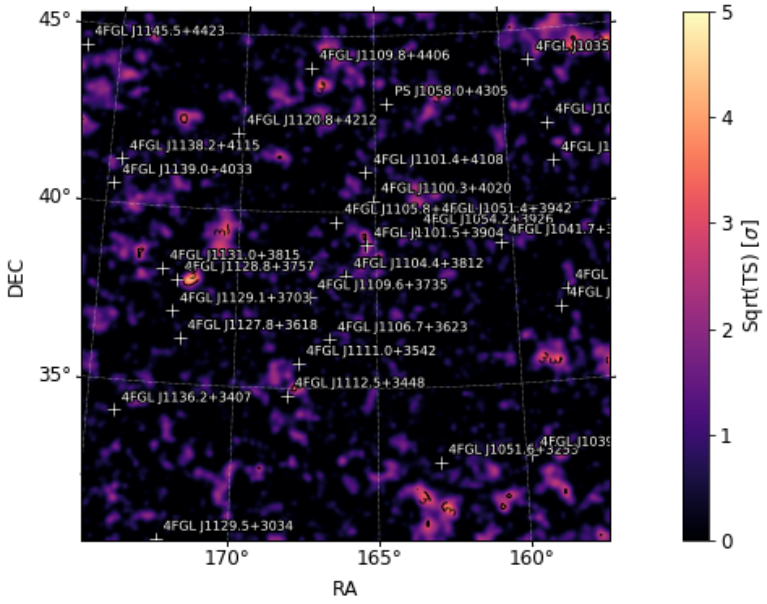

Figure 3.7: TS map showing the significance ($\sigma \sim \sqrt{\mathrm{TS}}$) calculated for a tentative source centred at each spatial bin in the RoI. The colour scales indicates the significance up to 5σ.

where $N_0 = 1.66 \pm 0.01 \times 10^{-11}$ is a normalisation constant in units of MeV cm^{-2} s^{-1}, $\alpha = 1.75 \pm 0.01$ is the spectral index, $\beta = 1.4 \pm 0.2$ is the curvature and $E_0 = 1,287$ MeV is the pivot energy.

3.4 Analysis of the 2010 Mrk 421 Flare

$p\gamma$ interactions with MeV photons could contribute to the VHE gamma-ray emission observed by the IACTs on consecutive nights during the flare. Therefore, a tailored *Fermi*-LAT analysis to the flaring data is used to obtain an input seed photon spectrum for the photohadronic model scenario.

3.4.1 Data reduction and source model

The datasets considered a list of all 'SOURCE' class events converted from the FRONT and BACK sections of the detector in a 15° radius RoI around Mrk 421

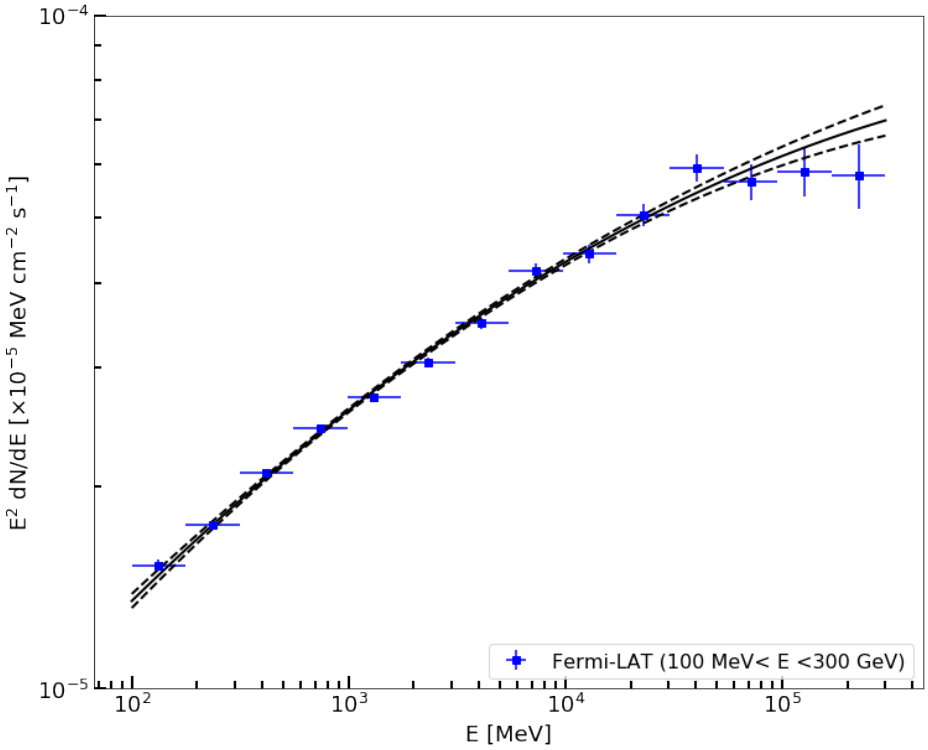

Figure 3.8: Mrk 421 SED calculated in an energy of 100 MeV to 300 GeV using *Fermi*-LAT data from 2008 August 4th to 2022 June 14th. For the calculation the energy range was split into 4 evenly spaced log-energy bins per decade. The black continuous line shows the best fit Log-Parabola curve, and the dotted lines represent the uncertainty region for the best fit.

location, with an energy range of 100 MeV to 1 GeV, from 2010 March 9th to 23rd (MJD 55264-55278). This energy range selection was based on the requirement for a good characterisation of the source's MeV region to enable further extrapolation. The flaring period studied was divided into shorter 2-day intervals; this time period was selected as it represents the minimum time scale to obtain enough photon events to calculate the SED at the MeV range.

The analysis steps described in Section 3.3 were applied to each 2-day interval in the flaring period studied to obtain the corresponding SED and best fit spectral parameters. A series of cuts and filters were applied to avoid gamma rays coming from the Earth's atmosphere and to remove sub-optimal data out of the GTIs in the 14-day flaring period. The gamma-ray data were binned using the `gtbin` with 0.1° as spatial bin size and 5 bins per decade in energy. This selection allowed to

split the chosen energy range (100 MeV to 1 GeV) in 5 sections.

In the 4FGL catalogue, Mrk 421 (4FGL J1104.4+3812) is listed as a source with a LP spectrum type. However, over the 2-day intervals considered, there were not sufficient photon statistics to allow a LP model to be distinguished from a PL model. The spectral models should not differ significantly below 100 MeV. The Mrk 421 spectrum derived from this analysis was therefore characterised using a PL model:

$$\frac{dN}{d\epsilon_\gamma} = N_{PL}\left(\frac{\epsilon_\gamma}{\epsilon_0}\right)^{-\kappa}, \tag{3.5}$$

where the normalisation constant N_{PL} and the spectral index κ act as free parameters that were optimised to get the best fit values and ϵ_0 is the pivot energy in MeV. The PL description was then used to extend the spectrum below 100 MeV.

Mrk 421 was the brightest source identified within the RoI during the 2-day datasets. Due to the low photon statistics, the source could not be significantly detected (i.e. TS < 25) in shorter time periods.

The Galactic diffuse and isotropic gamma-ray background components were also included in the gamma-ray models by using the templates developed by the LAT collaboration for the Pass8 IRFs (see Section 3.3).

3.4.2 Data analysis: Likelihood fitting

A baseline analysis was performed to fit the RoI in all of the 2-day datasets following the process in Section 3.3.3. The specific of these analyses are explained below.

The gamma-ray model considered all sources listed in the 4FGL-DR2 catalogue (Fermi-LAT Collaboration, 2020a) around a 20° radius from the RoI's centre. The sources in the model that were considered insignificant (TS < 9) were discarded. These sources predicted few to zero gamma-ray photon counts in the model.

The `gta.find_sources()` routine was executed to check for any point-sources not listed in the 4FGL catalogue. Any point in the RoI with a TS > 25 and with at

least 0.5° separation from a listed source, is considered as a new gamma-ray point-source, characterised with a PL spectrum and added to the RoI model before being re-optimised. No additional point-source candidates were found in the datasets analysed.

The RoI model paremeters were fitted with a MLM. The spectral parameters of the sources within a 5° radius around the RoI's centre were left free to vary, as well as the normalisation factors of the two background components (Galactic and isotropic diffuse emissions). The rest of the sources in the RoI model were fixed to the 4FGL catalogue reported values.

3.5 Results of Flare analysis

3.5.1 Analysis results: light curve

The light curve of Mrk 421 during the flaring period (MJD 55264-55278) was calculated in the MeV energy range (100 MeV to 1 GeV) using 2-day temporal bins (see Figure 3.9). The average photon flux obtained for Mrk 421 was $1.67 \pm 0.28 \times 10^{-7}$ ph cm^{-2} s^{-1}. For each significant bin (TS $>$ 25), the gamma-ray flux is reported in the third column of Table 3.2, in bins where the TS $<$ 25, upper limits are presented.

Figure 3.9 also shows the light curves measured by MAGIC, VERITAS and Whipple during the 14-day flaring period at energies above 200 GeV (MAGIC Collaboration and VERITAS Collaboration, 2015a). The maximum flux registered at VHE energies was reached between MJD 55266 and MJD 55269.

The MeV source spectrum for the days on which Mrk 421 was detected significantly are shown in Figure 3.10 and the spectral parameters for the selected days are summarised in Table 3.2.

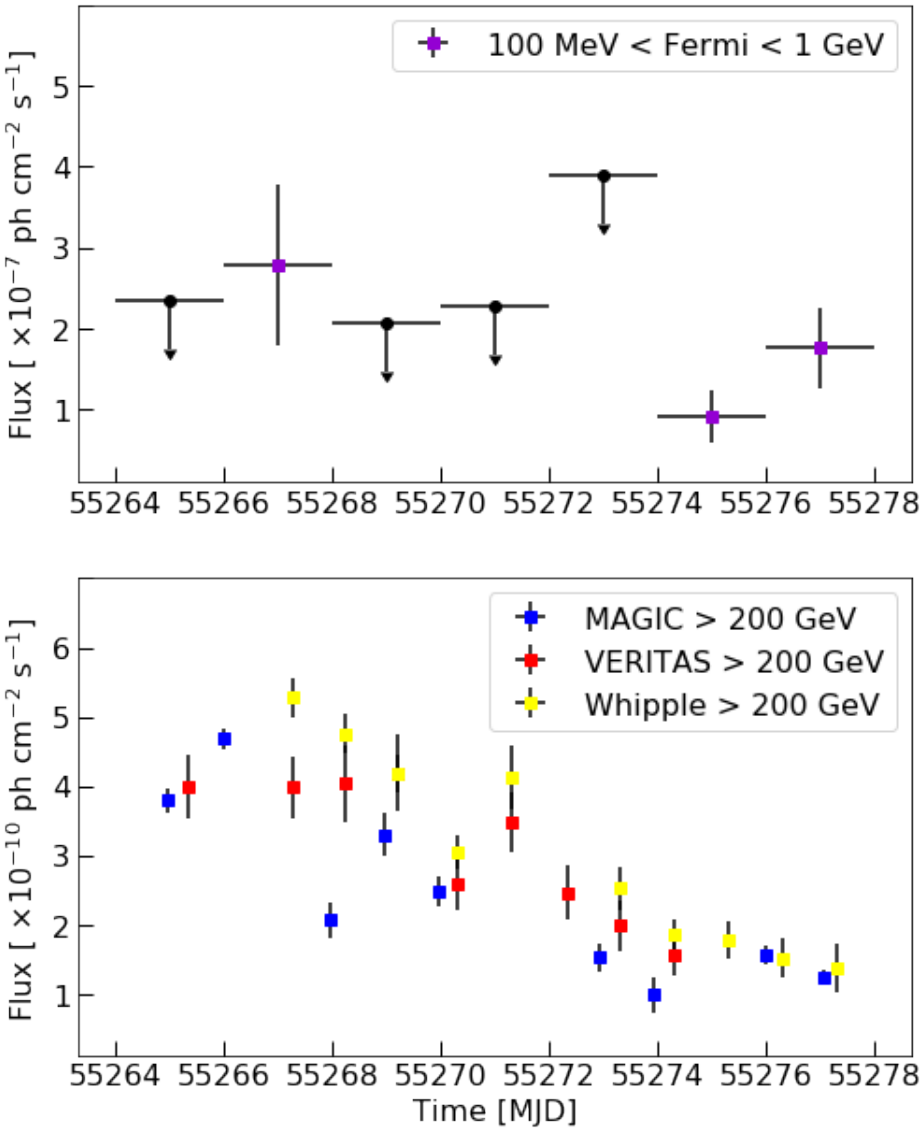

Figure 3.9: Light curve of Markarian 421 during the 14-day flaring period in March 2010. The upper plot shows the gamma-ray flux in the energy range 100 MeV $< E\gamma <$ 1 GeV with the points covering 2-day time bins. For bins with TS < 25, upper limits for the flux are shown. The lower plot presents the light curves for MAGIC, VERITAS and Whipple above 200 GeV. Data taken from MAGIC Collaboration and VERITAS Collaboration (2015a).

Time MJD	TS	Flux [10^{-7} ph cm^{-2} s^{-1}]	N_{PL} [10^{-11} MeV cm^{-2} s^{-1}]	κ
55266-67	29	2.78 ± 0.98	2.11 ± 1.32	2.21 ± 0.44
55274-75	42	0.91 ± 0.33	4.51 ± 2.60	1.17 ± 0.61
55276-77	47	1.76 ± 0.50	5.94 ± 3.12	1.11 ± 0.61
55264-65	10	< 2.34	-	-
55268-69	6	< 2.07	-	-
55270-71	18	< 2.27	-	-
55272-73	19	< 3.89	-	-

Table 3.2: Summary table of the spectral parameters of Mrk 421. The 2-day bins with significant TS values are listed on the top of the table. The 4th and 5th columns correspond to the optimised parameters for a PL fit coming from the *Fermi*-LAT analysis performed. The days with a low TS value are listed in the bottom of the table together with the upper limits for the gamma-ray flux.

3.5.2 Analysis results: MeV spectra

In the assumed $p\gamma$ emission scenario, the seed photons for the $p\gamma$ interactions are expected to be between 2 and 168 MeV to produce the VHE gamma-ray emission. For the *Fermi*-LAT analysis, a photon energy range from 100 MeV (the recommended starting energy) and up to 1 GeV was considered, then extrapolated to the lower energy range of interest, as described above.

The spectral parameters of the days on which the source was detected significantly (TS>25) are shown in Table 3.2 and the corresponding light curves from the *Fermi*-LAT analysis and in the VHE energy range are shown in Figure 3.9. This analysis extends the previous results by MAGIC Collaboration and VERITAS Collaboration (2015a), which started at 300 MeV rather than 100 MeV. There are no significant flux changes in the VHE band in the combined 2-day bins used for the *Fermi*-LAT analysis and subsequent modelling. The remaining days presented low photon statistics and were not considered for further VHE fitting with the photohadronic model. In order to get the final result, the gamma-ray spectrum of the source was studied in the MeV energy range, with the fitted spectrum serving as an input for the photohadronic modelling. For the time bins used in the *Fermi*-LAT analysis that coincide with VHE data from MAGIC Collaboration and VERITAS

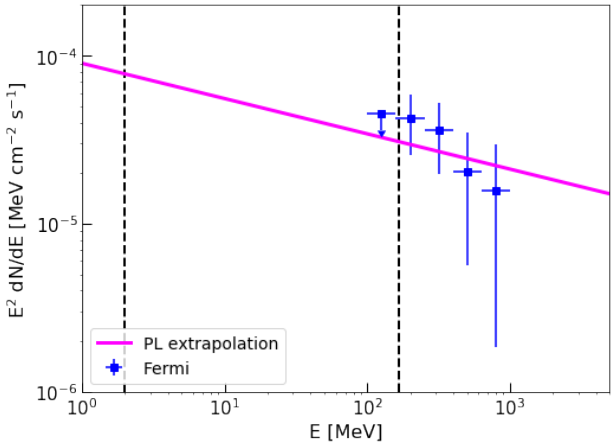

(a) MJD 55266-67

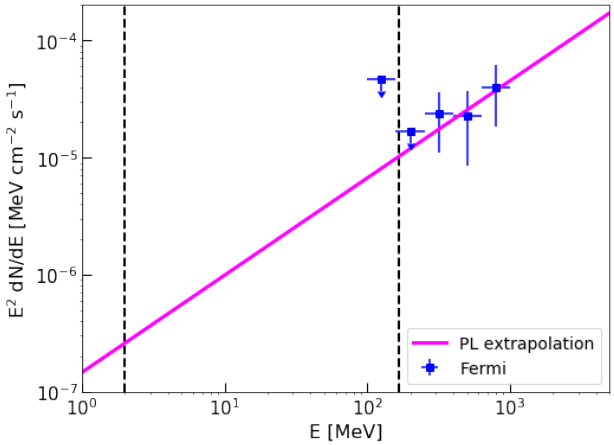

(b) MJD 55274-75

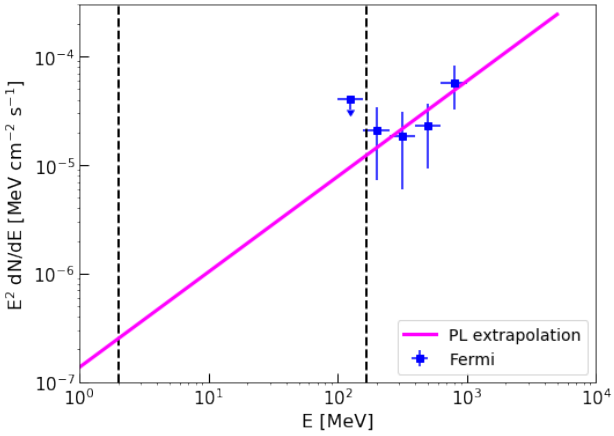

(c) MJD 55276-77

Figure 3.10: *Fermi*-LAT spectra (blue points) and power-law extrapolation (magenta line) for the MeV range in 2-day bins: (a) MJD 55266-67, (b) MJD 55274-75, (c) MJD 55276-77. The black dotted vertical lines are positioned at 2 and 168 MeV, which is the expected energy range for the seed photons. The spectral parameters for the selected days are summarised in Table 3.2.

Collaboration (2015a), the extended spectrum analysed with the updated IRF allowed us to calculate a PL extrapolation in our range of interest. The spectra of the source alongside the PL extrapolation are shown in Figure 3.10 for the selected bins.

Once the MeV region is characterised, the input seed photon spectrum for the photohadronic model can be expressed as

$$\Phi_{input} = \epsilon_\gamma^2 \frac{dN}{d\epsilon_\gamma} \, . \tag{3.6}$$

The uncertainty of the seed photon spectrum will impact on the optimisation process of the other free parameters within the model (α and A_γ), and therefore the final fitting result.

3.6 Photohadronic modelling of the 2010 gamma-ray flare

During the 2010 flaring period of Mrk 421, the VHE data recorded by the IACTs lies in an energy range of 80 GeV to 5 TeV (MAGIC Collaboration and VERITAS Collaboration, 2015a). The energy relation derived for the Δ^+-resonance approximation (Equation 2.33) indicates that the seed photon energy in the $p\gamma$ interaction is between 2 and 168 MeV (in the observer's reference frame). The reduction in the source flux, combined with the low sensitivity of the LAT below 100 MeV, are an impediment to obtaining precise measurements at these energies, and therefore the results presented in Section 3.5 are used to estimate the flux coming from the seed photons ($\Phi_{input}(\epsilon_\gamma)$). The PL input is shown in Figure 3.10.

The energy range of the seed photons along with the Δ^+-resonance threshold condition can be used to estimate proton energy. From Equation 2.32, we have that $E_p \sim 10E_\gamma$ in the observer's reference frame; if measured from Earth, these high energy protons, boosted by the blazar's jet, will be detected in an energy range of $\sim$ 800 GeV to 50 TeV, which corresponds in the emission region reference

frame to ~ 40 GeV $< E'_p <$ 2.45 TeV. This is the energy range of the protons to reach the threshold condition for the Δ^+-resonance.

The emission region has some physical parameters (magnetic field B, Doppler factor D, radius of the spherical blob R'_f) which are the same as those used in the calculation of the photohadronic component. These are fixed parameters taken from the one-zone emission region leptonic model of the MAGIC Collaboration and VERITAS Collaboration (2015a) and are: magnetic field of $B = 38$ mG, a Doppler factor $D = 21$ and a radius of the emission region $\log_{10}(R'_f[\text{cm}]) = 16.72$. The variability reported in MAGIC Collaboration and VERITAS Collaboration (2015a) corresponds to daily changes in the VHE emission, a time scale which in principle is related to the proton injection. The power index α and the normalisation constant A_γ were estimated daily for each VHE dataset considered (days at the top of Table 3.2). These two free parameters were optimised using a χ^2 minimisation method* within the `Scipy Python` package (Virtanen et al., 2020).

The photohadronic fit for the VHE gamma-ray data on flaring days with significant TS values is shown in Figure 3.11. The one-zone and two-zone SSC models from MAGIC Collaboration and VERITAS Collaboration (2015a) are also shown for comparison (see Section 2.6.1 for a larger discussion about two-zone models). The optimised values for the free parameters in the photohadronic model are shown in Table 3.3.

During the first days of the observations (MJD 55264-67) the source was in its maximum emission state. As the seed photon spectrum in Table 3.2 illustrates, the gamma-ray flux detected reaches a peak on this day, and the spectral index associated is also the highest at $\kappa \sim 2.2$. This behaviour is also reflected in the optimised free parameters (α and A_γ) which present their maximum values during these couple of days.

For the final days of the flaring period (MJD 55274 to 55278) three days of VHE

*See `https://docs.scipy.org/doc/scipy/reference/generated/scipy.optimize.minimize.html`. Last accessed on 08/08/22.

Time MJD	A_γ	α	Preferred Model	ΔAIC SSC, $p\gamma$	ΔAIC two-zone-SSC, $p\gamma$
55266	5.02 ± 2.74	3.12 ± 0.07	two-zone SSC	25.45	-48.78
55267	27.24± 12.79	3.41 ± 0.09	$p\gamma$	6.11	9.10
55274	0.19 ± 0.01	2.31 ± 0.03	inconclusive	2.54	0.73
55276	0.10 ± 0.02	2.17 ± 0.03	$p\gamma$	26.40	2.04
55277	0.18 ± 0.02	2.32 ± 0.03	$p\gamma$	5.92	2.90

Table 3.3: Summary table of the photohadronic fit for each day in Figure 3.11. The optimised values for the normalisation constant A_γ and the power index α are shown in the second and third column. The AIC difference between the one-zone and two-zone SSC model with respect to the photohadronic ($p\gamma$) model is shown on the fifth and sixth column respectively. An inconclusive result is obtained, if the AIC difference between the two models with the lowest values is less than 2.

data were available, there being no VHE observations on MJD 55275. The PL spectral parameters used as an input for the $p\gamma$ model are very similar for these 3 days. The spectral index during this period is $\kappa \sim 1.1$ and the power index of the proton spectrum is around $\alpha \sim 2.2 - 2.3$.

3.6.1 AIC model comparison

The $p\gamma$ model and the two leptonic models considered in MAGIC Collaboration and VERITAS Collaboration (2015a) were compared using the AIC difference test (see Section 2.8). The results for each dataset tested are shown in Table 3.3. Among the IACT observations from the 2010 flaring period (Figure 3.11), it was found that the photohadronic fit was the preferred model in 3 out of 5 cases. On one day (MJD 55266), the two-zone SSC model has the minimum AIC by a large difference with respect to the other models. Meanwhile on MJD 55274, the AIC test was inconclusive, as no difference larger than 2 was found between the $p\gamma$ and the two-zone SSC model.

In all cases, the comparison of the $p\gamma$ model with the one-zone SSC model results in a $\Delta AIC_{SSC,p\gamma} > 2$, which means the $p\gamma$ model is favoured over the one-zone SSC model and represents a significantly better fit (Table 3.3). Nevertheless, this does not necessarily means that the $p\gamma$ model fits all the datasets well.

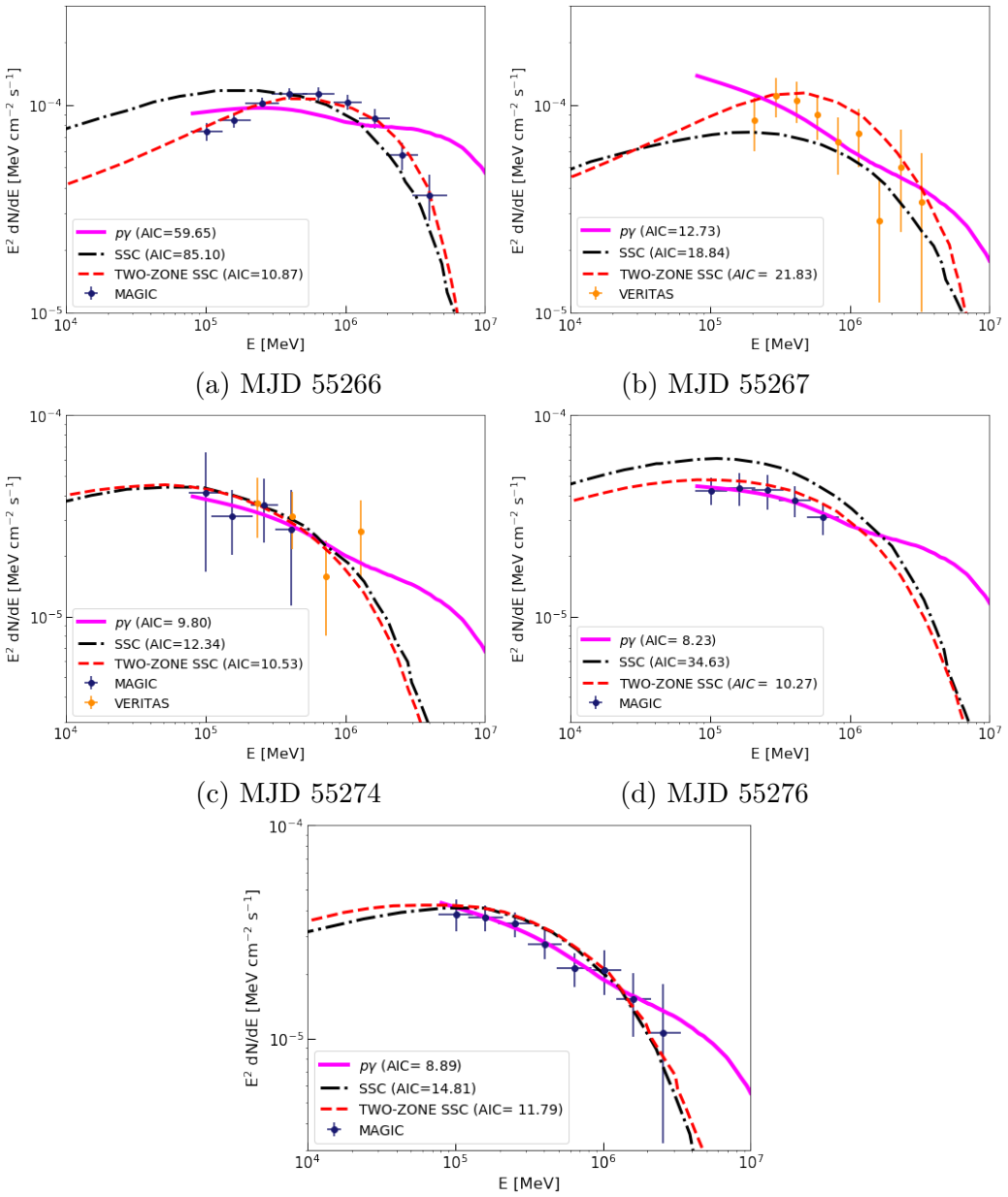

(a) MJD 55266 (b) MJD 55267

(c) MJD 55274 (d) MJD 55276

(e) MJD 55277

Figure 3.11: Photohadronic fit for the VHE gamma-ray data on flaring days with significant TS values: (a) MJD 55266, (b) MJD 55267, (c) MJD 55274, (d) MJD 55276, (e) MJD 55277. The photohadronic component calculated from the PL input is shown in magenta for the valid energy range of the model, which extends roughly down to 80 GeV. The one-zone (two-zone) SSC model from MAGIC Collaboration and VERITAS Collaboration (2015a) is shown as a dash-dot black (dashed red) line. The calculated AIC values for the three models are included for comparison. VHE data points are from MAGIC and VERITAS observations.

The fitting for MJD 55266 presents a large difference between the calculated AIC values, the two-zone SSC resulting in the lowest AIC and therefore favoured as the best fit for data from this day. The SSC model over-predicts the VHE flux just above 100 GeV, whereas the $p\gamma$ model over-predicts the flux above the TeV energy limit and is flatter below that point, thus underestimating the flux peak. Neither of these two models represent a good fit to the data, which is reflected in the AIC difference between them and the two-zone SSC model.

On the following day (MJD 55267), using the corresponding PL input to calculate the photohadronic contribution, the overall behaviour of the VERITAS observations can be fitted with the $p\gamma$ model, but the PL behaviour from the input takes over if extended below 100 GeV and predicts an increase in flux; this is a non-physical effect that is outside the validity range and represents a caveat of the model. Nonetheless, the $p\gamma$ model scored the lowest AIC value among the 3 models and the difference in this day is enough to consider it the best fit.

During the final part of the flaring period (MJD 55274 to 55278), the lowest AIC values found were from the $p\gamma$ model, indicating these are the best fits to the datasets and ranking the model as the preferred option on MJD 55276 and 55277.

On MJD 55274 the three models predict a similar flux in the 100 GeV to 1 TeV range, but the photohadronic contribution differs at higher energies where a larger contribution is expected. This is the only day on which the models were tested with data from both MAGIC and VERITAS. Although the $p\gamma$ model reached the lowest value of the three, the AIC difference with the two-zone SSC model was not significant enough ($\Delta AIC_{SSC,p\gamma} > 2$) for the $p\gamma$ model to be selected as the preferred model, therefore this day is listed as inconclusive in Table 3.3.

On MJD 55276, the photohadronic model is able to reproduce accurately the VHE gamma-ray data and has the lowest AIC in the period studied. In contrast, the SSC model over-predicts the MAGIC observations, and although the two-zone SSC is a better approximation to the data, the AIC difference in favour of the $p\gamma$ model

is enough to select it as the preferred model.

On the final day studied (MJD 55277) both leptonic models are a good approximation to the data; nevertheless, the $p\gamma$ model results in a much lower AIC value due to the accuracy of the fit and its simplicity (in terms of free parameters), remaining as the preferred model.

3.7 Expected neutrino emission

From the kinematics of Equation 2.26, each π^+ will produce 3 neutrinos and one e^+, which will carry 1/4 of the π^+ energy each. In the other channel, the π^0 will produce a pair of photons, so that the observed gamma-ray photon energy and the neutrino energy satisfy $E_\nu \sim E_\gamma/2$ (Mücke et al., 1999). Also from the kinematics of the decay chain, we have that $F_\nu \sim \frac{3}{4}F_{\pi^+} = \frac{3}{8}F_\gamma$ (Sahu et al., 2012, 2013). The estimated neutrino flux for only muon neutrinos will be a third of the all flavour flux, then $F_{\nu_\mu} \sim \frac{1}{8}F_\gamma$. In the considered scenario, the pion decay from the Δ^+-resonance gives a neutrino flavour ratio of $\nu_e : \nu_\mu : \nu_\tau = 1 : 2 : 0$. The expected flavor ratio at earth after neutrino oscillations will be $\nu_e : \nu_\mu : \nu_\tau = 1 : 1 : 1$, these are the averaged values given by propagation over astronomical distances, according to the transformation coefficients of the Pontecorvo–Maki–Nakagawa–Sakata (PMNS) mixing matrix to a $1 : 2 : 0$ ratio at the source (IceCube Collaboration, 2015b).

For the VHE gamma-ray photons in consideration from these observations, the energy threshold condition for the Δ^+-resonance leads to a starting point for the neutrino energy range (in the observer's reference frame) of around 0.04 TeV $< E_{\nu,min} <$ 2.5 TeV. From the maximum proton energy condition given by the Hillas criterion (see Section 2.4), the maximum neutrino energy in the observer's frame is expected to be $E_{\nu,max} \sim 680$ TeV.

If an upper limit is set at $F_\gamma < 10^{-4}$ MeV cm^{-2} s^{-1} (which is around the maximum value reached during the flare) and if we assume a neutrino spectrum of the type $\frac{dN}{dE_\nu} = A_\nu E_\nu^{-2}$, then the constant A_ν is estimated as a fraction of the gamma-

ray flux. From the highest flux state of the source, we have an approximation of $A_\nu \sim 3.1 \times 10^{-12}$ TeV cm^{-2} s^{-1}. Then, by integrating the neutrino spectrum using the effective areas $A_{eff}(E_\nu)$ of the 59-strings IceCube configuration (IC59) operating in 2010 (IceCube Collaboration, 2013c; Halzen and Hooper, 2005), we can set an upper limit of $N_{events} < 0.14$ for the expected number neutrino events that would have been detected during the Mrk 421 flaring event.

3.8 Discussion and comparison of results

The fits obtained using the $p\gamma$ model over the flaring period are a significantly better description of the VHE data than a purely one-zone leptonic model, due to a combination of the fit quality obtained and the simplicity of the model in terms of the approximations used and the number of free parameters adopted. The two-zone SSC model is more competitive, being selected as the preferred model on MJD 55266 and scoring a similar AIC value to $p\gamma$ model on MJD 55274.

It is worth noting that for the AIC calculation the number of free parameters in the leptonic model scenarios follow an optimistic estimation, 4 (5) from a total of 20 (11) parameters are considered as free for the two-zone (one-zone) SSC leptonic model during the flaring. As described by the authors in MAGIC Collaboration and VERITAS Collaboration (2015a), the two-zone model uses two independent blobs: one producing the steady emission, and the second blob producing the temporal evolution of the SED, which affects primarily the VHE gamma-ray band. The quiescent blob is described by fixing the model parameters to the same values as the one-zone SSC model, and for the second blob only 4 parameters are left free to vary. This is why after fixing the parameters, the two-zone SSC model describes the SED with one free parameter less than the one-zone SSC model. However counting all the parameters used in both models (fixed or free), the two-zone SSC model has almost double the number of parameters than the one-zone SSC model. The photohadronic flaring model used 4 free parameters to fit the VHE gamma-ray

data.

An interesting feature is that the best fits for a photohadronic contribution are obtained in the last 4 days of the flare. In a more complex hadronic scenario, besides the photo-pion production, there is gamma-ray radiation emitted by proton-synchrotron cooling and the synchrotron radiation of the secondary charged particles. These hadronically-induced gamma rays are in competition with synchrotron and inverse Compton photons radiated by primary electrons considered in the usual leptonic model (Rachen and Mészáros, 1998). On some days the hadronic component may be dominant at VHE, which is then followed by a dominant SSC leptonic component. If the proton injection occurs randomly, there is no preferred time for this to happen during the flare. The interplay between these mechanisms could lead to a time-dependent model with a dominant component at VHE (Diltz and Böttcher, 2016; Dimitrakoudis et al., 2012).

A common problem with hadronic modelling is the high proton energy required to produce the observed gamma-ray emission. However, in this case the high frequency of the seed photons considered in the $p\gamma$ interactions lowers the energy threshold for the accelerated protons to 40 GeV $< E'_p <$ 2.45 TeV in the comoving frame (the emission region), which is below the extreme energies considered in other hadronic models (Mannheim and Biermann, 1992; Mücke et al., 2003). This feature from the $p\gamma$ model can be considered an advantage that would facilitate the conditions for objects like blazars to produce VHE gamma rays and neutrinos from hadronic interactions. Using the Hillas criterion with the applied parameters of the emission region (B, D, R'_f), a proton could be accelerated up to $E'_{p,max} \sim 650$ TeV at the source, more than sufficient for the $p\gamma$ model to produce the VHE gamma-ray emission.

On MJD 55267, 55274 and 55277, below 10^5 MeV the photohadronic contribution behaves as an increasing PL. This is related to the type of seed photon input that we are using (a PL approximation), and does not necessarily represent a realistic physical description of the SED. This is a caveat of the current model which is

focused on the contribution of the photohadronic component at VHE and it is not designed to extend continuously to lower energies. A more complex input model would improve the overall final fit but at the expense of a larger number of free parameters. In addition for the PL description of the seed photon spectrum, due to the lack of photon statistics, two free parameters were optimised over bins lasting a couple of days; this was the shortest time period over which it was possible to obtain *Fermi*-LAT spectra in the > 100 MeV energy range. The parameters α and A_γ coming from the photohadronic contribution at VHE were calculated on daily intervals: this discrepancy between the time bins was dictated by the differences in instantaneous sensitivity between the space and ground-based telescopes and might affect the accuracy of the final fit.

The uncertainty of the seed photon spectrum impacts the optimisation process for the free model parameters α and A_γ which are chosen to get the best fit values to the VHE data and therefore the minimum AIC value for the model. Better data in the MeV energy range (1 MeV to 100 MeV) would enable a better description of the input seed photons and hence an improvement in the photohadronic fit and more reliable predictions. On this regard, the All-sky Medium Energy Gamma-ray Observatory (AMEGO) mission (McEnery et al., 2019), a space-based gamma-ray instrument expected to be launch no later than Dec. 2028, is planned to operate from 200 keV to >10 GeV with $\sim 5\times$ better angular resolution than *Fermi*-LAT, would be very helpful. The combination of MeV gamma-ray photon data with precise measurements from gamma rays in the 10s of TeV regime would be ideal to further test hadronic emission models.

A feature of the $p\gamma$ model (Figure 3.11) is the increase of the energy flux above TeV energies. This is where the one-zone SSC model and the $p\gamma$ model differ and needs to be tested in future observations. The forthcoming CTA gamma-ray observatories (CTA Consortium, 2019a) will be critical to differentiating between these scenarios. The expected sensitivity and capabilities of CTA will enable detection of the gamma-ray flux from Mrk 421 and other near blazars with unprecedented

accuracy and instantaneous sensitivity above tens of TeV in energy. CTA will also take part in the NToO program to look for gamma-ray counterparts to neutrino alerts in follow-up observations. The large field-of-view (FoV) and the rapidly re-position capabilities of CTA's telescopes working alongside the real time alert program from IceCube (Blaufuss et al., 2019) look very promising for the upcoming years. A more detailed discussion of the work and development of the NToO for CTA can be found in Chapter 5.

3.9 Conclusions

The hadronic modelling of flaring episodes from blazars is a complex challenge that has gained relevance. The scenario of a dominant hadronic contribution in the VHE region of the SED coming from $p\gamma$ interactions during the flaring period of Mrk 421 in 2010 was studied. A photohadronic model with 4 free parameters was used and the gamma-ray flux calculated using the Δ^+-resonance approximation. For the target photon spectrum, a PL description was estimated from a tailored analysis performed with *Fermi*-LAT data. The injected proton spectrum assumed for the model was also characterised by a PL. The VHE gamma-ray data was fitted with the $p\gamma$ model on the days with sufficient photon statistics and according to the AIC test, in all cases the $p\gamma$ model was favoured as a better fit description than a one-zone leptonic model, and in comparison with the two-zone SSC model, the $p\gamma$ was favoured by the AIC test on 3 out of the 5 days fitted (MJD 55267, 55276, 55277). The AIC test was inconclusive on MJD 55274 because the difference between the $p\gamma$ and the two-zone model was not meaningful. On MJD 55266 the two-zone model was favoured as a better description of the observations.

The results therefore show that a dominant contribution from the photohadronic component can be used to successfully fit the observations of a blazar flaring episode, which shows the potential of including $p\gamma$ interactions in blazar modelling. However, other contributions coming from leptonic processes, synchrotron emis-

sion from the charged particles in the hadronic decay chain and cascading effects can also play an important role at VHE.

To explore the neutrino/gamma-ray connection in the upcoming years, the next generation of gamma-ray and neutrino observatories, such as CTA, AMEGO and IceCube-Gen2, will play a crucial role; the improvements in observations at VHE and follow-up programmes will make possible to test hadronic components and discriminate between pure leptonic and hadronic scenarios.

Chapter 4

Photohadronic scenario for IceCube Neutrino Alerts

During an active state of a blazar, an overall enhancement in the SED, covering different wavebands in the electromagnetic spectrum, is expected. In a hadronic scenario this behaviour be accompanied by neutrino emission, and the simultaneous detection of HE neutrinos with a flaring source in gamma-rays would be evidence of cosmic ray acceleration.

In this chapter, the photohadronic flaring model scenario presented in Chapter 2 and used in Chapter 3 to study a flaring period of Mrk 421 in 2010 is applied to the blazar 4FGL J0658.6+0636, a suspected counterpart of the neutrino alert IC-201114A. The gamma-ray and neutrino emission around the time of the neutrino alert and during the periods of high activity detected with *Fermi*-LAT over 12.3 years are studied (Section 4.3) and the chances of 4FGL J0658.6+0636 being a neutrino emitter are discussed. The results obtained in this Chapter were presented at the International Cosmic-Ray Conference (ICRC) 2021 and can be found in Rosales de León et al. (2022).

A quick review of neutrino astronomy was given in Chapter 1 (Section 1.4), including a brief description of the IceCube Neutrino Observatory and its updated real-time neutrino alert system. The famous neutrino alert IC-170922A, associ-

ated at a $\sim 3\sigma$ statistical significance with the blazar TXS 0506+056 (IceCube Collaboration et al., 2018) is also reviewed in Section 1.5.2.

4.1 IC-201114A & Follow-up observations

The IceCube collaboration reported a track-like event on November 14th 2020 at 15:05:31.96 UT (T0=59167 MJD). This event was classified in the Gold alert stream channel, with a high probability of being from astrophysical origin (signalness of 0.562 and a false alarm rate of 0.92 events per year due to the atmospheric neutrino background). The refined best fit position (statistical uncertainty only) was RA=105.25° +1.28°/-1.12°, Dec= 6.05° ± 0.95° (J2000) for the 90% containment region. The energy of the neutrino, inferred from the amount of Cherenkov radiation observed, was 214.29 TeV (IceCube Collaboration, 2020a).

A source of the blazar type was identified by the *Fermi*-LAT collaboration inside the 90% localisation region of IC-201114A, at a distance of 0.81° from the best fit neutrino event position: 4FGL J0658.6+0636 (also known as NVSS J065844+063711), located at RA=104.64°, Dec=6.60° (J2000) (Garrappa and Buson, 2020). This source has been classified as a BL Lac object with a High-Synchrotron Peak (HSP; $\nu > 10^{15}$ Hz) and a redshift of $z > 0.5$ (Paiano, 2020).

A preliminary analysis of *Fermi*-LAT data on 1-day and 1-month timescales prior to the neutrino alert indicated no significant ($> 5\sigma$) detection of the source (Garrappa and Buson, 2020). Nor was any significant excess found in gamma-ray emission above 100 MeV from the best fit position of the alert on timescales of days to years. Nevertheless, an analysis of more than 12-years of LAT data (2008-08-04 to 2020-11-14 Universal Time Coordinated (UTC)) identified this object as a very high energy (VHE; E>20 GeV) source (Buson et al., 2020a), several photons above 10 GeV with a more than 90% probability of being associated with the source having been found. It was reported that on average, the *Fermi*-LAT detected one high energy photon per year associated with 4FGL J0658.6+0636, including

a 155 GeV photon (>95% probability) detected on 2018-01-28 07:14:07.976 UTC, providing the first evidence of VHE emission from this object. Also, within the 90% localisation region (1.2° offset from the best fit neutrino alert position), a new gamma-ray transient source was identified by *Fermi*-LAT: J0703.5+0505, with a best fit localisation of RA=105.89°, Dec=5.09° and best fit spectral parameters of photon flux=$3.2 \pm 2.8 \times 10^{-11}$ ph cm^{-2} s^{-1}, spectral index=2.1 ± 0.5. In an integrated analysis performed 1-day prior the neutrino alert time, in an energy range from 0.1 to 800 GeV, the source was detected at a statistical significance $>3\sigma$, and two photons (21 GeV and 1.3 GeV, respectively) with high probability ($>$ 90%) of being associated with this source were observed within an interval of 4.5-hours. However, the source was not significantly detected in a preliminary analysis of LAT data over 1-month period prior to the alert (Garrappa and Buson, 2020).

4FGL J0658.6+0636 was also detected and monitored at other frequencies as part of follow-up observations. In the X-ray band, the Swift Observatory started follow-up observations on 4FGL J0658.6+0636 about 16 hours after the neutrino detection. The detected unabsorbed X-ray flux was 1.9 (+2.3, -0.6) $\times 10^{-12}$ erg cm^{-2} s^{-1} in the 0.3-10 keV energy range (Buson et al., 2020b,c). The NICER X-ray telescope operating on the International Space Station also reported an unabsorbed flux estimate of 1.5×10^{-12} erg cm^{-2} s^{-1} in the 0.3-10 keV band between +31.5 and +86 hrs after T0 (Pasham et al., 2020). The eROSITA instrument, as part of its ongoing all-sky survey, performed observations 28-days prior to the IceCube neutrino detection, obtaining an X-ray flux of 4.7 (+1.8, -1.2) $\times 10^{-11}$ erg cm^{-2} s^{-1} in the 0.3-10 keV band (Gokus et al., 2020), which was consistent with NICER and Swift observations.

The source was also detected on November 17, 2020 at radio frequencies with the 100-m telescope of the MPIfR (Max-Planck-Institut fuer Radioastronomie) at Effelsberg with a flux density of 26 ± 3 mJy at 4.85GHz (Kadler et al., 2020a,b).

The ANTARES neutrino detector did not find any up-going muon neutrino can-

didate events within a ±1-hour and ±1-day time window centred on T0 and inside the 90% error region given by IceCube (Coleiro and Dornic, 2020).

4.2 *Fermi*-LAT analyses

Two *Fermi*-LAT analyses to 4FGL J0658.6+0636 were performed: one using a 12.3-year dataset (MJD 54683-59178) to characterise the historical gamma-ray flux and one concentrating on the 4-months around T0 of the neutrino alert (MJD 59108-59228). In both cases, the workflow followed the steps described in Section 3.3 for a point-source analysis. The Pass8 version of the IRFs with the 1.2.1 *Fermi Science Tools* were used alongside `Fermipy` 0.17.4 (Fermi-LAT Collaboration, 2017b).

4.2.1 Data reduction and source model

For the analyses, all 'SOURCE' class events* converted from the FRONT and BACK sections of the detector were considered. A 15° radius (RoI) around the source position (RA=104.64°, Dec=6.60°) was used for the analyses.

During the data reduction steps, a series of cuts and filters were applied to avoid gamma rays coming from the Earth's atmosphere and to obtain the events recorded during GTIs as described in Section 3.3. The data was binned using the `gtbin` tool specifying 4 logarithmic bins per decade in energy and a spatial bin size of 0.1° per pixel. The counts maps obtained from the 12.3-year and 4-month datasets are shown in Figure 4.1.

An initial model considering all gamma-ray sources listed in the 4FGL-DR2 catalogue (Fermi-LAT Collaboration, 2020a) inside a 20° radius from the RoI's centre was employed. 4FGL J0658.6+0636 is listed as a source with a PL spectrum:

$$\frac{dN}{d\epsilon_\gamma} = N_{PL} \left(\frac{\epsilon_\gamma}{\epsilon_0} \right)^{-\kappa}, \tag{4.1}$$

*See Table 3.1 for a description of all event classes

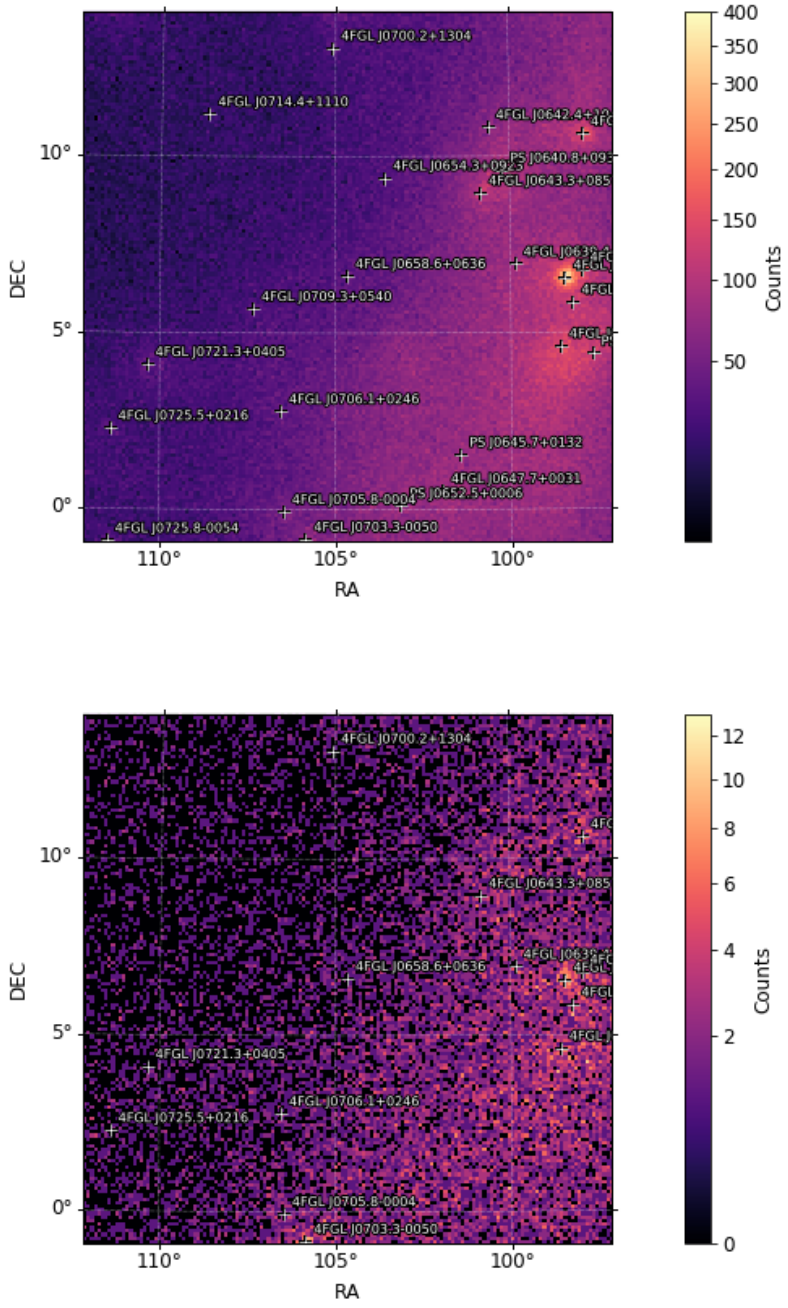

Figure 4.1: Counts maps of the of gamma-ray photons in a 15° RoI around 4FGL J0658.6+0636 using 12.3-year (top) and 4-month (bottom) *Fermi*-LAT datasets. The photons lie in an energy range between 200 MeV and 300 GeV. The gamma-ray data were binned using 4 bins per decade in energy, and 0.1° spatial bin size.

where N_{PL} represents a normalisation constant, κ is the spectral index associated with the source and ϵ_0 is the pivot energy in MeV.

4FGL J0658.6+0636 (TS=115) was not the brightest source identified in the RoI during the 12.3-year dataset; other notable point-sources include the FSRQ 4FGL J0643.3+0857 (TS=688), 4.46° away from the RoI centre, and 4FGL J0633.7+0632 (TS=14,154), a gamma-ray pulsar with a 6.18° offset. There are also a couple of extended sources, the Monoceros SNR listed as 4FGL J0639.4+0655e (TS=737), 4.78° away from the RoI centre, and the Rosette nebula (4FGL J0634.2+0436e, TS=6,228), located at a distance of 6.38° from the centre. Template models developed by the LAT collaboration were used for both of the extended sources (Katagiri et al., 2016). The spectral and spatial information of the sources were saved in a XML file (source model) and the model counts map for the RoI is shown in Figure 4.2.

For the 4-month dataset, the blazar 4FGL J0658.6+0636 was not significantly detected (TS $\leq$ 3), therefore only upper limits on the gamma-ray emission could be derived. The brightest sources detected in the RoI were the pulsar 4FGL J0633.7+0632 (TS=349), the point-source 4FGL J0703.3-0050 (TS=287) and the Rosette nebula (TS=128). The model counts map used for the 4-month dataset is also shown in Figure 4.2.

The Galactic diffuse and isotropic gamma-ray background components were also included in the gamma-ray models by using the templates developed by the LAT collaboration for the Pass8 IRFs, as explained in the analysis example of Section 3.3. The Galactic component is particularly significant below 200 MeV photon energy, so this value is used as a lower energy limit in my analyses.

4.2.2 Data analysis: Likelihood fitting

A baseline analysis was performed to fit the RoI in both datasets following the process described in Section 3.3.3. The specific of these analyses are explained

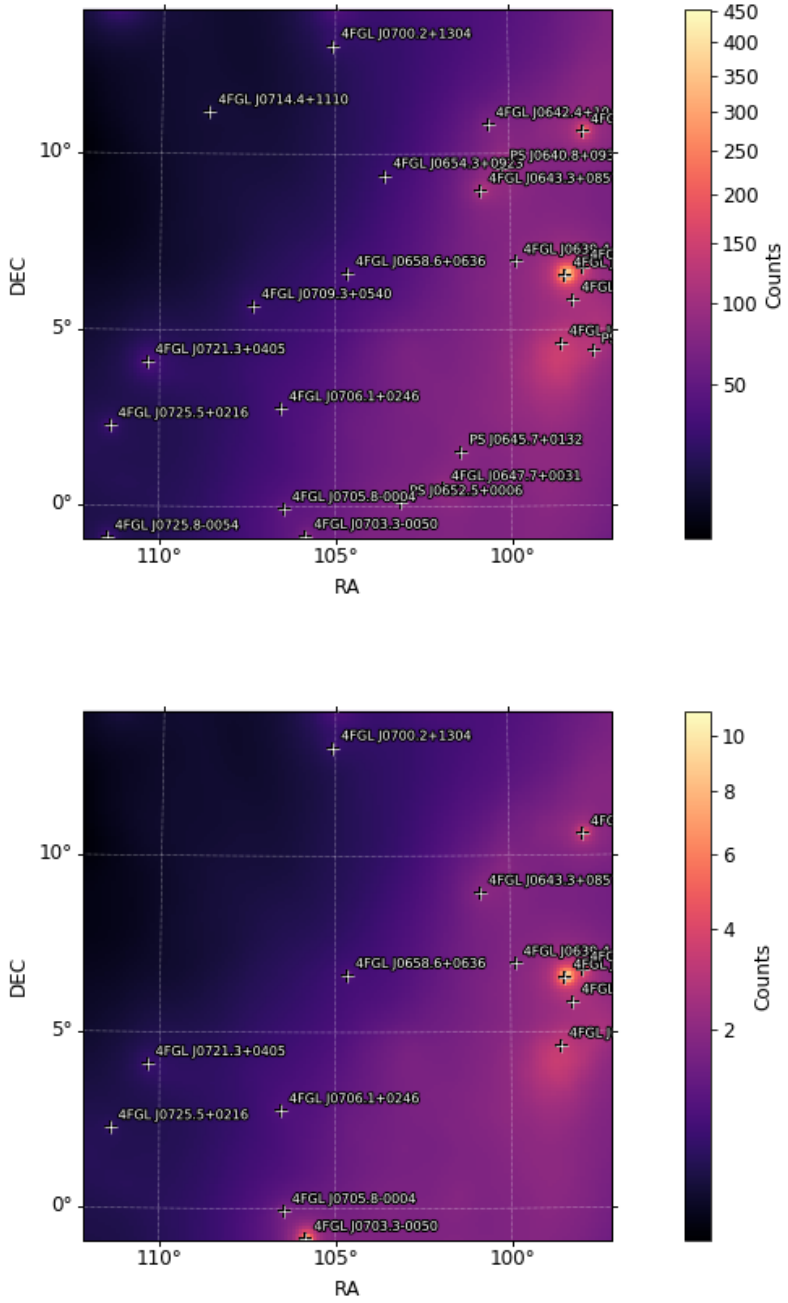

Figure 4.2: Model counts maps created for a 15° radius RoI around 4FGL J0658.6+0636 using the 12.3-year (top) and 4-month (bottom) *Fermi*-LAT datasets. The colour scales indicates the expected number of photons at each pixel in an energy range covering from 200 MeV to 300 GeV.

below.

The sources in the model that were considered insignificant (TS < 9) were discarded. These sources were undetected during the baseline analysis and predicted a few to zero gamma-ray photon counts in the model.

To check for any point-sources not listed in the 4FGL catalogue that may be significant to the model, the `gta.find_sources()` routine was implemented. If there is a point in the sky map with a TS > 25 and with at least 0.5° separation from a listed source, a new point-source characterised with a PL spectrum is added to the model and the RoI is re-optimised.

For the 12.3-year analysis, 4 new point-sources were found and added to the model: J0640.8+0935 (TS=73), J0630.6+0422 (TS=32), J0645.7+0132 (TS=29) and J0652.5+0006 (TS=26). The TS map plot in which these sources were identified is shown in Figure 4.3. In the 4-month analysis, no additional significant source candidates were found.

A likelihood fit was performed with all free parameters in the gamma-ray model, in which the spectral parameters of the sources within a 5° radius around the RoI's centre were left free to vary, as well as the normalisation factors of the two background components (Galactic and isotropic diffuse emissions). The rest of the sources in the RoI model were fixed to the 4FGL catalogue reported values.

4.2.3 Analysis results: light curves and SEDs

For both of the time periods studied, the corresponding light curves were calculated using a likelihood routine (`gta.lightcurve`) to fit each of the bins independently. The background components were left free to vary during the fitting. For the time periods in which the source was detected significantly, the SED was calculated in the energy range between 200 MeV and 300 GeV and fitted using the `gta.sed()` tool and a PL description. The results obtained from both of the analyses are summarised below.

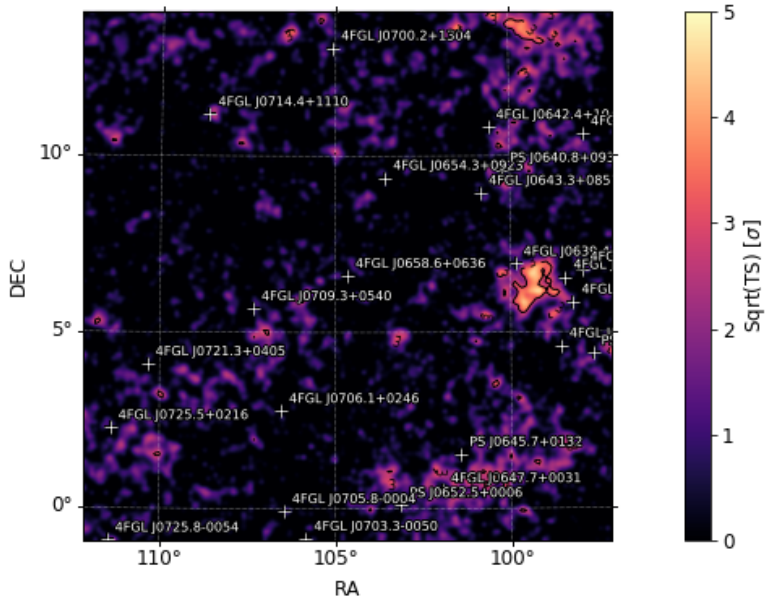

Figure 4.3: TS map of the modelled RoI centred at 4FGL J0658.6+0636's coordinates for the 12.3-year analysis. During the baseline analysis, 4 point-sources not listed in the 4FGL catalogue were found ($\sqrt{\mathrm{TS}} > 25$) and added to the gamma-ray model.

4.2.4 12.3-year dataset

This analysis used a dataset between 2008-08-04 and 2020-11-25 (MJD 54683 - 59178). After performing the baseline analysis described in Section 4.2 to prepare the data, the RoI was optimised and the model parameters fitted. 4FGL J0658.6+0636 was detected significantly over the selected energy range with a TS=115.

A light curve of 4FGL J0658.6+0636 was calculated for the 12.3-year dataset. Due to the low photon statistics on less than 1-year time scales, the whole time period was divided into 10 evenly spaced bins. The bins identified as significant are shown in Figure 4.4; these are labelled and referred to from now on as BIN-A and BIN-B. For the bins during which there was no significant detection of the source, 95% CL flux upper limits are shown. The average flux for the whole time period is 1.29×10^{-9} ph cm^{-2} s^{-1}, shown as a horizontal blue dotted line in Figure 4.4.

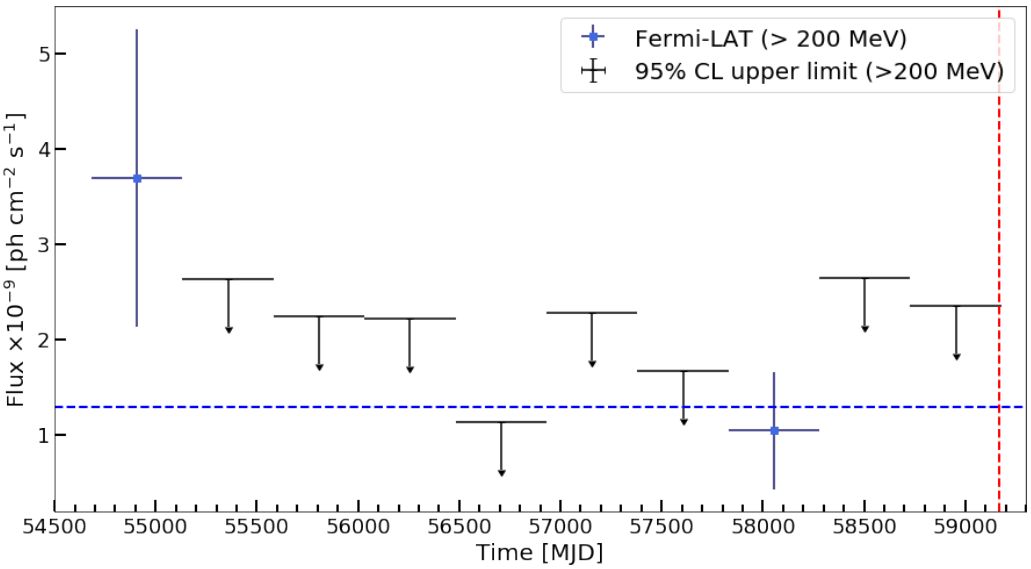

Figure 4.4: Light curve of 4FGL J0658.6+0636 using a 12.3-year dataset, 10 evenly spaced time bins in an energy range of 200 MeV to 300 GeV. Significant bins (TS>25) are shown as blue points, these are referred in the text as BIN-A (left) and BIN-B (right), otherwise 95% CL upper limits on the flux are plotted. The horizontal blue line corresponds to the average flux of the source, 1.29×10^{-9} ph cm^{-2} s^{-1}. The vertical dotted red line represents the reported time of IC-201114A (T0=59167 MJD).

The best fit spectral parameters obtained for the source are: a normalisation constant of $N_{PL} = (4.2 \pm 0.7) \times 10^{-14}$ MeV cm^{-2} s^{-1}, a spectral index of $\kappa = 1.9 \pm 0.1$ and a pivot energy of $\epsilon_0 = 2.75 \times 10^3$ MeV. The calculated SED points from the 12.3-year dataset and the PL description are shown in Figure 4.5.

The SEDs derived for BIN-A and BIN-B in the energy range of 200 MeV to 300 GeV are shown in Figure 4.6. The spectral parameters and fluxes of the significant bins are summarised in Table 4.1 alongside other model parameters used in the photohadronic fit.

The VHE emission (E>20 GeV) from 4FGL J0658.6+0636 was also studied over the 12.3-year period. Individual photons with a high probability of coming from the source were identified using the `gtsrcprob` routine. The VHE photons associated with a $> 90\%$ probability around 0.2° from the source were selected using the gamma-ray model generated during the baseline analysis. The diffuse background

BIN	TS	Flux 10^{-9} [ph cm^{-2} s^{-1}]	N_{PL} 10^{-14} [MeV cm^{-2} s^{-1}]	κ	A_γ 10^{-2}	A_ν 10^{-12} [TeV cm^{-2} s^{-1}]	Minimum Detection Time [days]	$F_{\nu,\mathrm{int}}$ 10^{-5} [TeV cm^{-2}]
BIN-A	38	3.69 ± 1.56	8.9 ± 2.2	2.1 ± 0.2	1.85 - 1.92	6.35 - 6.93	160 (IC40)	8.66 - 9.46
							100 (IC59)	5.54 - 6.05
BIN-B	34	1.04 ± 0.61	4.6 ± 2.1	1.5 ± 0.2	29.9 - 53.9	186.15 - 352.21	2.5 (IC86)	4.02 - 7.61

Table 4.1: Summary table of the bins in the 12.3-year dataset during which 4FGL J0658.6+0636 was detected significantly. The TS and flux for each bin are reported in the 2nd and 3rd columns. The spectral parameters for the PL model are shown on the 4th and 5th columns, and plotted in Figure 4.6. The gamma-ray and neutrino normalisation constants used in the photohadronic fit (Figure 4.10) appear in the 6th and 7th columns respectively. The Minimum Detection Time (MDT) expected to get a couple of neutrino events during an active state of the source, and the integrated flux over that period are shown in final two columns.

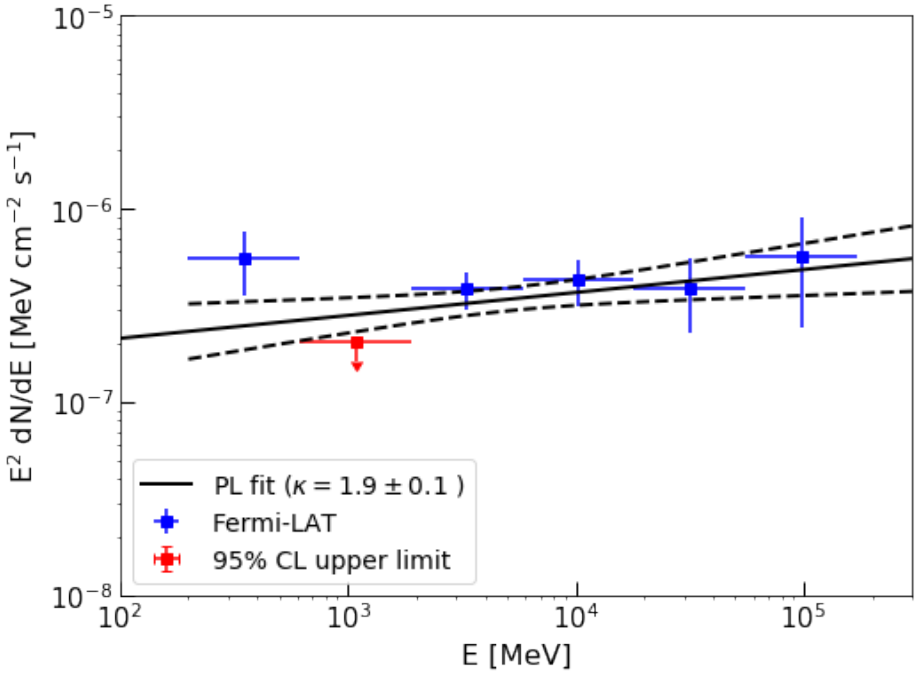

Figure 4.5: Average *Fermi*-LAT spectrum of 4FGL J0658.6+0636 from the 12.3-year dataset. An energy range between 200 MeV and 300 GeV was considered, bins with a TS$\geq$ 5 are shown as blue data points and the 95% CL upper limits are plotted in red. The PL model fitted to the data is also shown, a photon spectral index of $\kappa = 1.9 \pm 0.1$.

components were taken into account by using the `gtdiffrsp` tool, which calculates the diffuse response over a solid angle by integrating the diffuse source model convolved with the IRFs. The error in energy was calculated using the energy resolution performance of the Pass8 IRFs.

The VHE photons associated with 4FGL J0658.6+0636 are shown in Figure 4.7. The VHE photon of $\sim$ 155 GeV (MJD 58146) reported by Buson et al. (2020a) was found within the time range of BIN-B (MJD 57830 -58279) and represents the highest energy photon detected. Another VHE energy photon with an energy of $\sim$ 40 GeV was detected during BIN-A at MJD 54925.26.

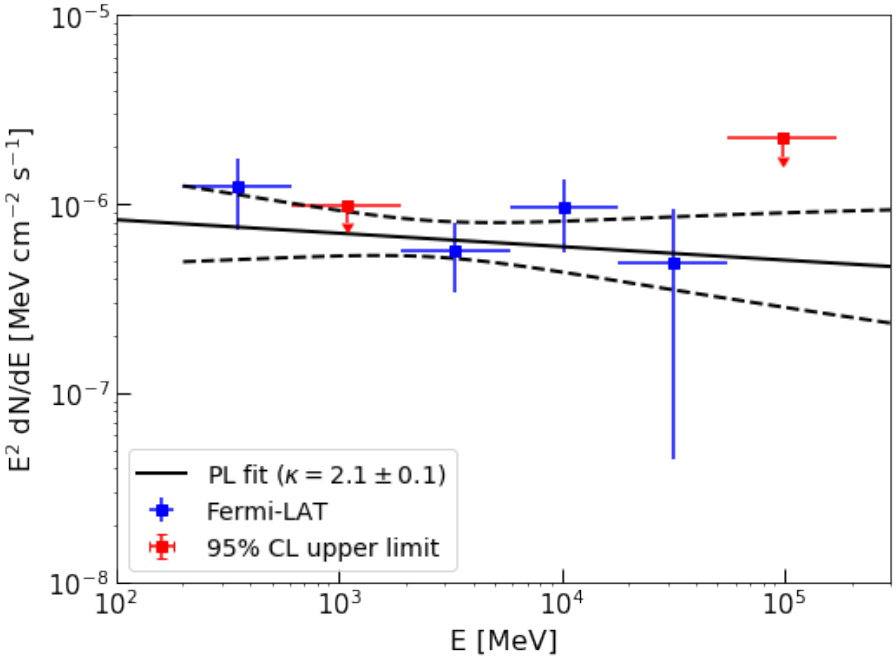

(a) Spectrum and PL approximation for BIN-A.

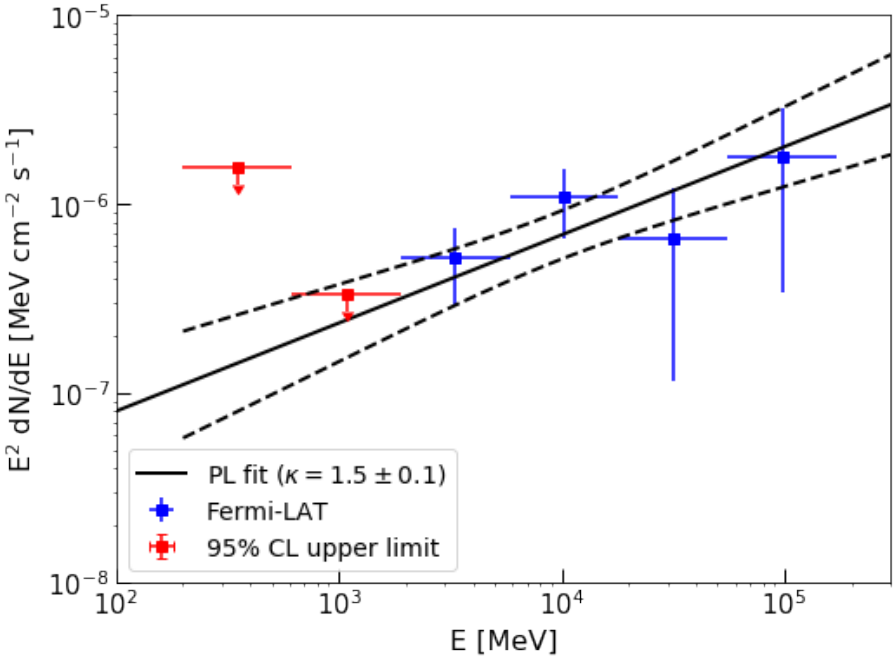

(b) Spectrum and PL approximation for BIN-B.

Figure 4.6: *Fermi*-LAT spectrum of 4FGL J0658.6+0636 obtained for the significant bins over 12.3-years of *Fermi*-LAT data in the 200 MeV to 300 GeV energy range. Bins with a TS$\geq$ 5 are shown as blue data points, otherwise the 95% CL upper limits are plotted. The PL description for both periods is included, where the change in the spectral photon index is appreciable. The best fit parameters for the PL model are shown in Table 4.1.

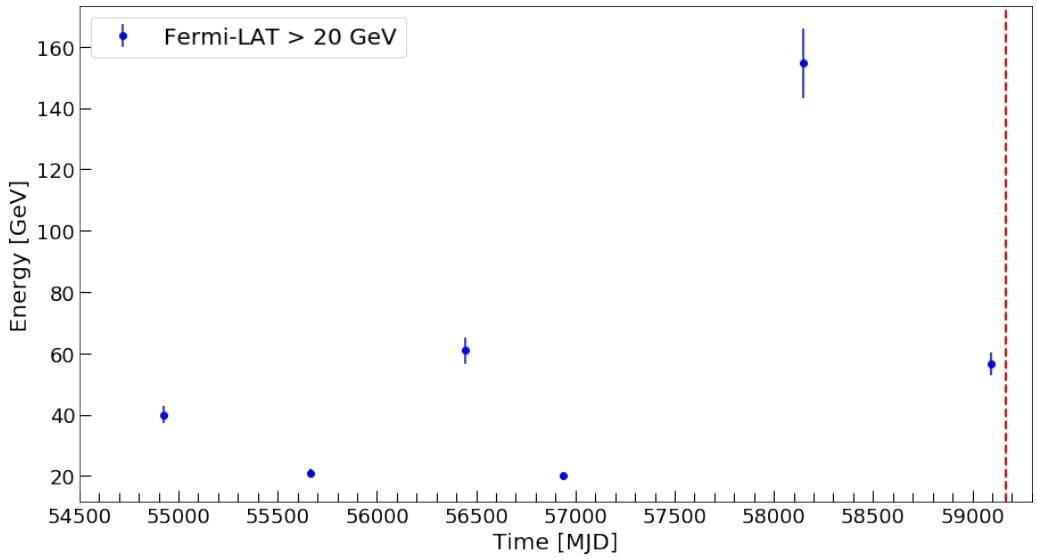

Figure 4.7: VHE photons (> 20 GeV) photons associated with 4FGL J0658.6+0636 in the 12.3-year dataset. Individual photons with an associated source origin probability above 90% are plotted. The vertical red line represents the reported time of IC-201114A (T0=59167 MJD).

4.2.5 4-month dataset

Around the time of the detection of the first neutrino event from the direction of TXS 0506+056, IC-170922A, the high-energy gamma-ray emission lasted for around 4 months (IceCube Collaboration et al., 2018; Tanaka et al., 2017). Assuming similar behaviour, gamma-ray emission within a 4-month time window centred on T0 would be expected, i.e. between 2020-09-16 (MJD 59108) and 2021-01-14 (MJD 59228).

The specifications for the baseline analysis (size, energy range, spatial and energy binning, IRFs used) were the same as those described for the 12.3-year dataset. The source 4FGL J0658.6+0636 (TS $\sim$ 3) was not significantly detected over the 4-month interval analysed. Only upper limits on the gamma-ray spectrum were obtained (see Figure 4.9).

A light curve was computed for this dataset using 2-week bins (see Figure 4.8). No significant enhanced gamma-ray activity was found around the time of the alert, therefore the 95% upper limits found for the flux are shown. In the 2-week bin

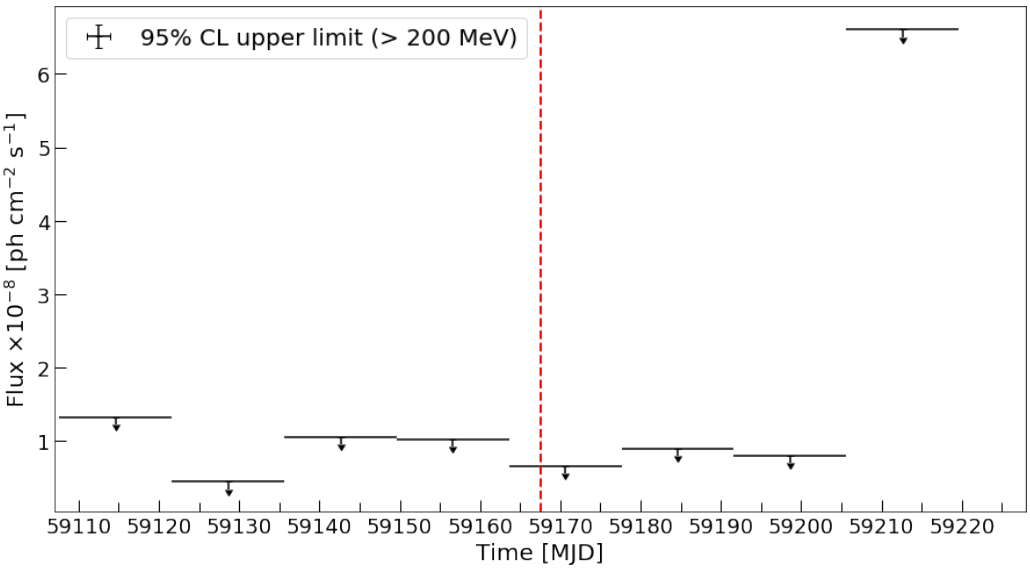

Figure 4.8: 4-month light curve around the time of IC-201114A plotted in 2-week time bins. An energy range of 200 MeV to 300 GeV is considered. No significant gamma-ray activity was detected and 95% upper limits are plotted. The vertical red line represents the reported time of IC-201114A (T0=59167 MJD).

covering T0, the upper limit is 9.0×10^{-9} ph cm^{-2} s^{-1}.

4.3 Photohadronic modelling of 4FGL J0658.6+0636

The motivation to study the behaviour from 4FGL J0658.6+0636, is whether the non-detection of neutrinos from 4FGL J0658.6+0636 before the IC-201114A event is compatible with the gamma-ray emission, in the context of the photohadronic scenario presented in Section 2.7.3, and whether the detection of neutrinos from the object is compatible with the non-detection in gamma-rays around the time of IC-201114A.

For the time bins during which the source was detected significantly, the *Fermi* spectrum was used as the seed photon input. The photohadronic contribution to the SED was calculated for a redshift range of $0.5 < z < 1.5$ (as there is no defined redshift value for the source), and typical value parameters were assumed for the modelling (see Table 4.2). The Doppler factor of $D = 13$ employed corresponds

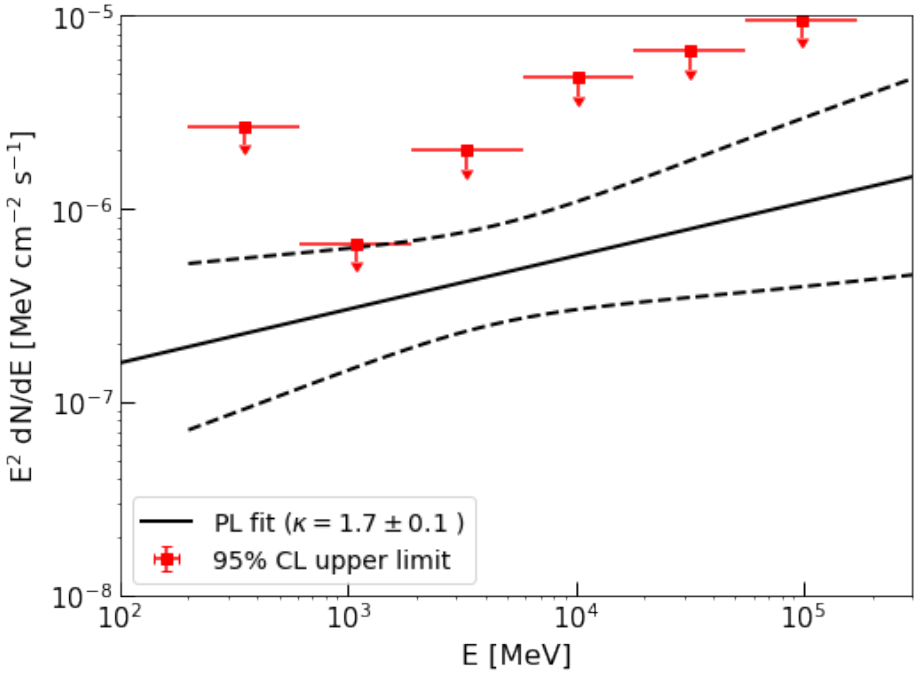

Figure 4.9: *Fermi*-LAT spectrum of 4FGL J0658.6+0636 obtained from the 4-month dataset. An energy range between 200 MeV and 300 GeV was considered, as the source was not significantly detected, only the 95% CL upper limits are plotted in red. The best fit PL model is also shown (black line) with its uncertainty (dotted black lines).

to an average value for *Fermi* blazars (Ghisellini et al., 2014; Zhang et al., 2020), and the magnetic field strength of $B = 1$ G represents the order of magnitude for a typical blazar jet (Ghisellini and Madau, 1996; Mücke et al., 2003). A radius of $R'_f \approx (1.35 - 2.25) \times 10^{16}$ cm was used for the size of the emission region, calculated by considering the minimum variability time scale to be 1-day over the redshift range.

For the redshift range considered, to produce gamma-ray photons from 100 GeV and up to TeV energies in the observer's reference frame, the seed photons for $p\gamma$ interactions should have energies between 0.08 and 24 MeV. The threshold condition given by the Δ^+-resonance sets the minimum proton energy to between 663 GeV and 1105 GeV. The proton spectrum is assumed to be described by a PL model with a power index of $\alpha = 2.2$. On the other hand, applying the Hillas criterion (Hillas, 1985) for a magnetic field strength of 1G and the given radius

Parameter	Typical Value / Range
z	0.5 - 1.5
R'_f	(1.35-2.25) $\times 10^{16}$ cm
B	1 G
D	13
α	2.2
E_p	663 GeV-47 PeV
E_ν	30 GeV- 2.35 PeV

Table 4.2: Summary table of the parameters used to characterise the emission region of 4FGL J0658.6+0636; typical values for blazars were assumed. The energy ranges for the accelerated protons and neutrinos produced, calculated over the redshift range in the observer's reference frame, are also given in the last two lines.

of the emission region, the maximum proton energy is estimated to be between 43.7 and 47 PeV. The kinematics of the $p\gamma$ interaction decay chain set the neutrino energy as a fraction of the proton energy $E_\nu \sim E_p/20$, which means the energy range of the produced neutrinos is expected to be 30 GeV to 2.35 PeV in the observer's reference frame. These limits are used in the calculation for the neutrino flux normalisation constant and the expected number of neutrino events.

For a high-significance point-source detection with IceCube, between 2 and 30 detected events above the atmospheric neutrino background are required (IceCube Collaboration, 2018). This number will vary depending on the energy spectrum, the proximity of the source and the clustering of events in time. The Minimum Detection Time (MDT)* for a couple of neutrino signal events using the average spectral state of 4FGL J0658.6+0636 can be approximated by using the corresponding neutrino flux and the operational IceCube configuration (see Section 2.7.4).

With a Dec=6.60°, 4FGL J0658.6+0636 has a difference in declination of less than 1° to that of TXS 0506+056, so similar conditions might be expected for 4FGL J0658.6+0636. Due to the given conditions of low earth absorption for high-energy neutrinos combined with a low atmospheric muon background, a low declination band (with $\delta \sim 0°$) has been identified by IceCube as the region with

*It is considered that at least two neutrino events above the background level are required for a high-significance point-source detection (IceCube Collaboration, 2018). The time to detect this minimum quota is referred in this thesis as the Minimum Detection Time (MDT), but it is noted that a higher number of events might be needed for a positive detection

the best point-source sensitivity (IceCube Collaboration, 2017e). Both neutrino source candidates, TXS 0506+056 and 4FGL J0658.6+0636, lies within this region. The mean background at the declination of TXS 0506+056 (Dec=5.69°) was ~ 6 events in a 1° radius bin during a 5-month time window (IceCube Collaboration, 2018). An excess of 13 ± 5 events above the background during same time window led to a $\sim 3.5\sigma$ significance estimated with a time-dependent analysis.

There are two types of gamma-ray behaviour that could lead to multiple neutrino detections from a source as modelled with the photohadronic flaring scenario: a series of bright, short flaring events or a more subtle sustained emission that accumulates over an extended period.

4.3.1 Historical Gamma-ray and Neutrino Emission

BIN-A: MJD 54683 - 55132

Over this time period, covering 2008-08-04 to 2009-10-28, the source was detected in gamma-rays with TS=38 and an average flux of $(3.69 \pm 1.56) \times 10^{-9}$ ph cm^{-2} s^{-1}. The spectral parameters shown in Table 4.1 were used as the target photon spectrum to calculate the $p\gamma$ interactions. The resulting fits are shown in Figure 4.10. A normalisation constant A_γ was computed for each fit made along the redshift range to respect the *Fermi*-LAT upper limits and SED data points at VHE (> 20 GeV). The fit parameters are also summarised in Table 4.1.

The expected neutrino flux is estimated by a PL of the type:

$$\frac{dN}{dE_\nu} = A_\nu E_\nu^{-\beta}\,, \tag{4.2}$$

with a power-index of $\beta = 2$, and a neutrino normalisation constant calculated for each fit at different redshifts, resulting in a range between $A_\nu = (6.35, 6.93) \times 10^{-12}$ TeV cm^{-2} s^{-1}.

The 40 string IceCube configuration (IC40) was operational between 2008-04-06 and 2009-05-20, covering $\sim$ 9-months of BIN-A. Considering the effective area for

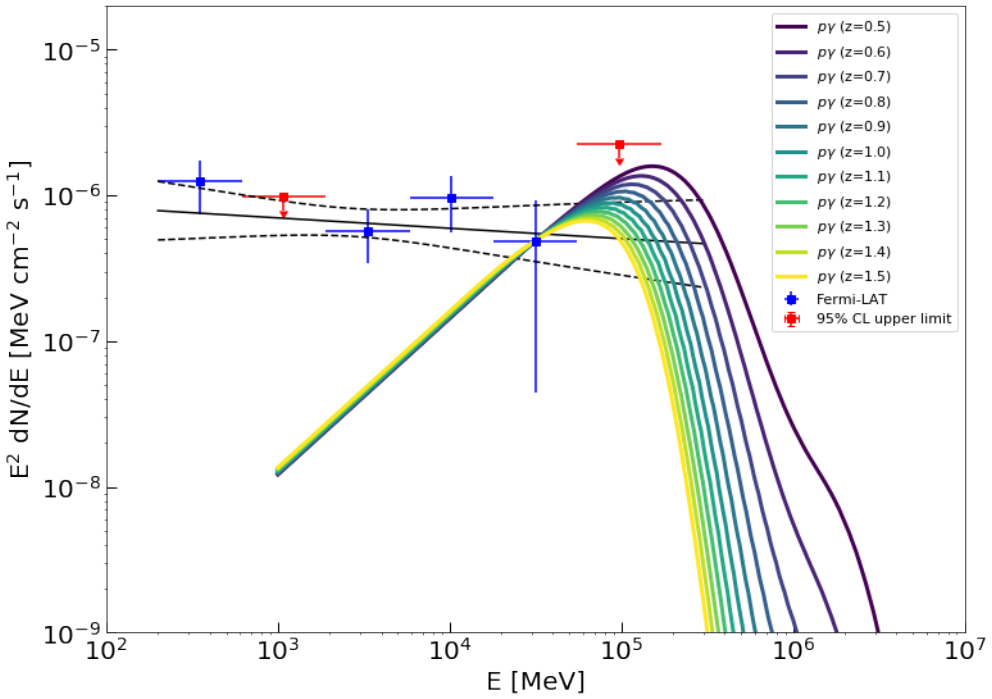

(a) Photohadronic fit for BIN-A

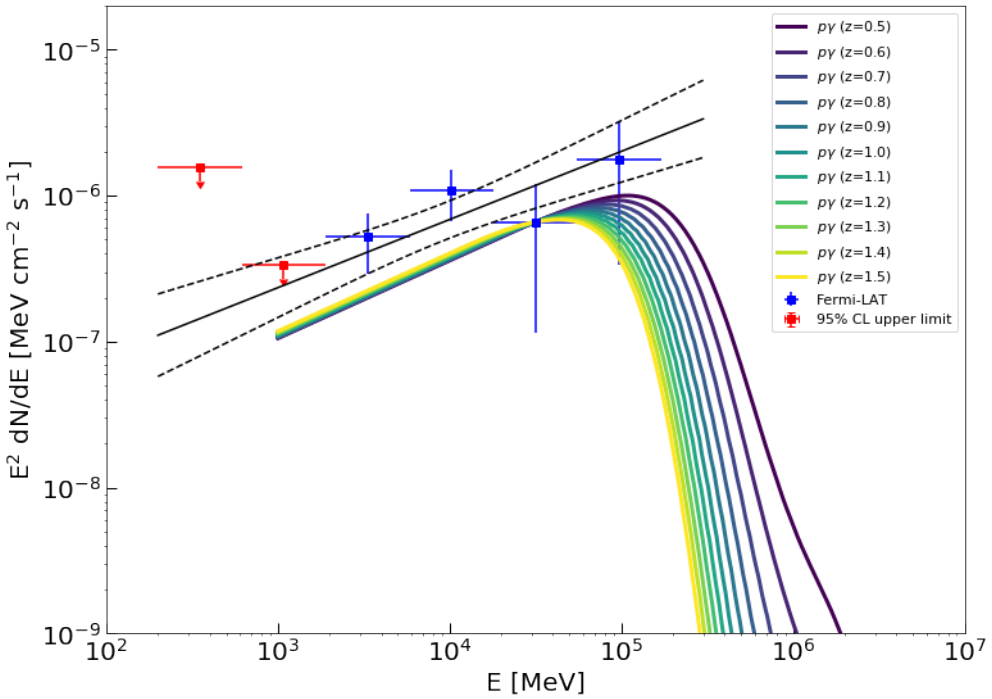

(b) Photohadronic fit for BIN-B

Figure 4.10: Photohadronic contribution to the 4FGL J0658.6+0636 gamma-ray spectrum based on the significant bins obtained from the 12.3-year analysis. The fits are shown in a colour scale depending on the redshift. The *Fermi*-LAT data points and 95% upper limits are shown alongside the PL description.

IC40, and assuming the gamma-ray flux and spectral index observed during BIN-A, a couple of events would be detected over an interval ~ 160 days. The expected integrated neutrino flux over an 160-day interval is between $F_{\nu,\mathrm{int}} = (8.66, 9.46) \times 10^{-5}$ TeV cm^{-2}. After 2009-05-20, IC59 was operational, overlapping with BIN-A for a $\sim$ 5-month period. In this case, two neutrino detections are expected over a $\sim$ 100-day interval, which corresponds to an integrated flux between $F_{\nu,\mathrm{int}} = (5.54, 6.05) \times 10^{-5}$ TeV cm^{-2}.

With the *Fermi*-LAT sensitivity it was not possible to bin the gamma-ray data sufficiently finely to identify a possible gamma-ray flare event. Nonetheless, given that there was no detection of the object on shorter timescales, it seems likely that the BIN-A gamma-ray detection was the result of low-level emission over an extended period rather than a single, bright event. In these circumstances, given the known background rate of the IC40 and IC59 IceCube detector configurations, it is unlikely that IceCube would have detected a significant neutrino signal during this time period.

BIN-B: MJD 57830 -58279

Between the time interval of 2017-03-17 and 2018-06-10, 4FGL J0658.6+0636 was detected in gamma-rays with TS=34 and an average observed gamma-ray flux of $(1.04 \pm 0.61) \times 10^{-9}$ ph cm^{-2} s^{-1}. The photohadronic contribution for this bin was calculated in the same way as BIN-A, using the spectral parameters shown in Table 4.1 as the target photon spectrum to calculate the $p\gamma$ interactions and the same values for D, B and R'_f. The photohadronic contribution to the SED is shown in Figure 4.10. Behaviour compatible with the hard gamma-ray spectrum was found for the photohadronic fits calculated for this time bin.

The neutrino flux normalisation constant values were estimated to be in the range of $A_\nu = (1.86, 3.52) \times 10^{-10}$ TeV cm^{-2} s^{-1}. The spectral model parameters and normalisation constants for BIN-B are summarised on the bottom line of Table 4.1. The IC86 configuration was operational for the whole time range of this bin. Assuming $p\gamma$ interactions and the average calculated neutrino flux, two neutrino

Assumed Behaviour	A_γ	A_ν [TeV cm^{-2} s^{-1}]	Minimum Detection Time	$F_{\nu,\mathrm{int}}$ $\times 10^{-5}$ [TeV cm^{-2}]
BIN-A like	0.11 - 0.20	(3.66 - 7.15)$\times 10^{-11}$	12-days	3.80- 7.42
BIN-B like	1.39 - 2.24	(1.05 - 1.78)$\times 10^{-8}$	$\sim$ 1-hours	3.79 - 6.41

Table 4.3: Summary table of the photohadronic fit results to 4FGL J0658.6+0636 in a 4-month time window around the IC-201114A alert. The historical behaviour of the source from BIN-A and BIN-B is assumed. The gamma-ray and neutrino normalisation constants for each bin are shown in the 2nd and 3rd columns. The minimum expected time for 2 neutrino detections during an active state of the source appears in the 4th column, and the integrated flux over that period is shown in the 5th column. The photohadronic contribution calculated for each bin is plotted on Figure 4.11.

event detections are expected in $\sim$ 2.5-days, which is the MDT associated to the redshift range considered. The integrated neutrino flux during this time span is predicted to be around $F_{\nu,\mathrm{int}} = (4.02, 7.61) \times 10^{-5}$ TeV cm^{-2}.

For comparison purposes, to emulate the 13 excess events detected during the 2014-2015 neutrino flare of TXS 0506+056 (IceCube Collaboration, 2018), a detection time of $\sim$ 16-days would be needed. It is therefore possible, assuming a $p\gamma$ interaction model, that IceCube would have detected an excess neutrino events during BIN-B. This is a strong motivation for investigating possible clustering of neutrino events from the direction of 4FGL J0658.6+0636 in historical IceCube data.

4.3.2 Gamma-ray emission around the IC-201114A alert

The analysis of the 4-month dataset around T0 shows no significant gamma-ray activity of the source during this time window. However, assuming the source has a gamma-ray spectrum similar to either BIN-A or BIN-B around the time of the IceCube alert, but a flux that is just below the *Fermi*-LAT upper limits derived from the 4-month analysis, an approximation for the photohadronic contribution to the SED and the expected neutrino flux can be calculated. The photohadronic model fits for both, BIN-A and BIN-B like behaviours, are shown in Figure 4.11. Here, the *Fermi*-LAT upper limits are used to set a normalisation constant A_γ, which depends on the redshift. The EBL model of Domínguez et al. (2011) is

used to account for the gamma-ray attenuation, which has a larger effect at higher energies and redshifts.

A summary of the ranges on the neutrino and gamma-ray normalisation constants are given in Table 4.3, as well as the integrated neutrino flux and the minimum expected time for two neutrino events detection assuming either BIN-A or BIN-B like behaviour for the seed photon input.

Taking the PL description from BIN-A as the seed photon input for the modelling and a neutrino spectral index of $\beta = 2$, the normalisation constants for the neutrino flux are in the range of: $A_\nu = (3.66 - 7.15) \times 10^{-11}$ TeV cm^{-2} s^{-1}. Considering the effective area from the IC86 configuration, two neutrino detections are expected from the source after a minimum time of at least 12-days, which leads to an integrated neutrino flux of $F_{\nu,\mathrm{int}} = (3.80 - 7.42) \times 10^{-5}$ TeV cm^{-2}.

Using the spectral description from BIN-B to calculate the photohadronic contribution, the corresponding neutrino flux normalisation constant is $A_\nu = (1.05 - 1.78) \times 10^{-5}$ TeV cm^{-2} s^{-1}. In this scenario, the minimum time for two neutrino events detection is $\sim$ 1-hours, with an integrated flux of $F_{\nu,\mathrm{int}} = (3.79 - 6.41) \times 10^{-5}$ TeV cm^{-2}. The harder gamma-ray photon index in this case shortens the estimated minimum neutrino detection time in comparison to the behaviour in BIN-A. Therefore, the non-detection of high-energy gamma-ray emission from 4FGL J0658.6+0636 around the time of the IC-201114A event is compatible with the detection of a neutrino, assuming the conditions within the photohadronic scenario.

4.4 Discussion: Is 4FGL J0658.6+0636 a neutrino emitter?

The possibility of the blazar 4FGL J0658.6+0636 being a neutrino emitter has been studied under a one-zone photohadronic scenario. For the physical parameters involved in the modelling process (D, B and R'_f), typical values for *Fermi* blazars

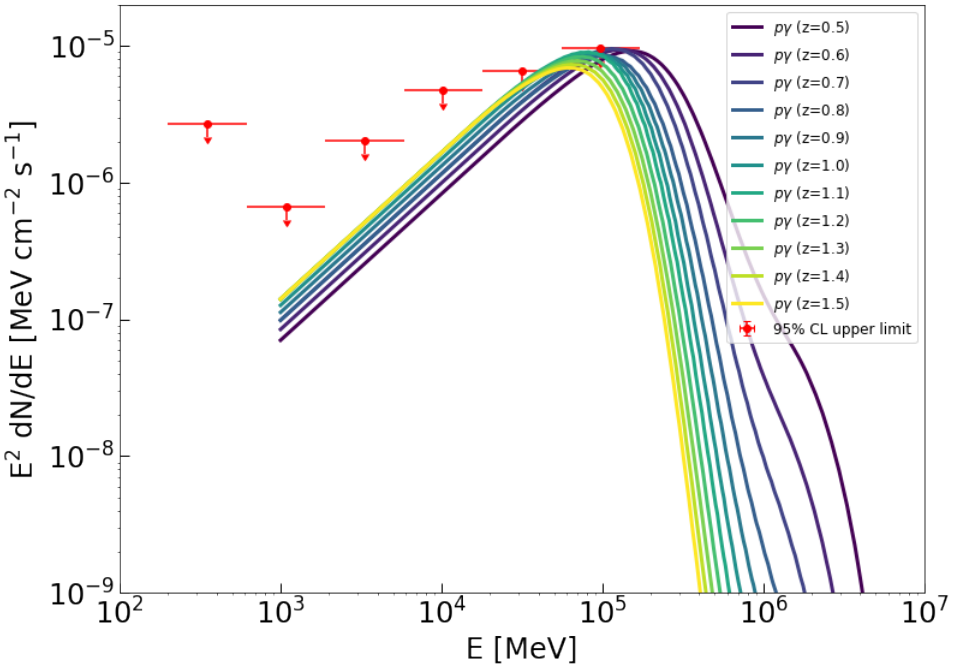

(a) Photohadronic fit assuming BIN-A seed photon spectrum

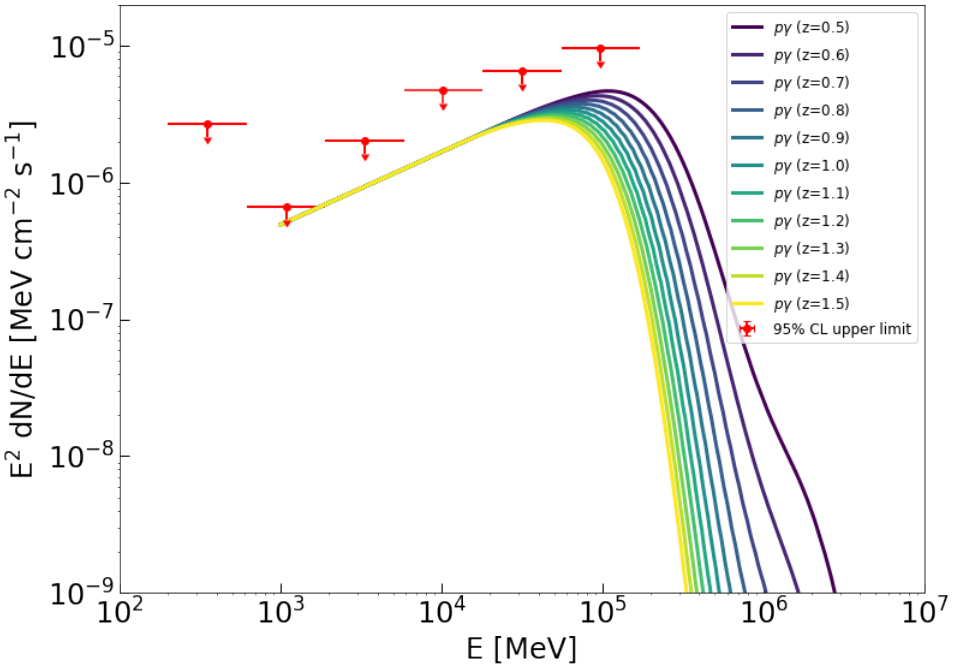

(b) Photohadronic fit assuming BIN-B seed photon spectrum.

Figure 4.11: Photohadronic contributions to the 4FGL J0658.6+0636 gamma-ray spectrum in a 4-month time window assuming BIN-A (top) or BIN-B (bottom) seed photon spectrum. The calculated photohadronic contribution is plotted over the redshift range indicated in a colour scale. 95% CL upper limits for the flux are shown as the source was not detected significantly over the 4-month time period.

were selected to calculate the photohadronic contributions, as summarised in Table 4.2. The Hillas criterion was used to calculate the maximum proton energy under these assumptions, and, as there is only available a lower limit to the redshift of 4FGL J0658.6+0636, a redshift range between $0.5 < z < 1.5$ was considered.

4.4.1 Overview of the historical behaviour

Looking at 12.3-years of *Fermi*-LAT historical data, 2 significant periods of gamma-ray activity were identified and characterised (BIN-A and BIN-B). It was found that a dominant photohadronic contribution is compatible with the SED behaviour of the source during BIN-B, which presents a hard gamma-ray spectrum ($\kappa = 1.5 \pm 0.2$). A set of VHE photons with a >90% probability of being from the source were detected within the 12.3-year dataset, confirming 4FGL J0658.6+0636 as a VHE source. In addition, the 155 ± 11 GeV photon mentioned by Buson et al. (2020a) was detected at MJD 58146, which coincides with BIN-B (see Figure 4.7). From the estimated neutrino flux for this bin, a minimum detection time of $\sim$ 2.5-days is expected for a couple of neutrino signal events and at least 16-days to emulate the 13 excess events recorded during the 2014-2015 neutrino flare of TXS 0506+056. These results support the hypothesis that 4FGL J0658.6+0636 can be a neutrino emitter and, according to the predictions, neutrinos could have been detected during the BIN-B time period (MJD 57830 -58279).

In contrast, for BIN-A the predicted spectrum does not match the *Fermi*-LAT data points at energies below 100 GeV; this may indicate that a hadronic component is not dominant and therefore leptonic components play a much important role to explain the emission during BIN-A. It also seems likely that low-level gamma-ray emission over an extended period of time is responsible for the significant gamma-ray detection on this bin, resulting in the longer expected detection times for two neutrino events. From these results, and taking into account the atmospheric neutrino background rate, it is unlikely that either IC40 or IC59 IceCube configurations would have detected any neutrinos during this time range.

The IceCube collaboration has made searches for point-like neutrino sources over 10-years of data (2008 to 2018) and no significant excess has been reported from the direction of 4FGL J0658.6+0636. (IceCube Collaboration, 2017a, 2020b). A catalogue of all previous neutrino events issued under the real-time alert system (IceCube Collaboration, 2017c), or would have since the 2010 operational season, were also made public to investigate possible correlations with *Fermi*-LAT sources. 4FGL J0658.6+0636 has no known association within this catalogue. Further data, or more detailed analysis of historical IceCube data, will be needed to obtain a positive confirmation of the source as a neutrino emitter.

4.4.2 IC-201114A and possible future events

The results obtained from the *Fermi*-LAT analysis in a 4-month time window around the IC-201114A alert, indicate that there is no significant gamma-ray flux detected from 4FGL J0658.6+0636. Nevertheless the possible photohadronic contribution can be calculated assuming a similar behaviour to that seen historically (BIN-A and BIN-B) but with the flux constrained using the *Fermi*-LAT upper limits around the time of the neutrino event.

The $p\gamma$ contribution calculated for the VHE part of the SED is highly dependent on the seed photon input considered; the PL approximation used dictates the behaviour at the 1-100 GeV energy range (see Figure 4.10). The photon index κ impacts the calculation of the estimated gamma-ray flux and therefore the normalisation constant for the predicted neutrino flux; the normalisation constants during the BIN-A and BIN-B emission events are $\sim$ 2 orders of magnitude different (Table 4.3). The resulting differences in the spectra can be seen in Figure 4.10.

The variation of the spectral photon index used between BIN-A and BIN-B resulted in a considerably higher neutrino flux estimation and a shorter expected time for the latter. In an optimistic scenario, it is predicted a minimum detection time of $\sim$ 1-hours using the assumed conditions from BIN-B seed photon spectrum. For

BIN-A, this minimum time goes up to at least 12-days. The associated gamma-ray spectra for BIN-B is compatible with the non-detection of the source in gamma-rays around the time of the neutrino alert, but the main reason behind the lack of an enhanced gamma-ray emission remains open to discussion.

One option to explain the non-detection of the source in gamma-rays around the alert time (T0), is to consider a high opacity given by a dense photon field inside the emission region. This condition might increase the efficiency of the photohadronic process, but it also means the internal absorption will diminish the observed gamma-ray flux through electromagnetic pair cascades. If the opacity is too large, then a possible neutrino detection will not be accompanied by an enhanced gamma-ray flux, similar to the scenario presented in the 2014-2015 neutrino flare from TXS 0506+056. This possibility has been discussed in other works: Brown et al. (2015); Murase et al. (2016); Halzen et al. (2019); Reimer et al. (2019); Plavin et al. (2021); Petropoulou et al. (2020).

In the TeV energy range, the predicted $p\gamma$ contribution might be observable with IACTs, depending on the redshift of the source and the internal absorption conditions. Further observations at VHE gamma-ray energies are crucial for constraining the photohadronic contribution to the observed gamma-ray flux. In this regard, the upcoming Cherenkov Telescope Array (CTA) is relevant. The two CTA observatory sites, one in each hemisphere, will provide at least an order of magnitude improvement in sensitivity with respect to its predecessors, in an energy range from 20 GeV to above 300 TeV.

It is also worth noticing that, with a reported signalness of 56%, an origin for IC-201114A other than the blazar is not discarded. There is a chance of this being a high energy atmospheric event or part of the small diffuse neutrino flux contribution from the Galactic plane (IceCube Collaboration, 2017b). However, working on the assumption that 4FGL J0658.6+0636 is the source of the neutrino, there are some caveats in relation to the analysis and modelling performed as part of the photohadronic scenario adopted.

The results from this Chapter concentrate on the predictions for a dominant photohadronic component at VHE under a one-zone emission scenario, based on the high cross-section of the photo-pion production process through the Δ^+-resonance. It remains possible that other contributions are relevant at the GeV energy band, either from leptonic processes (e.g. SSC radiation), or from other hadronic processes such as proton-synchrotron or synchrotron radiation emitted by the secondary charged particles produced in the $p\gamma$ decay chain. These multiple scenarios goes beyond the phenomenological description considered in this thesis, and represent an area of improvement that can be explored to evolve the photohadronic approach into a more robust framework.

4.5 Conclusions

The blazar 4FGL J0658.6+0636 was identified as a possible counterpart for the IC-201114A neutrino alert. The analysis of 12.3-years of *Fermi*-LAT data confirmed this blazar as a VHE source. Two significant periods of gamma-ray activity were found (BIN-A and BIN-B) which were studied using a one-zone photohadronic scenario with $p\gamma$ interactions. No gamma-ray emission was found around the time of the neutrino alert.

It was found that a photohadronic model is compatible with the behaviour of the source during BIN-B, though another emission component is likely needed to explain the gamma-ray emission during BIN-A. The gamma-ray emission during BIN-B was also coincident with the highest energy photon recorded by the LAT from the source (E = 155 GeV). Using this spectrum in the photohadronic model, and taking into account the IceCube sensitivity at the time, a minimum detection time of $\sim$ 2.5-days was required to get a couple of neutrino events, making the detection of an excess of neutrino events above the atmospheric background possible.

The neutrino flux coming from photohadronic interactions around the time of the

IC-201114A alert was estimated using the gamma-ray spectra as detected during the two episodes of emission and assuming that the flux was just below the *Fermi*-LAT sensitivity. In an optimistic scenario, the results predicted a minimum detection time (for a couple of neutrino events with IceCube) between $\sim$ 1-hour with the BIN-B spectrum, and 12-days using a BIN-A like behaviour. Taking into account the previous considerations, the lack of a gamma-ray signal around the time of the IC-201114A alert is compatible with the neutrino emission that would be expected from a photohadronic emission model for 4FGL J0658.6+0636.

In the upcoming years, the next generation of gamma-ray and neutrino observatories, such as CTA and IceCube-Gen2, will be crucial for understanding the possible neutrino gamma-ray connection in blazars and indeed other objects. With the improved IceCube alert system (Blaufuss et al., 2019) an average of 30 alerts per year are expected, which provides an opportunity to continue the quest for astrophysical sources with follow-up multi-wavelength observations. The NToO program for CTA will look for promising source candidates in the VHE gamma-ray sky and possible neutrino alert counterparts. With a large field of view (FoV) and quick telescope re-positioning capabilities ($\sim$ 20 seconds for elevation angles above 30° and less than 90 seconds for any position in the sky), CTA will play an important role in the follow-up program during the upcoming years Satalecka et al. (2019). In Chapter 5, I describe the highlights and results obtained from the last 3 years of work with the NToO program for CTA.

Chapter 5

The Neutrino Target of Opportunity for CTA

The study of transient phenomena has been included in the key science objectives for CTA (CTA Consortium, 2019a), so that CTA will perform follow-up observations when public alerts are issued by other observatories. These alerts will have multi-messenger coverage and will include VHE neutrino events, GRBs, flaring blazars, GW events and UHE cosmic-rays, amongst other events. A total of 5 hours per site, per year, has been allocated to neutrino alert event observations, during the first 10 years of array operations. The telescopes are designed with a wide FoV and a rapid re-positioning system, so that they can re-point to any position in the sky above 30° elevation in about 20 seconds, minimising the response time between receiving the alerts and starting observations.

If sources of the blazar type are responsible of some VHE neutrino alerts, the gamma-ray identification of the neutrino counterparts will be crucial to confirm a hadronic origin. To study this type of transient phenomenon, CTA founded the Neutrino Target of Opportunity (NToO) team, a small research group formed of 5 different institutions: Durham University in the UK, DESY in Germany, Georgia Tech University in the USA, the Taras Shevchenko National University of Kyiv in Ukraine and the Federico II University of Naples in Italy. The goals of the NToO

program for CTA include, among others:

- Investigating CTA's chances of detecting gamma-rays from possible neutrino sources.
- Predicting the potential science reach of the NToO program.
- Deriving optimal follow-up strategies for neutrino alerts.

The NToO program aims to predict CTA's detection probability for possible neutrino hot-spots and alerts issued by the IceCube alert system (Blaufuss et al., 2019), which involved processing $> 100,000$ simulated neutrino hot-spots with the subsequent gamma-ray simulated observations. The large number of simulations required a common effort to compute them, assemble the results and interpret them. The workflow showing the different steps of the process is given in Figure 5.1.

My contribution to this project included the set-up and test of a pipeline for the gamma-ray simulations, computing 1/3 of the gamma-ray simulations using `Ctools`, helping to integrate the results to predict CTA performance, analysing the redshift distribution of the detected sources and the differences between the detected source distributions.

The results obtained from the neutrino simulations were used as an input to calculate the gamma-ray contribution of the possible IceCube detected sources, using the phenomenological model proposed by Ahlers and Halzen (2018) (Section 5.2). A pipeline was developed by the NToO team and set-up to compute the gamma-ray simulations with `Ctools` (Section 5.3).

CTA performance is measured in terms of the calculated detection probability. The results from the simulations were filtered using visibility constraints for CTA-N and CTA-S sites, the combined probability was then calculated and is presented for the different sites. The results are summarised in Section 5.4. The best chances of detection were identified within the parameter space tested, and the main results

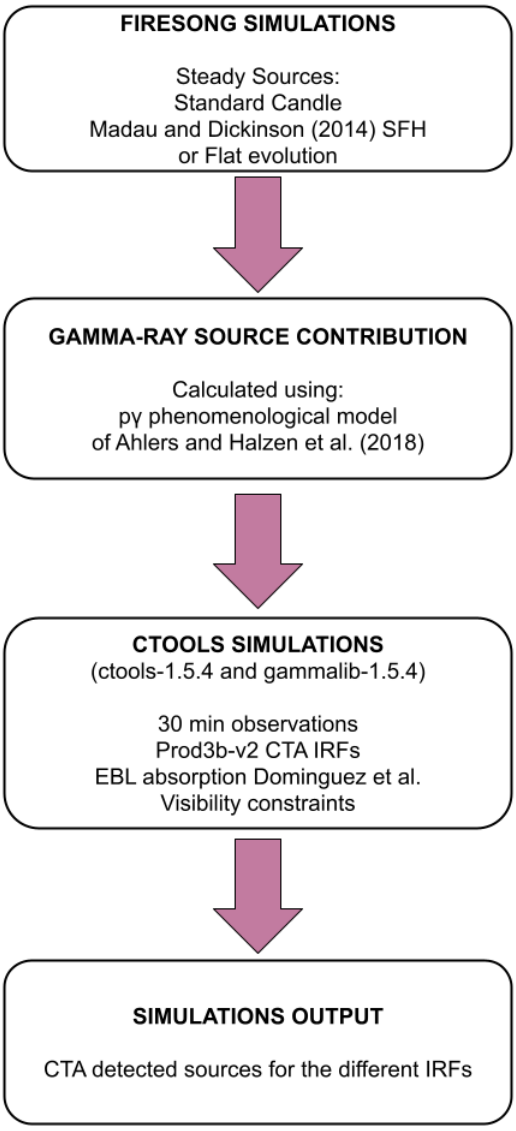

Figure 5.1: Workflow of the NToO program for CTA. Neutrino population sources were simulated using FIRESONG, then the gamma-ray contribution was calculated using the phenomenological model of Ahlers and Halzen (2018) and the CTA response simulated. Preliminary results of the project are summarised in Section 5.4.

are discussed in terms of their impact on the NToO program and the scientific reach of CTA.

5.1 Neutrino simulations

In the first stage of the NToO program, it was necessary to simulate the neutrino source populations that could be responsible for the astrophysical diffuse flux as measured by IceCube. These simulations were performed using FIRESONG (Tung et al., 2021). FIRESONG is a `Python` package written and maintained by IceCube collaboration members, which operates assuming a source evolution model and luminosity constraints as inputs. The simulations used for the NToO project were computed by the Experimental Particle Astrophysics group based at Georgia Tech University, USA, led by Prof. Ignacio Taboada.

Assuming a population of neutrino point-sources, emitting neutrinos isotropically with an intrinsic luminosity L_ν, over a certain redshift range z, confined in a spherical volume given by:

$$V_C = \frac{4\pi}{3} d_C^3 \tag{5.1}$$

where d_C is the comoving distance, defined as

$$d_C = d_H \int_0^z \frac{z'}{\sqrt{\Omega_M (1+z)^3 + \Omega_\Lambda}} \tag{5.2}$$

in which Ω_M is the matter density, Ω_Λ the critical density and d_H is the Hubble distance $d_H = \frac{c}{H_0}$, which in turn depends on the cosmological model adopted. For this work, the ΛCDM cosmological model was employed, alongside the parameters derived from the Planck-2015 data Planck Collaboration (2016): $\Omega_M = 0.308$, $\Omega_\Lambda = 1 - \Omega_M = 0.692$ and $H_0 = 67.8\text{km s}^{-1}\ \text{Mpc}^{-1}$ the value of the Hubble constant.

As discussed in Murase and Waxman (2016) and Kowalski (2015), the neutrino population can be characterised by two main parameters: the source luminosity

(L_ν) and the density (ρ) of the source population. The product of the luminosity per source and the source density over the volume of the observable universe corresponds to the total energy flux:

$$F_\nu = \int_0^{R_H} \rho \frac{L_\nu}{4\pi r^2} d^3r = \frac{1}{4\pi} \int_0^{R_H} L_\nu \rho dr d\Omega \tag{5.3}$$

where r is the distance to each neutrino source, and $R_H \sim 4$ Gpc is the Hubble radius. The differential energy flux can be expressed as:

$$\frac{dF_\nu}{d\Omega} = \xi \frac{L_\nu \rho_o}{4\pi} R_H = E_\nu \frac{dN_\nu}{d\Omega d \ln E_\nu} = E_\nu^2 \frac{dN_\nu}{dE_\nu d\Omega}, \tag{5.4}$$

where ξ is a dimensionless factor that accounts for the source evolution and ρ_o is the local neutrino source density. IceCube's measurement of the all-flavour diffuse neutrino flux (IceCube Collaboration, 2019a):

$$\frac{dN_\nu}{dE_\nu d\Omega} = 3 \times 10^{-18} \frac{\text{GeV}}{\text{cm}^2\text{s}} = 1.4 \times 10^{46} \frac{\text{erg}}{\text{Mpc}^2\text{yr}} \tag{5.5}$$

can be used to set a power density ($\rho_o L_\nu$) of neutrino sources that saturate the astrophysical neutrino flux:

$$\rho_o L_\nu = \frac{4.4 \times 10^{43}}{\xi} \frac{\text{erg}}{\text{Mpc}^3\text{yr}}. \tag{5.6}$$

In the simulations performed, the accumulated neutrino emission from the point-sources that are spread over the universe (up to redshift $z = 4$) has to be high enough to saturate the astrophysical neutrino flux measured by IceCube, while keeping a balance between the local source density and the luminosity parameters.

The local source density scales with the distance as $\rho_o \propto d^{-3}$, and the source flux scales as $\phi \propto L_\nu / d^2$. Thus, the source density for a given neutrino luminosity is expected to scale like $\rho_o \propto L_\nu^{-3/2}$. Each combination in the parameter space of ρ_o vs L_ν can be translated into a population of neutrino sources that can be tested via simulations to check the chances of detection with CTA.

To perform the neutrino simulations, 3 main assumptions have to be made with regards to: 1) the luminosity distribution of the sources $\frac{dN}{dL_\nu}$, 2) the source density evolution $\rho(z)$, and 3) the source spectrum $\phi(E)$.

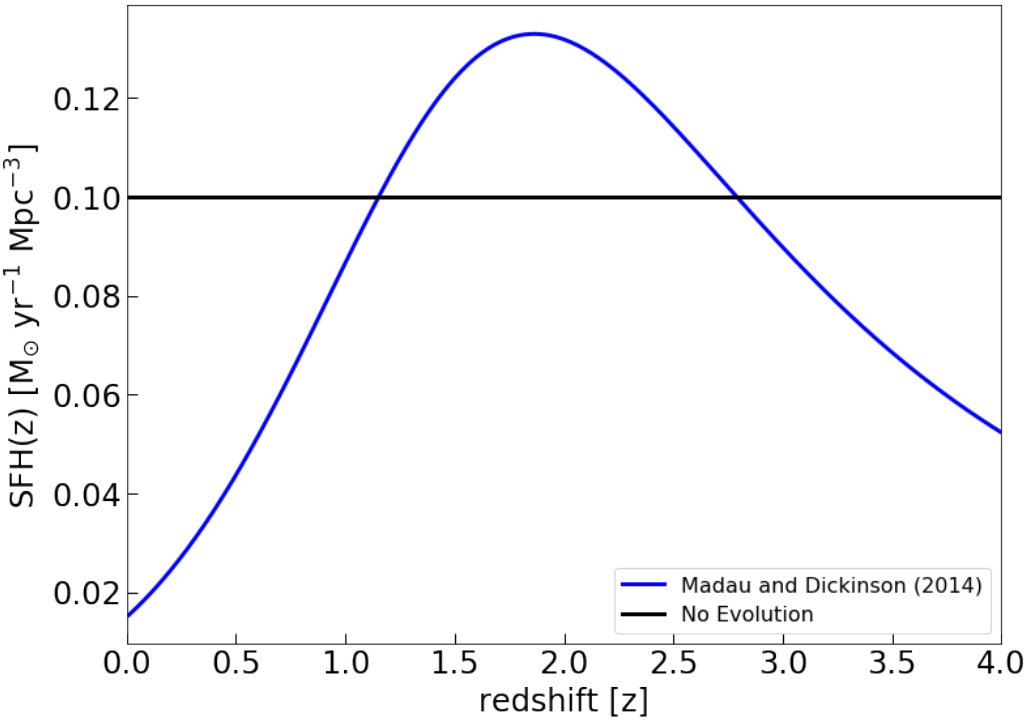

Figure 5.2: Comparison between the SFH model of (Madau and Dickinson, 2014) (blue line) and the flat evolution model (black line) used for the neutrino steady simulations. These two options are used to simulate the neutrino populations with FIRESONG.

1) For the luminosity distribution function, benchmark sources with a single luminosity were assumed; this is a standard candle luminosity condition that is described as a delta function:

$$\frac{dN}{dL_\nu} = \delta(L_\nu - L_0) \tag{5.7}$$

where L_0 will be the density parameter assigned for all the sources in the simulated population.

2) For the source density evolution $\rho(z)$, two different scenarios were considered: one following a flat evolution description, and the second following the SFH evolution model of Madau and Dickinson (2014). These are compared in Figure 5.2.

The total number of sources confined in spherical volume can be calculated as:

$$N_{\text{Total}} = \int_0^{R_{\text{max}}} 4\pi\rho(r)r^2 dr \tag{5.8}$$

where $\rho(r)$ is the density of sources as a function of distance from Earth (r), and $R_{\max}$ is the maximum distance considered.

Making a change of variable, from distance r to redshift z, and taking into account that $d^2V_C/drd\Omega = r^2$, the total number of sources up to a given redshift $z_{\max}$ is given by:

$$N_{\text{Total}} = \int_0^{z_{\max}} 4\pi\rho(z)\frac{d^2V_C}{dzd\Omega}dz \tag{5.9}$$

The first and simplest assumption to model the source density evolution $\rho(z)$, would be to consider a flat evolution model described as a constant value:

$$\rho(z) = 0.10 M_{\odot}\text{year}^{-1}\text{Mpc}^{-3} \tag{5.10}$$

where $M_{\odot}$ is the value of a solar mass. A flat evolution implies that there is no change in the number of sources with redshift, therefore the source density will remain the same.

For the second scenario, the SFH evolution model of Madau and Dickinson (2014) is adopted, which is based on UV and IR data. This evolution model is parameterised as a double power-law in $(1+z)$:

$$\rho(z) = 0.015\frac{(1+z)^{2.7}}{1+[(1+z)/2.9]^{5.6}} M_{\odot}\text{year}^{-1}\text{Mpc}^{-3} \tag{5.11}$$

resulting in a rising curve that peaks at a redshift $1.5 < z < 2$ (see Figure 5.2).

3) Finally, we assume a power-law description for the source spectra:

$$\Phi_{\nu}(E) = A_{\nu}\left(\frac{E}{E_0}\right)^{-\Gamma} \tag{5.12}$$

where $E_0 = 100$ TeV is the pivot energy, A_{ν} the neutrino normalisation constant and $\Gamma = 2.19$ the power-index used. The value for the spectral index is adopted from the IceCube 8-year search for steady point-like sources (IceCube Collaboration, 2019a), in which the best fit parameterisation for the diffuse astrophysical neutrino flux was given by a power-law function with a spectral index of 2.19 ± 0.10 and a flux normalisation, at 100 TeV, of $1.01^{+0.26}_{-0.23} \times 10^{-18}$ GeV^{-1} cm^{-2} s^{-1}:

$$\frac{d\Phi_{\nu_\mu+\bar{\nu}_\mu}}{dE} = (1.01^{+0.26}_{-0.23})\left(\frac{E}{100\text{TeV}}\right)^{-2.19\pm0.10} \times 10^{-18}\text{GeV}^{-1}\text{cm}^{-2}\text{s}^{-1} \tag{5.13}$$

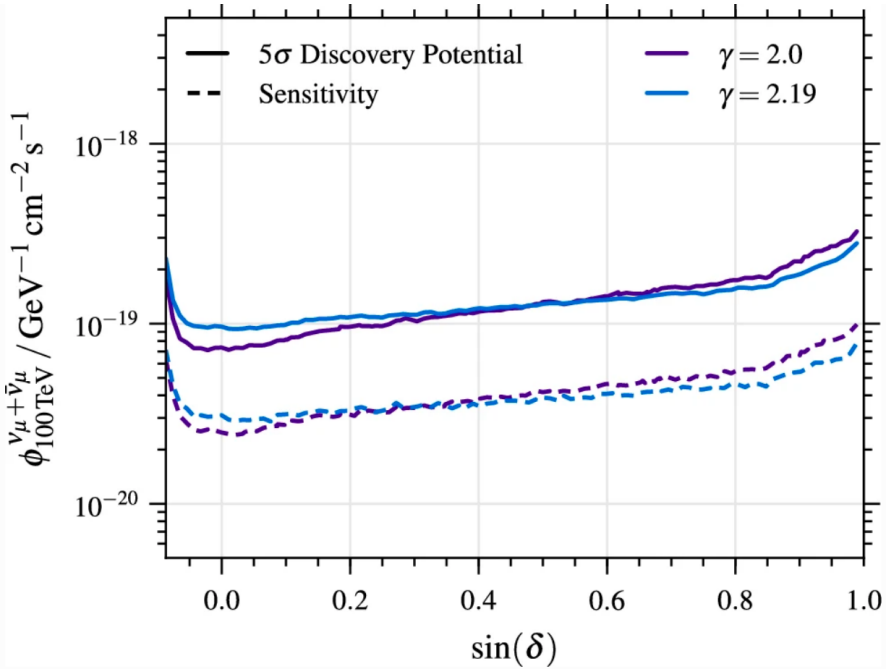

Figure 5.3: Discovery potential and sensitivity on the flux normalisation at 100 TeV as a function of $\sin(\delta)$ for a power-law spectrum of $\Gamma = 2.19$ (blue) and $\Gamma = 2.0$ (purple). Image credits: IceCube collaboration; taken from (IceCube Collaboration, 2019a).

Due to its location, the effective area and differences in the background characteristics IceCube is more sensitive to sources located in the northern hemisphere. IceCube's discovery potential is defined as the minimum flux required to have a 50% probability to claim a discovery of a point-source with a $E^{-\Gamma}$ neutrino spectrum with a CL equivalent to 5σ (IceCube Collaboration, 2019a). The discovery potential of IceCube for a power-law neutrino spectrum of $\Gamma = 2.19$ and $\Gamma = 2.0$ is shown in Figure 5.3. The IceCube sensitivity, defined as the median expected 90% CL upper limit on the flux normalisation, is also shown in Figure 5.3.

5.1.1 Parameter space tested

The source populations were simulated with luminosities that lead to between 10% and 90% of probabilities of having at least one source exceeding IceCube discovery potential. Figure 5.4 shows a representation of the parameter space explored, in which a colour scale shows the probability of detecting at least one hot-spot

exceeding the IceCube 5σ discovery potential at the corresponding combination of density and luminosity. The FIRESONG simulations scanned a wide sector in the parameter space, up to 6 orders of magnitude in the local density parameter: $10^{-12} < \rho_o < 10^{-6}$ Mpc^{-3} for the flat evolution scenario and $10^{-12} < \rho_o < 10^{-5}$ Mpc^{-3} for the SFH evolution scenario. The luminosity range covered over 9 orders of magnitude: 1.78×10^{49} to 3.16×10^{56} erg/year for the flat evolution scenario, and 5.62×10^{47} to 5.62×10^{56} erg/year for the SFH evolution scenario. The luminosity range lies between over-saturating the all-sky neutrino flux by one or two orders of magnitude and under-saturating it by one order of magnitude.

The output from the FIRESONG simulations is a list of sources exceeding IceCube's discovery potential that were catalogued as hot-spots. The list of hot-spots include for each of the sources the information about redshift (z), declination (δ), and the value of the neutrino flux normalisation constant (A_ν) in GeV cm^{-2} s^{-1} units as measured at Earth. The simulations were calculated in a redshift range up to $z = 4.0$.

In Figure 5.5, the neutrino normalisation constant (A_ν) and the redshift corresponding to simulated hot-spots are presented in a couple of plots, depending whether the sources were simulated with: (a) the SFH evolution model of Madau and Dickinson (2014), or (b) the flat evolution model. Each point on the plots represents a neutrino source with a possible gamma-ray counterpart that could be detected by CTA. The hot-spots found at different local source densities (ρ_o) are shown with different colours. For each density, only the population with the highest source luminosity is plotted. The detected hot-spots amongst the highest source densities are biased towards lower redshifts. This is a pre-selection effect given by IceCube, which is exemplified in Figure 5.5. In both of the plots shown, a redshift limit in the source density distributions can be observed: for $\rho_o = 10^{-10}$ Mpc^{-3} all the hot-spots are below redshift $z = 2.0$, for $\rho_o = 10^{-9}$ Mpc^{-3} the redshift is below $z = 1.0$, and for higher densities ($\rho_o > 10^{-8}$ Mpc^{-3}), all the hot-spots simulated with FIRESONG are below $z = 0.5$. For the simulated populations with

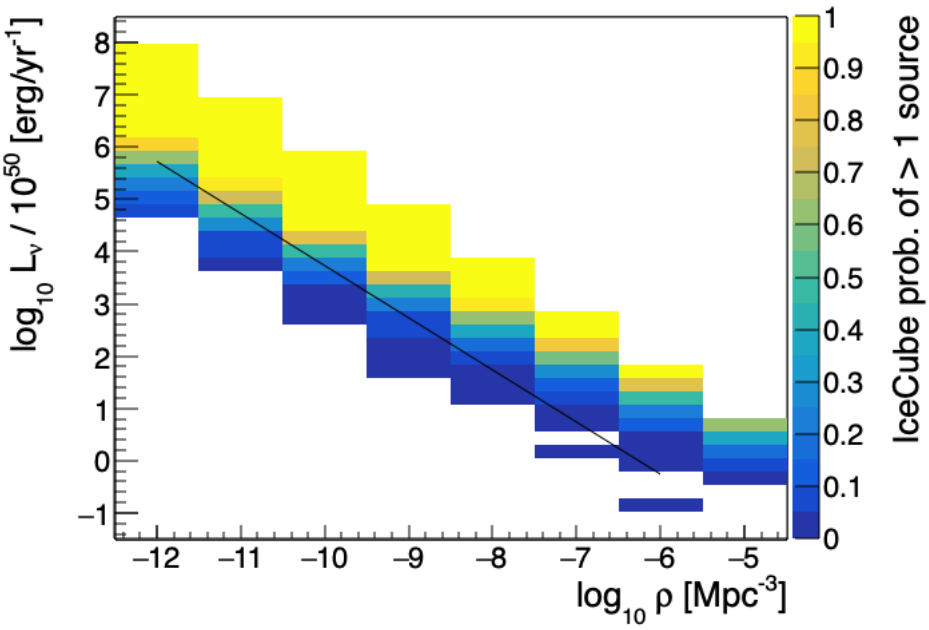

(a) SFH evolution model of (Madau and Dickinson, 2014)

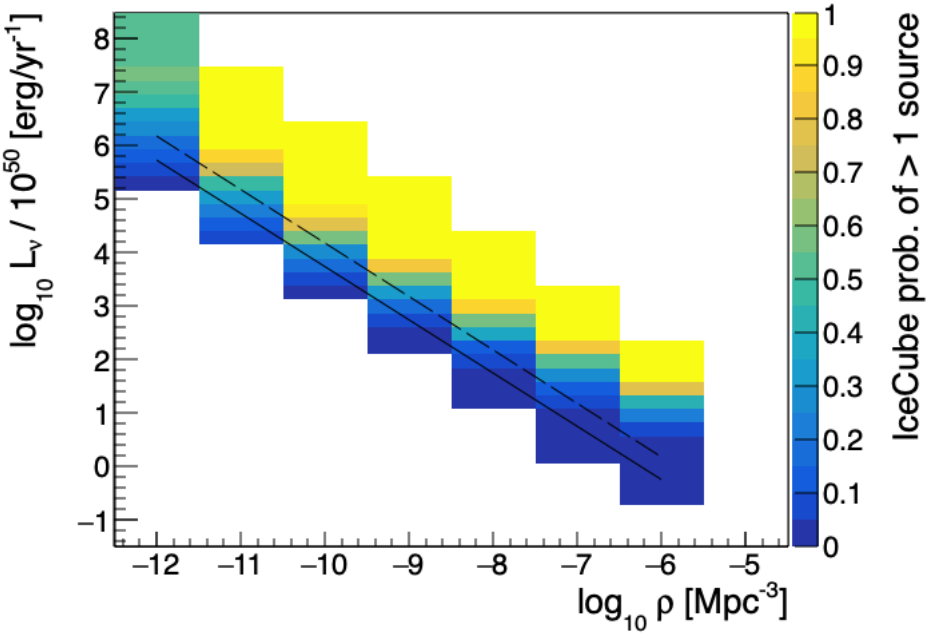

(b) Flat evolution

Figure 5.4: Discovery potential of the simulated neutrino steady sources using: (a) SFH model of Madau and Dickinson (2014) and (b) the flat evolution model specified on section 5.1. Both plots were generated by the FIRESONG Team (Tung et al., 2021). The parameter space explored (local source density (ρ_o) vs source luminosity (L_ν)) follows a line marking the saturation point of the all-sky IceCube neutrino astrophysical flux (black line). The colour scale shows the probability of finding at least one hot-spot in IceCube. Blank spaces in the parameter space represent not tested combinations with FIRESONG.

$\rho_o = 10^{-12}$ and $\rho_o = 10^{-11}$ Mpc^{-3}, the hot-spots expand over the whole redshift range considered, up to $z = 4.0$.

The simulated populations have to saturate the IceCube neutrino diffuse flux, therefore populations with high local source densities ($\rho_o \geq 10^{-9}$ Mpc^{-3}) will contain a large number of simulated sources, although with a lower luminosity range ($L_\nu \leq 10^{55}$ erg/year). Hence, the hot-spots detected by IceCube amongst the high source density range correspond only to the nearest sources ($z < 1$) that are able to exceed IceCube discovery potential.

As we move towards lower source densities, the simulated neutrino sources can reach higher luminosities and therefore be detected as hot-spots across larger distances, which is the case of the simulated populations with $\rho_o = 10^{-11}$, 10^{-12} Mpc^{-3}. All the identified hot-spots have a neutrino flux described by a normalisation constant above $A_\nu \sim 10^{-8}$ GeV cm^{-2} s^{-1}.

5.2 Neutrino/gamma-ray model

The first approach considered by the NToO was to test the hypothesis of a large population of faint, blazar-like, steady point-sources. These sources were assumed to produce neutrinos and gamma-rays through $p\gamma$ interactions, and simulated over a parameter space (ρ_o vs L_ν) in which the accumulated flux from the sources would saturate the IceCube diffuse astrophysical neutrino flux. All the possible neutrino hot-spots generated with FIRESONG were treated as point-sources and have associated a gamma-ray flux.

For calculating the corresponding gamma-ray flux of the neutrino simulated source populations from Section 5.1, the model proposed in Ahlers and Halzen (2018) was adopted. Within this model, it is assumed that neutrinos and gamma-rays are produced by $p\gamma$ interactions when HE accelerated protons reach the photon fields associated with the source. A HE neutrino flux is produced from the subsequent

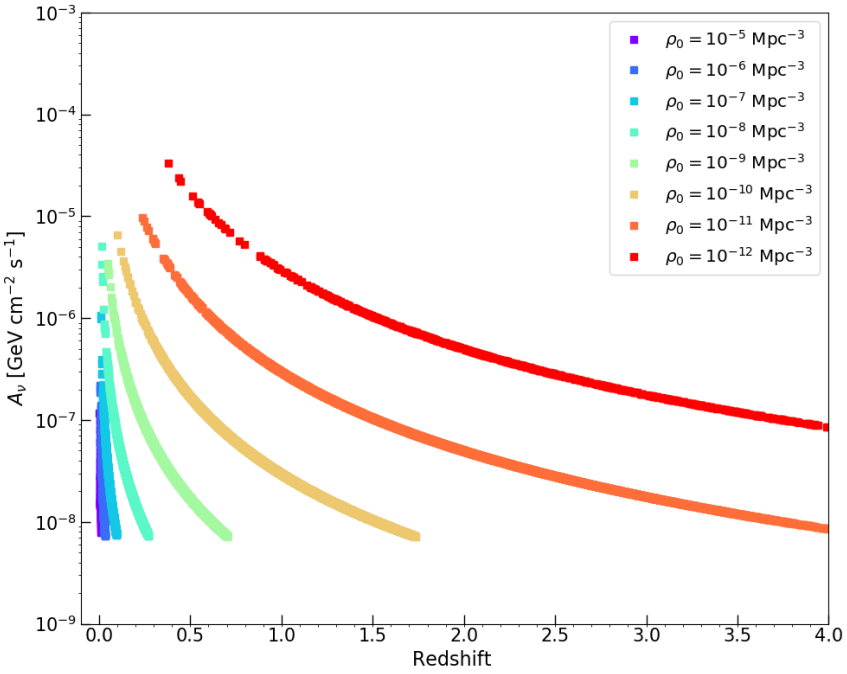

(a) SFH source evolution model of Madau and Dickinson

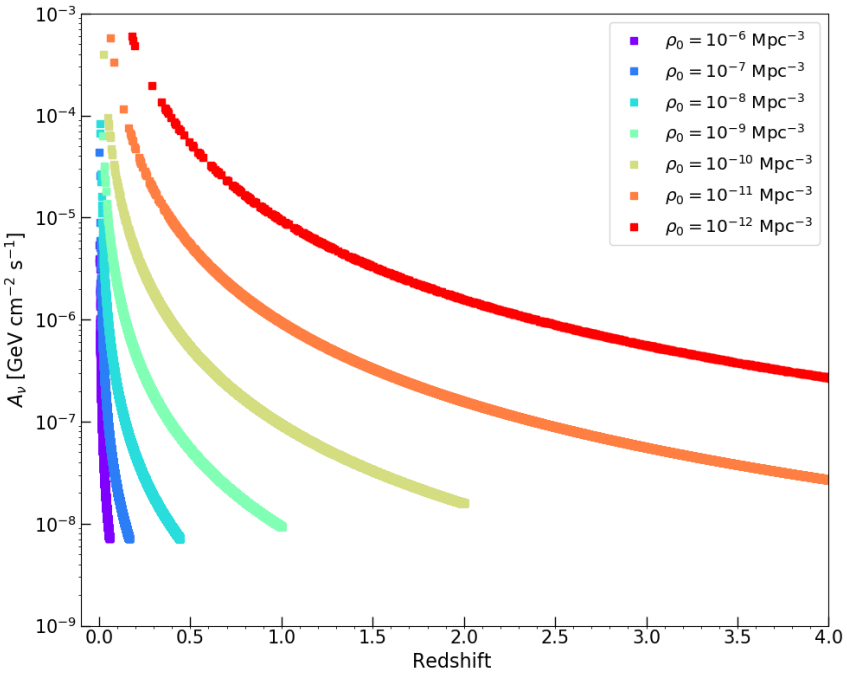

(b) Flat source evolution model

Figure 5.5: Distribution of the highest luminosity hot-spots simulated with FIRESONG for each neutrino local source density with: a) the SFH source evolution model of Madau and Dickinson (2014) and b) a flat source evolution model. The neutrino normalisation constant A_ν is plotted as a function of redshift. Any simulated point-source is considered a hot-spot if exceeds the IceCube discovery potential for a power-law spectrum of $\Gamma = 2.19$.

decay of charged pions ($\pi^{\pm}$), while, a gamma-ray flux is obtained from the decay of neutral pions ($\pi^0 \rightarrow \gamma + \gamma$).

The intrinsic emission spectrum of gamma-rays and neutrinos produced from the pion decay is directly related to the proton spectrum (after accounting for the different normalisations and energy scales) due to its common origin. The assumed proton spectrum is described by a power-law, i.e. $\propto E_p^{-\Gamma}$, where the spectral index Γ is inherited to the gamma-ray and neutrino spectrum. The spectral index $\Gamma = 2.19$ is adopted from the published IceCube 8-year analysis (IceCube Collaboration, 2019a). The neutrino flux arriving at Earth will follow the description presented in Eq. 5.12.

The neutrino production rate Q_{ν_α} is related to the charged pion production rate $Q_{\pi^{\pm}}$ as Ahlers and Halzen (2018):

$$\sum_{\alpha} E_\nu Q_{\nu_\alpha}(E_\nu) \approx 3[E_\pi Q_{\pi^{\pm}}(E_\pi)]_{E_\pi \approx 4E_\nu} \tag{5.14}$$

Similarly, the photo-pion gamma-ray production rate is related to the neutral pion production rate as:

$$E_\gamma Q_\gamma(E_\gamma) \approx 2[E_\pi Q_{\pi^0}(E_\pi)]_{E_\pi \approx 2E_\gamma} \tag{5.15}$$

the production rates of neutrinos and gamma-rays depend only on the ratio between charged (π^+, π^-) and neutral pions (π^0) produced in the $p\gamma$ process. This ratio can be expressed as:

$$K_\pi = \frac{N_{\pi^{\pm}}}{N_{\pi^0}} \tag{5.16}$$

where $N_{\pi^{\pm}}$ is the number of charged pions, and N_{π^0} the number of neutral pions produced.

According to Ahlers and Halzen (2018), $K_\pi \sim 1$ for $p\gamma$ interactions. With this approximation, and combining the equations of the photo-pion gamma-rays and neutrino production rates, a relation between these two rates can be written as:

$$\frac{1}{3}\sum_{\alpha} E_\nu^2 A_{\nu_\alpha}(E_\nu) = \frac{K_\pi}{4} E_\gamma^2 A_\gamma(E_\gamma) \tag{5.17}$$

where the factor of 1/4 on the right side of the equation accounts for the fact that two gamma-rays are produced in the neutral pion decay and $E_\gamma = 2E_\nu$.

Equation 5.17 can be used to relate the neutrino and gamma-ray normalisation constants, without making any reference to the acceleration mechanism of the particles. It is a phenomenological approach that enables the calculation of a gamma-ray flux of the type $F_\gamma(E_\gamma) = A_\gamma(E_\gamma/E_0)^{-\Gamma}e^{-\tau(E_\gamma,z)}$, where A_γ can be computed from the neutrino normalisation A_{ν_α}, given by the output from the FIRESONG neutrino simulations. The spectral index Γ adopted for the gamma-ray flux is considered to be identical to the neutrino spectral index assumed for the FIRESONG neutrino simulations (2.19). The EBL absorption effect is taken into account using the model of Domínguez et al. (2011) (see Section 2.5 for more details). Other effects, such as internal absorption from the photon field or gamma-ray cascading within the source, are not considered in this model.

The photohadronic model described in Chapter 2 and applied to blazars in Chapter 3 and 4, also refers to a hadronic scenario with $p\gamma$ interactions, however it is proposed as an extension of a one-zone SSC model, therefore relying on the leptonic scenario interpretationof the lower energy emission and based on the prominent cross-section provided by the Δ^+-resonance approximation. The Δ^+ particle decays into $(p + \pi^0)$ in 2/3 of all cases while it goes to $(n + \pi^+)$ in 1/3 of all cases due to iso-spin conservation (Longair, 2011), therefore the pion production ratio given by the Δ^+-resonance results in $K_\pi \sim 1/2$. The model of Ahlers and Halzen (2018) considers not only the resonant channel, but also additional contributions from non-resonant pion production channels, which finally gives a ratio of $K_\pi \sim 1$. The Δ^+-resonance is considered as a first approximation due to its low threshold energy and its prominent cross-section (see Section 2.7.2), which is why is used in phenomenological and semi-analytical models. Multi-pion production becomes the dominant production channel at higher energies (photons of $\epsilon' > 1.5$ GeV in the proton's rest frame), where the total photohadronic cross-section becomes roughly constant at $\sim 125\mu$barn and the K_π ratio becomes ~ 1 (Rachen, 1996).

The Δ^+-resonance model was testing the possibility of a dominant hadronic component at VHE, while the more optimistic gamma-ray flux calculation for the NToO gamma-ray simulations was adopted as the best scenario of the possible incoming gamma-ray flux from a neutrino source. In the next section the specifics related to gamma-ray simulations are described in detail.

5.3 Gamma-ray simulations

From each simulated neutrino population with FIRESONG, a list of hot-spots was generated and treated as possible gamma-ray counterparts to simulate observations with CTA. The CTA response and detection probability for each simulated source were calculated using `Gammalib` and `Ctools` software.

`Gammalib` (Knödlseder et al., 2016) is a versatile computer framework developed for the analysis of gamma-ray data. It consists of a `C++` library and a `Python` module which can be used with a variety of gamma-ray telescopes. `Gammalib` is available to perform analysis of data from *CGRO/COMPTEL*, *Fermi*-LAT, H.E.S.S., MAGIC, VERITAS, and CTA simulations.

`Ctools` (Knödlseder et al., 2016) is a software package that works on top of the `Gammalib` framework; it contains a set of executable tools, allowing interactive data analysis through a `Python` notebook or command-line. The `Ctools` installation comes with a calibration database that contains the Instrument Response Functions (IRFs) developed for the CTA observatory.

5.3.1 CTA Omega configuration IRFs

The IRFs developed by the CTA collaboration were derived from detailed Monte-Carlo simulations, starting from the development of air showers in the atmosphere and going through the telescope optics and camera electronics (CTA Consortium, 2019b). The IRFs simulate the response of a particular configuration to the incident

Site	Longitude [deg]	Latitude [deg]	Altitude [m]	LSTs	MSTs	SSTs	B_x [μT]	B_z [μT]
La Palma (CTA-N)	17.89W	28.76N	2180	4	15	-	30.8	23.2
Paranal (CTA-S)	70.30W	24.07S	2150	4	25	70	21.4	-8.9

Table 5.1: Summary info for CTA-N site at La Palma in the canary islands, and CTA-S site at Paranal, Chile. The geographical coordinates are specified for each site in the first 3 columns. The number of telescopes within the Omega configuration array for each site are also specified. The horizontal and vertical component of the Earth's magnetic field are given in the last 2 columns by B_x and in the 9th column by B_z (Maier, 2019).

gamma-ray photons, depending on the effective area (A_{eff}), the PSF and the energy dispersion (E_{disp}), which in turn depend on the observation angle (zenith/azimuth) and the energy of the incident gamma-ray photons. The instrument response is also dependent on the telescopes' design and the array layout. For the NToO gamma-ray simulations, 30-min observations were assumed, alongside a nominal telescope pointing scheme, with all telescopes pointing parallel to each other.

The IRFs version used in this work are the `prod3b-v2` for the Omega configuration array (CTA Consortium, 2016). This is the full-scope configuration that is the desired ultimate configuration of CTA. The Omega IRF set was developed for both CTA sites: at Paranal, Chile (Southern site, CTA-S) and La Palma, Spain (northern site, CTA-N). The Omega configuration array layouts for the northern and southern hemispheres are shown in Figure 5.6. CTA-N consists of 4 LSTs and 15 MSTs located over a 0.6 km^2 area on the island of La Palma, Spain. For CTA-S, an array of 4 LSTs, 25 MSTs and 70 SSTs is assumed in a 4 km^2 array at Paranal observatory in Chile. Table 5.1 summarises information about the two sites and further information about the capabilities of the CTA observatory can be found in Chapter 1.

The Omega IRF set contains the information on the effective area for three telescope pointing zenith angles, 20°, 40° and 60°. The zenith angle affects the lower energy threshold at which CTA becomes sensitive to the gamma-ray sources. The gamma-ray absorption in the atmosphere increases with the zenith angle, so that the energy threshold increases. The energy thresholds given by the IRF specifica-

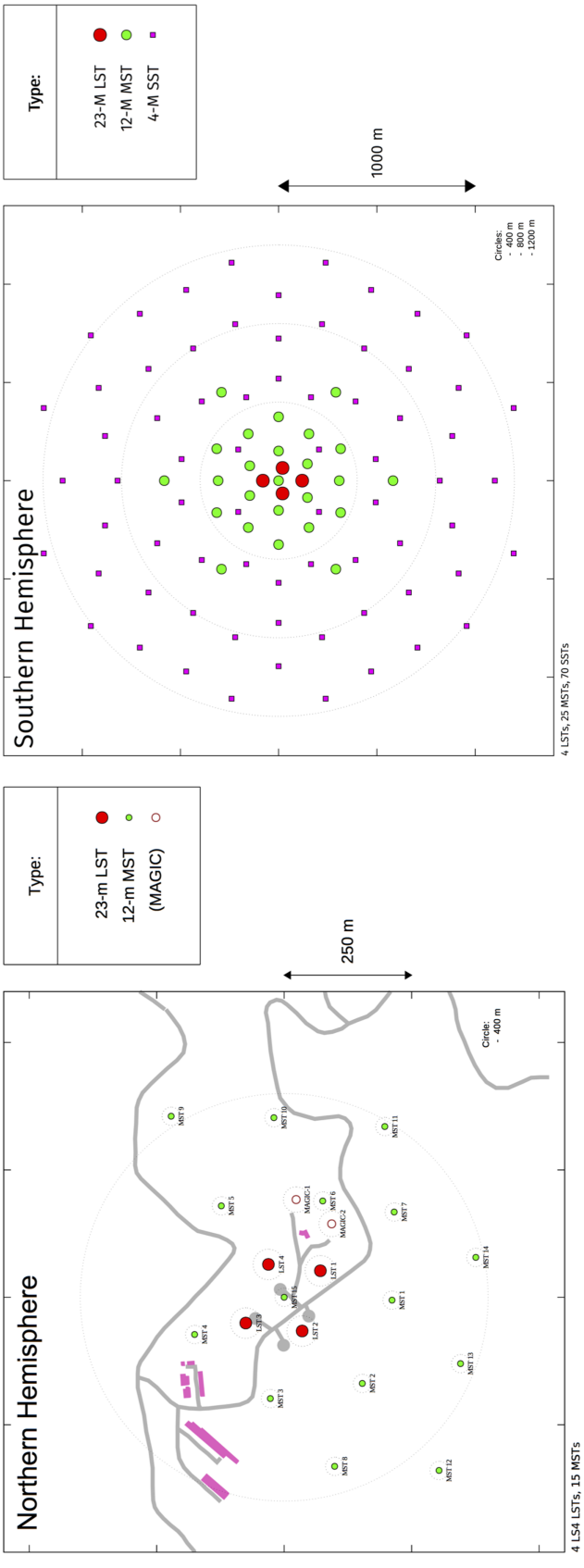

Figure 5.6: Omega configuration array layouts for both CTA sites. The northern hemisphere site is projected to have 4 LSTs and 15 MSTs located in a 0.6 km^2 area in the island of La Palma, Spain. For the southern hemisphere site, an array of 4 LSTs, 25 MSTs and 70 SSTs are expected in a 4 km^2 array at Paranal observatory in Chile. Image credits: CTA collaboration, CTA Consortium (2016).

tions start at 30 GeV for 20° zenith angle, 40 GeV for 40° zenith angle and 110 GeV for 60° zenith angle.

The effective areas (A_{eff}) as a function of energy at the different zenith angle options are plotted in Figure 5.8. The value of A_{eff} depends on the photon energy and the incident direction, the observational conditions, such as the pointing direction of the telescopes (zenith/azimuth angle), and the level of Night Sky Background (NSB). At low zenith angles, the effective area is maximised and the differential sensitivity optimised, while the energy threshold for observations is lower. These are the optimal conditions for observations.

The `prod3b-v2` IRFs also allow for three options in the azimuth pointing direction with regards to the Earth's magnetic field lines: North pointing (parallel), South pointing (anti-parallel) and the average value over the whole azimuth range. These options produce performance differences when pointing the telescopes at different zenith angles and azimuth directions (CTA Consortium, 2017). The most notable difference between the two sites is the strength and direction of the geomagnetic field, which has direct implications for the instrument sensitivity, angular and energy resolution, due to its influence on the air shower development as described below. The magnetic field strength as a function of the azimuth angle direction (ϕ) is shown in Figure 5.7 for both sites.

The `prod3b-v2` IRFs also contain a background model template based on the estimated event rate from cosmic-ray protons and electron/positron particles. Background rates are calculated as average values in rings around the pointing directions, where simulated proton and electron events are generated. The background model is affected by the position in the FoV and the measured energy. Further information about the construction of the background models and the assumed cosmic-ray spectra can be found in CTA Consortium (2013) and Maier (2019).

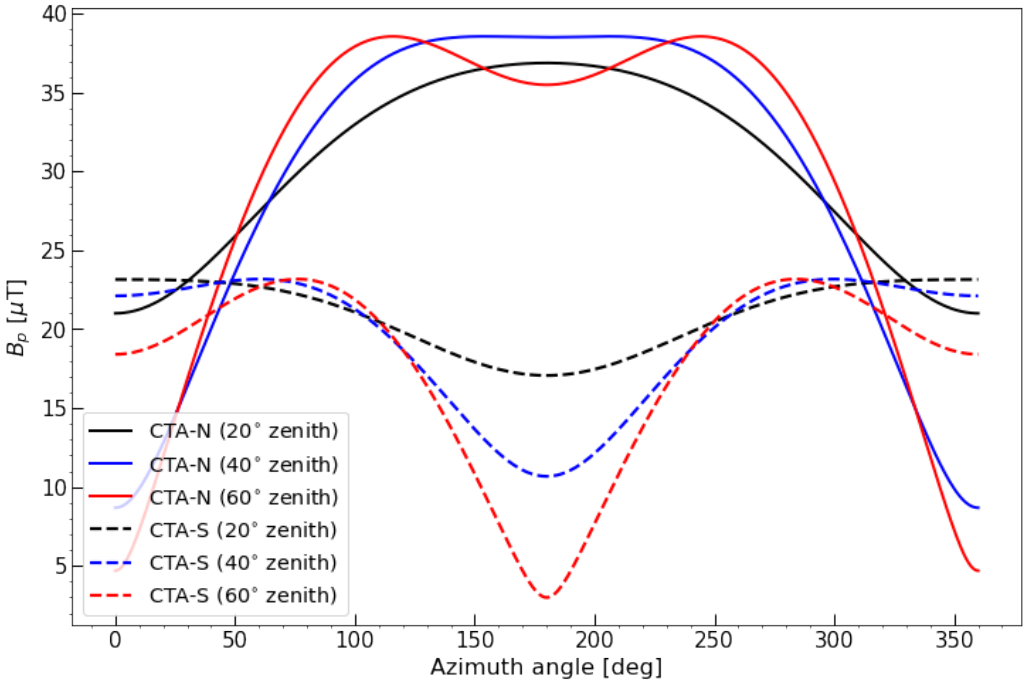

Figure 5.7: CTA magnetic field strength dependence with respect the azimuth angle direction (ϕ) at both sites. For CTA-N (CTA-S) the three different zenith angle options are plotted as solid (dotted) lines. At 20°/40°/60° zenith angle the curves are plotted in black/blue/red colours respectively.

5.3.2 Ctools simulations

A pipeline was developed to simulate the CTA response to the corresponding gamma-ray flux from all the simulated neutrino hot-spots and identify the possible detections using `Ctools-1.6.2` version software, and the IRFs for 30-min observations with the Omega configuration array.

Each identified neutrino hot-spot possesses a defined redshift (z), a spectrum normalisation constant (A_ν) and a declination coordinate (δ). For the gamma-ray simulations, the right ascension for each hot-spot was assigned randomly and the corresponding gamma-ray spectrum was derived assuming the model of Ahlers and Halzen (2018). The gamma-ray simulations followed a series of steps as described in Figure 5.9 to get the final list of detected sources.

For each hot-spot tested, an input XML model file was created, in which the

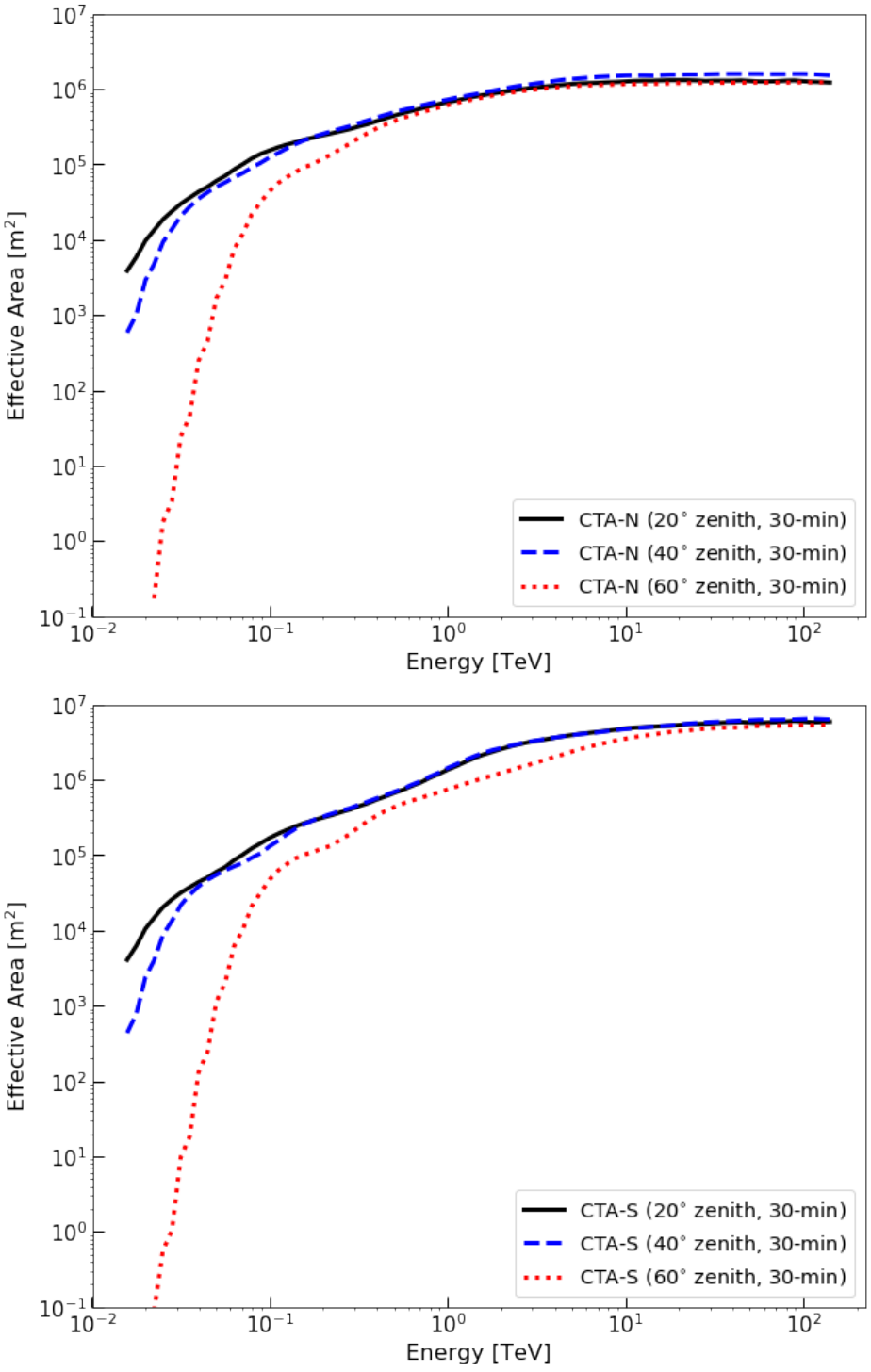

Figure 5.8: Effective area for the Omega configuration array as a function of energy for: (top) CTA-N site and (bottom) CTA-S site. The black (blue dashed, red dotted) curves show the effective area for 20° (40°, 60°) zenith angle and 30-min observations.

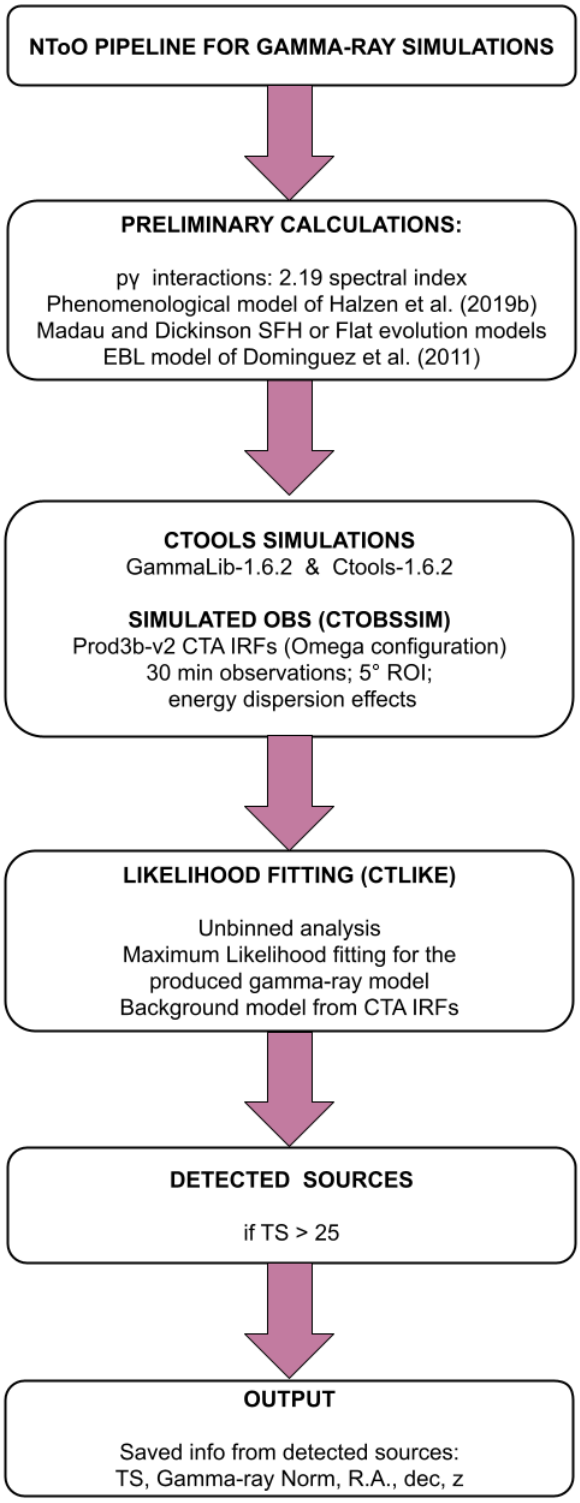

Figure 5.9: Simulation steps for the NToO pipeline. Each neutrino hot-spot was tested under the different `prod3b-v2` IRF configurations. A wider description of the simulation steps is presented in Section 5.3, including the Omega IRF characteristics and the `Ctools` algorithms used.

spatial and spectral models are specified. `Ctools` uses this information to generate a simulated source. A point-source type is adopted for the spatial model, while a power-law with a fixed spectral index and EBL absorption effect is considered for the spectral model:

$$\frac{dN_\gamma}{dE_\gamma} = A_\gamma \left(\frac{E_\gamma}{E_0}\right)^{-\Gamma} e^{-\tau_{\gamma\gamma}(E_\gamma, z)} \tag{5.18}$$

where the value for the spectral index $\Gamma = 2.19$ (see Section 5.2). A_γ is the normalisation constant estimated using the phenomenological model of Ahlers and Halzen (2018). The attenuation effect of the high energy gamma-ray flux by pair production process with the EBL photons is accounted for by the factor of $e^{-\tau_{\gamma\gamma}(E_\gamma, z)}$, where $\tau_{\gamma\gamma}$ is the EBL optical depth which depends on the gamma-ray photon energy (E_γ) and redshift (z) of the simulated source. The EBL model of Domínguez et al. (2011) (see Section 5.2) is employed.

An example of the intrinsic and observed gamma-ray energy spectra for a couple of simulated sources is shown in Figure 5.10. The differential sensitivities for 30-min exposure time at 20° zenith angle for both CTA-N and CTA-S are also given for comparison. Depending on the source conditions (such as redshift and gamma-ray flux normalisation) when simulating 30-min of observations with CTA, the observed attenuated spectrum could lead to a positive detection with one or more configurations given in the `prod3b-v2` IRFs.

The steady source simulations were divided into 2 categories, depending on whether neutrino populations were computed following the evolution model of Madau and Dickinson (2014) or the flat evolution model. The maximum redshift considered for both cases was $z = 4.0$, and the energy range for the simulated observations was from 20 GeV and to 200 TeV.

After setting the input model, a photon event list was simulated with the `ctobsssim` tool. For the different `prod3b-v2` IRFs within the Omega configuration, observations were simulated for a RoI of 5.0° centred at the hot-spot coordinates; the declination coordinate was taken from the neutrino simulations output, while the

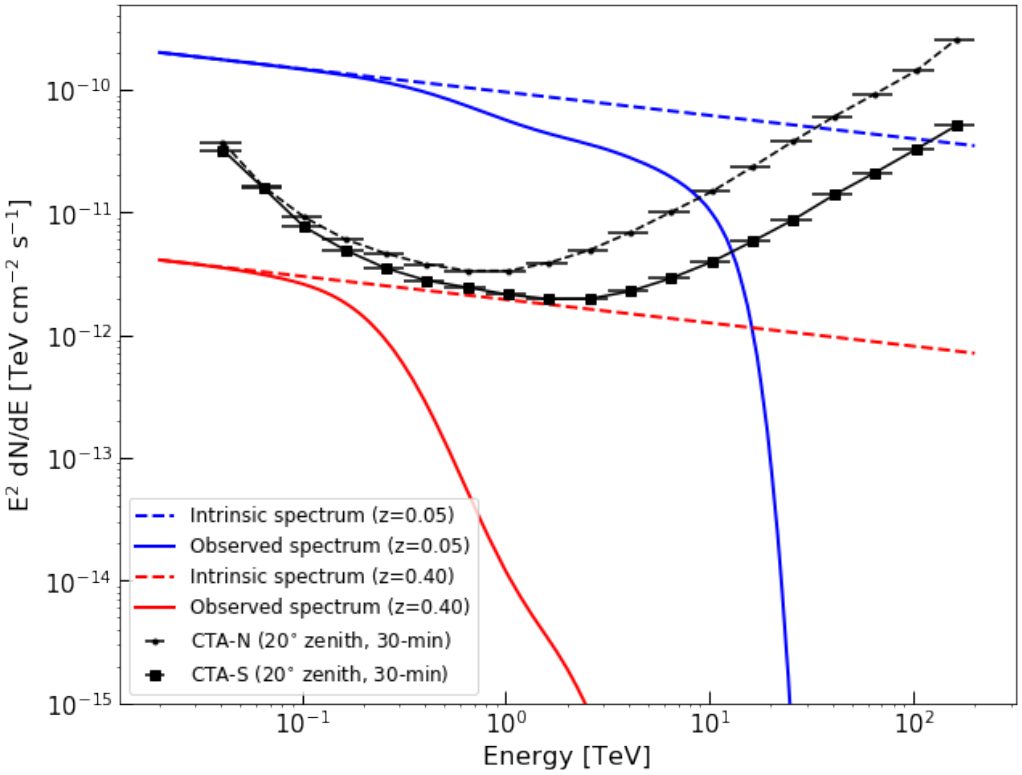

Figure 5.10: Energy spectrum of a detected (blue) and an undetected (red) simulated source. The intrinsic spectrum is shown as a dotted line while the attenuated spectrum calculated with the EBL model of Domínguez et al. (2011) is shown as solid line for each source. The CTA differential sensitivity for 30-min observations at 20° zenith for both sites is shown for comparison.

R.A. was assigned randomly. The energy dispersion effect is fully implemented within `Ctools`, and considered in the simulated observations by activating the `edisp` parameter option in `ctobsssim`. This effect accounts for the difference between the reconstructed and true energies of the simulated gamma-ray events and is particularly significant at low energies.

Having the simulated photon events, and the gamma-ray model, a maximum likelihood fit was performed using the `ctlike` tool in an unbinned mode. This tool estimates the model parameters that maximise the likelihood function $L(M)$ for a given model M.

Maximising the likelihood function $L(M)$ is equivalent to minimising the negative of the log-likelihood function $-\ln L(M)$. For unbinned data, the Poisson formula

is applied (Knödlseder et al., 2016):

$$-\ln L(M) = E(M) - \sum_i \ln P(p'_i, E'_i, t'_i|M) \tag{5.19}$$

where $P(p'_i, E'_i, t'_i|M)$ is the probability density that, given the model M, an event with instrument direction p'_i, measured energy E'_i and trigger time t'_i occurs. The the sum is taken over all events i, and $E(M)$ is the total number of events that are predicted to occur.

`Ctools` uses an iterative Levenberg-Marquardt algorithm for maximum likelihood estimation (Knödlseder et al., 2016). The algorithm stops when the log-likelihood difference between consecutive iterations is less than a small value, typically 5×10^{-3}, and the process converges to the best fit parameter values.

The simulated observation data could be explained by a combination of a point-like source with a power-law spectrum plus a background model ($M_S + M_B$), or alternatively the background model only (M_B). Under the hypothesis that the model $M_S + M_B$ will provide a satisfactory fit of the data, the detection significance of the source model is estimated using the so called TS (Knödlseder et al., 2016):

$$\mathrm{TS} = 2(\ln L(M_S + M_B) - \ln L(M_B)) \tag{5.20}$$

where $\ln L(M_S + M_B)$ is the log-likelihood function considering the source and background model components, while $\ln L(M_B)$ is the log-likelihood function for the background model only. The background model (M_B) used was derived from the cosmic-ray spectra of proton and electron/positron particles according to measurements from cosmic-ray instruments (CTA Consortium, 2013; Maier, 2019).

The TS function follows asymptotically a χ^2_n distribution when the size of the data sample approaches to infinity as a consequence of Wilk's theorem (Wilks, 1938), where n is the number of free parameters in the source model. The TS value can be converted into the detection significance σ; for simplicity, we use the approximation that this is given by $\sqrt{TS}$. If the TS is equal or higher than 25 (corresponding to the 5σ significance level), it is regarded as a positive source detection.

The output from the simulations is a list of the detected sources for each of the tested neutrino source populations, containing the source information (TS value, gamma-ray normalisation constant, R.A., dec., redshift) for each IRF configuration. The results obtained for the different IRFs were used to calculate CTA performance which are presented in the next section.

5.4 CTA performance

The results from the gamma-ray simulations were divided into two sections, depending on whether the neutrino source populations were simulated using the evolution model of Madau and Dickinson (2014) (Section 5.4.1) or followed a flat evolution model (Section 5.4.2). The main results for both cases are summarised in a series of plots that describe CTA performance for both North and South arrays, while showing the differences in detection probability for each of the Omega IRF configurations tested, and the impact of the magnetic field effect on the observations.

In the first instance, given that the simulated neutrino sources are considered steady, i.e. they have a constant neutrino and γ-ray emission, and assuming the most optimistic case, in which all the simulated hot-spots are visible with CTA, the detection probability for each simulated population is calculated as:

$$P_{\mathrm{CTA}} = \frac{N_{\mathrm{detected}}}{N_{\mathrm{hot\text{-}spots}}} \tag{5.21}$$

where N_{detected} is the number of CTA detected hot-spots obtained from the gamma-ray simulations and $N_{\mathrm{hot\text{-}spots}}$ is the total number of neutrino hot-spots simulated with FIRESONG.

5.4.1 Madau and Dickinson SFH scenario

Figure 5.11 shows the detection probability for CTA-N site assuming 30-min observations and a visibility of 100% of the tested sources. The detection probability is specified in a colour scale that goes from $P_{\mathrm{detection}} = 0$ (blue) to $P_{\mathrm{detection}} = 1$

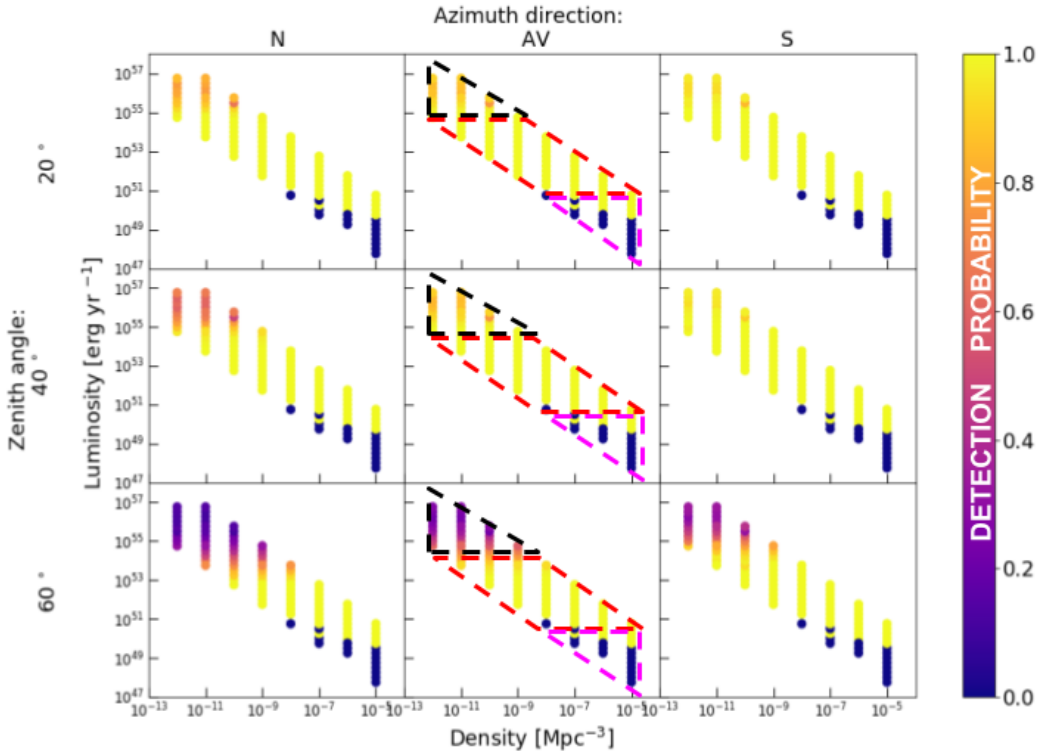

Figure 5.11: CTA-N Omega configuration array performance assuming 30-min observations and the SFH evolution model of Madau and Dickinson (2014). Each point in the plot represents a simulated neutrino population with an associated value for CTA detection probability that goes from $P_{\text{detection}} = 0$ (blue) to $P_{\text{detection}} = 1$ (yellow) in the colour scale. The rows (from top to bottom) correspond to the different zenith angle options: 20°, 40° and 60°. The columns (from left to right) represent the three different magnetic field alignments in the azimuth direction: North (N), Average (AV) and South (S). The blue points with null detection probability on the lower right corner of each subplot represent simulated populations with no hot-spots exceeding IceCube's discovery potential. The behaviour of the zones highlighted by dotted lines is described in Section 5.4.1.

(yellow). The calculated probability for each simulated population tested within the parameter space (ρ_o vs L_ν) is presented as a single coloured point in the plot. The rows from top to bottom show the results for the different zenith pointing angles: 20°, 40° and 60°. The columns (from left to right) represent the three different magnetic field alignments according to the azimuth pointing direction: towards North (N), towards South (S), or Average (AV) over azimuth.

Figure 5.12 shows the corresponding plot for CTA-S and employs the same colour scale and order in the rows (zenith angles) and columns (magnetic field alignments)

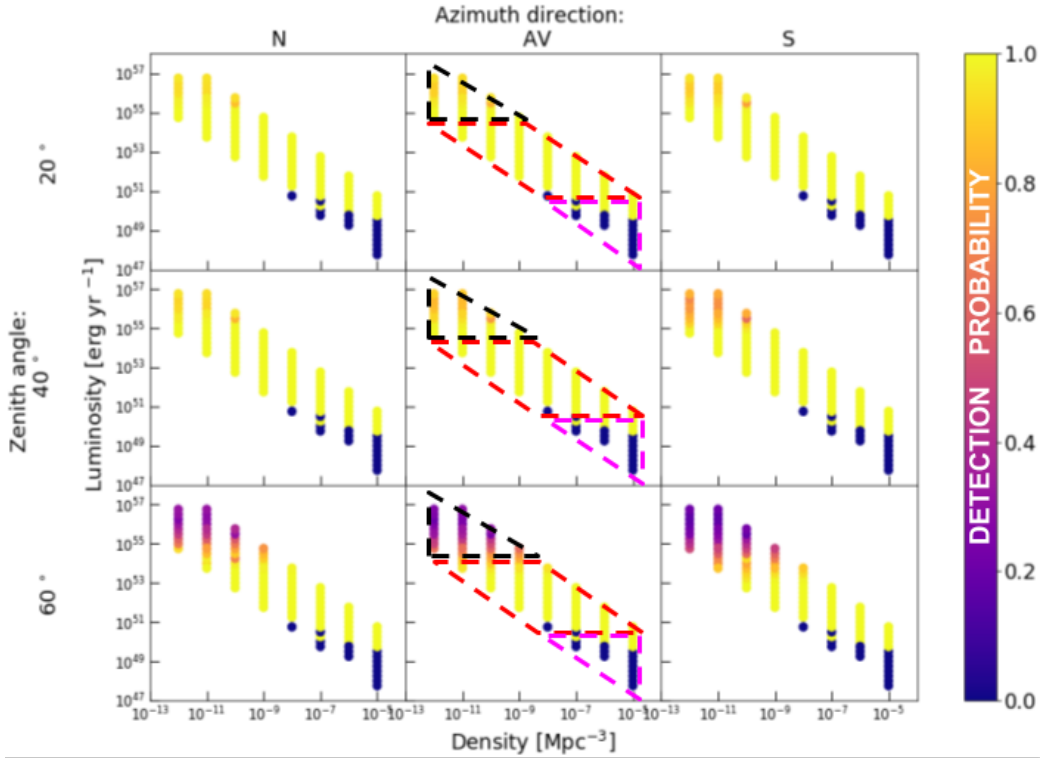

Figure 5.12: CTA-S Omega configuration array performance assuming 30-min observations and the SFH evolution model of Madau and Dickinson (2014). The colour scale and order in the rows (zenith angles) and columns (magnetic field alignments), are the same as in Figure 5.11. See Figure 5.11 for further details.

as CTA-N.

We can observe 3 distinct behaviours in the performance plots for both CTA-N and CTA-S depending on the region of the parameter space tested. These zones are delineated by coloured dotted lines in the central columns of the figures.

- The first zone is highlighted by a pink triangle; the blue points located inside this region (lower right corner for each subplot) indicates a null detection probability. This zone contains the simulated neutrino populations with a combination of high local source densities (10^{-8} Mpc^{-3} $< \rho_o <$ 10^{-5} Mpc^{-3}) and low source luminosities ($L_\nu < 10^{51}$ erg/yr), in which there were no identified hot-spots exceeding IceCube's discovery threshold, therefore a zero chance of detection is associated for both CTA-N and CTA-S arrays.

- The second zone highlighted in Figures 5.11 and 5.12 appears inside a black dotted triangular zone. This region seems to be more sensitive to the differences in the zenith angle observations. The neutrino populations inside this zone are simulated with the lowest local source densities ($\rho_o \leq 10^{-10}$ Mpc^{-3}) but high source luminosities ($L_\nu > 10^{55}$ erg/yr). It is observed that the detection probability for CTA-N (CTA-S) decreases, reaching minimum values of $P_{\text{detection}} \sim 0.85$ (~ 0.9) at 20° zenith angle, $P_{\text{detection}} \sim 0.85$ (~ 0.85) at 40° zenith and $P_{\text{detection}} \sim 0.2$ (~ 0.25) at 60° zenith.

- Finally, the central region of the parameter space is highlighted in a red dotted rhomboid. Inside this zone, all the luminosity/density combinations have a detection probability of ~ 1. For the CTA-N site (Figure 5.11), the high detection zone extends over the simulated populations with densities above 10^{-10} Mpc^{-3} and luminosities between 10^{50} and 10^{54} erg/yr. For CTA-S (Figure 5.12) a similar trend is observed for the same density range and luminosities up to $\sim 5 \times 10^{54}$ erg/yr.

5.4.2 Flat evolution scenario

This section presents the results obtained for the simulated neutrino populations when assuming a flat source evolution model as the one presented in Figure 5.2. The performance plots are presented in the same format as the results for the Madau and Dickinson (2014) evolution model scenario. Figure 5.13 shows the detection probability for 30-min observations with CTA-N assuming a 100% visibility of the tested sources. The detection probability was calculated following the same methodology as in the SFH evolution model scenario. Each simulated neutrino population tested with the `prod3b-v2` IRFs is represented by a coloured point, which has assigned a value between 0 (purple) and 1 (yellow) that corresponds to the detection probability. The subplots show the detection probability for different options in zenith angle (20°, 40° and 60°) and azimuth pointing direction (North

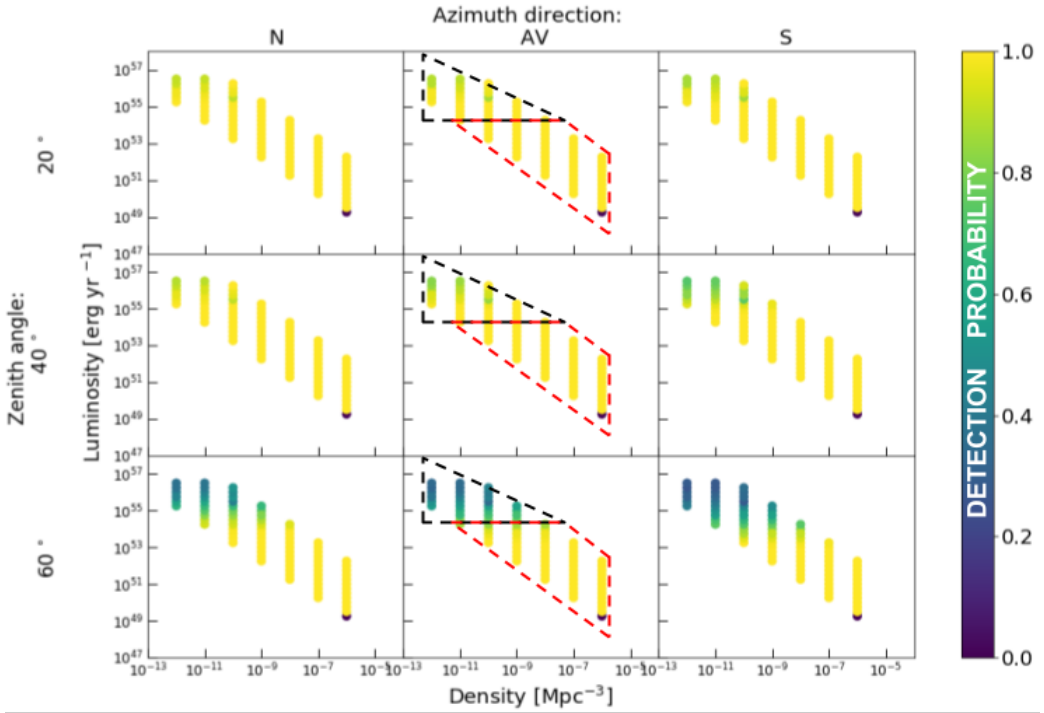

Figure 5.13: CTA-N Omega configuration array performance assuming 30-min observations and a flat source evolution model. Each point in the plot represents a simulated neutrino population with an associated value for CTA detection probability that goes from $P_{\text{detection}} = 0$ (purple) to $P_{\text{detection}} = 1$ (yellow) in the colour scale. The behaviour of the zones highlighted with dotted lines is described in Section 5.4.2. The order in the rows (zenith angles) and columns (magnetic field alignments) is the same as in Figure 5.11.

(N), Average (AV) and South (S)). Figure 5.14 shows the corresponding detection probability for CTA-S, using the same colour scale and order as employed in Figure 5.13.

In this scenario we can observe 2 zones of the parameter space with notable behaviours which have been highlighted in the CTA performance plots shown in Figures 5.14 and 5.13.

- The first zone is highlighted with a black dotted triangle. Similar to the SFH scenario, this region seems to be more sensitive to the changes in zenith angle observations. The simulated neutrino populations inside this triangular zone consist of the lowest local source densities ($\rho_o \leq 10^{-9}$ Mpc^{-3}) but high source luminosities ($L_\nu > 10^{53}$ erg/yr). The zone is marked in the central

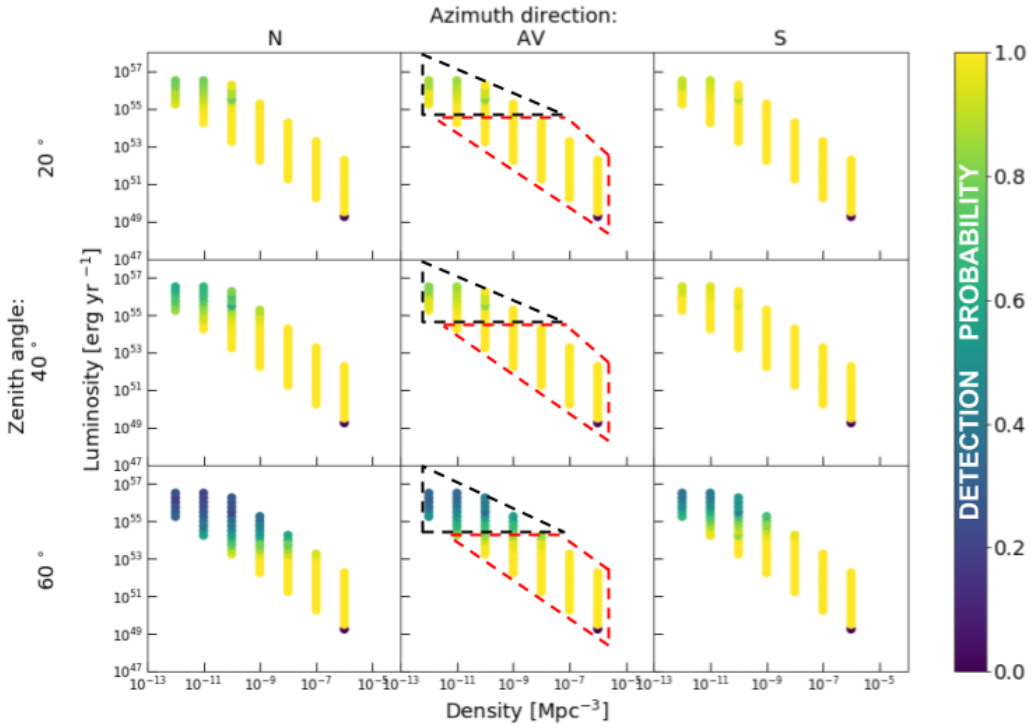

Figure 5.14: CTA-S Omega configuration array performance assuming 30-min observations and a flat source evolution model. The colour scale and order in the rows (zenith angles) and columns (magnetic field alignments), are the same as in Figure 5.13.

column of the Figures 5.14 and 5.13. The calculated detection probability for CTA-N (CTA-S) decreases in this corner of the tested parameter space, reaching minimum values of $P_{\text{detection}} \sim 0.8$ (~ 0.9) at 20° zenith angle, $P_{\text{detection}} \sim 0.65$ (~ 0.85) at 40° and $P_{\text{detection}} \sim 0.2$ (~ 0.4) at 60°.

- The second zone is highlighted inside a red dotted trapezoid in Figures 5.11 and 5.12. Inside this region, there is a uniform high detection probability ($P_{\text{detection}} \sim 1$). The mid and high local source densities tested (10^{-10} Mpc^{-3} $< \rho_o <$ 10^{-5} Mpc^{-3}) with low luminosities (3.16×10^{49} erg/yr $< L_\nu < 10^{54}$ erg/yr) are contained in this region. The only point that presents a null detection probability is located in the lower right corner in each subplot, which represents the simulated population with the lowest luminosity (1.78×10^{49} erg/year) and the highest local source density (10^6 Mpc^{-3}) in the flat evolution scenario. In a similar way to the SFH scenario, for this

simulated neutrino population there were no hot-spots exceeding IceCube's discovery threshold.

The zenith angle dependence and differences in performance due to the effect of the magnetic fields for both scenarios are discussed in the following sections.

5.4.3 Zenith angle dependence

CTA's performance is quantified by the differences in the calculated detection probability for the various `prod3b-v2` IRFs options considered within the Omega configuration array. There is a drastic loss of performance observed when simulating high zenith angle observations (IRF sets with 60° zenith). For the sensitive zone of the simulations (highlighted by the black triangle in Figures 5.11, 5.12, 5.13 and 5.14), it is registered up to -70% of detected sources in comparison to simulated observations at 20° zenith.

As mentioned in Section 5.3.1, the energy threshold of the arrays has a zenith angle dependence which increases at higher observation angles. Also the worse effective area for 60° zenith IRFs (see Figure 5.8) particularly affects observations at lower energies (below 1 TeV), while the difference in performance obtained between the IRF set with zenith angles at 20° and 40° is $< 10\%$.

For the CTA Omega configuration array the energy threshold for triggering observations starts from 30 GeV at 20° zenith angle. By going this low in energy threshold, usually an amount of soft spectrum sources would not be detected. With an assumed spectral index of $\Gamma = 2.19$, the simulated gamma-ray sources were detected almost entirely ($P_{\mathrm{CTA}} = 1$) using CTA-N for redshifts $z < 1$, and with a high detection probability between ($0.8 < P_{\mathrm{CTA}} < 1$) for the simulated sources with $1 < z < 3$. To preserve a high detection probability at high zenith angle observation, the LSTs will play a crucial role as they are designed to be sensitive even to the faint low-energy showers (below 200 GeV). In case of an hypothetical neutrino source with a harder spectrum ($\Gamma < 2.2$) and as bright as the simulated

sources, the chances of observing it by CTA would be or equal or higher as the results presented in this work.

5.4.4 Magnetic field effect

The influence of the Earth's magnetic field depending on the azimuth angle direction is perceptible in the calculated detection probability, especially for the CTA-N array with observations at high zenith angles (Figure 5.11). In the most extreme case, for observations at 60° zenith angle with CTA-N, the detection probability when pointing towards the North/South direction can diverge by ±30% with respect to the average magnetic field. The difference in the detection probability for 20° zenith is $^{+9\%}_{-10\%}$, and for 40° zenith is $^{+14\%}_{-26\%}$ (see Figure 5.11). For the CTA-S site, the difference in detection probability is: $^{+3.5\%}_{-5\%}$ for 20° zenith, $^{+8\%}_{-13\%}$ for 40° zenith, and ±15% for 60° zenith (see Figure 5.12). According to these results, the impact of the magnetic field effect is stronger in the CTA-N array than in CTA-S.

Another difference in performance can be observed in the left (right) column of Figures 5.11 and 5.12, where the azimuth direction is set to point North (South). In the most extreme case, for observations at 60° zenith, the detection probability when pointing towards the North/South direction can diverge by ±30% with respect to the average magnetic field.

The greater sensitivity of the CTA-N site to changes in the azimuth direction is explained by the difference in strength of the magnetic field configurations between both CTA sites (see Table 5.1 and Figure 5.7). The field strength for CTA-N when pointing in the North azimuth direction is 2 to 8 times higher than for the South pointing direction (depending on the zenith angle, see Figure 5.7). The impact of the magnetic field for CTA-N is large enough to influence the air shower development noticeably and affect the detection probability performance by (See Figures 5.11 and 5.13).

For CTA-S, the magnetic field strength difference between North/South pointing

directions is $< 15\mu$T, which is around a half of the difference encountered for CTA-N, leading to a $\pm 10\%$ difference in detection probability (Figures 5.12 and 5.14).

5.5 Combined detection probability

Both IceCube and CTA have certain constraints that have to be taken into consideration to calculate the combined detection probability associated with the simulated source populations. Assuming optimal CTA observing conditions, such as a dark night and low zenith angle observations, an optimistic prediction can be calculated using the simulations results.

5.5.1 IceCube probability

For IceCube, the detection probability is calculated as the ratio of the selected hot-spots ($N_{\text{hot-spots}}$), point-sources exceeding the 5σ discovery potential (see Figure 5.3), to the total number of simulated neutrino sources ($N_{\text{Total sources}}$):

$$P_{\text{IceCube}} = \frac{N_{\text{hot-spots}}}{N_{\text{Total sources}}} \tag{5.22}$$

The IceCube probability is calculated for all the simulated populations with density/luminosity combinations considered in the parameter space tested.

To describe the IceCube probability for each local source density as a continuous function of the source luminosity, the probability data points were fitted using a tanh function:

$$P_{\text{IceCube},\rho_o}(L_\nu) = \frac{1}{2}\tanh[a_2(\log_{10} L_\nu - \log_{10} a_1)] + \frac{1}{2} \tag{5.23}$$

where a_2, a_1 are the curve parameters that were adjusted to each local source density (ρ_o) to fit the IceCube data. The best fit parameters are presented in Table 5.2 and were calculated using a non-linear least squares method* to fit a

*See `https://docs.scipy.org/doc/scipy/reference/generated/scipy.optimize.curve_fit.html` for further details. Last accessed on 08/08/22.

SFH evolution		
Source density [Mpc^{-3}]	a_2	a_1
10^{-12}	1.9 ± 0.1	55.59 ± 0.01
10^{-11}	2.4 ± 0.1	54.76 ± 0.01
10^{-10}	2.5 ± 0.1	54.01 ± 0.01
10^{-9}	2.3 ± 0.1	53.31 ± 0.01
10^{-8}	2.5 ± 0.1	52.61 ± 0.01
10^{-7}	2.4 ± 0.1	51.26 ± 0.01
10^{-6}	2.3 ± 0.1	55.59 ± 0.01
10^{-5}	2.14 ± 0.04	50.63 ± 0.01
Flat evolution		
Source density [Mpc^{-3}]	a_2	a_1
10^{-12}	0.91 ± 0.03	56.75 ± 0.02
10^{-11}	1.8 ± 0.1	55.24 ± 0.02
10^{-10}	2.2 ± 0.1	54.22 ± 0.02
10^{-9}	2.6 ± 0.1	53.42 ± 0.02
10^{-8}	2.9 ± 0.2	53.42 ± 0.02
10^{-7}	3.2 ± 0.2	51.98 ± 0.01
10^{-6}	3.2 ± 0.2	51.28 ± 0.01

Table 5.2: Best fit parameters for the IceCube detection probability curves as a function of luminosity L_ν. The probability curve for each source density is fitted with a tanh function and plotted as a dashed line in Figures 5.15 and 5.16.

function in `Python Scipy` (Virtanen et al., 2020). The best fit probability curves calculated for IceCube are shown as coloured dashed curves in Figure 5.15 for the SFH source evolution scenario and in Figure 5.16 for the flat source evolution scenario. The coloured stars that also appear in both Figures mark the point at which the simulated populations saturate the IceCube neutrino diffuse flux. For higher luminosities along the curves, the simulated populations are over-saturating the all-sky IceCube neutrino diffuse flux.

It is also worth mentioning that the neutrino simulations were performed to find possible IceCube hot-spots within the source populations, therefore CTA observations are going to be biased towards the northern hemisphere as IceCube sensitivity is better for the northern hemisphere (see Figure 5.3). In addition, some simulated sources will be out of the visible range for the CTA-S site; this is accounted for in the calculated detection probability for CTA.

SFH evolution	CTA-N		CTA-S	
Source density Mpc^{-3}	b_2	b_1	b_2	b_1
10^{-12}	$(-17 \pm 6) \times 10^{-59}$	0.98 ± 0.01	$(-4 \pm 1) \times 10^{-58}$	0.76 ± 0.02
10^{-11}	$(-20 \pm 5) \times 10^{-59}$	0.98 ± 0.01	$(-5 \pm 1) \times 10^{-58}$	0.81 ± 0.01
10^{-10}	$(-16 \pm 7) \times 10^{-58}$	0.99 ± 0.01	$(-39 \pm 9) \times 10^{-58}$	0.81 ± 0.02
10^{-9}	$(16 \pm 2) \times 10^{-71}$	0.99 ± 0.01	$(-2 \pm 7) \times 10^{-58}$	0.84 ± 0.01
10^{-8}	$(13 \pm 5) \times 10^{-70}$	0.99 ± 0.01	$(-3 \pm 4) \times 10^{-56}$	0.86 ± 0.02
10^{-7}	$(-10 \pm 2) \times 10^{-69}$	0.99 ± 0.01	$(8 \pm 6) \times 10^{-55}$	0.85 ± 0.03
10^{-6}	$(2 \pm 7) \times 10^{-57}$	0.99 ± 0.01	$(2 \pm 4) \times 10^{-54}$	0.83 ± 0.03
10^{-5}	$(7 \pm 7) \times 10^{-67}$	0.99 ± 0.01	$(2 \pm 4) \times 10^{-53}$	0.83 ± 0.03
Flat evolution	CTA-N		CTA-S	
Source density Mpc^{-3}	b_2	b_1	b_2	b_1
10^{-12}	$(-67 \pm 3) \times 10^{-59}$	1.000 ± 0.003	$(-9 \pm 3) \times 10^{-58}$	0.76 ± 0.02
10^{-11}	$(-41 \pm 4) \times 10^{-59}$	1.001 ± 0.002	$(-12 \pm 2) \times 10^{-58}$	0.81 ± 0.01
10^{-10}	$(-1 \pm 2) \times 10^{-58}$	0.99 ± 0.01	$(-11 \pm 3) \times 10^{-58}$	0.81 ± 0.02
10^{-9}	$(-3 \pm 1) \times 10^{-71}$	1.00 ± 0.01	$(-56 \pm 9) \times 10^{-58}$	0.84 ± 0.01
10^{-8}	$(-3 \pm 7) \times 10^{-60}$	0.99 ± 0.01	$(-3 \pm 2) \times 10^{-56}$	0.86 ± 0.02
10^{-7}	$(-3 \pm 2) \times 10^{-69}$	1.00 ± 0.01	$(-2 \pm 5) \times 10^{-55}$	0.85 ± 0.03
10^{-6}	$(-4 \pm 1) \times 10^{-68}$	1.00 ± 0.01	$(2 \pm 5) \times 10^{-54}$	0.83 ± 0.03

Table 5.3: Best fit parameters for the CTA detection probability curves as a function of luminosity L_ν. The probability curve for each source density is fitted with a one-degree polynomial function and plotted as dotted a line in Figures 5.15 and 5.16.

5.5.2 CTA visibility constraints

For CTA, the best observing configuration within the `prod3b-v2` IRFs is selected by assuming observations are made for each source at culmination. Depending on the difference between the source declination and the site latitude (28.76° for CTA-N and -24.07° for CTA-S), the zenith angle value used could be 20°, 40°, or 60°. For all pointing directions below 33° in zenith angle 20° was used, for all pointing directions between 33° in zenith and 54°, 40° was used, and for all pointing directions above 54° but below 66°, a value of 60° was used. Any possible observations above 66° in zenith angle were discarded. The azimuth direction (North or South pointing) was automatically defined by the source culmination point. The gamma-ray simulations also assume dark night observations with optimal observation conditions.

CTA detection probability curves for each local source density were modelled as a

function of the source luminosity with a one-degree polynomial as:

$$P_{\mathrm{CTA},\rho_o}(L_\nu) = b_2 L_\nu + b_1 \tag{5.24}$$

in which the coefficients b_2, b_1 were adjusted to fit the detection probability points calculated for the gamma-ray simulations using the least squares polynomial fit method in `Numpy Polyfit`* (Harris et al., 2020). The best fit probability curves calculated for CTA are shown as coloured dotted curves in Figure 5.15 for the SFH source evolution scenario and in Figure 5.16 for the flat source evolution scenario, while the best fit parameters are given in Table 5.3.

Over the luminosity range considered, the CTA detection probability curves for each local source density could be described as an horizontal line (almost constant value) with a curvature at higher luminosities where the detection probability drops.

5.5.3 Combined detection probability

The combined detection probability (IceCube+CTA) for each local source density considered is calculated as:

$$P_{\mathrm{combined},\rho_o}(L_\nu) = P_{\mathrm{IceCube},\rho_o}(L_\nu) \times P_{\mathrm{CTA},\rho_o}(L_\nu) \tag{5.25}$$

where both individual probabilities for IceCube and CTA were extrapolated and plotted as a function of the source luminosity L_ν. The combined detection probability curves are shown as coloured solid lines in Figure 5.15 for the SFH scenario and in Figure 5.16 for the flat evolution scenario. The curves' style, colour scale and symbols follow the same format as Figure 5.15.

When comparing the detection probability curves for each local source density, CTA-N has in general a higher chance of detecting a neutrino source counterpart than CTA-S. This is because IceCube is more sensitive to sources located in the

*See `https://numpy.org/doc/stable/reference/generated/numpy.polyfit.html` for further details. Last accessed on 08/08/22.

northern hemisphere; such sources are visible from CTA-S at higher zenith angles than from CTA-N, and some of them are not visible at all, decreasing the detection probability.

Figures 5.15 and 5.16 show that the final detection probability value is determined mostly by the IceCube sensitivity. The sources that pass the IceCube discovery potential are usually very bright and nearby. If visible, therefore, they will almost always be detected with CTA. This parameter region is also clear in Figures 5.11 and 5.12, where the high detection probability zone is coloured uniformly for both CTA sites.

In both scenarios (the SFH evolution model of Madau and Dickinson (2014) and flat source evolution), the detection probability for CTA-N site is $P_{\mathrm{CTA},\rho_o} = 1$ for the local source density region ($\rho_o \geq 10^{-9}$ Mpc^{-3}); consequently, the final shape of the combined detection probability is determined purely by IceCube. In this density range, it can be seen that the combined detection probability increases drastically when the flux is over-saturated by moving higher in luminosity. The combined detection probability below the saturation point does not reach 10%. At lower densities ($\rho_o < 10^{-9}$ Mpc^{-3}), the CTA detection probability curves decrease gradually down to about 0.9, which provokes a bending in the final shape of the combined detection probability, but even here the IceCube detection probability is still the dominant factor. The combined detection probability for the flat evolution scenario given in Figure 5.16 shows similar trends than the plots calculated with the SFH model of Madau and Dickinson (2014). The differences between the results obtained in both scenarios are explored in Chapter 6.

For CTA-S, the combined detection probability is lower in comparison to CTA-N. This is expected as IceCube is more sensitive to the neutrino sources in the northern hemisphere. A drop in CTA-S detected sources plays a bigger role in the final shape of the combined detection probability curves, especially at low densities ($\rho_o < 10^{-9}$ Mpc^{-3}). The drop in CTA-S detection probability is related to the visibility constraints for the simulated IceCube hot-spots describe above.

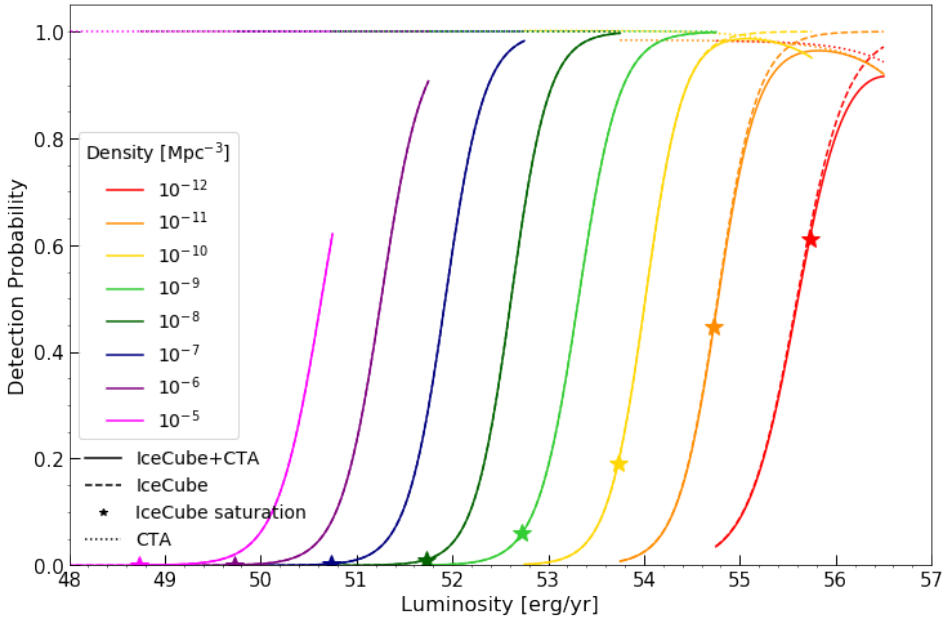

(a) Combined detection probability for CTA-N

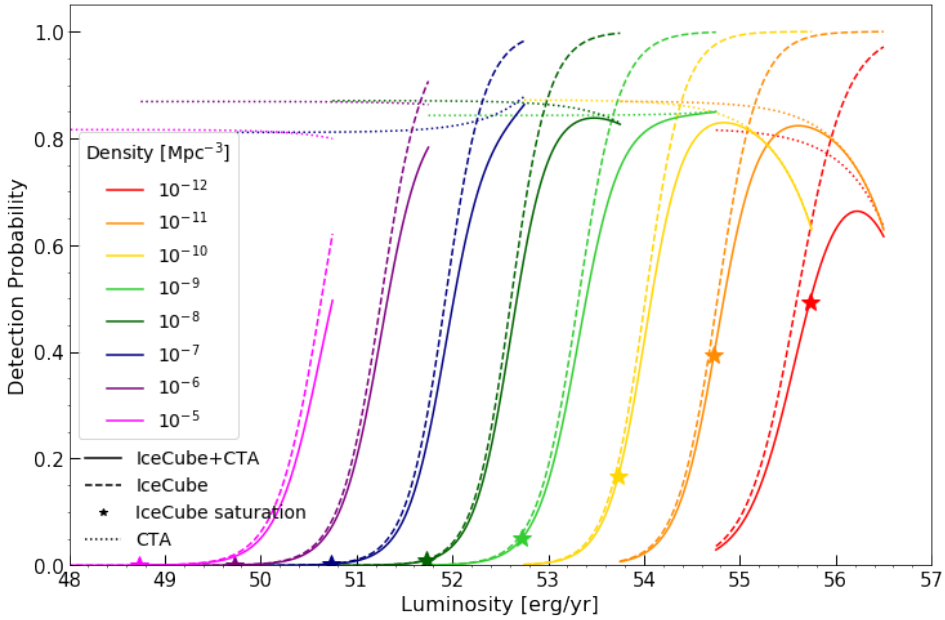

(b) Combined detection probability for CTA-S

Figure 5.15: Detection probability for the simulated neutrino hot-spots detected by IceCube and observed with (a) CTA-N and (b) CTA-S in 30-min observations. The SFH evolution model of Madau and Dickinson (2014) was used to perform the neutrino simulations. The coloured dashed curves show the IceCube detection probability, the coloured dotted curves the CTA detection probability and the solid curves the combined detection probability. The coloured stars mark the points at which the simulated populations saturate the IceCube neutrino diffuse flux.

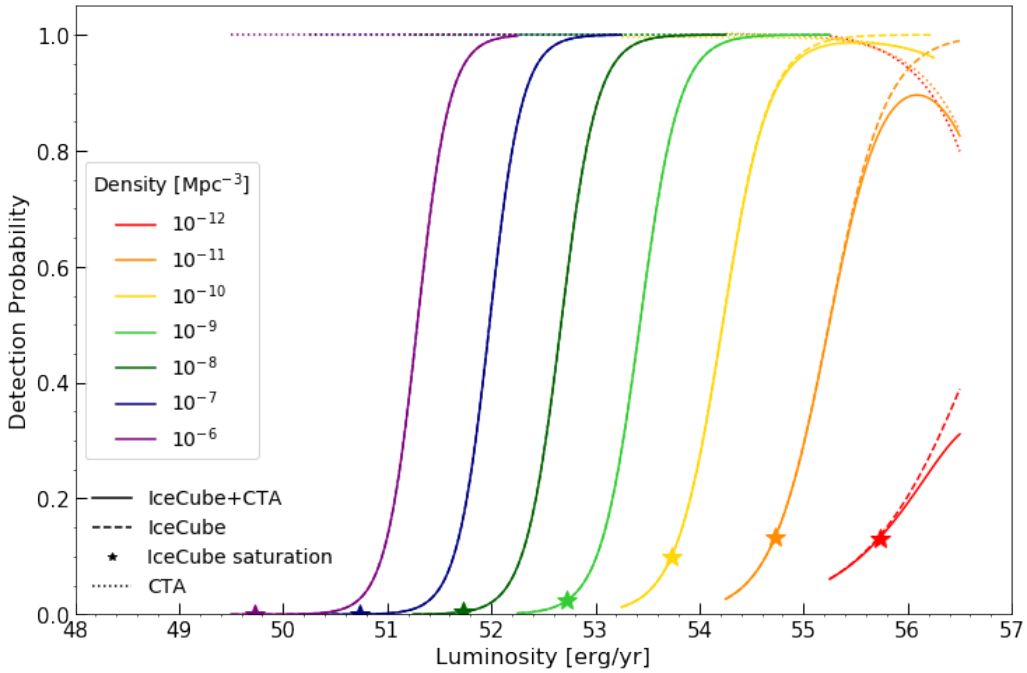

(a) Combined detection probability for CTA-N

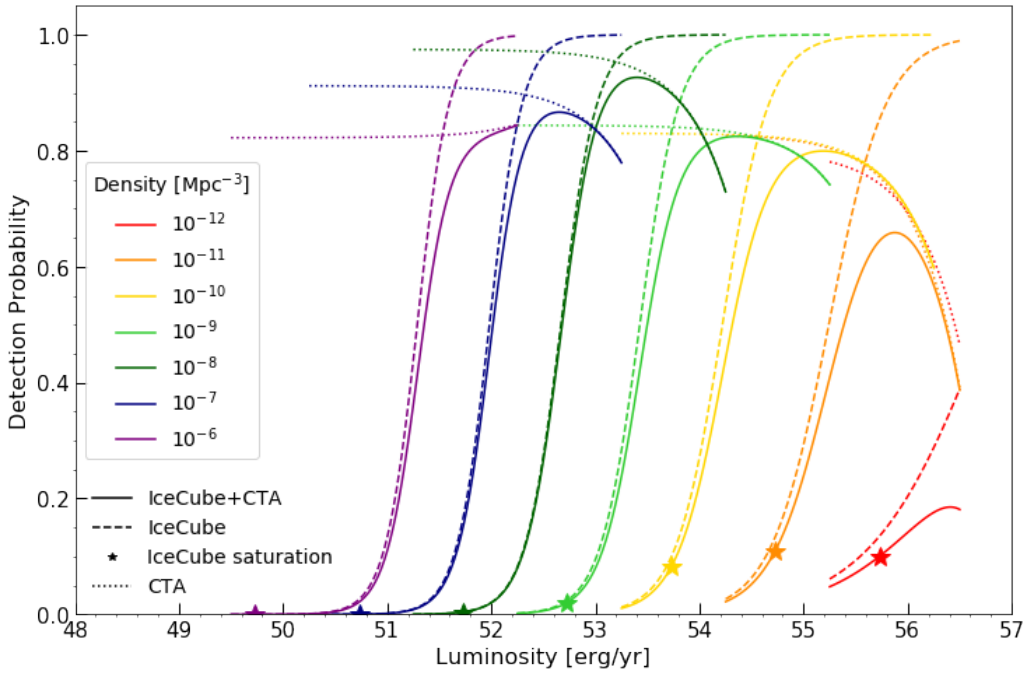

(b) Combined detection probability for CTA-S

Figure 5.16: Detection probability for the simulated neutrino source populations detected by IceCube and observed with (a) CTA-N and (b) CTA-S in 30-min observations. A flat source evolution model was employed to simulate the neutrino source populations tested. The curve styles and colours follow the same nomenclature as Figure 5.15. The coloured stars mark the points at which the simulated populations saturate the IceCube neutrino diffuse flux.

5.5.4 Conclusions

The NToO program for CTA performed a large number of neutrino and gamma-ray simulations to predict the detection probability of the blazar-like, steady point-source populations able to saturate the IceCube diffuse flux, and produced performance plots for both CTA sites, assuming the Omega configuration array and taking into account visibility constraints. High zenith angle observations and the magnetic field effect (particularly at CTA-N site) were the two main reasons for drops in the calculated CTA detection probability. A drastic performance loss, up to 70%, was found at angles between 40° and 60°. The difference in performance found for observation angles below 40° in zenith is less than 10%. The magnetic field effect impact on CTA detection probability was quantified depending on the azimuth pointing direction, reaching ±30% for CTA-N and ±15% for CTA-S.

The combined detection probability (IceCube + CTA) was calculated by extrapolating the simulation results into probability curves dependent on the source luminosity (L_ν). The IceCube detection probability turned out to be the dominant factor over CTA detection probability. Results show a high CTA detection probability for steady source populations with a local source density $\rho_o \geq 10^{-9}$ Mpc^{-3} able to over-saturate IceCube diffuse flux. Under optimal observation conditions, CTA-N performance was outstanding in most of the parameter space tested.

CTA-S has in general a lower detection probability than CTA-N throughout all the simulated parameter space, explained by the fact that the neutrino simulations were performed to identify hot-spots with IceCube, which is more sensitive to neutrino sources in the northern hemisphere. A neutrino observatory in the northern hemisphere with similar capabilities as IceCube, like KM3NeT (KM3NeT Collaboration, 2016) or the Pacific Ocean Neutrino Experiment (P-ONE) (P-ONE Collaboration, 2020), would be able to provide a list of possible hot-spots that could be complemented by CTA-S observations.

Both KM3NeT and P-ONE are planned to be multi-cubic-kilometre arrays and

optimised to detect TeV–PeV cosmogenic neutrinos. An early phase of P-ONE will be deployed in 2023-2024 at Cascadia Basin, in the Pacific coast of Canada, and the full array is planned to be completed by 2030. On the other hand ARCA, the KM3NeT array designated for HE neutrino astronomy, is under construction in the coast of Sicily, and will improve in size and sensitivity compared to the ANTARES experiment (KM3NeT Collaboration, 2019). An all-sky coverage for neutrinos in the TeV to PeV scales in connection to the multi-messenger astronomy community through real-time neutrino alerts would increase the chances of a potential significant association between a high energy neutrino alert and an astrophysical source.

Chapter 6

Effects of Source Evolution Models on CTA Observations

In Chapter 5, two source evolution scenarios were implemented within the neutrino simulations, the first following the SFH model of Madau and Dickinson (2014) and the second considering a flat source evolution model. For both cases, the performance plots and the detection probability for CTA were calculated using the same methodology. In this chapter the impact of the source evolution models is analysed by comparing the results coming from the CTA-detected source populations. In both cases the redshift reach is calculated from the source distributions detected with CTA (Section 6.1) and a statistical test is applied to evaluate the difference between the two scenarios (Section 6.2).

6.1 Redshift reach

In the neutrino simulations performed for the NToO program for CTA, the simulated steady source populations were spread over the universe (a spherical volume) up to redshift $z = 4$. Only the points in the sky exceeding the 5σ discovery potential from IceCube were treated as hot-spots and the corresponding gamma-ray emission as observed by CTA in 30-min observations was simulated assuming optimal

observing conditions.

The CTA-detected source distributions for the simulated populations under the Madau and Dickinson (2014) source evolution scenario are shown in Appendix A and an example plot of the detected source distributions for the source density $\rho_o = 10^{-12}$ Mpc^{-3} is shown in Figure 6.1. The plot shows the number of CTA-detected sources with CTA-N, assuming 20° zenith angle observations, in redshift bins of 0.05. The histograms are normalised to the total number of identified hot-spots from the neutrino simulations. In the plot we can see how the distributions grow wider as we go higher in luminosity, with some outliers visible for $L_\nu > 10^{56}$ erg/yr.

Similarly, an example plot of the detected source distributions for the flat source evolution scenario at density $\rho_o = 10^{-12}$ Mpc^{-3} is shown in Figure 6.1. The rest of the simulated populations for the flat source evolution scenario are presented in Appendix A with the same format as given in Figure 6.1.

To calculate the redshift reach of each of the simulated populations, the CTA-detected sources were sorted in ascending order according to their redshift and divided in bins of $\Delta z = 0.05$. The tail of the distribution usually included isolated values from a few sources that can be considered outliers from the main distribution, as exemplified in Figure 6.1. The redshift reach is then defined as an upper limit set at 90% of CTA-detected sources in the distribution, i.e. the highest value found up to the cut-off point, excluding the last 10%.

The highest redshift reach values for each local source density analysed are found among the highest luminosities, as can be seen in Table 6.1, in which results are shown for both of the source evolution models for each CTA site. The redshift reach obtained for both sites is comparable. Figures 6.2 and 6.3 show the redshift reach for both CTA sites under the Madau and Dickinson (2014) SFH and flat source evolution models respectively. Each local source density tested is identified with a different colour, and the arrows represent the redshift reach value calculated

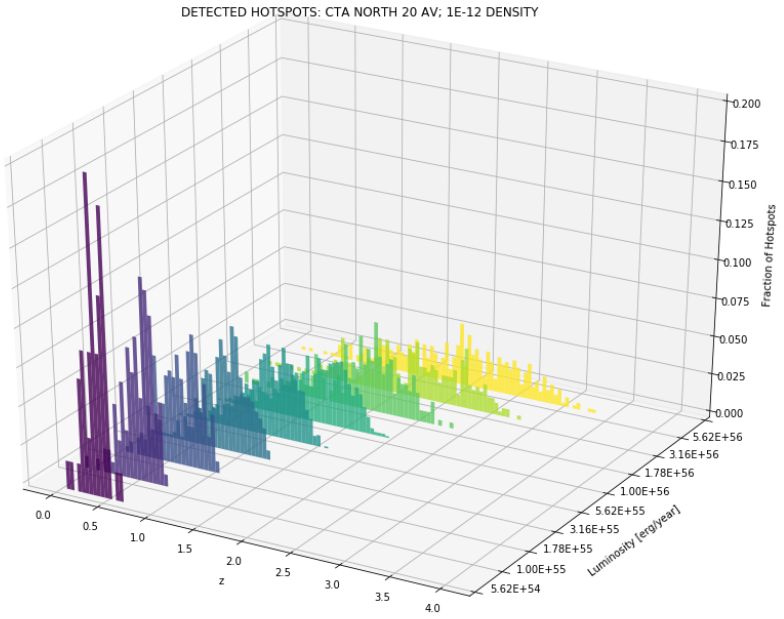

(a) SFH source evolution model

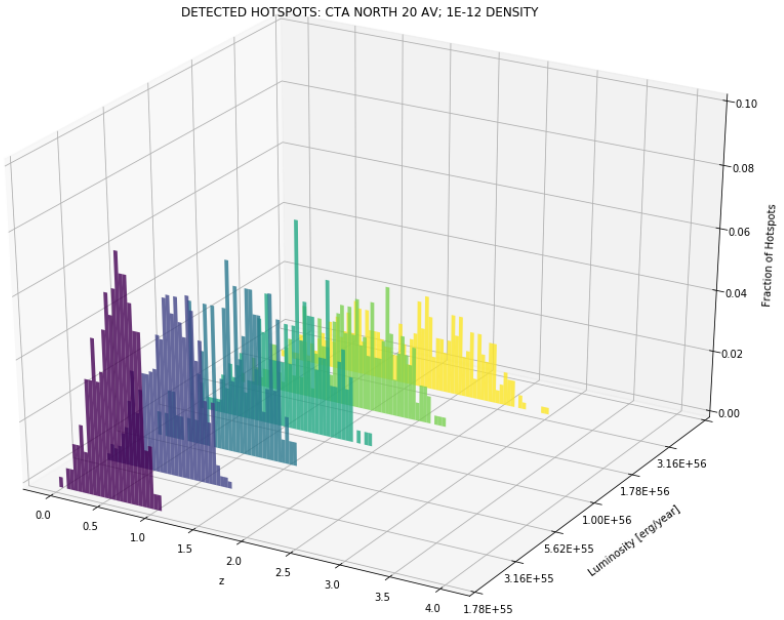

(b) Flat source evolution model

Figure 6.1: Detected source distributions for $\rho_o = 10^{-12}$ Mpc^{-3} density with CTA-N at 20° zenith angle. The sources were simulated using (a) the SFH source evolution scenario of Madau and Dickinson (2014) and (b) a flat source evolution model. The colour scale shows the simulated distributions, with the lowest luminosities in blue and the highest luminosities in yellow. The distributions are normalised to the total number of detected sources.

SFH evolution Source density Mpc^{-3}	Max Luminosity 5.62× erg/year	Redshift reach CTA-N	CTA-S
10^{-5}	10^{50}	0.01	0.01
10^{-6}	10^{51}	0.03	0.03
10^{-7}	10^{52}	0.08	0.09
10^{-8}	10^{53}	0.2	0.2
10^{-9}	10^{54}	0.6	0.6
10^{-10}	10^{55}	1.4	1.4
10^{-11}	10^{56}	3.0	3.0
10^{-12}	10^{56}	2.8	2.9
Flat evolution Source density Mpc^{-3}	Max Luminosity erg/year	Redshift reach CTA-N	CTA-S
10^{-6}	1.78×10^{52}	0.05	0.05
10^{-7}	1.78×10^{53}	0.1	0.1
10^{-8}	1.78×10^{54}	0.4	0.4
10^{-9}	1.78×10^{55}	0.9	0.9
10^{-10}	1.78×10^{56}	1.9	1.9
10^{-11}	3.16×10^{56}	3.0	3.1
10^{-12}	3.16×10^{56}	2.9	3.0

Table 6.1: Summary table of redshift reach values for the CTA-detected sources in the SFH and flat source evolution scenario. The table presents the redshift reach for the maximum luminosity on each local source density tested of the parameter space. The redshift reach for the SFH (flat) evolution scenario is plotted in Figure 6.2 (Figure 6.3).

for each simulated source population over the given luminosity range.

The calculated redshift reach was fitted with a second-degree polynomial as a function of the source luminosity (L_ν) in log-log space. The best fit curve for each source evolution scenario and CTA site is:

$$\log_{10}(z_{\mathrm{reach}}) = c_2(\log_{10}(L_\nu))^2 + c_1 \log_{10}(L_\nu) + c_0 \tag{6.1}$$

where the coefficients c_2, c_1, c_0 were adjusted with `Numpy Polyfit`* module (Harris et al., 2020) in `Python` to fit the redshift reach data, and are summarised in Table 6.2.

As expected, Figures 6.2 and 6.3 show that the redshift reach increases with higher luminosities. Generally speaking, the redshift reach for the flat source evolution scenario follows a similar trend to the SFH evolution scenario, although the flat

*See `https://numpy.org/doc/stable/reference/generated/numpy.polyfit.html` for further details. Last accessed on 08/08/22.

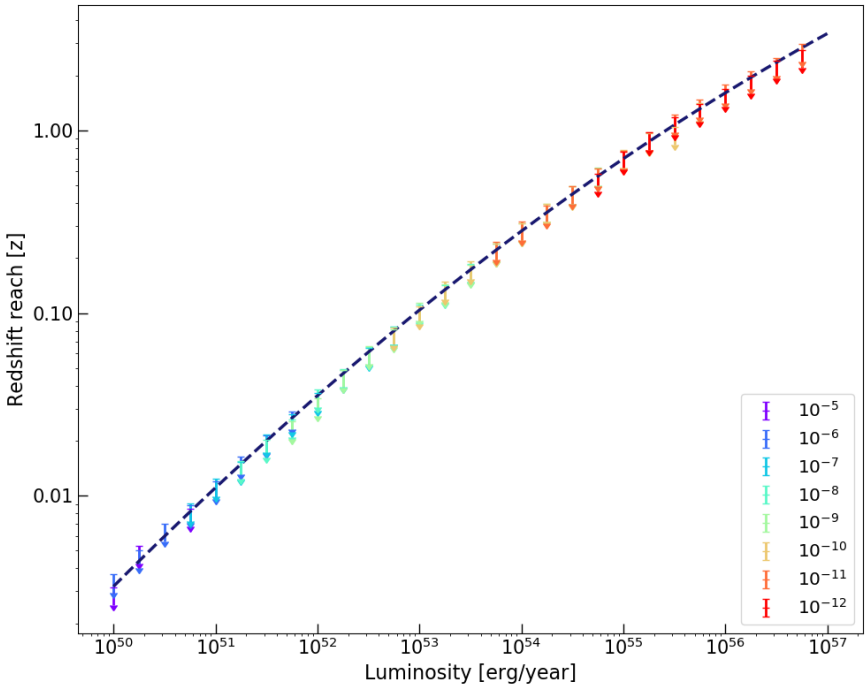

(a) redshift reach for CTA-N

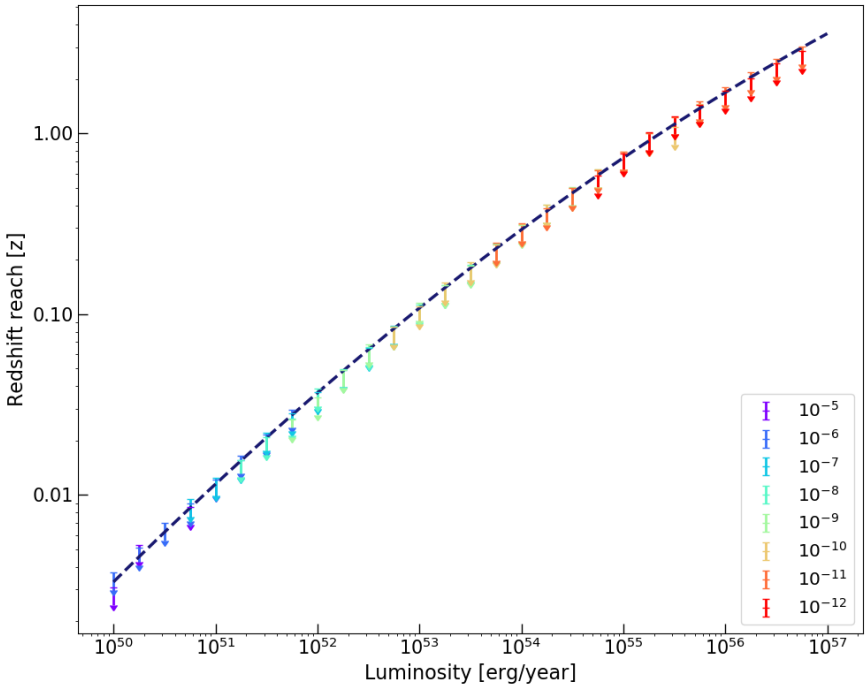

(b) redshift reach for CTA-S

Figure 6.2: Redshift reach for (a) CTA-N and (b) CTA-S in the steady source scenario following the SFH evolution model of Madau and Dickinson (2014). Each coloured arrow represents the redshift reach of a different simulated population in the parameter space. The dotted line is the best fit curve to the redshift reach points in log-log space. The best fit curve parameters are given in Table 6.2.

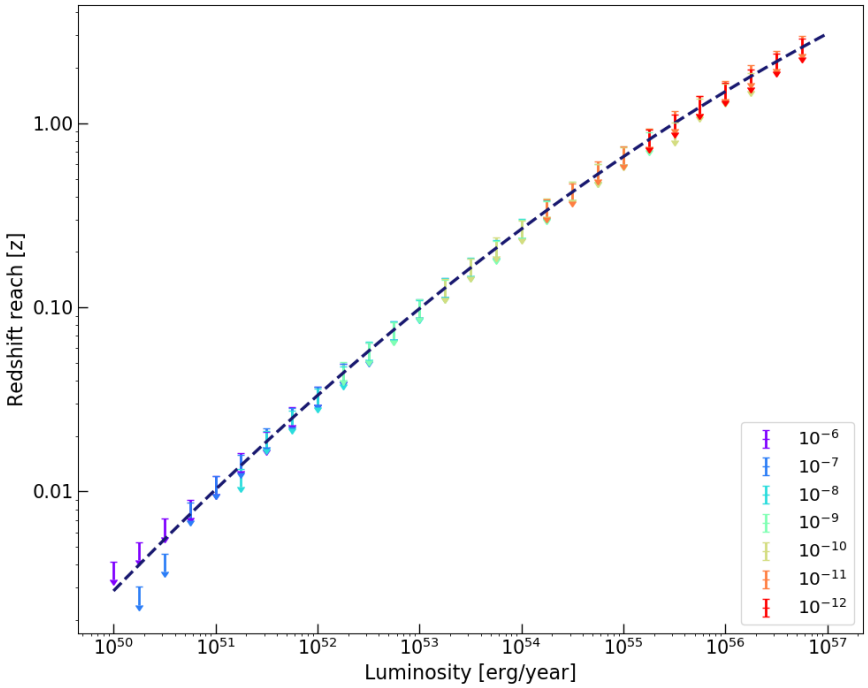

(a) redshift reach for CTA-N

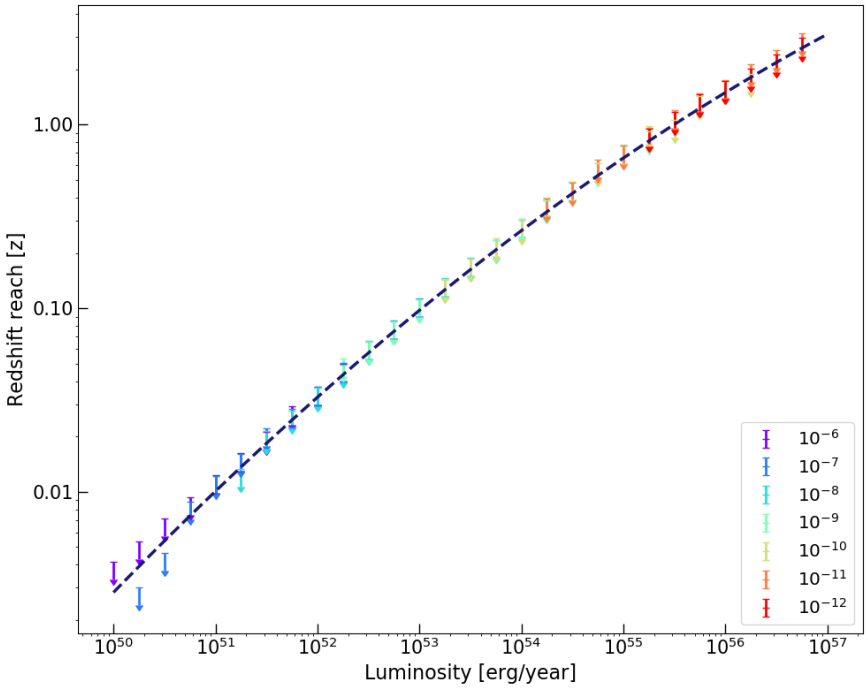

(b) redshift reach for CTA-S

Figure 6.3: Redshift reach for (a) CTA-N and (b) CTA-S detected sources following a flat source evolution scenario. Each coloured arrow represents the redshift reach of a different simulated population in the parameter space. The dotted line is the best fit curve to the redshift reach points in log-log space. The best fit curve parameters are given in Table 6.2.

SFH evolution best fit parameters	c_2	c_1	c_0
CTA-N	(-7.8±0.3)×10^{-3}	2.36±0.07	-173±4
CTA-S	(-7.8±0.3)×10^{-3}	2.35±0.07	-173±4
Flat evolution best fit parameters	c_2	c_1	c_0
CTA-N	(-8.5±0.5)×10^{-3}	2.5±0.1	-184±7
CTA-S	(-8.4±0.5)×10^{-3}	2.5±0.1	-183±7

Table 6.2: Best fit parameters for the second degree polynomial fit curve to the redshift reach data with the Madau and Dickinson (2014) SFH and flat source evolution scenario. The best fit curves are plotted in Figure 6.2 for the SFH scenario and in Figure 6.3 for the flat evolution scenario.

evolution scenario has higher redshift reach values at densities $\rho_o \geq 10^{-10}$ Mpc^{-3}. This is because the luminosity range of the simulated neutrino populations for the flat source evolution scenario gets up to higher values in order to saturate the IceCube diffuse flux (see Table 6.1). At the lowest densities ($\rho_o = 10^{-11}, 10^{-12}$ Mpc^{-3}) the redshift reach in both scenarios is practically the same, and extends up to $z \sim 3$. In Figure 6.3, there are a couple of values for $\rho_o = 10^{-7}$ Mpc^{-3} that appears below the best fit curve, this is due to the low number of hot-spots found in the neutrino simulations (< 5 hot-spots) for the simulated populations below $L_\nu = 5.62 \times 10^{50}$.

The identified IceCube hot-spots for $\rho_o = 10^{-11}$ and 10^{-12} Mpc^{-3} reached $z = 4.0$ in the neutrino simulations (Section 5.1) for the most luminous source populations (up to 5.62×10^{56} erg/years), which means CTA is not able to detect the sources with $z > 3$ although they are very bright. The EBL absorption effect at $z > 3$ is the main factor limiting the propagation of VHE gamma-ray photons. In this work the model of Domínguez et al. (2011) is used to calculate the observed gamma-ray spectrum and taken into account in the CTA simulated observations. Domínguez et al. (2011) model uses the evolution of the galaxy populations directly observed over a redshift range that reaches z=4. It is based on near-IR measurements (Cirasuolo et al., 2010) and on multi-wavelength galaxy data from AEGIS (AEGIS Collaboration, 2007) (see Section 2.5). This model is consistent with the predicted transparency of the universe to gamma-rays from the EBL models of Franceschini

et al. (2008) and Gilmore et al. (2012) and is also in agreement with the upper limits formulated from gamma-ray astronomy (Aharonian et al., 2006; Mazin and Raue, 2007; MAGIC Collaboration, 2008a). Since there would be no significant difference between the Domínguez et al. (2011) model and the other mentioned models, and given its easy access and practicality, Domínguez et al. (2011) model was selected for this work.

6.2 Implications of source of evolution scenarios

Both the SFH and flat source evolution models were applied to a common region in the parameter space, 10^{-6} Mpc^{-3} $< \rho_o <$ 10^{-12} Mpc^{-3} in the local source density, and $1.78 \times 10^{49} < L_\nu < 5.62 \times 10^{56}$ erg/yr for the source luminosity range. The simulated neutrino populations in this region were assumed to have the same neutrino spectrum and to saturate the IceCube diffuse neutrino flux. The gamma-ray spectrum for both scenarios was calculated using the same methodology as explained in Section 5.2 and the EBL model of Domínguez et al. (2011) was applied to account for the gamma-ray attenuation in the simulated observations in both scenarios as well. The only difference assumed between these two scenarios is the source evolution model used in the neutrino simulations; we can therefore use a statistical test to analyse the CTA-detected source results from both scenarios, compare them, and tell if there is any significant difference. The Kolmogorov-Smirnov (KS) test is employed to make this comparison between the CTA-detected source distributions.

6.2.1 The Kolmogorov-Smirnov test

This section introduces the concept of the Kolmogorov-Smirnov test and is based on the article from Arnold and Emerson (2011) and the book *'Practical nonparametric statistics'* by Conover (1999). The Kolmogorov-Smirnov test (KS-1; Kolmogorov (1933)) is a non-parametric goodness-of-fit test that can be used to compare a

data sample with a reference probability distribution. Given the Cumulative Distribution Function (CDF) $F_0(x)$ of the hypothesised distribution and the Empirical Distribution Function (EDF) $F_{\text{data}}(x)$ of the observed data, the test statistic D is given by:

$$D = \sup_x |F_0(x) - F_{\text{data}}(x)| \tag{6.2}$$

where $F_0(x)$ is a continuous function, and $F_{\text{data}}(x)$ is a step function drawn from a data sample. The EDF will converge to a continuous CDF as the size of the data sample approaches infinity. The value of D is also known in literature as the KS distance and represents the maximum difference between the hypothesised cumulative distribution function and the empirical distribution function. The distribution of the KS-1 statistic is calculated under the null hypothesis that the sample is drawn from the reference distribution.

The KS test can also be adapted to check whether two data samples have a common origin by comparing their EDFs. If we have two data samples, the KS test can determine whether the two distribution functions associated with the samples are the same. While other statistical tests are sensitive to differences between specific quantities, such as the mean or median values, they usually do not detect differences in variance or other variables. On the other hand, the KS test is consistent against all types of differences that may exist between the two distribution functions.

Let's consider two data samples of different sizes, the first one represented by a set $x_1, x_2, ..., x_n$ of size n with a distribution function given by $F_n(x)$, and the second data sample represented by a set $y_1, y_1, ..., y_m$ of size m which has a distribution function $G_m(x)$. Assuming the null hypothesis (H_0) that both samples have identical distribution functions ($H_0 : F_n = G_m$), the Kolmogorov-Smirnov two-sample (KS-2) test statistic is defined as:

$$D_{nm} = \sup_x |F_n(x) - G_m(x)| \tag{6.3}$$

where D_{nm} is the maximum distance between the two EDFs considered. Both EDFs look like discontinuous step functions that converge to continuous distribu-

tions as $n, m \to \infty$. The KS-2 test makes no preliminary assumptions about the specifics of the data distributions, but it assumes that the data samples are random and independent. The KS-2 test is calculated with the unbinned data from both samples.

Once the D_{nm} distance has been calculated, it is necessary to determine if the null hypothesis is accepted or rejected. This can be achieved by calculating the probability of observing equal or greater distances if both samples came from the same distribution. Since a large value of D_{nm} would appear to be inconsistent with the null hypothesis, if the calculated value is large enough, then the null hypothesis is rejected at a critical value α if:

$$D_{n,m} \geq c(\alpha)\sqrt{\frac{n+m}{nm}} \tag{6.4}$$

where $c(\alpha)$ is the inverse of the cumulative KS distribution at α ($c(\alpha) = 1 - KS(\alpha)$). The p-value is then defined as the probability of observing a test statistic as extreme as, or more extreme than, the observed value under the null hypothesis, and is calculated using the asymptotic formula given for the KS cumulative distribution:

$$\text{p-value} = \text{Prob}\left[D_{n,m} \geq c(\alpha)\sqrt{\frac{n+m}{nm}}\right] = 1 - 2\sum_{k=1}^{\infty}(-1)^{k-1}e^{-2k^2\alpha^2} \tag{6.5}$$

where α is the critical value to reject the null hypothesis. For p-values $< \alpha$ it can be considered that the two distribution functions tested are significantly different, and therefore do not come from the same parent distribution. The critical value α can be adjusted to be as low as desired to claim a significant difference at the α level. The significance level of an event is defined as the probability that the event could have occurred by chance. If the significance level is quite low, then probability of occurring by chance is quite small, and the event is called significant. Some experiments set $\alpha = 0.05$ or $\alpha = 0.01$ by convention, while experimental physical sciences have established a more strict standard, and a discovery is usually claimed only at the 5σ significance level. For comparison, in a normal distribution the 5σ significance level is translated to p-values $< 3 \times 10^{-7}$.

6.2.2 Evolution models comparison

The KS-2 test thus can be used to discriminate between the SFH evolution model scenario and the flat source evolution model scenario in the shared region of the parameter space tested. By using the CTA-detected source distributions, the EDFs for both distributions can be obtained and the KS-2 test applied to check if there is a significant difference between the two scenarios. The KS-2 test statistic and p-values were calculated using unbinned data from the CTA-detected source simulations and the `Scipy Stats`* module (Virtanen et al., 2020) in `Python`. The results obtained for the KS-2 test statistic and the corresponding p-values calculated over the common region of the parameter space are summarised in Table 6.3.

Figure 6.4 shows two example plots comparing the detected source distributions with CTA for a given simulated neutrino population: $\rho_o = \times 10^{-10}$ Mpc^{-3} and $L_\nu = 1.78 \times 10^{54}$ erg/yr (left plot) for the first case; and $\rho_o = \times 10^{-11}$ Mpc^{-3} and $L_\nu = 3.16 \times 10^{55}$ erg/yr (right plot). The histograms show the number of detected sources for both source evolution models used: Madau and Dickinson (2014) in blue, and flat evolution in black. In the first example (left plot) the p-value associated to the KS-2 test was 0.27, which represents no significant difference between the two distributions, therefore the null hypothesis was accepted and the two source distributions were determined to be likely the same. For the second example (right plot) the p-value calculated was 5×10^{-8}, which is small enough to reject the null hypothesis to an equivalent 5σ significance level, therefore the distributions were categorised as different from each other, which means the choice in the source evolution scenario is producing a measurable difference in the observed CTA results.

Figure 6.5 shows the EDFs corresponding to the example plots presented in Figure 6.4. The EDF for the Madau and Dickinson (2014) SFH source evolution scenario is

*See `https://docs.scipy.org/doc/scipy/reference/generated/scipy.stats.kstwo.html#scipy.stats.kstwo` for further details. Last accessed on 08/08/22.

Source density	10^{-6}	Mpc-3									
Luminosity [erg/year]	10^{50}	1.78×10^{50}	3.16×10^{50}	5.62×10^{50}	10^{51}	1.78×10^{51}	3.16×10^{51}	5.62×10^{51}			
D_{nm}	0.34	0.22	0.19	0.11	0.04	0.05	0.03	0.03			
p-value	0.31	0.29	0.40	0.50	0.99	0.37	0.70	0.96			
Source density	10^{-7}	Mpc-3									
Luminosity [erg/year]	5.62×10^{50}	10^{51}	1.78×10^{51}	3.16×10^{51}	5.62×10^{51}	10^{52}	1.78×10^{52}	3.16×10^{52}	5.62×10^{52}		
D_{nm}	0.07	0.06	0.14	0.11	0.05	0.02	0.02	0.09	0.05		
p-value	0.93	0.75	0.20	0.39	0.76	0.97	0.97	0.01	0.23		
Source density	10^{-8}	Mpc-3									
Luminosity [erg/year]	1.78×10^{51}	3.16×10^{51}	5.62×10^{51}	10^{52}	1.78×10^{52}	3.16×10^{52}	5.62×10^{52}	10^{53}	1.78×10^{53}	3.16×10^{53}	5.62×10^{53}
D_{nm}	0.29	0.18	0.15	0.08	0.06	0.04	0.03	0.02	0.02	0.04	0.07
p-value	0.76	0.01	0.33	0.71	0.94	0.95	0.68	0.94	0.99	0.57	0.01
Source density	10^{-9}	Mpc-3									
Luminosity [erg/year]	1.78×10^{52}	3.16×10^{52}	5.62×10^{52}	10^{53}	1.78×10^{53}	3.16×10^{53}	5.62×10^{53}	10^{54}	1.78×10^{54}	3.16×10^{54}	5.62×10^{54}
D_{nm}	0.13	0.09	0.09	0.05	0.04	0.03	0.10	0.09	0.09	0.09	0.13
p-value	0.89	0.75	0.41	0.97	0.89	0.67	0.02	7×10^{-3}	9×10^{-4}	2×10^{-4}	2×10^{-8}
Source density	10^{-10}	Mpc-3									
Luminosity [erg/year]	1.78×10^{53}	3.16×10^{53}	5.62×10^{53}	10^{54}	1.78×10^{54}	3.16×10^{54}	5.62×10^{54}	10^{55}	1.78×10^{55}	3.16×10^{55}	5.62×10^{55}
D_{nm}	0.14	0.06	0.10	0.09	0.05	0.10	0.12	0.16	0.13	0.13	0.16
p-value	0.36	0.87	0.20	0.03	0.27	4×10^{-5}	$7E\times10^{-5}$	5×10^{-12}	2×10^{-7}	4×10^{-6}	6×10^{-11}
Source density	10^{-11}	Mpc-3									
Luminosity [erg/year]	1.78×10^{54}	3.16×10^{54}	5.62×10^{54}	10^{55}	1.78×10^{55}	3.16×10^{55}	5.62×10^{55}	10^{56}	1.78×10^{56}	3.16×10^{56}	5.62×10^{56}
D_{nm}	0.09	0.14	0.07	0.13	0.15	0.16	0.12	0.14	0.12	0.13	0.06
p-value	0.45	0.06	0.40	4×10^{-5}	9×10^{-9}	5×10^{-8}	3×10^{-6}	5×10^{-9}	4×10^{-6}	2×10^{-7}	0.04
Source density	10^{-12}	Mpc-3									
Luminosity [erg/year]	1.78×10^{55}	3.16×10^{55}	5.62×10^{55}	10^{56}	1.78×10^{56}	3.16×10^{56}	5.62×10^{56}				
D_{nm}	0.11	0.19	0.11	0.14	0.18	0.15	0.09				
p-value	0.02	1×10^{-9}	0.13	2×10^{-3}	5×10^{-4}	5×10^{-4}	0.04				

Table 6.3: Summary table for the KS-2 test statistic results between the (Madau and Dickinson, 2014) SFH evolution scenario and the flat source scenario. The results are subdivided into sections for each local source density. The first line of each section corresponds to the neutrino source population luminosity in erg/year. The second line corresponds to the D_{nm} test statistic between the two distributions, calculated as given in Equation 6.5. The third line of each section shows the calculated p-value, which is the probability of observing a test statistic value (D_{nm}) as extreme as, or more extreme than, the observed value under the null hypothesis. The D_{nm} test statistic and p-values were calculated using unbinned data. The comparison plots between the two models source distribution and the respective CDFs are given in Appendix B.

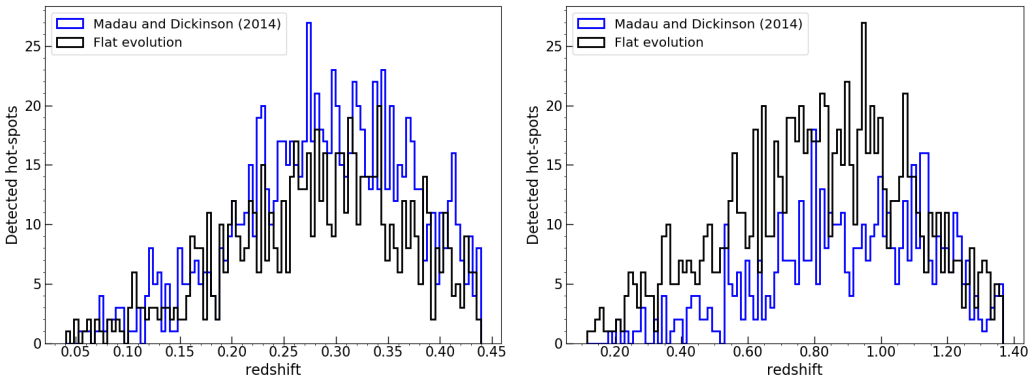

Figure 6.4: Examples of detected source distributions with CTA for 2 simulated neutrino populations: $\rho_o = \times 10^{-10}$ Mpc^{-3} and $L_\nu = 1.78 \times 10^{54}$ erg/yr (left) and $\rho_o = \times 10^{-11}$ Mpc^{-3} and $L_\nu = 3.16 \times 10^{55}$ erg/yr (right). The histograms show the number of detected sources for each of the evolution models used: Madau and Dickinson (2014) in blue, and flat evolution in black. The p-value associated to the left (right) plot is 0.27 (5×10^{-8}), therefore the null hypothesis is accepted (rejected). The corresponding CDFs are shown in Figure 6.5.

shown in blue, and for the flat source evolution is shown in black. The redshift range from each distribution was segmented into 100 bins to show a good approximation of the expected CDF. The D_{nm} between the two distributions is calculated as the maximum distance between the two EDFs considered. In the first example case (left plot) the calculated value for the KS-2 test statistic was $D_{nm} = 0.05$, while in the second case (right plot), the calculated KS-2 test statistic was $D_{nm} = 0.16$. The comparison plots between the distributions of the two source evolution models and their respective EDFs are given in Appendix B. An unbinned KS-2 test was performed to obtain the p-values shown in Table 6.3.

Using the results from Table 6.3, the calculated p-value for the common parameter space is shown in a logarithmic colour scale in Figure 6.6. Lower p-values are associated with a higher confidence level. The cases in which the null hypothesis was rejected with an equivalent 5σ significance level (p-values $< \alpha = 3 \times 10^{-7}$) are shown in dark blue, while the cases in which the KS-2 test was not able to find a significant difference between the CTA-detected source distributions are shown in white.

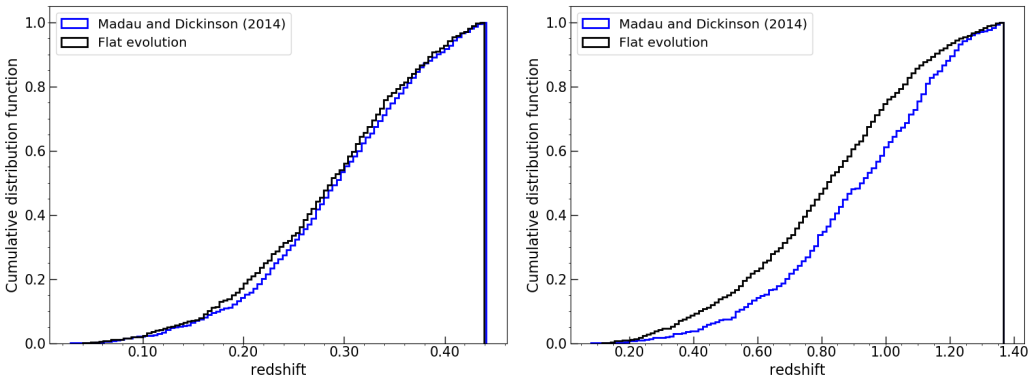

Figure 6.5: Cumulative distribution functions (CDFs) for the CTA-detected source distributions given in Figure 6.4. The CDF for the Madau and Dickinson (2014) SFH source evolution scenario is presented in blue, and for the flat source evolution scenario is presented in black. The D_{nm} test statistic is calculated as the maximum distance between the two CDFs considered. For the left plot $D_{nm} = 0.05$, while in the right plot the $D_{nm} = 0.16$. The associated p-value to the left (right) plot is 0.27 (5×10^{-8}), therefore the null hypothesis is accepted (rejected). All the comparison plots between the two source evolution models are given in Appendix B.

The range of values that appear in lighter blue colour have associated p-values small enough compared to the equivalent 3σ significance level (p-values $< 3 \times 10^{-3}$) and 4σ significance level (p-values $< 7 \times 10^{-5}$). For $\rho_o = 10^{-12}$ Mpc^{-3} 3 simulated populations around $L_\nu \sim \times 10^{56}$ erg/yr have associated p-values lower than the equivalent 3σ significance level, and at $L_\nu = 3.16 \times 10^{55}$ erg/yr, the simulated populations are significantly different at the 5σ significance level. For $\rho_o = 10^{-11}$ Mpc^{-3} all the simulated populations between $10^{55} \leq L_\nu \leq 3.16 \times 10^{56}$ erg/yr have a associated p-values lower than the equivalent 4σ significance level, and in 4 cases the simulated populations can be considered significantly different at the 5σ significance level. Finally, the simulated populations with local source density of $\rho_o = 10^{-10}$ Mpc^{-3} and luminosities $L_\nu \geq 3.16 \times 10^{54}$ have associated p-values lower than the equivalent 4σ significance level and for $L_\nu \geq 10^{55}$ 3 of the 4 simulated populations have associated p-values lower than the equivalent 5σ significance level.

The blue zone corresponds to a region of the parameter space with the lowest local source densities and highest luminosities which extends up to $z \sim 3$; many of these simulated populations coincide with the sensitive corner of the parameter space

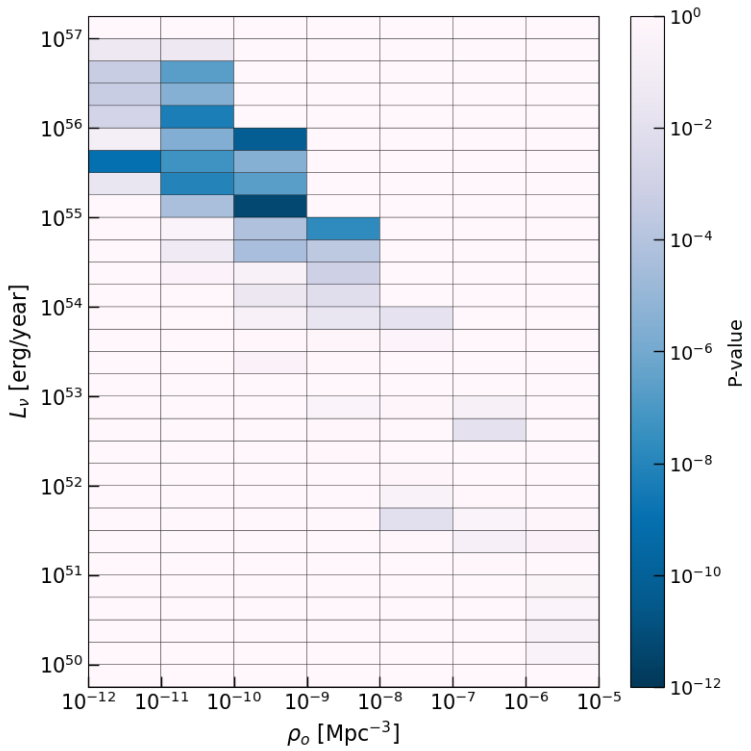

Figure 6.6: Results of the KS-2 test performed in the common region of the parameter space between the two source evolution models employed (SFH source evolution vs flat source evolution).

identified with a black triangle in Figures 5.11 and 5.13. These results show that the two models used to simulate the source evolution of the neutrino populations can be only discriminated above redshift $z \sim 1$ and up to the redshift reach limit $z \sim 3$, in a range where the source evolution model by Madau and Dickinson (2014) peaks ($z \sim 1.8$) and is above the constant value considered for the flat evolution model (0.10 $M_\odot$ yr^{-1} Mpc^{-3}, see Figure 5.2 in Section 5.1).

On the other hand, at lower redshifts the impact of the selection of the source evolution model is not perceptible in the CTA-detected source distributions. According to the results obtained in Chapter 5 for the simulated neutrino populations with a high local source density ($10^{-5} \geq \rho_o \geq 10^{-9}$ Mpc^{-3}) and modest luminosities ($L_\nu < 10^{55}$ erg/year), IceCube hot-spots (points in the sky above the 5σ discovery potential) were identified only for $z < 1$. In most of these simulated source populations, the calculated p-values are below the equivalent 3σ significance level. The

only exceptions are the 3 highest luminosity populations for $\rho_o = 10^{-9}$ Mpc^{-3}, which have calculated p-values going down to the equivalent 4σ significance level, and only in the case of the simulated populations at $L_\nu = 5.62 \times 10^{54}$ erg/year the calculated p-value does not reach the equivalent 5σ significance level.

The jumps observed in the p-values in Figure 6.6 might be related to 3 different factors: the relatively small size (<100 CTA-detected sources) of the samples used for the KS-2 test in some regions of the parameter space (limited by the conditions of the simulations), the effects induced by the two different SFH models, and statistical fluctuations/noise related to the neutrino and gamma-ray simulations.

In practical terms, a simple flat source evolution model such as the one used for the neutrino simulations, would make no significant difference to the CTA results at redshifts $z < 1$. It is only when looking at high redshift regions and analysing distributions with $> 10^2$ detected sources that a significant statistically difference between the detected source distributions may be found.

6.3 Conclusions

The calculated redshift reach of the simulated gamma-ray observations with CTA for the considered neutrino source populations in the simulations showed similar trends for both source evolution scenarios tested (SFH model of Madau and Dickinson (2014) and a flat source evolution model). As expected, the redshift reach increases with the source luminosity and at redshifts $z < 1$ the CTA detection probability is almost 100%. The redshift reach values for all the simulated populations at different local source densities and source luminosities are summarised in Figures 6.2 and 6.3. It was found that at $z > 3$ the EBL attenuation effect would limit CTA observations.

The underlying SFH models produced significant changes in the CTA-detected source distributions in a sensitive region of the parameter space (highlighted in Figure 6.6 in dark blue colour), in which the detected hot-spots are distributed

over a larger redshift range (up to $z \sim 1.8$ for $\rho_o = 10^{-10}$ Mpc^{-3} and $z \sim 3$ for $\rho_o = 10^{-11}$, 10^{-12} Mpc^{-3}), allowing the SFH source evolution model of (Madau and Dickinson, 2014) to peak at $z \sim 1.8$ (see Figure 5.2) and producing measurable differences in the CTA-detected source distributions. However, a simple assumption of a flat source evolution model can be used in the neutrino simulations and produce similar results at redshifts $z < 1$, where the simulated populations had the highest local source densities ($\rho_o \geq 10^{-9}$ Mpc^{-3}) and modest luminosities ($L_\nu < 10^{55}$ erg/year).

Applying a statistical tool (the KS-2 test), an EDF of CTA-detected sources can be compared to simulated CDFs with different evolution models. According to the results obtained in this Chapter, if there is enough volume of data (> 100 detected sources) in the EDF expanding over redshifts $z > 2$, it will be feasible to discriminate SFH between models to a certain significance level and tell if there is a preferred model.

The results from the NToO program have shown the potential of the CTA Omega configuration arrays to detect under optimal observing conditions IceCube hotspots exceeding the 5σ discovery potential. A high detection probability was found for the simulated sources at redshifts $z < 1$ and luminosities between $10^{51} < L_\nu < 10^{55}$ erg/year, these 'nearby' sources would be easily detected with CTA (practically 100%) according to the gamma-ray simulations performed. However more scenarios can be studied within the NToO program, which include using other options for SFH source evolution models in the simulation of the neutrino source populations, trying as well other EBL models when simulating the gamma-ray observations with CTA, test CTA intermediate array layouts, and study CTA performance under high NSB conditions. The future plans for the NToO program are detailed in Chapter 7.

Chapter 7

Conclusion

In this thesis, the connection between VHE neutrinos and gamma-rays has been explored in the context of a photohadronic ($p\gamma$) interaction scenario. A summary of the main scientific results obtained is given below, highlighting the conclusions for each chapter. The next steps to consider in the near and mid term future are discussed in Section 7.2 before giving the final remarks in Section 7.3 to conclude this work.

7.1 Summary

Chapter 1 serves as an introduction to the thesis, starts with an overview of the last 6 decades in gamma-ray astronomy, the main space-based gamma-ray detectors and their discoveries are reviewed, with a special emphasis on the *Fermi*-LAT Gamma-ray Space Telescope. Then, the physics behind the imaging atmospheric Cherenkov technique used in modern IACTs is discussed alongside the development of ground-based gamma-ray observatories, including the 3rd generation of IACTs (such as VERITAS, H.E.S.S. and MAGIC) before introducing the CTA Observatory. Finally, a quick review about neutrino astronomy is also given, including the IceCube neutrino observatory, its updated real-time alert system, and the highlights of the neutrino alert IC-170922A, for which a $\sim 3\sigma$ significance level correlation was found with the flaring blazar TXS-0506+056.

In Chapter 2 the theoretical framework for $p\gamma$ interactions is reviewed. The chapter starts by going through the categories of gamma-ray sources, the AGN classification and properties, and then proceeds to describe the main object of study in this thesis, blazars. Some key concepts are explored in this chapter, like the Fermi acceleration mechanism, the EBL attenuation effect and the differences between leptonic and hadronic scenarios in blazars. The photohadronic flaring model scenario and the Δ^+-resonance approximation used in Chapters 3 and 4 are explained, and finally the AIC test, a statistical tool for model comparison, is defined.

Chapter 3 presents a study of the blazar Mrk 421 during a flaring state in March 2010. The VHE gamma-ray data from MAGIC, VERITAS and Whipple were fitted with the photohadronic model and the possibility of a dominant photoharonic contribution is explored. A tailored *Fermi*-LAT data analysis was performed in the 100 MeV to 1 GeV energy range, and the steps involved in a typical point-source analysis are described in detail. Using a power-law (PL) extrapolation of the MeV spectrum as the target photon spectrum for $p\gamma$ interactions, the Mrk 421 spectrum was fitted on the days with sufficient photon statistics to have a significant detection (TS > 25) in the MeV range, a total of 5 datasets from IACTs observations.

The photohadronic flaring model was fitted to the VHE gamma-ray data and compared with the results of a one-zone and a two-zone leptonic model given in MAGIC Collaboration and VERITAS Collaboration (2015a) using the Akaike information criterion (AIC). In all cases the photohadronic model was favoured as a better fit description than the one-zone leptonic model, similarly for the two-zone leptonic model in 3 observations out of the 5.

The evaluation and comparison of the models using the AIC test showed the potential of including $p\gamma$ interactions in blazar modelling. It is concluded that a hadronic component could be dominant on specific days of the flaring, followed by a dominant SSC emission. If the proton injection occurs randomly, there is no preferred time for hadronic dominance during the flare. The expected number of neutrino events which would have been detected with IceCube during the 14-day period of

Mrk 421's flare was estimated using the effective area ($A_{\text{eff}}(E_\nu)$) of the 59-string IceCube configuration operating in 2010. With a resulting value of $N_{\text{events}} < 0.14$, any neutrino emission from Mrk 421 resulting from a $p\gamma$ process would have not been detected with IceCube.

In Chapter 4 the gamma-ray emission and possible neutrino detection from the blazar 4FGL J0658.6+0636, a counterpart candidate for the neutrino alert IC-201114A, was studied over 12.3-years of historical data from *Fermi*-LAT and during a 4-month time window around the time of the neutrino alert.

Two significant periods (named BIN-A and BIN-B) of gamma-ray activity from 4FGL J0658.6+0636 were identified by performing a *Fermi*-LAT data analysis of the source in the 200 MeV to 300 GeV energy range over 12.3-years. The photohadronic contribution to the gamma-ray spectrum and associated neutrino emission were calculated for both periods. The minimum detection time (MDT, defined as the time taken by IceCube to detect two neutrino events above the background level) for the corresponding IceCube configuration was estimated using the neutrino spectrum for each period.

The results obtained with the photohadronic emission model were compatible with the behaviour of the source during BIN-B (MJD 57830 -58279), which is also coincident with the highest energy photon recorded ($E_\gamma = 155$ GeV) by the LAT from the source. The approximate MDT calculated for BIN-B was $\sim$ 2.5-days, making the detection of an excess of neutrino events above the atmospheric background plausible during this period with IceCube (IC86 configuration). During BIN-A (MJD 54683 - 55132) the calculated MDT was $\sim$ 160 days and given that there was no significant detection of the source in gamma-rays on shorter timescales, BIN-A behaviour points towards low-level emission over an extended period rather than a single bright event.

No significant gamma-ray emission was found around the time of the neutrino alert, therefore the photohadronic flaring model was employed assuming a gamma-ray

flux just below the *Fermi*-LAT sensitivity with the two known historical behaviours of the source (BIN-A/BIN-B like, see Figure 4.11). MDTs of between $\sim$ 1-hour with the BIN-B spectrum, and 12-days assuming BIN-A like behaviour are predicted. Although the lack of a gamma-ray signal around the time of the IC-201114A alert is compatible with the photohadronic flaring model scenario, further evidence is needed to establish 4FGL J0658.6+0636 as a neutrino emitter.

The last two chapters from this thesis describe the work done by myself and collaborators for the Neutrino Target of Opportunity (NToO) program for CTA. A pipeline was set up to compute gamma-ray simulations to predict the CTA detection probability of blazar-like, steady point-source populations simulated with FIRESONG and able to saturate the IceCube diffuse neutrino flux. Performance plots for both CTA sites were produced, in which the magnetic field effect on the shower development (more important for CTA-N), and high zenith angle observations were identified as the main reasons for falls in the calculated CTA detection probability. A performance loss, up to 70% in detection probability, was found when simulating observations with zenith angles between 40° and 60°. On the other hand, the difference found for observation angles below 40° in zenith was less than 10% detection probability. The regions with a high CTA detection probability were identified in the parameter space tested (local source density ρ_o vs source luminosity L_ν). Results show a high CTA detection probability for steady source populations with a local source density $\rho_o \geq 10^{-9}$ Mpc^{-3}.

Combined detection probability (IceCube+CTA) curves were calculated as a function of the source luminosity taking into account CTA visibility constraints. The IceCube detection probability turned out to dominate over CTA's detection probability in the final result.

The neutrino simulations used two different source evolution models, one following a flat evolution and the second based on the SFH model by Madau and Dickinson (2014). In Chapter 6 the differences between the simulated results under these two models for CTA are studied. For both source evolution scenarios the redshift reach

increases with source luminosity, and at redshifts $z < 1$ practically 100% of the simulated sources were detected by CTA. It was also found that at $z > 3$ the EBL attenuation effect would limit CTA observations.

The CTA-detected source distributions from the two source evolution models were compared using a statistical tool, the Kolmogorov-Smirnov two-sample test (KS-2). A significant difference between the results were found only in a sensitive region of the parameter space, in which the detected sources are distributed up to $z \sim 1.8$ for $\rho_o = 10^{-10}$ Mpc^{-3} and up to $z \sim 3$ for $\rho_o = 10^{-11}$, 10^{-12} Mpc^{-3}. In contrast, no significant differences were found for the simulated steady source populations with the highest local source densities ($\rho_o \geq 10^{-9}$ Mpc^{-3}) and modest luminosities ($L_\nu < 10^{55}$ erg/year) which were detected at redshifts $z < 1$.

7.2 Future work

7.2.1 Modelling of flaring gamma-ray blazars

The photohadronic flaring model presented in Chapter 2 takes a phenomenological approach to calculate the $p\gamma$ contribution to the VHE gamma-ray spectrum of the source and the associated neutrino spectrum. The model assumes that electrons and protons are co-accelerated into a single emission region inside the blazar's jet, in which the $p\gamma$ interactions occur between the high energy protons and SSC photons produced in the MeV energy range.

The photohadronic contribution to the VHE gamma-ray emission is dependent on the target photon spectrum considered for the source. In Chapters 3 and 4, an extrapolation of the *Fermi*-LAT gamma-ray photon spectrum is used; however, the addition of experimental gamma-ray data in the Mev and sub-MeV regime would enable the model results to be improved. In this regard, the AMEGO mission (McEnery et al., 2019), a space-based gamma-ray instrument expected to launch no later than Dec. 2028, would provide coverage for the 200 keV to > 10 GeV energy

range with $> 20\times$ better sensitivity than COMPTEL and $\sim 5\times$ better angular resolution than *Fermi*-LAT. Precise measurements from AMEGO in combination with CTA observations up to tens of TeV would be ideal to test the photohadronic flaring model to a source. In addition, the expected sensitivity of CTA at multi-TeV energies will make possible to discriminate between pure leptonic and hadronic scenarios.

To evolve the photohadronic flaring model, extending it to lower energy regions (below 100 GeV), it would be necessary to include leptonic contributions, such as the SSC leptonic component and the synchrotron emission from charged particles in the hadronic decay chain (p, π^+, π^-, μ^-), as these other contributions could play an important role at VHE. This is not a trivial step, as the additional components would need to be calculated through Monte Carlo simulation methods (Mücke et al., 2000; Mücke and Protheroe, 2001), which require long computational times and efficient implementation codes, or as an alternative, by using semi-analytical numerical methods (Kelner and Aharonian, 2008) to compute the particle energy distributions for protons, electrons, neutrinos and photons to derive the final energy spectra. The inclusion of these components would lead to a lepto-hadronic model scenario able to fit the available multi-wavelength SED data from blazars, and provide a wider picture of the source.

7.2.2 NToO program for CTA

The NToO program for CTA has plans to expand the study of steady and transient sources that could lead to a significant correlated detection between high energy neutrino events and their corresponding gamma-ray counterpart. In the near and midterm future, the following would be useful:

- Simulating longer observation times for steady sources (5-hours, 50-hours) with the Omega configuration array: The results obtained for the simulated steady source populations with 30-min observations showed a region in the

parameter space (low local source densities and high source luminosities) with the lowest CTA detection probability. It would be worth study CTA performance in this region with longer observation times.

- Study CTA performance with the Alpha configuration array: The Alpha configuration array is planned to be deployed in the the early years of CTA science operations, with a lower number of operational telescopes: 4 LSTs and 5 MSTs for CTA-N and 15 MSTs and 50 SSTs for CTA-S.

- CTA performance under high NSB: For the results on steady sources, dark night observations (low background noise) were assumed for CTA. The NSB is the diffuse light from the night sky and accounts for the light coming from several sources that produce noise in the images and reduce the performance of IACTs. CTA observations with up to 5 times the NSB level in normal dark sky observations are anticipated when the moon is above the horizon (CTA Consortium, 2017). A performance study of CTA under high NSB conditions would be useful to get an idea of target of opportunity observations with moon light and how to extend the duty cycle of the telescopes within the NToO program.

- CTA response to transient sources mimicking the 2014-15 neutrino flare of TXS 0506+056: It is important to investigate immediate follow-up observation scenarios for sources of transient nature. A population of neutrino sources with different flaring fractions that saturates the diffuse neutrino flux would recreate the IceCube high energy astrophysical neutrino alerts. The sources would be modelled using the phenomenological approach of (Halzen et al., 2019) to the blazar TXS 0506+056 during the 2014-15 neutrino flare. By applying minimal changes to the pipeline developed for the steady source gamma-ray simulations in Chapter 5, CTA follow-up observations can be simulated and the detection probability curves calculated, alongside performance plots for the Omega/Alpha IRFs set in a similar way. Visibility constraints,

and the effect of delays introduced by the alert system and the telescope re-pointing, can also be included.

In addition, the construction of cubic-km neutrino detectors in the northern hemisphere, like KM3NeT or P-ONE, would be essential to complement CTA-S observations, as the results presented in this thesis obtained from the NToO simulations are 'IceCube biased'. With IceCube-Gen2 (2033) operating in the southern hemisphere, KM3NeT/ARCA (under construction) and P-ONE (2024) in the northern hemisphere, alongside both CTA sites running (2026), full-sky coverage of the NToO program will be reached in the next decade.

7.3 Final remarks

Multi-messenger astronomy has already provided some hints of hadronic acceleration in blazars, the follow-up of the IC-170922A neutrino alert resulted in a quick identification of the flaring blazar TXS 0506+056 as the most likely source candidate and gave a multi-wavelength picture of its SED. The modelling of the VHE gamma-ray and neutrino emission from blazars remains an important piece of the puzzle, as we continue to study possible source candidates and discriminate between hadronic production scenarios.

In the upcoming years, the next generation of gamma-ray observatories, such as CTA and AMEGO, together with the next generation of neutrino detectors, like IceCube-Gen2, KM3NeT and P-ONE; will play a crucial role as we try to identify and understand sources capable of cosmic-ray acceleration and their emission mechanisms.

Appendix **A**

Redshift Distribution Plots

The plots in Figures A.1 to A.3 summarise the detected source distributions with CTA for the different simulated populations for the source evolution model of Madau and Dickinson (2014). Each Figure contains the CTA-detected source distributions for the luminosity range (L_ν) simulated for each local source density (ρ_o). Figures A.4 to A.6 summarise the CTA-detected source distributions simulated with flat source evolution scenario.

The results are presented for three different zenith angle options: 20° (first row), 40° (second row) and 60° (third row). The results for CTA-N are given in the left columns and for CTA-S in the right column of each Figure. The colour scale shows the lowest luminosities in blue and the highest luminosities in yellow. The distributions are normalised to the total number of CTA detected sources for each simulated population.

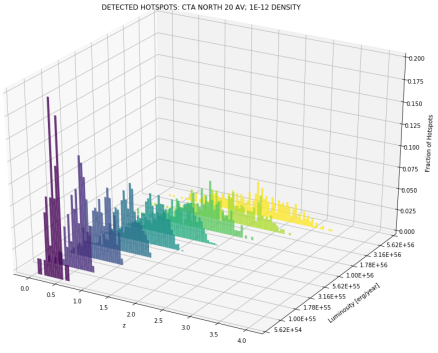

(a) CTA-N 20° zenith

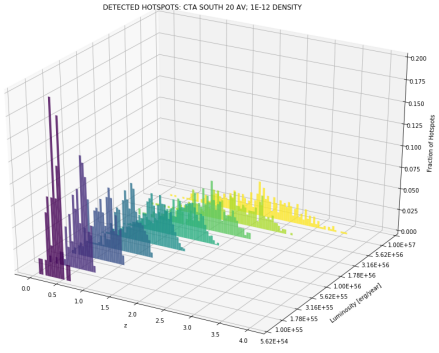

(b) CTA-S 20° zenith

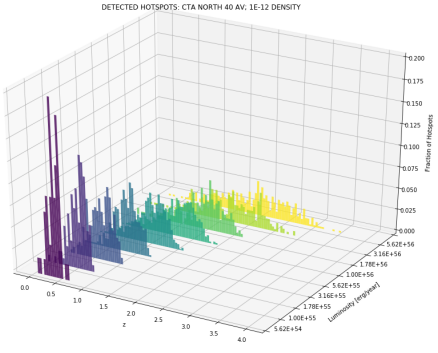

(c) CTA-N 40° zenith

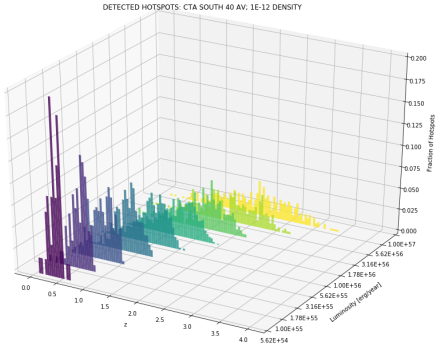

(d) CTA-S 40° zenith

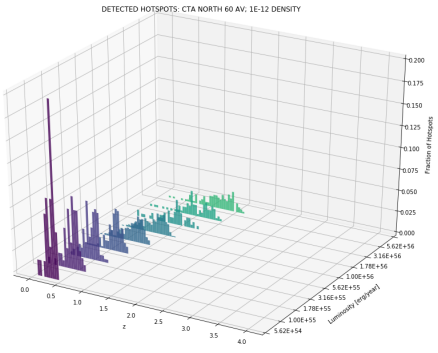

(e) CTA-N 60° zenith

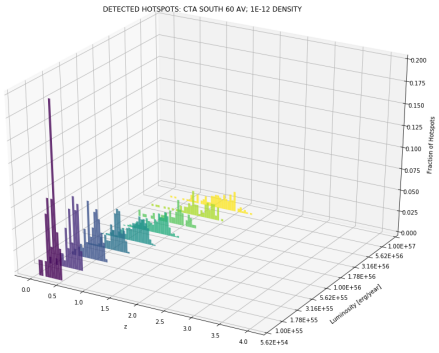

(f) CTA-S 60° zenith

Figure A.1: Detected source distributions for $\rho_0 = 1 \times 10^{-12}$ Mpc^{-3} local source density simulated with the SFH source evolution model of Madau and Dickinson (2014).

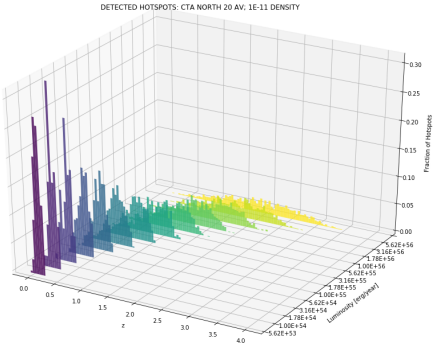

(a) CTA-N 20° zenith

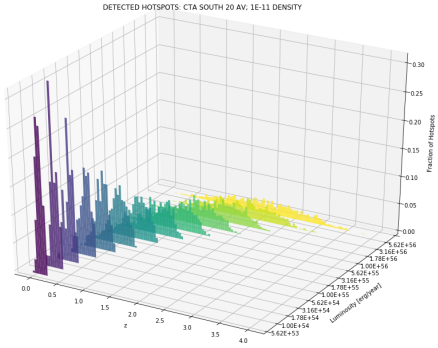

(b) CTA-S 20° zenith

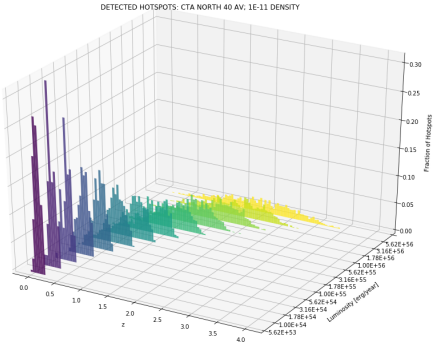

(c) CTA-N 40° zenith

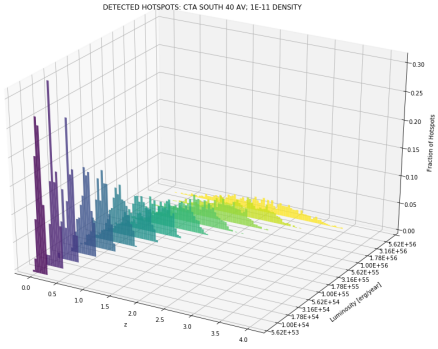

(d) CTA-S 40° zenith

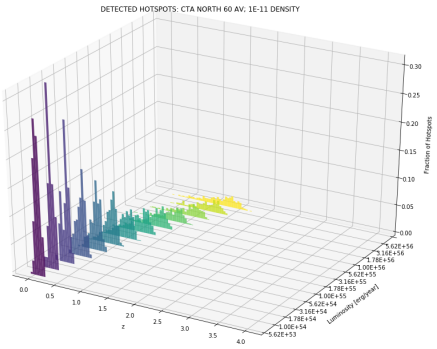

(e) CTA-N 60° zenith

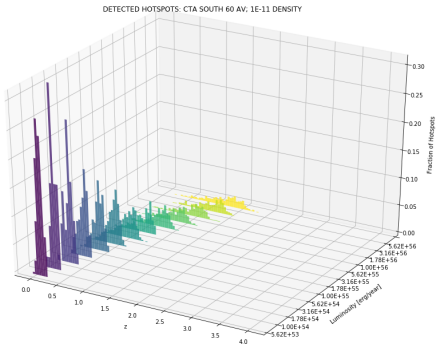

(f) CTA-S 60° zenith

Figure A.2: Detected source distributions for $\rho_0 = 1 \times 10^{-11}$ Mpc^{-3} local source density simulated with the SFH source evolution model of Madau and Dickinson (2014).

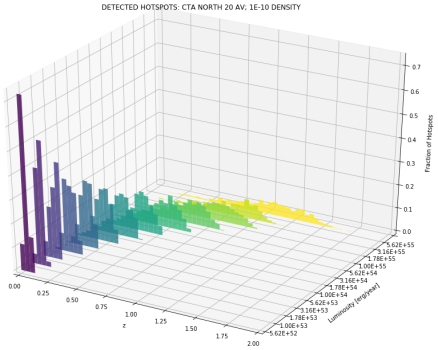

(a) CTA-N 20° zenith

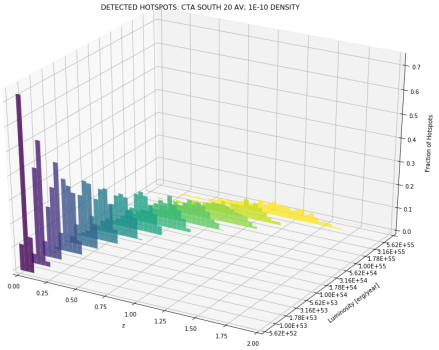

(b) CTA-S 20° zenith

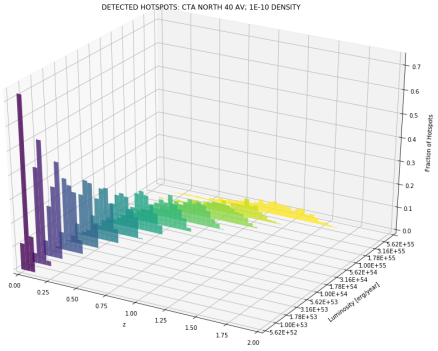

(c) CTA-N 40° zenith

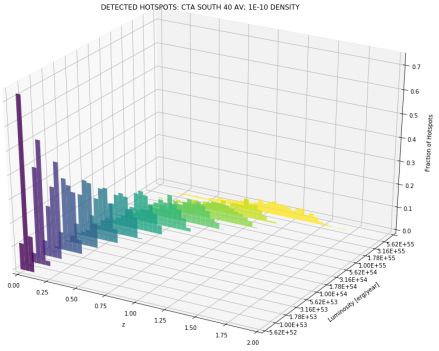

(d) CTA-S 40° zenith

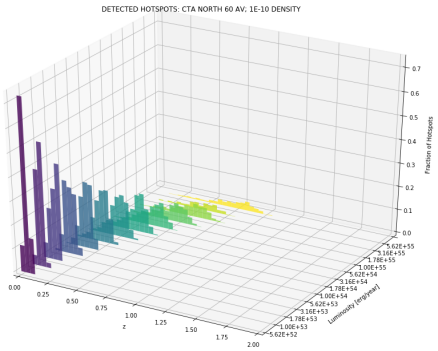

(e) CTA-N 60° zenith

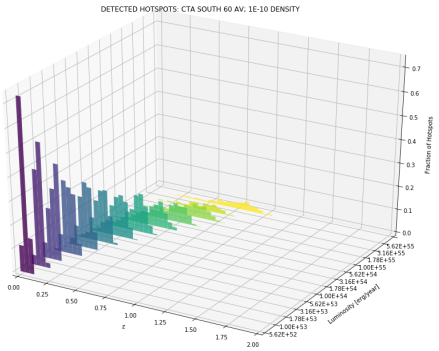

(f) CTA-S 60° zenith

Figure A.3: Detected source distributions for $\rho_0 = 1 \times 10^{-10}$ Mpc^{-3} local source density simulated with the SFH source evolution model of Madau and Dickinson (2014).

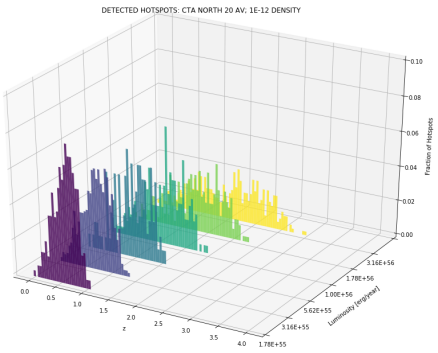

(a) CTA-N 20° zenith

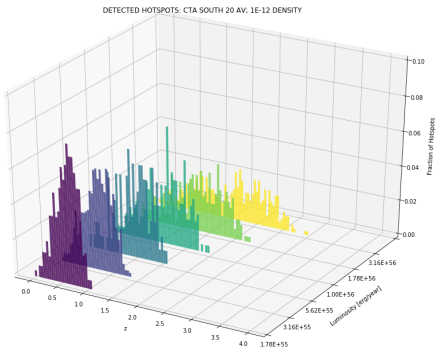

(b) CTA-S 20° zenith

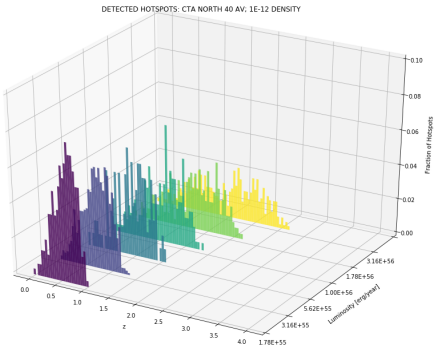

(c) CTA-N 40° zenith

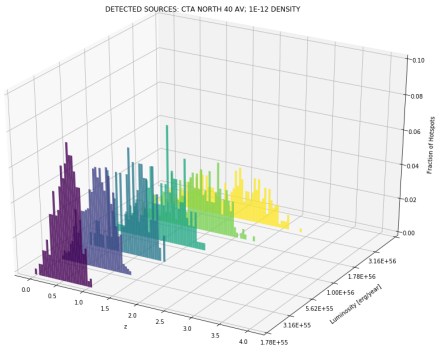

(d) CTA-S 40° zenith

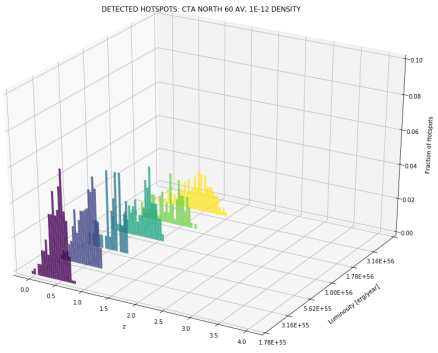

(e) CTA-N 60° zenith

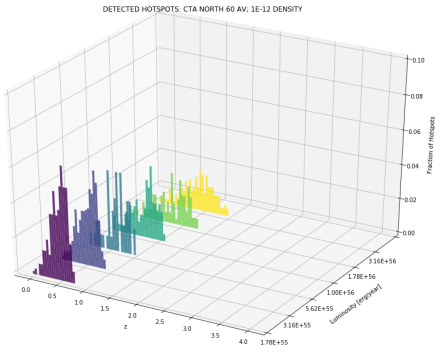

(f) CTA-S 60° zenith

Figure A.4: Detected source distributions for $\rho_0 = 1 \times 10^{-12}$ Mpc^{-3} local source density simulated with a flat evolution scenario.

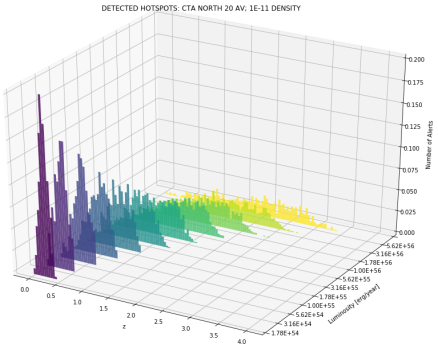

(a) CTA-N 20° zenith

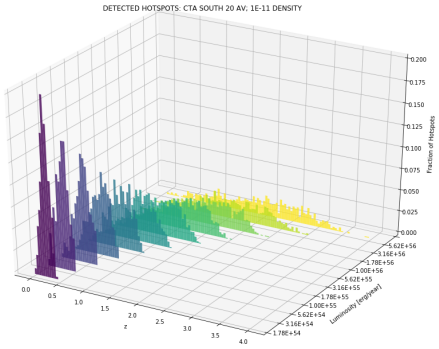

(b) CTA-S 20° zenith

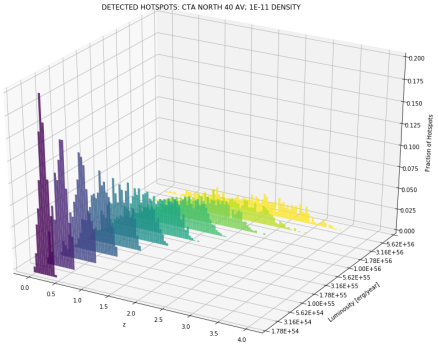

(c) CTA-N 40° zenith

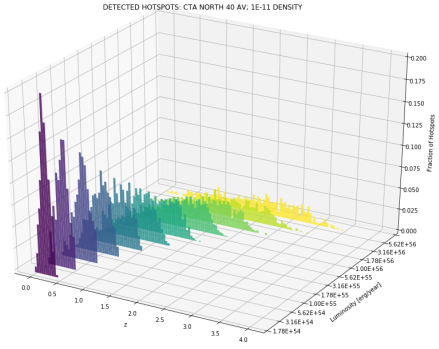

(d) CTA-S 40° zenith

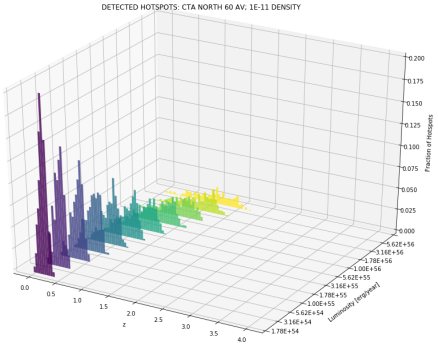

(e) CTA-N 60° zenith

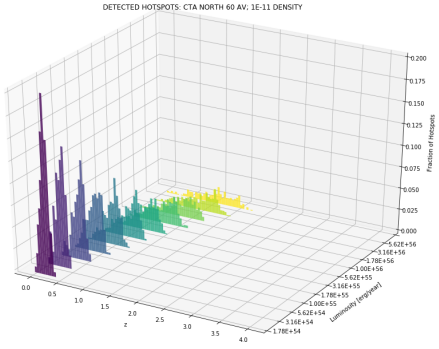

(f) CTA-S 60° zenith

Figure A.5: Redshift distributions for $\rho_0 = 1 \times 10^{-11}$ local source density simulated with a flat evolution scenario.

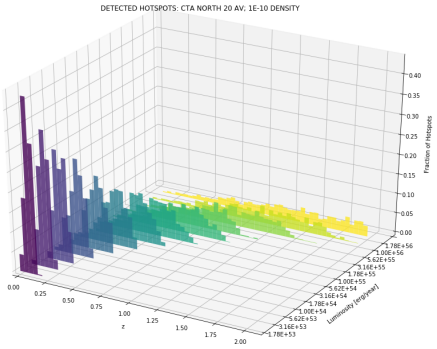

(a) CTA-N 20° zenith

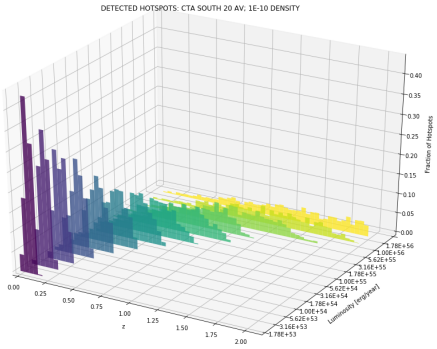

(b) CTA-S 20° zenith

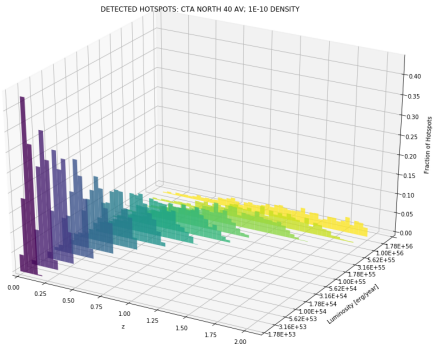

(c) CTA-N 40° zenith

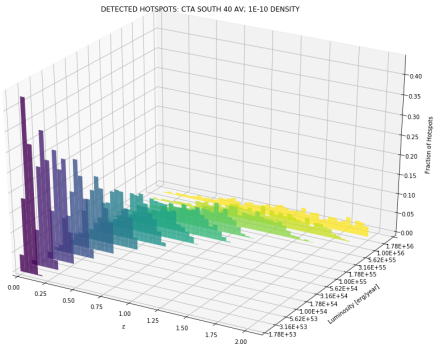

(d) CTA-S 40° zenith

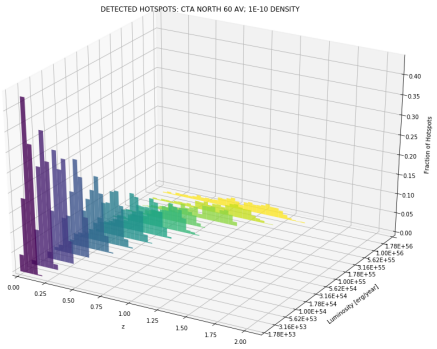

(e) CTA-N 60° zenith

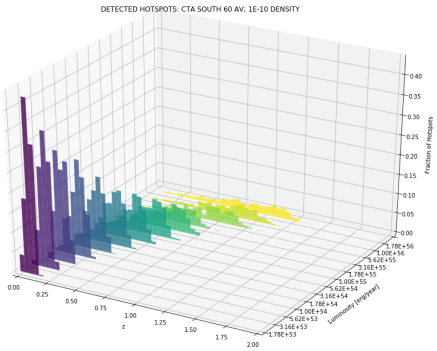

(f) CTA-S 60° zenith

Figure A.6: Detected source distributions for $\rho_0 = 1 \times 10^{-10}$ Mpc^{-3} local source density simulated with a flat evolution scenario.

Appendix B

Cumulative Distribution Plots for CTA-detected Sources

The following plots show the CTA-detected source distribution plots (left columns) and the corresponding cumulative distribution function plots (CDFs, right columns) for each combination in the parameter space (ρ_o vs L_ν) in which both, the SFH source evolution model of Madau and Dickinson (2014) and a flat source evolution model were used. The results for the SFH model are presented in blue, and for the flat source evolution scenario are shown in black.

The Kolmogorov-Smirnov two-sample (KS-2) test statistic is used to compare the SFH and the flat source evolution scenario (see Chapter 6). The KS-2 test makes no assumption about the distribution of data. The calculated values for the (KS-2) test statistic and p-values for all cases are summarised in Table 6.3.

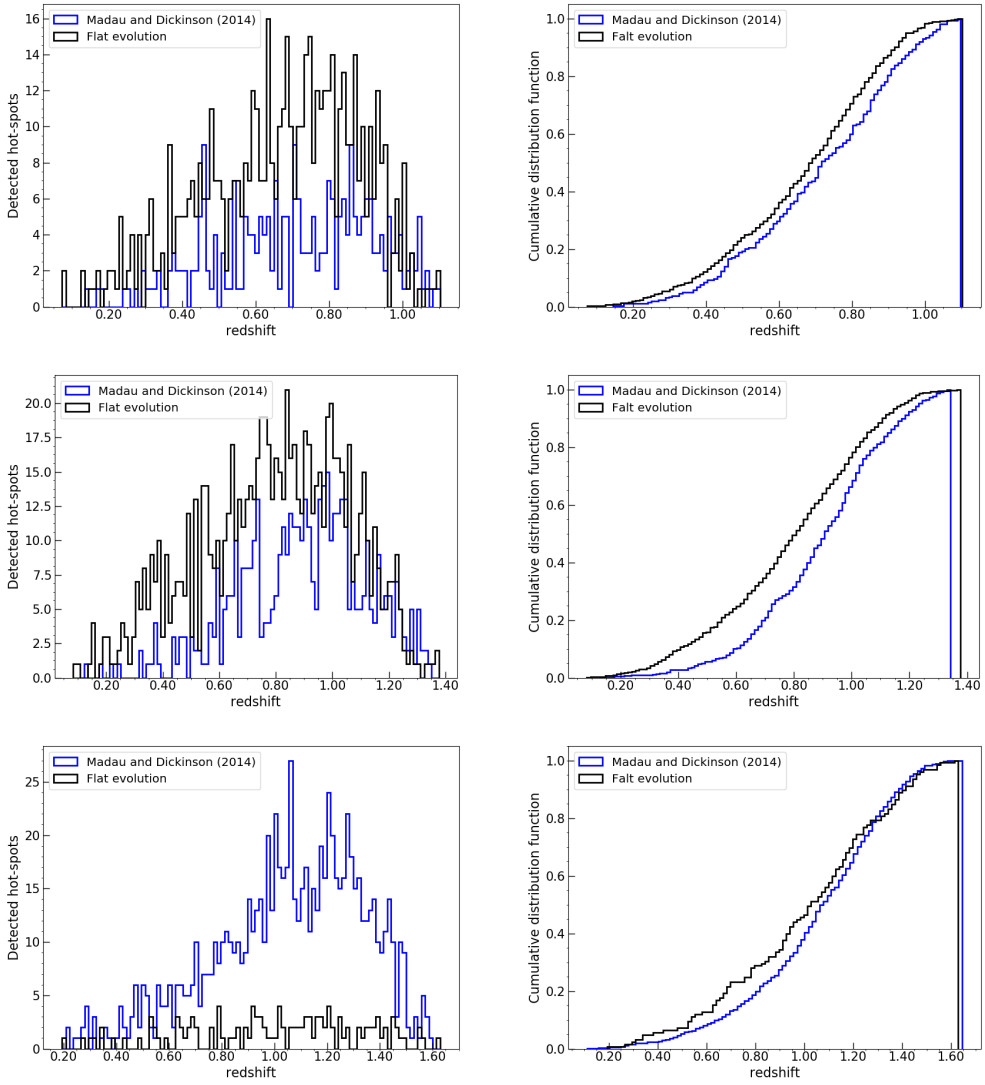

Figure B.1: Detected source distributions and cumulative distribution functions for $\rho_0 = 1 \times 10^{-12}$ Mpc^{-3}, and $L_\nu = 1.78 \times 10^{55}$, 3.16×10^{55}, 5.62×10^{55} (top to bottom).

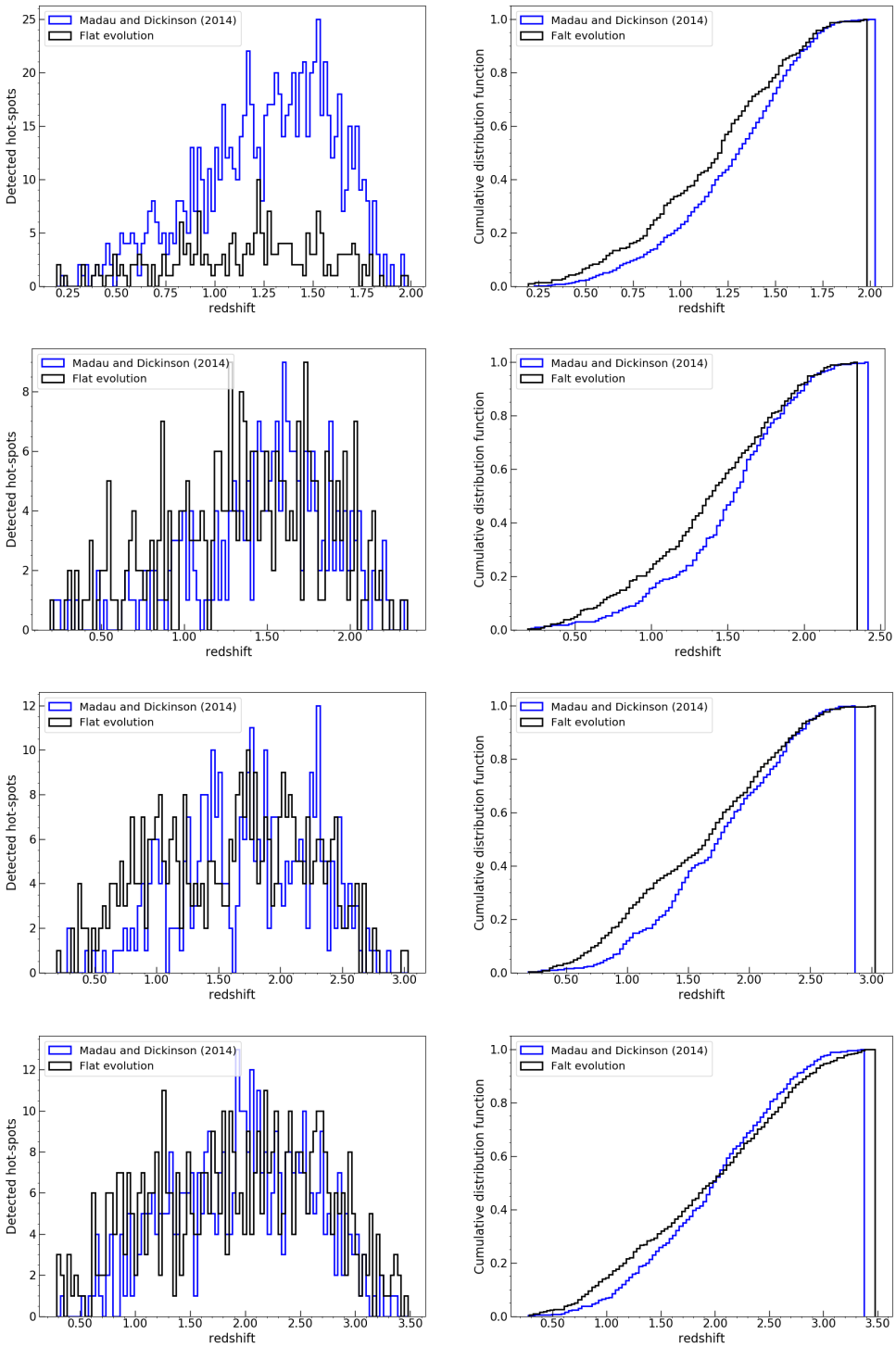

Figure B.2: Detected source distributions and cumulative distribution functions for $\rho_0 = 1 \times 10^{-12}$ Mpc^{-3} and $L_\nu = 1 \times 10^{56}$, 1.78×10^{56}, 3.16×10^{56}, 5.62×10^{56} (top to bottom).

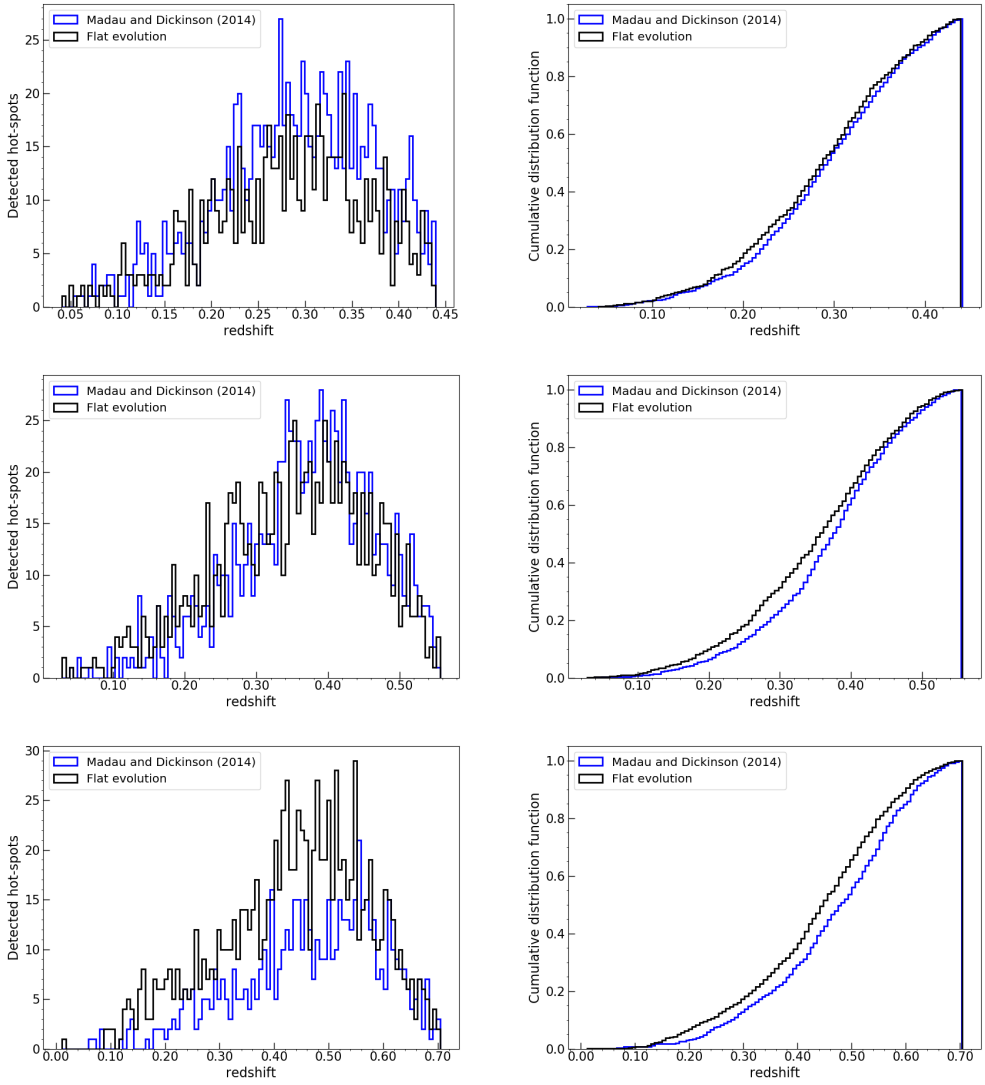

Figure B.3: Detected source distributions and cumulative distribution functions for $\rho_0 = 1 \times 10^{-11}$ Mpc^{-3} and $L_\nu = 1.78 \times 10^{54}$, 3.16×10^{54}, 5.62×10^{54} (top to bottom).

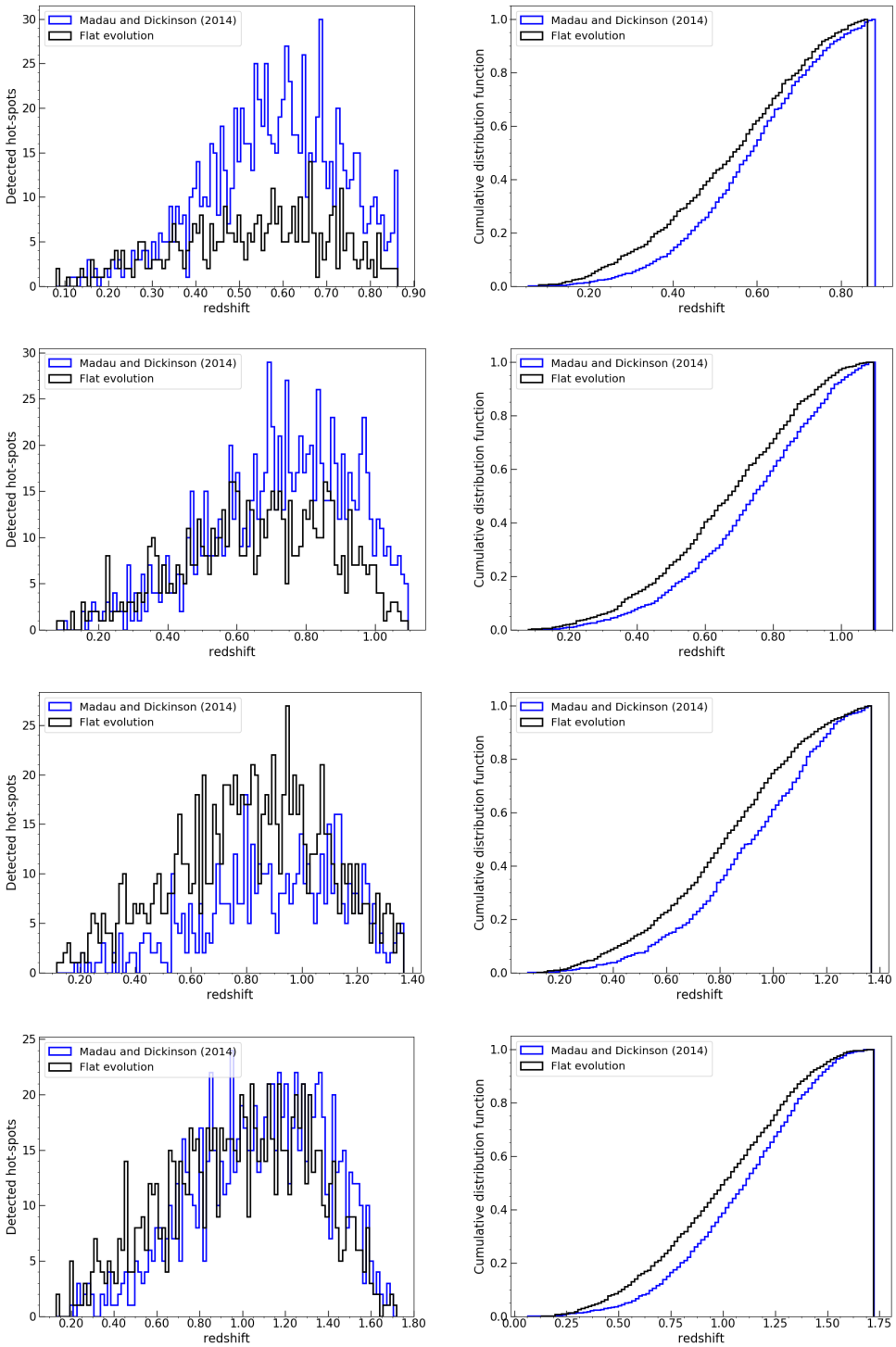

Figure B.4: Detected source distributions and cumulative distribution functions for $\rho_0 = 1 \times 10^{-11}$ Mpc^{-3} and $L_\nu = 1 \times 10^{55}$, 1.78×10^{55}, 3.16×10^{55}, 5.62×10^{55} (top to bottom).

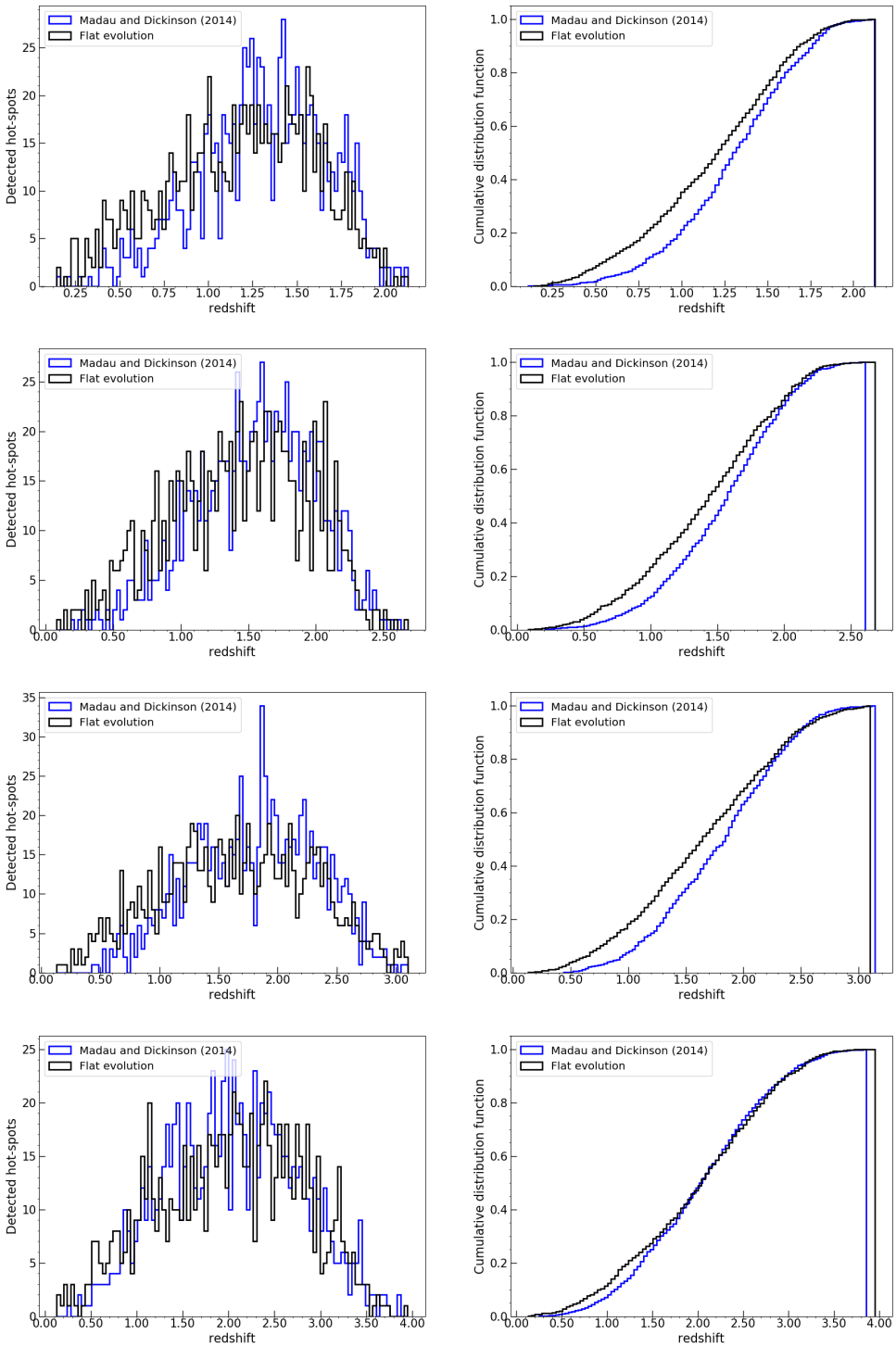

Figure B.5: Detected source distributions and cumulative distribution functions for $\rho_0 = 1 \times 10^{-11}$ Mpc^{-3} and $L_\nu = 1 \times 10^{56}$, 1.78×10^{56}, 3.16×10^{56}, 5.62×10^{56} (top to bottom).

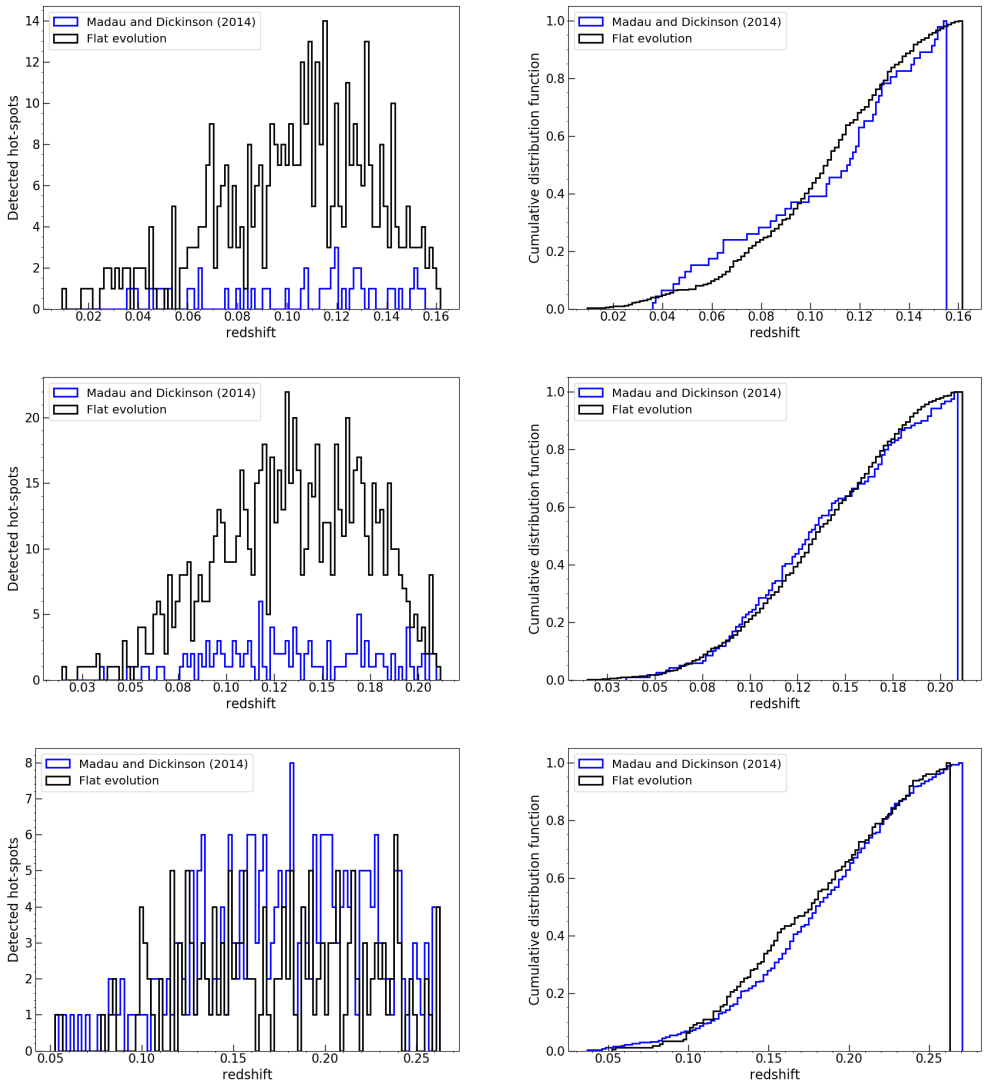

Figure B.6: Detected source distributions and cumulative distribution functions for $\rho_0 = 1 \times 10^{-10}$ Mpc^{-3} and $L_\nu = 1.78 \times 10^{53}$, 3.16×10^{53}, 5.62×10^{53} (top to bottom).

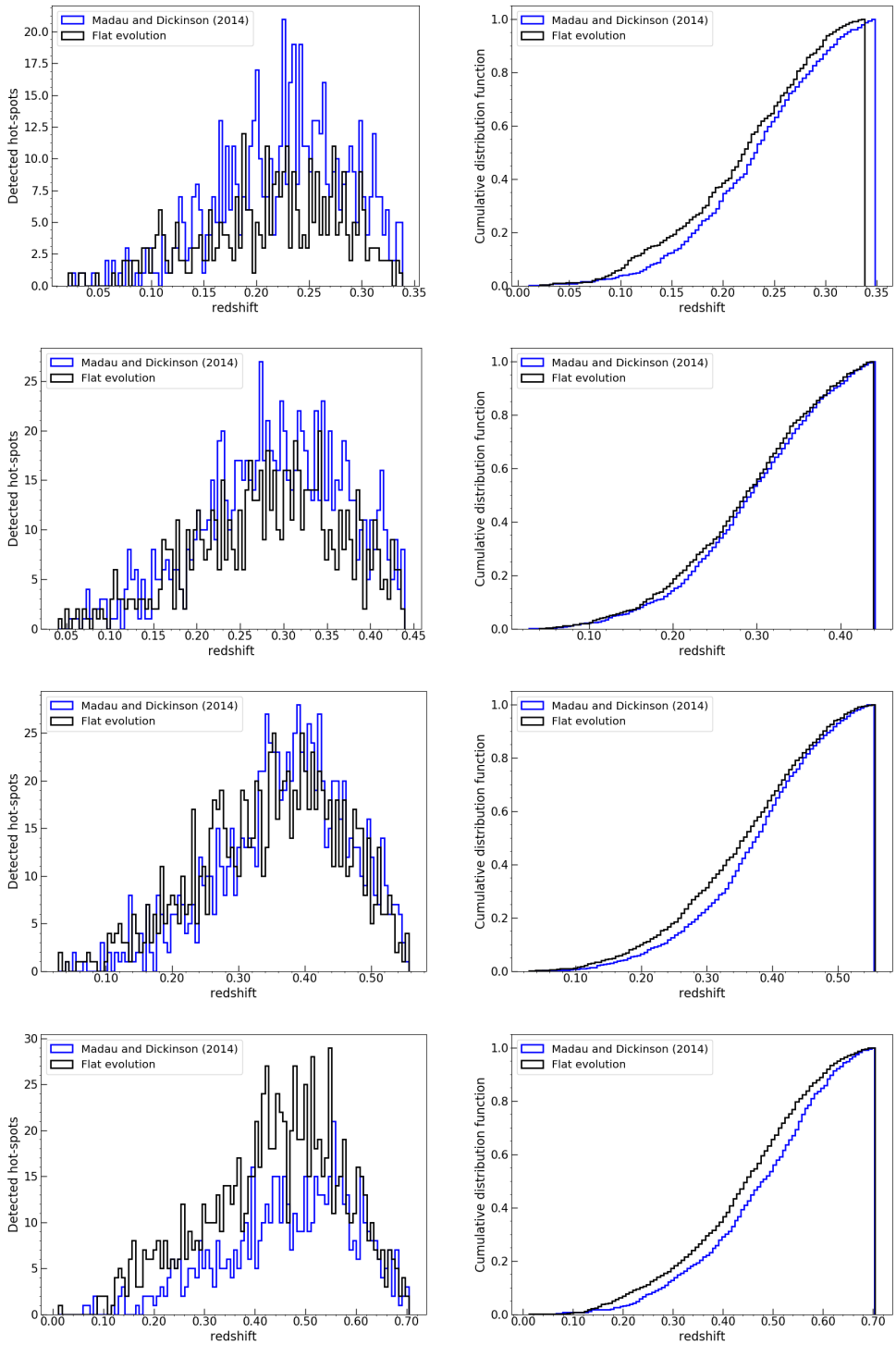

Figure B.7: Detected source distributions and cumulative distribution functions for $\rho_0 = 1 \times 10^{-10}$ Mpc^{-3} and $L_\nu = 1 \times 10^{54}$, 1.78×10^{54}, 3.16×10^{54}, 5.62×10^{54} (top to bottom).

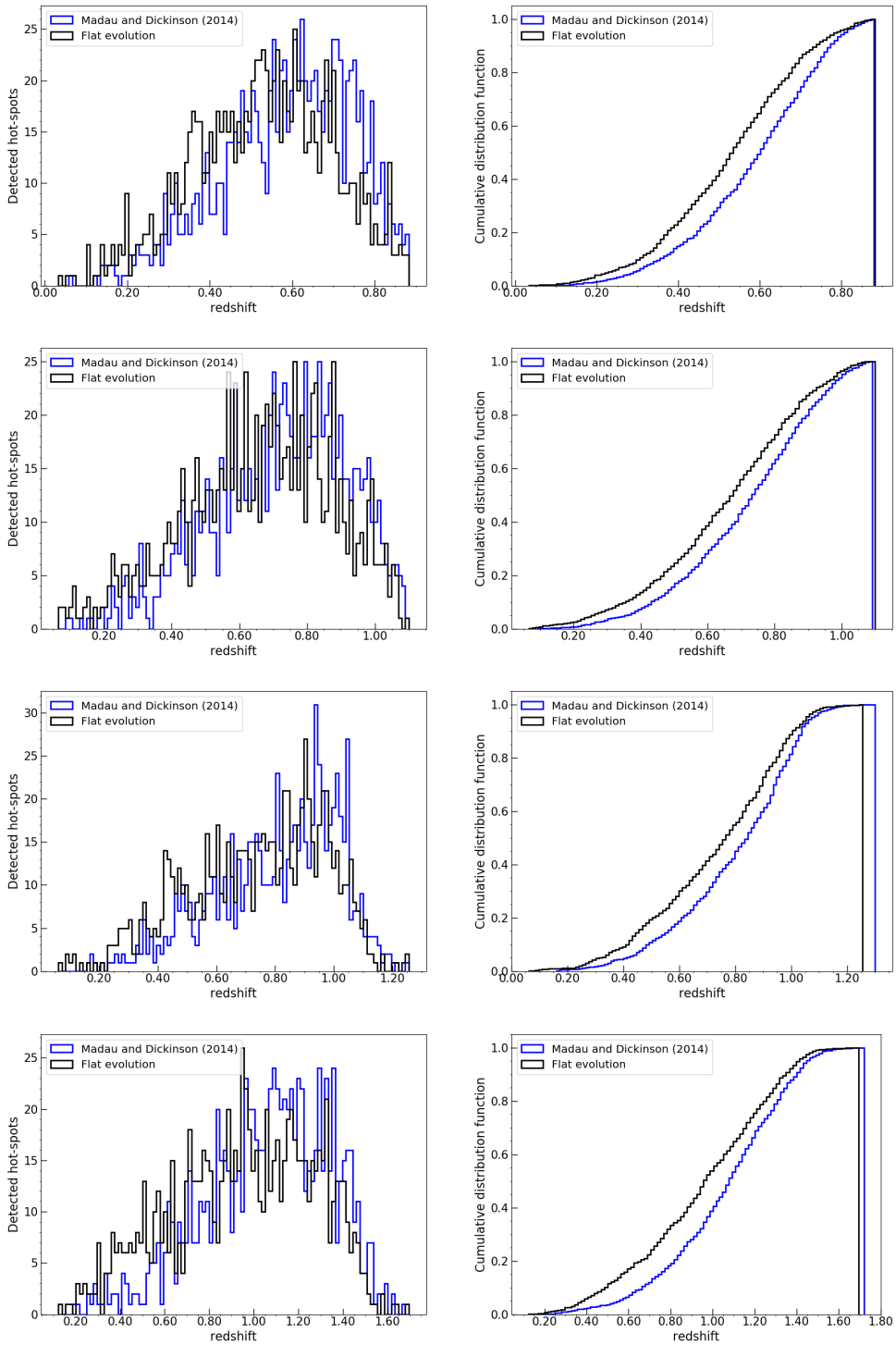

Figure B.8: Detected source distributions and cumulative distribution functions for $\rho_0 = 1 \times 10^{-10}$ Mpc^{-3} and $L_\nu = 1 \times 10^{55}$, 1.78×10^{55}, 3.16×10^{55}, 5.62×10^{55} (top to bottom).

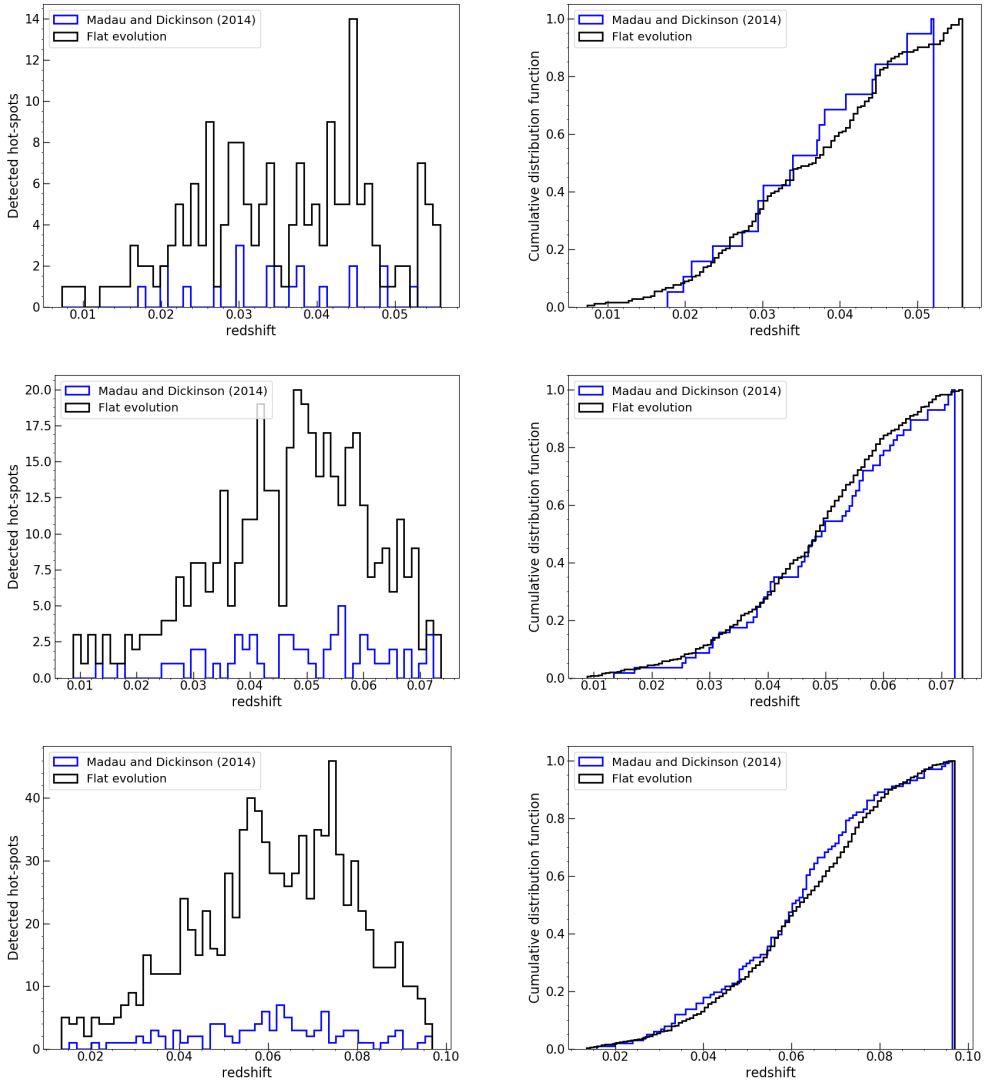

Figure B.9: Detected source distributions and cumulative distribution functions for $\rho_0 = 1 \times 10^{-9}$ Mpc^{-3} and $L_\nu = 1.78 \times 10^{52}$, 3.16×10^{52}, 5.62×10^{52} (top to bottom).

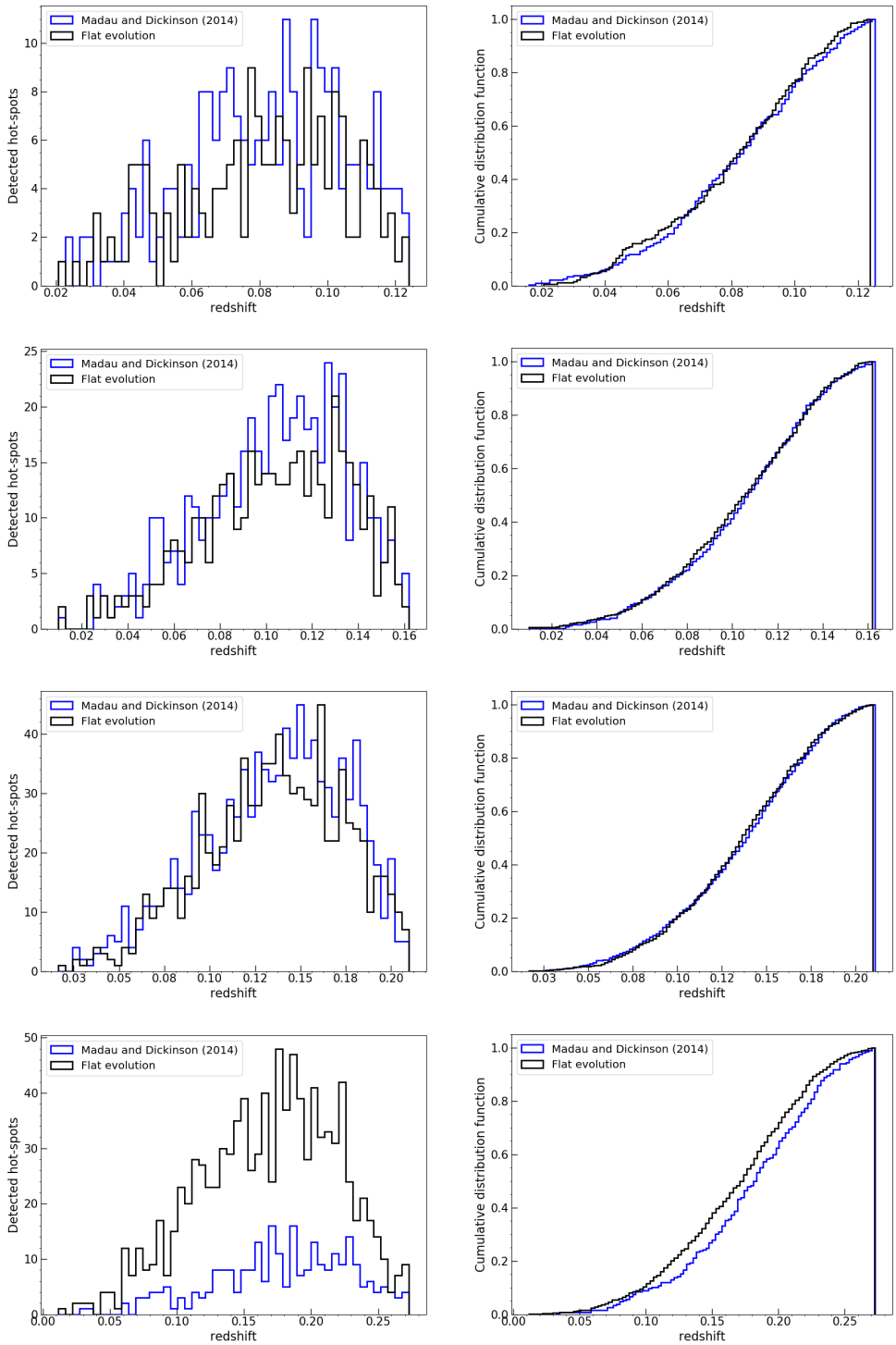

Figure B.10: Detected source distributions and cumulative distribution functions for $\rho_0 = 1 \times 10^{-9}$ Mpc^{-3} and L_ν 1×10^{53}, 1.78×10^{53}, 3.16×10^{53}, 5.62×10^{53} (top to bottom).

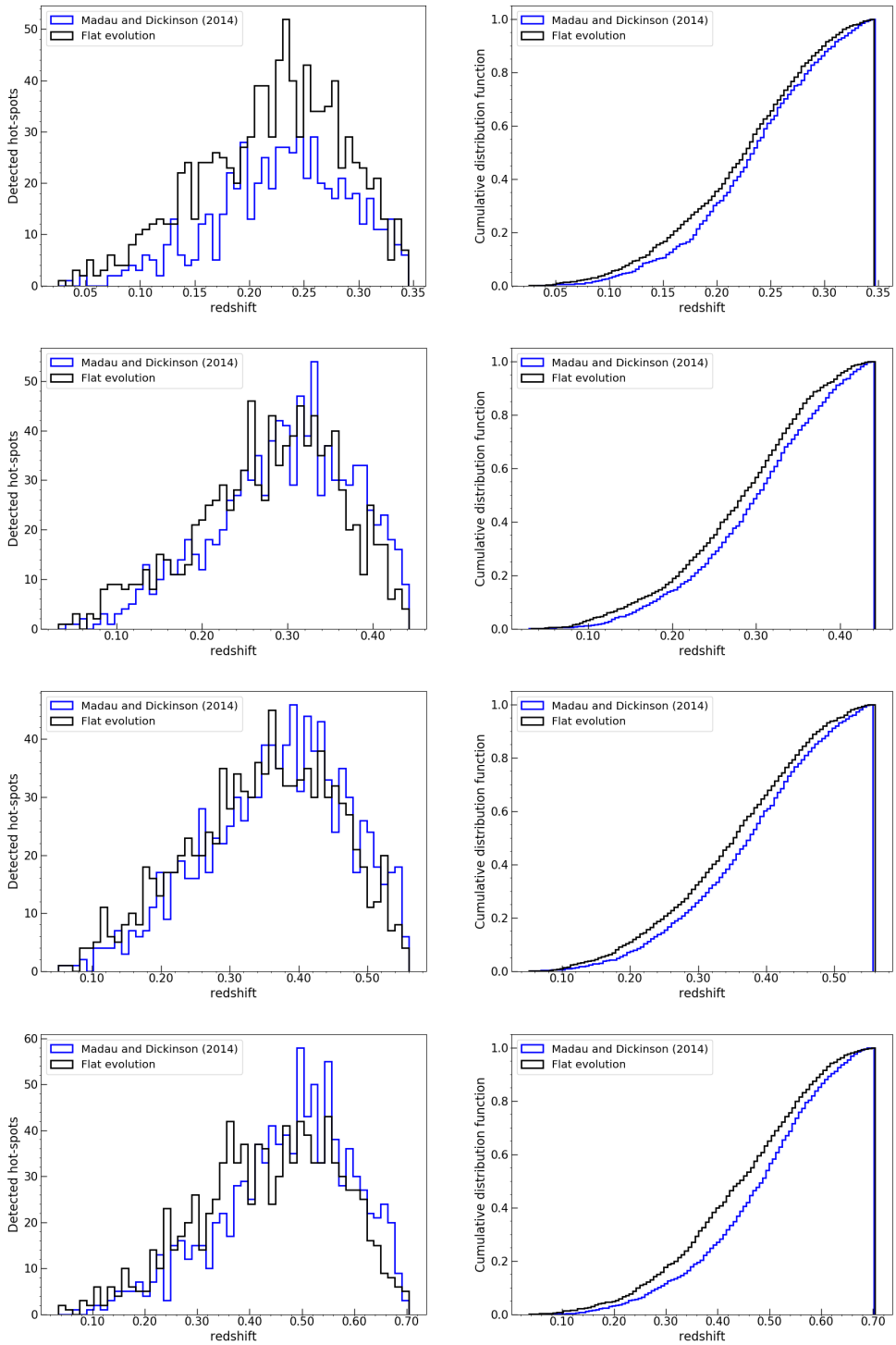

Figure B.11: Detected source distributions and cumulative distribution functions for $\rho_0 = 1 \times 10^{-9}$ Mpc^{-3} and $L_\nu = 1 \times 10^{54}$, 1.78×10^{54}, 3.16×10^{54}, 5.62×10^{54} (top to bottom).

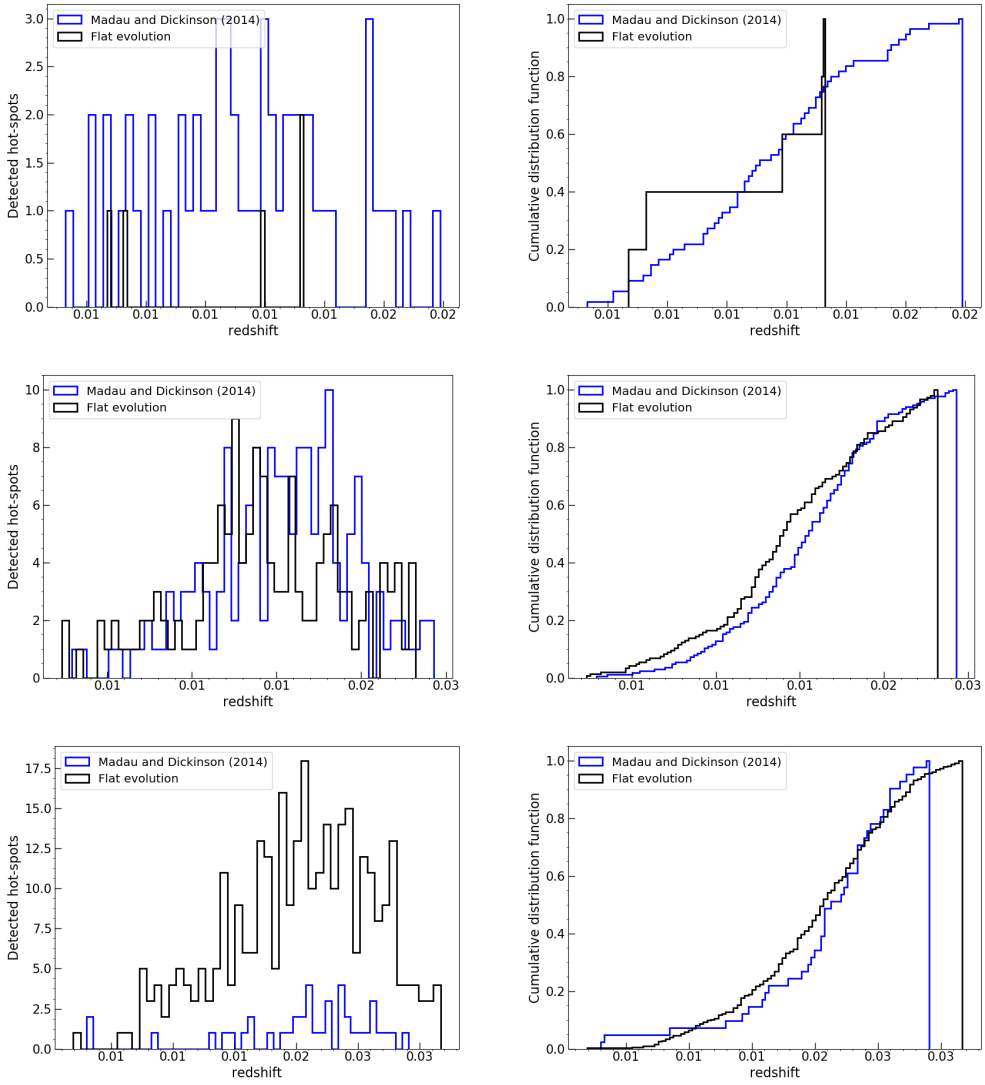

Figure B.12: Detected source distributions and cumulative distribution functions for $\rho_0 = 1 \times 10^{-8}$ Mpc^{-3} and $L_\nu = 1.78 \times 10^{51}$, 3.16×10^{51}, 5.62×10^{51} (top to bottom).

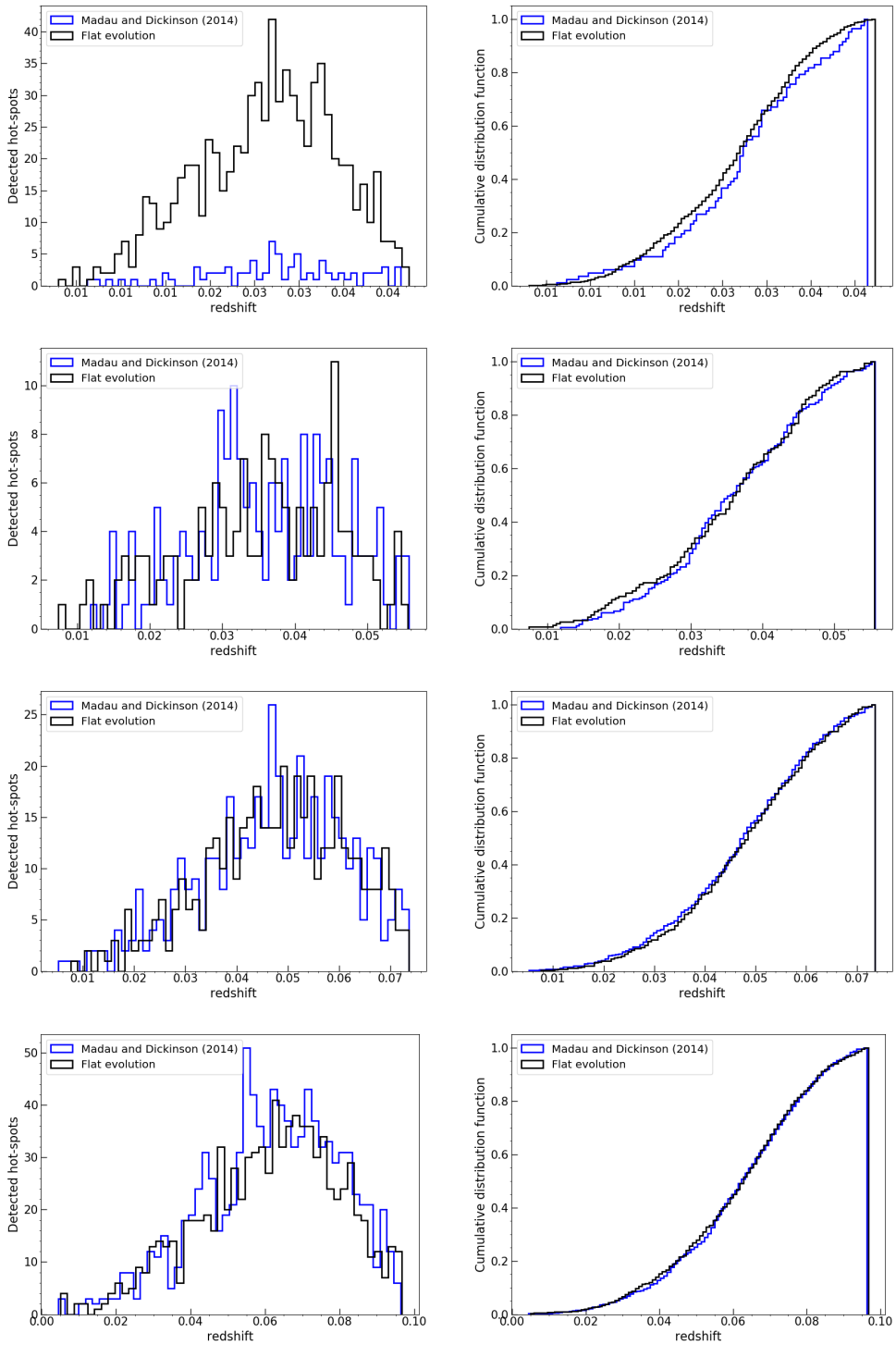

Figure B.13: Detected source distributions and cumulative distribution functions for $\rho_0 = 1 \times 10^{-8}$ Mpc^{-3} and $L_\nu = 1 \times 10^{52}$, 1.78×10^{52}, 3.16×10^{52}, 5.62×10^{52} (top to bottom).

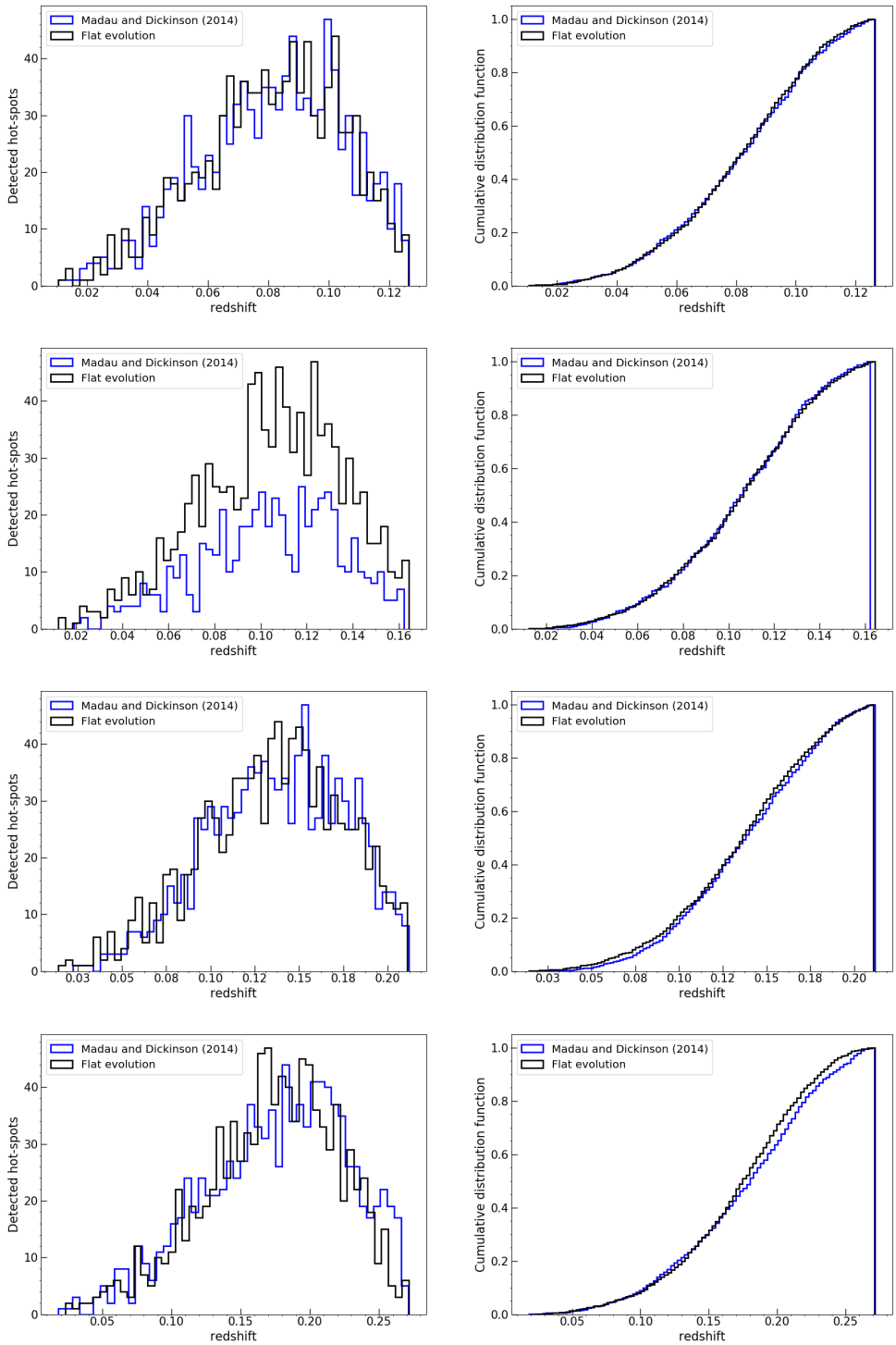

Figure B.14: Detected source distributions and cumulative distribution functions for $\rho_0 = 1 \times 10^{-8}$ Mpc^{-3} and $L_\nu = 1 \times 10^{53}$, 1.78×10^{53}, 3.16×10^{53}, 5.62×10^{53} (top to bottom).

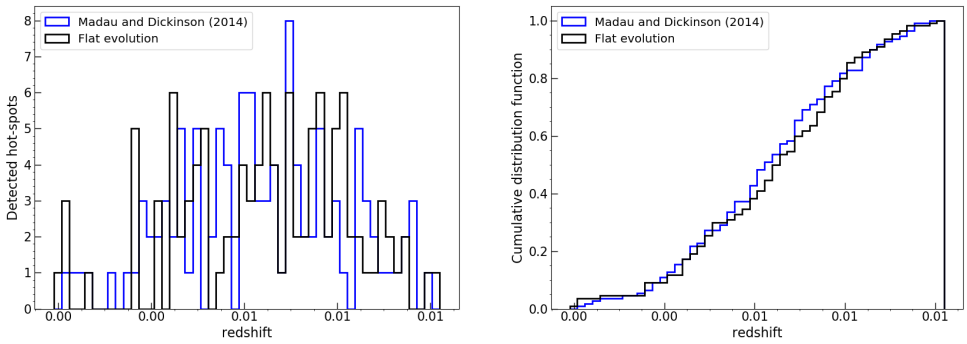

Figure B.15: Detected source distributions and cumulative distribution functions for $\rho_0 = 1 \times 10^{-7}$ Mpc^{-3} and 5.62×10^{50}.

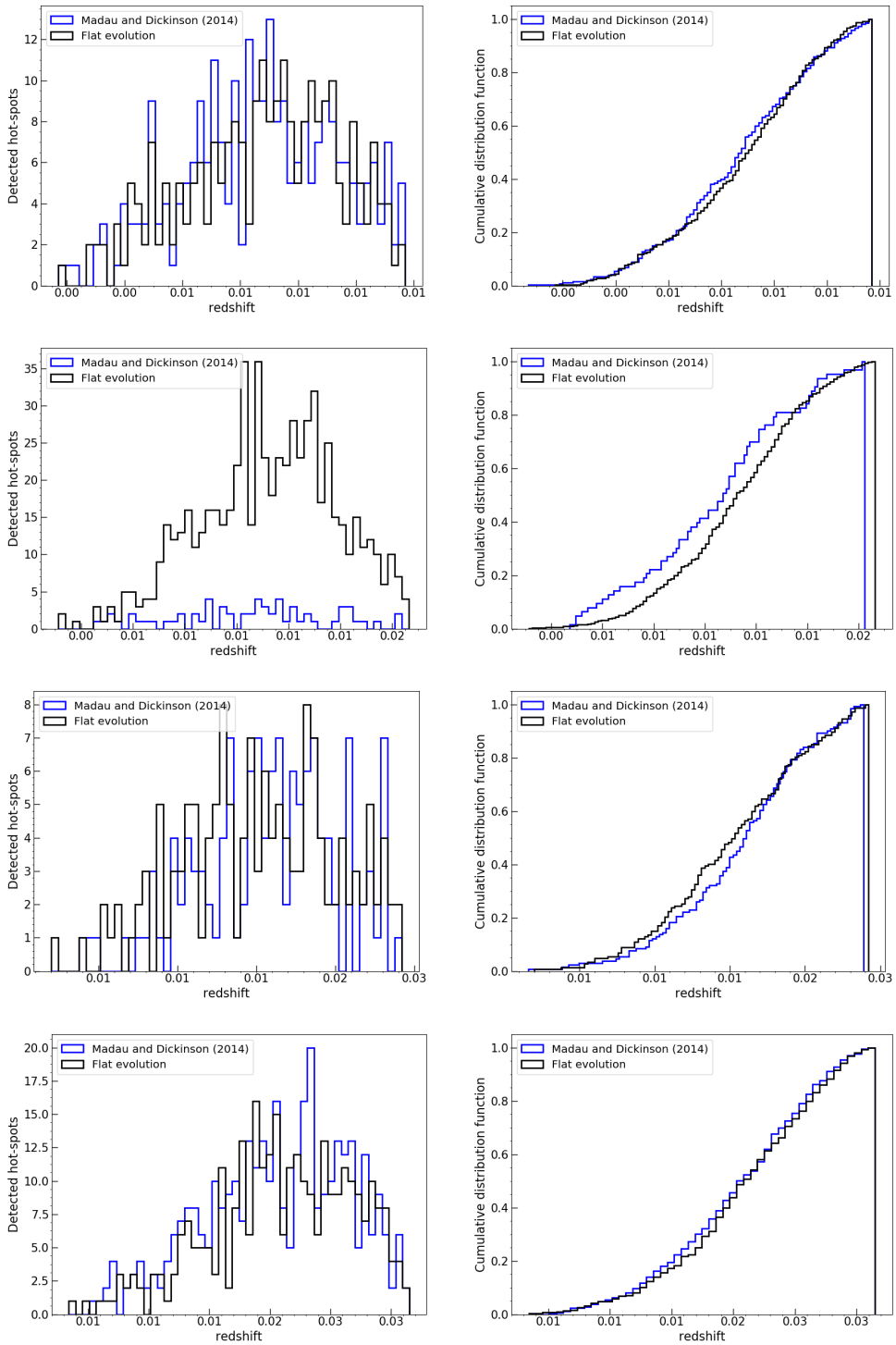

Figure B.16: Detected source distributions and cumulative distribution functions for $\rho_0 = 1 \times 10^{-7}$ Mpc^{-3} and $L_\nu = 1 \times 10^{51}$, 1.78×10^{51}, 3.16×10^{51}, 5.62×10^{51} (top to bottom).

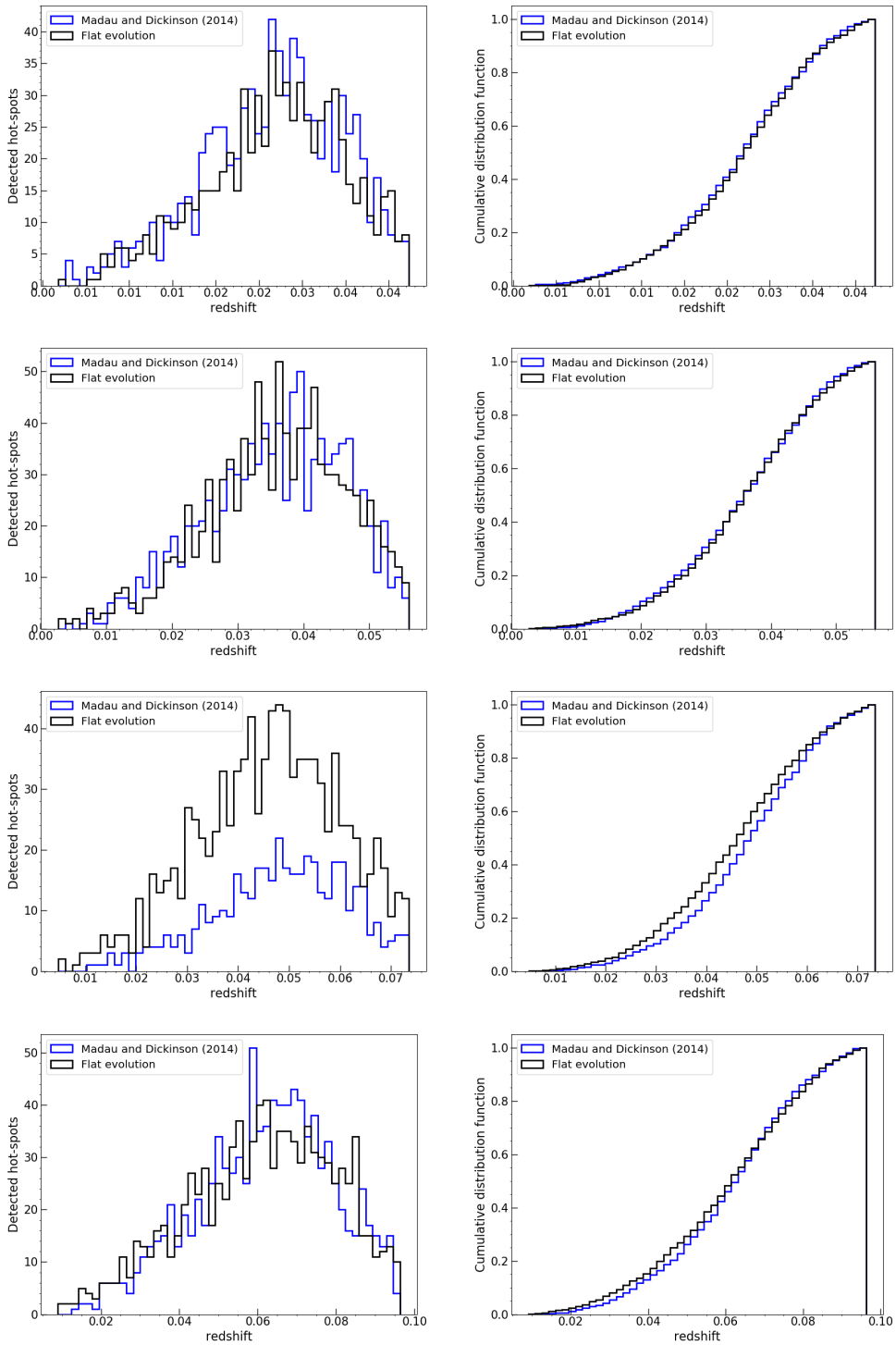

Figure B.17: Detected source distributions and cumulative distribution functions for $\rho_0 = 1 \times 10^{-7}$ Mpc^{-3} and $L_\nu = 1 \times 10^{52}$, 1.78×10^{52}, 3.16×10^{52}, 5.62×10^{52} (top to bottom).

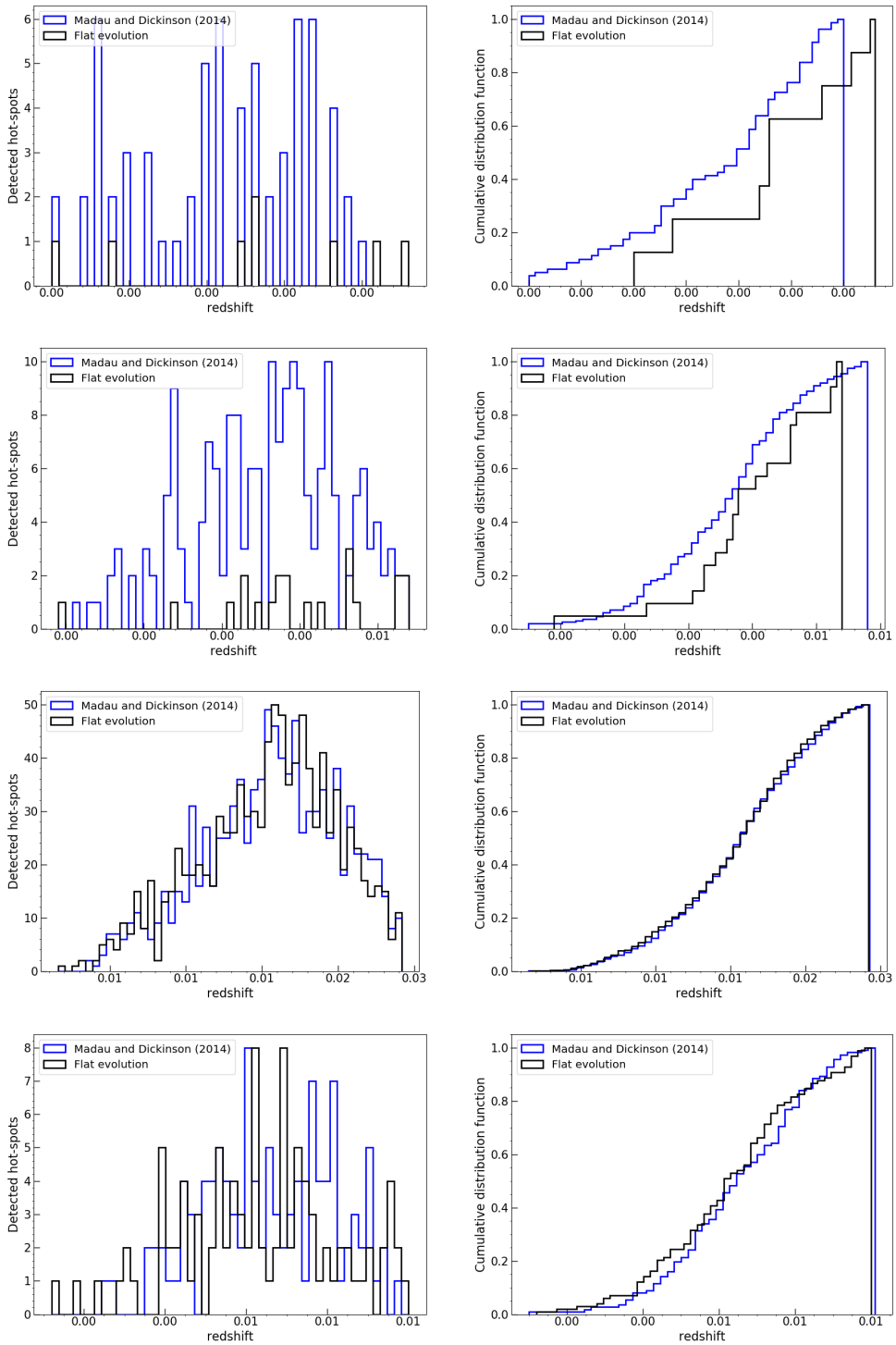

Figure B.18: Detected source distributions and cumulative distribution functions for $\rho_0 = 1 \times 10^{-6}$ Mpc^{-3} and $L_\nu = 1 \times 10^{50}$, 1.78×10^{50}, 3.16×10^{50}, 5.62×10^{50} (top to bottom).

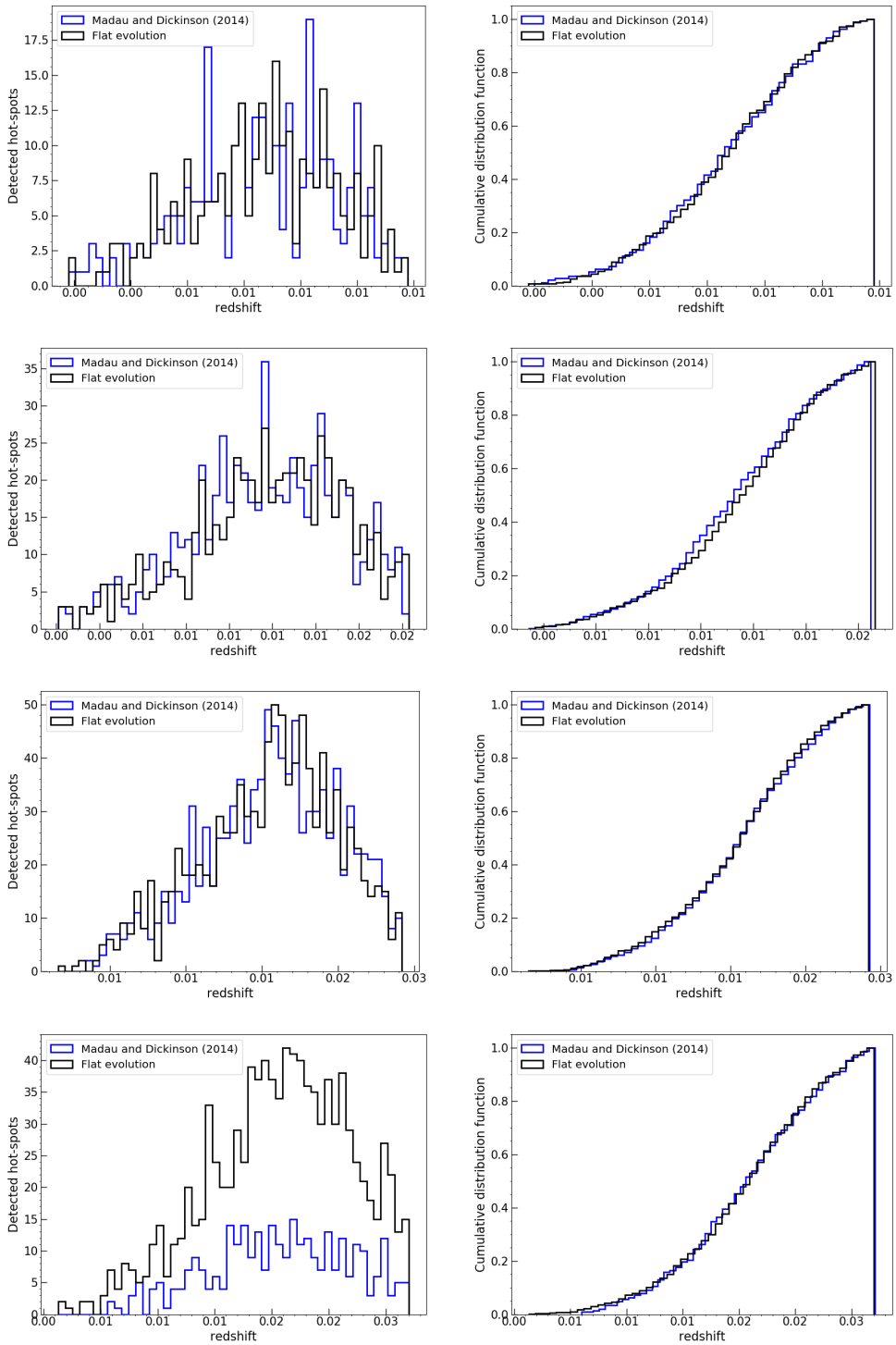

Figure B.19: Detected source distributions and cumulative distribution functions for $\rho_0 = 1 \times 10^{-6}$ Mpc^{-3} and $L_\nu = 1 \times 10^{51}$, 1.78×10^{51}, 3.16×10^{51}, 5.62×10^{51} (top to bottom).

Bibliography

I. Adler, J. I. Trombka, P. Lowman, et al. Apollo 15 and 16 Results of the Integrated Geochemical Experiment. *Moon*, 7(3-4):487–504, Sept. 1973. doi: 10.1007/BF00564649.

AEGIS Collaboration. The All-Wavelength Extended Groth Strip International Survey (AEGIS) Data Sets. *ApJ*, 660(1):L1–L6, May 2007. doi: 10.1086/517931.

AGILE Collaboration. The AGILE Mission. *A&A*, 502(3):995–1013, Aug. 2009. doi: 10.1051/0004-6361/200810527.

AGILE Collaboration. Detection of terrestrial gamma-ray flashes with the AGILE/MCAL. *Rendiconti Lincei. Scienze Fisiche e Naturali*, 30:265–269, Dec. 2019. doi: 10.1007/s12210-019-00762-3.

F. Aharonian, A. G. Akhperjanian, A. R. Bazer-Bachi, et al. A low level of extragalactic background light as revealed by γ-rays from blazars. *Nature*, 440 (7087):1018–1021, Apr 2006. doi: 10.1038/nature04680.

F. A. Aharonian. TeV gamma rays from BL Lac objects due to synchrotron radiation of extremely high energy protons. *New Astronomy*, 5(7):377–395, Nov. 2000. doi: 10.1016/S1384-1076(00)00039-7.

M. Ahlers and F. Halzen. Opening a new window onto the universe with IceCube. *Progress in Particle and Nuclear Physics*, 102:73–88, Sept. 2018. doi: 10.1016/j.ppnp.2018.05.001.

H. Akaike. A New Look at the Statistical Model Identification. *IEEE Transactions on Automatic Control*, 19:716–723, Jan. 1974. doi: 10.1109/TAC.1974.1100705.

J. Alvarez-Muñiz and F. Halzen. Possible High-Energy Neutrinos from the Cosmic Accelerator RX J1713.7-3946. *ApJ*, 576(1):L33–L36, Sept. 2002. doi: 10.1086/342978.

AMANDA Collaboration. The AMANDA neutrino telescope. *Nuclear Physics B Proceedings Supplements*, 77(1-3):474–485, May 1999. doi: 10.1016/S0920-5632(99)00469-7.

AMANDA Collaboration. Observation of high-energy neutrinos using Cherenkov detectors embedded deep in Antarctic ice. *Nature*, 410(6827):441–443, Mar. 2001. doi: 10.1038/35068509.

AMANDA Collaboration. Muon track reconstruction and data selection techniques in AMANDA. *Nuclear Instruments and Methods in Physics Research A*, 524(1-3):169–194, May 2004. doi: 10.1016/j.nima.2004.01.065.

AMANDA Collaboration. Search for point sources of high energy neutrinos with final data from AMANDA-II. *Phys. Rev. D*, 79(6):062001, Mar. 2009. doi: 10.1103/PhysRevD.79.062001.

ANTARES Collaboration. The construction of ANTARES, the first undersea neutrino telescope. *Nuclear Instruments and Methods in Physics Research A*, 602(1):1–6, Jan. 2009. doi: 10.1016/j.nima.2008.12.015.

ANTARES Collaboration. ANTARES: The first undersea neutrino telescope. *Nuclear Instruments and Methods in Physics Research A*, 656(1):11–38, Nov. 2011. doi: 10.1016/j.nima.2011.06.103.

ANTARES Collaboration. First all-flavor neutrino pointlike source search with the ANTARES neutrino telescope. *Phys. Rev. D*, 96(8):082001, Oct. 2017. doi: 10.1103/PhysRevD.96.082001.

ANTARES Collaboration and KM3NeT Collaboration. Neutrino astronomy and oscillation research in the Mediterranean: ANTARES and KM3NeT. *Nuclear Instruments and Methods in Physics Research A*, 952:161653, Feb. 2020. doi: 10.1016/j.nima.2018.11.112.

R. Antonucci. Unified models for active galactic nuclei and quasars. *ARA&A*, 31: 473–521, Jan. 1993. doi: 10.1146/annurev.aa.31.090193.002353.

A. T. Araudo, V. Bosch-Ramon, and G. E. Romero. Gamma rays from cloud penetration at the base of AGN jets. *A&A*, 522:A97, Nov. 2010. doi: 10.1051/0004-6361/201014660.

P. Armstrong, P. M. Chadwick, P. J. Cottle, et al. The University of Durham Mark 6 Gamma Ray Telescope. *Experimental Astronomy*, 9(2):51–80, Jan. 1999. doi: 10.1023/A:1008018503904.

T. B. Arnold and J. W. Emerson. Nonparametric Goodness-of-Fit Tests for Discrete Null Distributions. *The R Journal*, 3(2):34–39, 2011. doi: 10.32614/RJ-2011-016.

ASGAT Collaboration. ASGAT: A new Ground-based Gamma-Ray Telescope in the French Pyrenees. In *Proceedings of the 21st International Cosmic Ray Conference (ICRC1989)*, volume 4, page 231, Jan. 1990.

J. L. Atteia, C. Barat, K. Hurley, et al. A Second Catalog of Gamma-Ray Bursts: 1978–1980 Localizations from the Interplanetary Network. *ApJS*, 64:305, May 1987. doi: 10.1086/191198.

P. Auger, P. Ehrenfest, R. Maze, et al. Extensive Cosmic-Ray Showers. *Reviews of Modern Physics*, 11(3-4):288–291, July 1939. doi: 10.1103/RevModPhys.11.288.

W. I. Axford, E. Leer, and G. Skadron. The Acceleration of Cosmic Rays by Shock Waves. In *Proceedings of the 15th International Cosmic Ray Conference (ICRC1977)*, volume 11, page 132, Jan. 1977.

H. A. Ayala Solares, S. Coutu, D. F. Cowen, et al. The Astrophysical Multimessenger Observatory Network (AMON): Performance and science program. *Astroparticle Physics*, 114:68–76, Jan. 2020. doi: 10.1016/j.astropartphys.2019.06.007.

V. Aynutdinov, V. Balkanov, I. Belolaptikov, et al. The Baikal neutrino experiment: from NT200 to NT200+. In *Proceedings of the 29th International Cosmic Ray Conference (ICRC2005)*, volume 5, page 75, Jan. 2005. doi: 10.48550/arXiv.astro-ph/0609743.

Baikal-GVD Collaboration. Baikal-GVD. In *European Physical Journal Web of Conferences*, volume 136, page 04007, Mar. 2017. doi: 10.1051/epjconf/201713604007.

Baikal-GVD Collaboration. Neutrino Telescope in Lake Baikal: Present and Nearest Future. In *Proceedings of the 37th International Cosmic Ray Conference (ICRC2021)*, page 2, Mar. 2022. doi: 10.22323/1.395.0002.

C. Barat, G. Chambon, K. Hurley, et al. The Signe 2 Franco-Soviet interplanetary gamma ray burst experiment network. *Space Science Instrumentation*, 5:229–235, Jan. 1981.

M. G. Baring. Diffusive Shock Acceleration: the Fermi Mechanism. In *Proceedings of XXXII Rencontres de Moriond, "Very High Energy Phenomena in the Universe"*, page 97, Jan. 1997. doi: 10.48550/arXiv.astro-ph/9711177.

M. V. Barkov, F. A. Aharonian, and V. Bosch-Ramon. Gamma-ray Flares from Red Giant/Jet Interactions in Active Galactic Nuclei. *ApJ*, 724(2):1517–1523, Dec. 2010. doi: 10.1088/0004-637X/724/2/1517.

P. M. Bauelo and J. Rodriguez Martino. The dawn of the particle astronomy era in ultra-high-energy cosmic rays. *Nature*, 458(7948):847–851, Apr. 2009. doi: 10.1038/nature07948.

V. Beckmann and C. Shrader. The AGN phenomenon: open issues. In *Proceedings of the 9th INTEGRAL Workshop*, page 69, Jan. 2012. doi: 10.48550/arXiv.1302.1397.

A. R. Bell. The acceleration of cosmic rays in shock fronts - I. *MNRAS*, 182: 147–156, Jan. 1978. doi: 10.1093/mnras/182.2.147.

W. Benbow and VERITAS Collaboration. Highlights from the VERITAS AGN Observation Program. In *Proceedings od the 34th International Cosmic Ray Conference (ICRC2015)*, volume 34, page 821, July 2015. doi: 10.22323/1.358.0632.

D. R. Bergman and J. W. Belz. Cosmic rays: the Second Knee and beyond. *Journal of Physics G Nuclear Physics*, 34(10):R359–R400, Oct. 2007. doi: 10.1088/0954-3899/34/10/R01.

P. Bhat, A. John, and S. Upadhyaya. Real time data acquisition system for very high energy gamma ray astronomy experiment. *Nuclear Instruments and Methods in Physics Research Section A: Accelerators, Spectrometers, Detectors and Associated Equipment*, 292(2):494–504, 1990. doi: 10.1016/0168-9002(90)90407-W.

G. F. Bignami, G. Boella, J. J. Burger, et al. The COS-B experiment for gamma-ray astronomy. *Space Science Instrumentation*, 1:245–268, Aug. 1975.

P. M. S. Blackett. Emission spectra of the night sky and aurora. *Physical Society of London Gassiot Committee Report*, 1:34, 1948.

R. D. Blandford and J. P. Ostriker. Particle acceleration by astrophysical shocks. *ApJ*, 221:L29–L32, Apr. 1978. doi: 10.1086/182658.

E. Blaufuss, T. Kintscher, L. Lu, et al. The Next Generation of IceCube Real-time Neutrino Alerts. In *Proceedings of the 36th International Cosmic Ray Conference (ICRC2019)*, volume 36, page 1021, July 2019. doi: 10.22323/1.358.1021.

M. Błażejowski, M. Sikora, R. Moderski, et al. Comptonization of Infrared Radiation from Hot Dust by Relativistic Jets in Quasars. *ApJ*, 545(1):107–116, Dec. 2000. doi: 10.1086/317791.

S. D. Bloom and A. P. Marscher. An Analysis of the Synchrotron Self-Compton Model for the Multi-Wave Band Spectra of Blazars. *ApJ*, 461:657, Apr. 1996. doi: 10.1086/177092.

G. R. Blumenthal and R. J. Gould. Bremsstrahlung, Synchrotron Radiation, and Compton Scattering of High-Energy Electrons Traversing Dilute Gases. *Reviews of Modern Physics*, 42(2):237–271, Jan. 1970. doi: 10.1103/RevModPhys.42.237.

J. Blümer, R. Engel, and J. R. Hörandel. Cosmic rays from the knee to the highest energies. *Progress in Particle and Nuclear Physics*, 63(2):293–338, Oct. 2009. doi: 10.1016/j.ppnp.2009.05.002.

B. Boccardi, T. P. Krichbaum, E. Ros, et al. Radio observations of active galactic nuclei with mm-VLBI. *A&ARv*, 25(1):4, Nov. 2017. doi: 10.1007/s00159-017-0105-6.

V. Bosch-Ramon, M. Perucho, and M. V. Barkov. Clouds and red giants interacting with the base of AGN jets. *A&A*, 539:A69, Mar. 2012. doi: 10.1051/0004-6361/201118622.

M. Böttcher. A Hadronic Synchrotron Mirror Model for the "Orphan" TeV Flare in 1ES 1959+650. *ApJ*, 621(1):176–180, Mar. 2005. doi: 10.1086/427430.

M. Böttcher, A. Reimer, and A. P. Marscher. Implications of the very High Energy Gamma-Ray Detection of the Quasar 3C279. *ApJ*, 703:1168–1175, Sept. 2009. doi: 10.1088/0004-637X/703/1/1168.

M. Böttcher, A. Reimer, K. Sweeney, et al. Leptonic and Hadronic Modeling of Fermi-detected Blazars. *ApJ*, 768(1):54, May 2013. doi: 10.1088/0004-637X/768/1/54.

C. C. G. Bowden, S. M. Bradbury, K. T. S. Braier, et al. The University of Durham MarK V Composite Gamma Ray Telescope. In *Proceedings of the 22nd International Cosmic Ray Conference, (ICRC1991)*, volume 2, page 626, Aug. 1991.

H. Bozdogan. Model Selection and Akaike's Information Criterion (AIC): The General Theory and Its Analytical Extensions. *Psychometrika*, 52:345–370, 02 1987. doi: 10.1007/BF02294361.

F. Bradascio and T. Gluesenkamp. An Improved Muon Track Reconstruction for IceCube. In *Proceedings of the 36th International Cosmic Ray Conference (ICRC2019)*, volume 36, page 846, July 2019. doi: 10.22323/1.358.0846.

K. T. Brazier, A. Carramiñana, P. M. Chadwick, et al. The University of Durham Southern Hemisphere Very High Energy Gamma-Ray Telescope. *Experimental Astronomy*, 1(2):77–99, Mar. 1989. doi: 10.1007/BF00457984.

K. T. S. Brazier, A. Carramiñana, P. M. Chadwick, et al. 400 Gev gamma rays from the X-ray pulsar 1E2259+586. *Nuclear Physics B Proceedings Supplements*, 14(1):196–199, Mar. 1990a. doi: 10.1016/0920-5632(90)90420-Y.

K. T. S. Brazier, A. Carraminana, P. M. Chadwick, et al. New Measurements of the 12.6 Millisecond Pulsar in Cygnus X-3. *ApJ*, 350:745, Feb. 1990b. doi: 10.1086/168425.

K. T. S. Brazier, A. Carraminana, P. M. Chadwick, et al. Scorpius X-1: a source of 300 GeV gamma-rays. *A&A*, 232:383, June 1990c.

C. Brink, B. C. Raubenheimer, G. van Urk, et al. The Nooitgedacht MK II TeV gamma-Ray Telescope. In *Proceedings of the 22nd International Cosmic Ray Conference (ICRC1991)*, volume 2, page 622, Aug. 1991.

A. M. Brown, J. Adams, and P. M. Chadwick. γ-ray observations of extraterrestrial neutrino track events. *MNRAS*, 451(1):323–331, July 2015. doi: 10.1093/mnras/stv899.

R. Buccheri, K. Bennett, G. F. Bignami, et al. Search for pulsed γ-ray emission from radio pulsars in the COS-B data. *A&A*, 128:245–251, Dec. 1983.

K. P. Burnham and D. R. Anderson. Kullback-Leibler information as a basis for strong inference in ecological studies. *Wildlife Research*, 28(2):111, 2001. doi: 10.1071/wr99107.

K. P. Burnham and D. R. Anderson. *Model selection and multimodel inference: A practical information-theoretic approach*. Springer-Verlag New York, 2002. doi: 10.1007/b97636.

S. Buson, S. Garrappa, and C. C. Cheung. Fermi-LAT evidence for VHE emission from NVSS J065844+063711. *The Astronomer's Telegram*, 14200:1, Nov. 2020a.

S. Buson, M. Santander, S. Garrappa, et al. Swift XRT observations of the Fermi-LAT source 4FGL J0658.6+0636, positionally consistent with the IceCube high-energy neutrino alert IceCube-201114A. *The Astronomer's Telegram*, 14178:1, Nov. 2020b.

S. Buson, M. Santander, S. Garrappa, et al. Correction to ATel #14199 (Swift XRT observations of the Fermi-LAT source 4FGL J0658.6+0636, positionally consistent with the IceCube high-energy neutrino alert IceCube-201114A). *The Astronomer's Telegram*, 14201:1, Nov. 2020c.

CANGAROO Collaboration. The Cangaroo project. In *Proceedings of the 22nd International Cosmic Ray Conference (ICRC1991)*, volume 2, page 611, Aug. 1991.

CANGAROO Collaboration. Very High Energy Gamma Rays from PSR 1706-44. *ApJ*, 438:L91, Jan. 1995. doi: 10.1086/187723.

CANGAROO Collaboration. Detection of Gamma Rays of up to 50 TeV from the Crab Nebula. *ApJ*, 492(1):L33–L36, Jan. 1998a. doi: 10.1086/311077.

CANGAROO Collaboration. Discovery of TeV Gamma Rays from SN 1006: Further Evidence for the Supernova Remnant Origin of Cosmic Rays. *ApJ*, 497(1): L25–L28, Apr. 1998b. doi: 10.1086/311267.

CANGAROO Collaboration. Initial performance of CANGAROO-II 7m telescope. In *GeV-TeV Gamma Ray Astrophysics Workshop : towards a major atmospheric*, volume 515 of *American Institute of Physics Conference Series*, pages 313–317, June 2000. doi: 10.1063/1.1291385.

CANGAROO Collaboration. The sensitivity of the CANGAROO I analyses of the Crab and Vela plerions to image selection cuts. *Astroparticle Physics*, 15(3): 313–321, June 2001. doi: 10.1016/S0927-6505(00)00162-6.

CANGAROO Collaboration. Design study of CANGAROO-III, stereoscopic imaging atmospheric Cherenkov telescopes for sub-TeV /γ-ray detection. *Astroparticle Physics*, 16(3):235–244, Jan. 2002. doi: 10.1016/S0927-6505(01)00112-8.

CANGAROO Collaboration. Status of CANGAROO-III. In *Proceedings of the 28th International Cosmic Ray Conference (ICRC2003)*, volume 5, page 2807, July 2003.

A. Carraminana. Pair absorption of the TeV gamma-rays in accreting binaries. *A&A*, 264:127–137, Oct. 1992.

A. Carraminana, P. M. Chadwick, N. A. Dipper, et al. 300 GeV Gamma Rays from VELA X-1. *ApJ*, 346:967, Nov. 1989. doi: 10.1086/168077.

J. M. Casandjian and I. A. Grenier. A revised catalogue of EGRET γ-ray sources. *A&A*, 489(2):849–883, Oct. 2008. doi: 10.1051/0004-6361:200809685.

A. J. Castro-Tirado and J. Gorosabel. *Gamma-ray Bursts: 15 Years of GRB Afterglows: Progenitors, Environments and Host Galaxies from the Nearby to the Early Universe*. EDP Sciences, 2021. doi: 10.1051/978-2-7598-1002-4.

CAT Collaboration. A new analysis method for very high definition imaging atmospheric Cherenkov telescopes as applied to the CAT telescope. *Nuclear Instruments and Methods in Physics Research A*, 416(2):425–437, Oct. 1998a. doi: 10.1016/S0168-9002(98)00750-5.

CAT Collaboration. The CAT imaging telescope for very-high-energy gamma-ray astronomy. *Nuclear Instruments and Methods in Physics Research A*, 416(2): 278–292, Oct. 1998b. doi: 10.1016/S0168-9002(98)00749-9.

CAT Collaboration. Very High Energy Gamma-ray spectral properties of MKN 501 from CAT Cherenkov telescope observations in 1997. *A&A*, 350:17–24, Oct. 1999. doi: 10.48550/arXiv.astro-ph/9906060.

M. Cerruti, A. Zech, C. Boisson, et al. Leptohadronic single-zone models for the electromagnetic and neutrino emission of TXS 0506+056. *MNRAS*, 483(1):L12–L16, Feb. 2019. doi: 10.1093/mnrasl/sly210.

P. M. Chadwick. *Very high energy cosmic gamma rays from radio and x-ray pulsars*. PhD thesis, Durham University, Sept. 1987. URL `http://etheses.dur.ac.uk/6720/`.

P. M. Chadwick. 35 years of ground-based gamma-ray astronomy. *Universe*, 7(11): 432, Nov 2021. doi: 10.3390/universe7110432.

P. M. Chadwick, N. A. Dipper, J. C. Dowthwaite, et al. Further Evidence for the Emission of 1000 GeV Gamma Rays with 12 ms Periodicity from Cygnus X-3. In K. E. Turver, editor, *Very High Energy Gamma Ray Astronomy*, volume 199 of *NATO Advanced Study Institute (ASI) Series C*, page 115, Jan. 1987. doi: 10.1007/978-94-009-3831-1.

P. M. Chadwick, K. Lyons, T. J. L. McComb, et al. Very High Energy Gamma Rays from PKS 2155-304. *ApJ*, 513(1):161–167, Mar. 1999. doi: 10.1086/306862.

P. M. Chadwick, K. Lyons, T. J. L. McComb, et al. Very High Energy Gamma Rays from Young Pulsars and Supernova Remnants in the Southern Hemisphere. *ApJ*, 537(1):414–421, July 2000a. doi: 10.1086/309014.

P. M. Chadwick, K. Lyons, T. J. L. McComb, et al. TeV observations of X-ray binaries. In B. L. Dingus, M. H. Salamon, and D. B. Kieda, editors, *GeV-TeV Gamma Ray Astrophysics Workshop : towards a major atmospheric*, volume 515 of *American Institute of Physics Conference Series*, pages 271–275, June 2000b. doi: 10.1063/1.1291378.

P. M. Chadwick, K. Lyons, T. J. L. McComb, et al. Very high energy gamma ray observations of southern hemisphere AGNs. In N. E. White, G. Malaguti, and G. G. C. Palumbo, editors, *X-ray Astronomy: Stellar Endpoints, AGN, and the Diffuse X-ray Background*, volume 599 of *American Institute of Physics Conference Series*, pages 570–573, Dec. 2001. doi: 10.1063/1.1434688.

P. A. Cherenkov. Visible light from clear liquids under the action of gamma radiation. *Doklady Akademil Mauk SSSR*, 2(451), 1934.

K.-W. Chuang. *Identification and Analysis of Cosmic Gamma Ray Bursts from Pioneer Venus Orbiter*. PhD thesis, California Univ., Riverside., Jan. 1990. URL `https://www.osti.gov/biblio/6265309`.

A. Chudakov and N. Nesterova. Observation of cherenkov radiation accompanying extensive air showers of cosmic rays. *Sov. Phys. JETP*, 28:384, 1955.

A. E. Chudakov, V. L. Dadykin, V. I. Zatsepin, et al. On the high energy photons from local sources. *Proceedings of the 8th International Cosmic Ray Conference (ICRC1963)*, 1963.

A. E. Chudakov et al. A search for photons with energy 1013 eV from local sources of cosmic radiation. *Proceedings of Lebedev Institute*, 26:118–141, 1965.

M. Cirasuolo, R. J. McLure, J. S. Dunlop, et al. A new measurement of the evolving near-infrared galaxy luminosity function out to z=4: a continuing challenge to theoretical models of galaxy formation. *MNRAS*, 401(2):1166–1176, Jan. 2010. doi: 10.1111/j.1365-2966.2009.15710.x.

R. W. Clay, D. H. Giles, A. G. Gregory, et al. The design and construction of the university of Adelaide bicentennial gamma-ray telescope. *PASA*, 8(1):41–45, Jan. 1989. doi: 10.1017/S1323358000022876.

A. Coleiro and D. Dornic. Search for counterpart to IceCube-201114A with ANTARES. *The Astronomer's Telegram*, 14176:1, Nov. 2020.

COMPTEL Collaboration. Instrument Description and Performance of the Imaging Gamma-Ray Telescope COMPTEL aboard the Compton Gamma-Ray Observatory. *ApJS*, 86:657, June 1993a. doi: 10.1086/191794.

COMPTEL Collaboration. Firsts results from COMPTEL measurements of the 26 AL 1.8 MeV gamma-ray line from the galactic center region. *A&AS*, 97:181–184, Jan. 1993b.

W. Conover. *Practical nonparametric statistics*. Wiley series in probability and statistics. Wiley, New York, NY, 3rd edition edition, 1999.

CTA Consortium. Monte Carlo design studies for the Cherenkov Telescope Array. *Astroparticle Physics*, 43:171–188, Mar. 2013. doi: 10.1016/j.astropartphys.2012.10.002.

CTA Consortium. CTAO Instrument Response Functions - version prod3b-v2, Apr. 2016. URL `https://doi.org/10.5281/zenodo.5163273`.

CTA Consortium. Monte Carlo performance studies for the site selection of the Cherenkov Telescope Array. *Astroparticle Physics*, 93:76–85, July 2017. doi: 10.1016/j.astropartphys.2017.05.001.

CTA Consortium. *Science with the Cherenkov Telescope Array*. World Scientific Publishing, New Jersey, USA, 1st edition edition, 2019a. doi: 10.1142/10986.

CTA Consortium. Monte Carlo studies for the optimisation of the Cherenkov Telescope Array layout. *Astroparticle Physics*, 111:35–53, Sept. 2019b. doi: 10.1016/j.astropartphys.2019.04.001.

E. Curie. *Madame Curie: Haar Leven en Werk*. H. P. Leopold's Uitgeversmij N. V., Den Haag, Netherlands, 1959.

A. Dar and A. Laor. Hadronic Production of TeV Gamma-Ray Flares from Blazars. *ApJ*, 478(1):L5–L8, Mar. 1997. doi: 10.1086/310544.

M. de Naurois. Highlights from H.E.S.S. In *European Physical Journal Web of Conferences*, volume 209, page 01025, Sept. 2019. doi: 10.1051/epjconf/201920901025.

M. de Naurois and D. Mazin. Ground-based detectors in very-high-energy gamma-ray astronomy. *Comptes Rendus Physique*, 16(6-7):610–627, Aug. 2015. doi: 10.1016/j.crhy.2015.08.011.

B. Degrange and E. Paré. CAT & CELESTE: Gamma Astronomy at Thémis. *Nuclear Physics B Proceedings Supplements*, 60(3):199–204, Jan. 1998. doi: 10.1016/S0920-5632(97)00515-X.

C. D. Dermer and B. Giebels. Active galactic nuclei at gamma-ray energies. *Comptes Rendus Physique*, 17(6):594–616, June 2016. doi: 10.1016/j.crhy.2016.04.004.

C. D. Dermer and R. Schlickeiser. Model for the High-Energy Emission from Blazars. *ApJ*, 416:458, Oct. 1993. doi: 10.1086/173251.

C. D. Dermer and R. Schlickeiser. On the Location of the Acceleration and Emission Sites in Gamma-Ray Blazars. *ApJS*, 90:945, Feb. 1994. doi: 10.1086/191929.

C. D. Dermer and R. Schlickeiser. Transformation Properties of External Radiation Fields, Energy-Loss Rates and Scattered Spectra, and a Model for Blazar Variability. *ApJ*, 575(2):667–686, Aug. 2002. doi: 10.1086/341431.

C. D. Dermer, R. Schlickeiser, and A. Mastichiadis. High-energy gamma radiation from extragalactic radio sources. *A&A*, 256:L27–L30, Mar. 1992.

C. Diltz and M. Böttcher. Leptonic and Lepto-Hadronic Modeling of the 2010 November Flare from 3C 454.3. *ApJ*, 826(1):54, July 2016. doi: 10.3847/0004-637X/826/1/54.

S. Dimitrakoudis, A. Mastichiadis, R. J. Protheroe, et al. The time-dependent one-zone hadronic model. First principles. *A&A*, 546:A120, Oct. 2012. doi: 10.1051/0004-6361/201219770.

A. V. Diyachkov, I. V. Éstulin, N. G. Havenson, et al. Catalogue of gamma-bursts detected by the Soviet-French experiment "signe 2M" (Venera-11, 12 and Prognoz-7). *Advances in Space Research*, 3:211–219, 1983. doi: 10.1016/0273-1177(83)90033-9.

G. Dobler, D. P. Finkbeiner, I. Cholis, et al. The Fermi Haze: A Gamma-ray Counterpart to the Microwave Haze. *ApJ*, 717(2):825–842, July 2010. doi: 10.1088/0004-637X/717/2/825.

A. Domínguez, J. R. Primack, D. J. Rosario, et al. Extragalactic background light inferred from AEGIS galaxy-SED-type fractions. *MNRAS*, 410(4):2556–2578, Feb 2011. doi: 10.1111/j.1365-2966.2010.17631.x.

L. Dondi and G. Ghisellini. Gamma-ray-loud blazars and beaming. *MNRAS*, 273 (3):583–595, Apr. 1995. doi: 10.1093/mnras/273.3.583.

M. Doro. A review of the past and present MAGIC dark matter search program and a glimpse at the future. In *XXV European Cosmic Ray Symposium*, page C16, Jan. 2017. doi: 10.48550/arXiv.1701.05702.

J. C. Dowthwaite. *Very energetic gamma rays from binary x-ray sources and other astronomical objects*. PhD thesis, Durham University, jun 1987. URL `http://etheses.dur.ac.uk/7064/`.

G. Dubus. Gamma-ray emission from binaries in context. *Comptes Rendus Physique*, 16(6-7):661–673, Aug. 2015. doi: 10.1016/j.crhy.2015.08.014.

DUMAND Collaboration. *DUMAND-II: Proposal to Construct a Deep-ocean Laboratory for the Study of High Energy Neutrino Astrophysics and Particle Physics*. Manoa Hawaii University, Honolulu, HI, aug 1988.

E. Dwek and F. Krennrich. Simultaneous Constraints on the Spectrum of the Extragalactic Background Light and the Intrinsic TeV Spectra of Markarian 421, Markarian 501, and H1426+428. *ApJ*, 618(2):657–674, Jan. 2005. doi: 10.1086/426010.

E. Dwek and F. Krennrich. The extragalactic background light and the gamma-ray opacity of the universe. *Astroparticle Physics*, 43:112–133, Mar. 2013. doi: 10.1016/j.astropartphys.2012.09.003.

EGRET Collaboration. EGRET Observations of the Diffuse Gamma-Ray Emission from the Galactic Plane. *ApJ*, 481(1):205–240, May 1997. doi: 10.1086/304012.

EGRET Collaboration. EGRET Observations of the Extragalactic Gamma-Ray Emission. *ApJ*, 494(2):523–534, Feb. 1998. doi: 10.1086/305222.

EGRET Collaboration. The Third EGRET Catalog of High-Energy Gamma-Ray Sources. *ApJS*, 123(1):79–202, July 1999. doi: 10.1086/313231.

J. Engelfried. Ring imaging cherenkov detectors. *AIP Conference Proceedings*, 857 (2):340–346, 2006. doi: 10.1063/1.2359418.

J. Engelfried. Cherenkov light imaging: Fundamentals and recent developments. *Nuclear Instruments and Methods in Physics Research A*, 639(1):1–6, May 2011. doi: 10.1016/j.nima.2010.10.023.

E. Fermi. On the Origin of the Cosmic Radiation. *Physical Review*, 75(8):1169–1174, Apr. 1949. doi: 10.1103/PhysRev.75.1169.

Fermi-GBM Collaboration. The Fermi Gamma-ray Burst Monitor. *ApJ*, 702(1): 791–804, Sept. 2009. doi: 10.1088/0004-637X/702/1/791.

Fermi-GBM Collaboration. An Ordinary Short Gamma-Ray Burst with Extraordinary Implications: Fermi-GBM Detection of GRB 170817A. *ApJ*, 848 (2):L14, Oct. 2017. doi: 10.3847/2041-8213/aa8f41.

Fermi-GBM Collaboration. Fermi-GBM GRBs with Characteristics Similar to GRB 170817A. *ApJ*, 876(1):89, May 2019. doi: 10.3847/1538-4357/ab10d8.

Fermi-GBM Collaboration. The Fourth Fermi-GBM Gamma-Ray Burst Catalog: A Decade of Data. *ApJ*, 893(1):46, Apr. 2020. doi: 10.3847/1538-4357/ab7a18.

Fermi-LAT Collaboration. The Large Area Telescope on the Fermi Gamma-Ray Space Telescope Mission. *ApJ*, 697(2):1071–1102, June 2009. doi: 10.1088/0004-637X/697/2/1071.

Fermi-LAT Collaboration. The Spectral Energy Distribution of Fermi Bright Blazars. *ApJ*, 716(1):30–70, June 2010a. doi: 10.1088/0004-637X/716/1/30.

Fermi-LAT Collaboration. Spectrum of the Isotropic Diffuse Gamma-Ray Emission Derived from First-Year Fermi Large Area Telescope Data. *Phys. Rev. Lett.*, 104 (10):101101, Mar. 2010b. doi: 10.1103/PhysRevLett.104.101101.

Fermi-LAT Collaboration. The Fermi Large Area Telescope on Orbit: Event Classification, Instrument Response Functions, and Calibration. *ApJS*, 203(1):4, Nov. 2012. doi: 10.1088/0067-0049/203/1/4.

Fermi-LAT Collaboration. Constraints on the Galactic Population of TeV Pulsar Wind Nebulae Using Fermi Large Area Telescope Observations. *ApJ*, 773(1):77, Aug. 2013a. doi: 10.1088/0004-637X/773/1/77.

Fermi-LAT Collaboration. Detection of the Characteristic Pion-Decay Signature in Supernova Remnants. *Science*, 339(6121):807–811, Feb. 2013b. doi: 10.1126/science.1231160.

Fermi-LAT Collaboration. Pass 8: Toward the Full Realization of the Fermi-LAT Scientific Potential. In *4th International Fermi Symposium*, page C121028, Mar. 2013c. doi: 10.48550/arXiv.1303.3514.

Fermi-LAT Collaboration. The Spectrum and Morphology of the Fermi Bubbles. *ApJ*, 793(1):64, Sept. 2014. doi: 10.1088/0004-637X/793/1/64.

Fermi-LAT Collaboration. The Third Catalog of Active Galactic Nuclei Detected by the Fermi Large Area Telescope. *ApJ*, 810(1):14, Sept. 2015. doi: 10.1088/0004-637X/810/1/14.

Fermi-LAT Collaboration. Fermi-LAT Observations of High-Energy Gamma-Ray Emission toward the Galactic Center. *ApJ*, 819(1):44, Mar. 2016a. doi: 10.3847/0004-637X/819/1/44.

Fermi-LAT Collaboration. The First Fermi LAT Supernova Remnant Catalog. *ApJS*, 224(1):8, May 2016b. doi: 10.3847/0067-0049/224/1/8.

Fermi-LAT Collaboration. Characterizing the population of pulsars in the inner Galaxy with the Fermi Large Area Telescope. *ArXiv e-prints*, art. arXiv:1705.00009, Apr. 2017a.

Fermi-LAT Collaboration. Fermipy: An open-source Python package for analysis of Fermi-LAT Data. In *Proceedings of the 35th International Cosmic Ray Conference (ICRC2017)*, volume 301, page 824, Jan. 2017b. doi: 10.22323/1.301.0824.

Fermi-LAT Collaboration. Fermipy: Fermi-LAT data analysis package. Astrophysics Source Code Library, record ascl:1812.006, Dec. 2018a. URL `https://github.com/Fermipy/fermipy`.

Fermi-LAT Collaboration. Fermi-LAT improved Pass8 event selection. In *8th International Fermi Symposium*, page C181014, Oct. 2018b. doi: 10.48550/arXiv.1810.11394.

Fermi-LAT Collaboration. Fermi Large Area Telescope Fourth Source Catalog. *ApJS*, 247(1):33, Mar. 2020a. doi: 10.3847/1538-4365/ab6bcb.

Fermi-LAT Collaboration. The Fourth Catalog of Active Galactic Nuclei Detected by the Fermi Large Area Telescope. *ApJ*, 892(2):105, Apr. 2020b. doi: 10.3847/1538-4357/ab791e.

Fermi-LAT Collaboration. Catalog of Long-term Transient Sources in the First 10 yr of Fermi-LAT Data. *ApJS*, 256(1):13, Sept. 2021. doi: 10.3847/1538-4365/ac072a.

Fermi-LAT Collaboration, MAGIC Collaboration, et al. Fermi Large Area Telescope Observations of Markarian 421: The Missing Piece of its Spectral Energy Distribution. *ApJ*, 736(2):131, Aug. 2011. doi: 10.1088/0004-637X/736/2/131.

Fermi-LAT Collaboration, IceCube Collaboration, and ASAS-SN Collaboration. Investigation of Two Fermi-LAT Gamma-Ray Blazars Coincident with High-energy Neutrinos Detected by IceCube. *ApJ*, 880(2):103, Aug. 2019. doi: 10.3847/1538-4357/ab2ada.

J. D. Finke. External Compton Scattering in Blazar Jets and the Location of the Gamma-Ray Emitting Region. *ApJ*, 830(2):94, oct 2016. doi: 10.3847/0004-637X/830/2/94.

J. D. Finke, S. Razzaque, and C. D. Dermer. Modeling the Extragalactic Background Light from Stars and Dust. *ApJ*, 712(1):238–249, Mar. 2010. doi: 10.1088/0004-637X/712/1/238.

M. R. Forster. Key concepts in model selection: Performance and generalizability. *Journal of Mathematical Psychology*, 44(1):205 – 231, 2000. doi: 10.1006/jmps.1999.1284.

G. Fossati, L. Maraschi, A. Celotti, et al. A unifying view of the spectral energy distributions of blazars. *MNRAS*, 299(2):433–448, Sept. 1998. doi: 10.1046/j.1365-8711.1998.01828.x.

G. Fossati, J. H. Buckley, I. H. Bond, et al. Multiwavelength Observations of Markarian 421 in 2001 March: An Unprecedented View on the X-Ray/TeV Correlated Variability. *ApJ*, 677(2):906–925, Apr. 2008. doi: 10.1086/527311.

A. Franceschini, G. Rodighiero, and M. Vaccari. Extragalactic optical-infrared background radiation, its time evolution and the cosmic photon-photon opacity. *A&A*, 487(3):837–852, Sept. 2008. doi: 10.1051/0004-6361:200809691.

A. Franckowiak, S. Garrappa, V. Paliya, et al. Patterns in the Multiwavelength Behavior of Candidate Neutrino Blazars. *ApJ*, 893(2):162, Apr. 2020. doi: 10.3847/1538-4357/ab8307.

J. A. Gaidos, C. W. Akerlof, S. Biller, et al. Extremely rapid bursts of TeV photons from the active galaxy Markarian 421. *Nature*, 383(6598):319–320, Sept. 1996. doi: 10.1038/383319a0.

T. K. Gaisser, F. Halzen, and T. Stanev. Particle astrophysics with high energy neutrinos. *Physics Reports*, 258(3):173 – 236, 1995. doi: 10.1016/0370-1573(95)00003-Y.

W. Galbraith and J. Jelley. Light-pulses from the night sky and Cherenkov radiation: Part I. *Journal of Atmospheric and Terrestrial Physics*, 6(1-6):250–252, 1955. doi: 10.1016/0021-9169(55)90038-6.

W. Galbraith and J. V. Jelley. Light Pulses from the Night Sky associated with Cosmic Rays. *Nature*, 171(4347):349–350, Feb. 1953. doi: 10.1038/171349a0.

S. Gao, A. Fedynitch, W. Winter, et al. Modelling the coincident observation of a high-energy neutrino and a bright blazar flare. *Nature Astronomy*, 3:88–92, Jan. 2019. doi: 10.1038/s41550-018-0610-1.

S. Garrappa and S. Buson. Fermi-LAT Gamma-ray Observations of IceCube-201114A. *The Astronomer's Telegram*, 14188:1, Nov. 2020.

N. Gehrels and C. Shrader. Status of the Compton Gamma Ray Observatory. In M. L. McConnell and J. M. Ryan, editors, *The Fifth Compton Symposium*, volume 510 of *American Institute of Physics Conference Series*, pages 3–10, Apr. 2000. doi: 10.1063/1.1303165.

N. Gehrels, E. Ramirez-Ruiz, and D. B. Fox. Gamma-Ray Bursts in the Swift Era. *ARA&A*, 47(1):567–617, Sept. 2009. doi: 10.1146/annurev.astro.46.060407.145147.

M. Georganopoulos and D. Kazanas. Relativistic and Slowing Down: The Flow in the Hot Spots of Powerful Radio Galaxies and Quasars. *ApJ*, 589(1):L5–L8, May 2003. doi: 10.1086/375796.

M. Georganopoulos and D. Kazanas. Decelerating flows in TeV blazars. *New Astronomy Reviews*, 48(5-6):403–405, Apr. 2004. doi: 10.1016/j.newar.2003.12.047.

G. Ghisellini and P. Madau. On the origin of the gamma-ray emission in blazars. *MNRAS*, 280(1):67–76, May 1996. doi: 10.1093/mnras/280.1.67.

G. Ghisellini, F. Tavecchio, and M. Chiaberge. Structured jets in TeV BL Lac objects and radiogalaxies. Implications for the observed properties. *A&A*, 432 (2):401–410, Mar 2005. doi: 10.1051/0004-6361:20041404.

G. Ghisellini, F. Tavecchio, L. Maraschi, et al. The power of relativistic jets is larger than the luminosity of their accretion disks. *Nature*, 515(7527):376–378, Nov. 2014. doi: 10.1038/nature13856.

A. I. Gibson. Transient Pulsed Gamma-Rays from PSR0531. *Irish Astronomical Journal*, 15:103, Sept. 1981.

R. C. Gilmore, R. S. Somerville, J. R. Primack, et al. Semi-analytic modelling of the extragalactic background light and consequences for extragalactic gamma-ray spectra. *MNRAS*, 422(4):3189–3207, June 2012. doi: 10.1111/j.1365-2966.2012.20841.x.

P. Giommi, P. Padovani, and G. Polenta. A simplified view of blazars: the γ-ray case. *MNRAS*, 431(2):1914–1922, May 2013. doi: 10.1093/mnras/stt305.

P. Giommi, P. Padovani, F. Oikonomou, et al. 3HSP J095507.9+355101: A flaring extreme blazar coincident in space and time with IceCube-200107A. *A&A*, 640: L4, Aug. 2020. doi: 10.1051/0004-6361/202038423.

G. Glatting, P. Kletting, S. Reske, et al. Choosing the optimal fit function: Comparison of the akaike information criterion and the f-test. *Medical physics*, 34: 4285–92, 12 2007. doi: 10.1118/1.2794176.

T. Glüsenkamp. Analysis of the cumulative neutrino flux from Fermi LAT blazar populations using 3 years of IceCube data. In *European Physical Journal Web of Conferences*, volume 121, page 05006, July 2016. doi: 10.1051/epjconf/201612105006.

A. Gokus, S. Haemmerich, A. Rau, et al. SRG/eROSITA detection of 4FGL J0658.6+0636 prior to high-energy neutrino alert IceCube-201114A. *The Astronomer's Telegram*, 14199:1, Nov. 2020.

R. W. Goodrich. Spectropolarimetry of "Narrow-Line" Seyfert 1 Galaxies. *ApJ*, 342:224, July 1989. doi: 10.1086/167586.

R. J. Gould and G. P. Schréder. Opacity of the Universe to High-Energy Photons. *Physical Review*, 155(5):1408–1411, Mar. 1967. doi: 10.1103/PhysRev.155.1408.

P. B. Graff, M. Georganopoulos, E. S. Perlman, and D. Kazanas. A Multizone Model for Simulating the High-Energy Variability of TeV Blazars. *ApJ*, 689(1): 68–78, Dec. 2008. doi: 10.1086/592427.

K. Greisen. End to the Cosmic-Ray Spectrum? *Phys. Rev. Lett.*, 16(17):748–750, Apr. 1966. doi: 10.1103/PhysRevLett.16.748.

I. A. Grenier and A. K. Harding. Gamma-ray pulsars: A gold mine. *Comptes Rendus Physique*, 16(6-7):641–660, Aug. 2015. doi: 10.1016/j.crhy.2015.08.013.

S. Griffin and VERITAS Collaboration. VERITAS Observations under Bright Moonlight. In *Proceedings of the 34th International Cosmic Ray Conference (ICRC2015)*, volume 34, page 989, July 2015. doi: 10.48550/arXiv.1508.07186.

H. E. S. S. Collaboration. The H.E.S.S. Galactic plane survey. *A&A*, 612:A1, Apr. 2018. doi: 10.1051/0004-6361/201732098.

F. Halzen and D. Hooper. High energy neutrinos from the TeV Blazar 1ES 1959 + 650. *Astroparticle Physics*, 23(6):537–542, July 2005. doi: 10.1016/j.astropartphys.2005.03.007.

F. Halzen, A. Kheirandish, T. Weisgarber, and S. P. Wakely. On the Neutrino Flares from the Direction of TXS 0506+056. *ApJ*, 874(1):L9, Mar 2019. doi: 10.3847/2041-8213/ab0d27.

C. R. Harris, K. J. Millman, S. J. van der Walt, et al. Array programming with NumPy. *Nature*, 585(7825):357–362, Sept. 2020. doi: 10.1038/s41586-020-2649-2.

J. Harris, P. M. Chadwick, and M. K. Daniel. An investigation into the spectral properties of bright Fermi blazars. *MNRAS*, 441(4):3591–3599, July 2014. doi: 10.1093/mnras/stu787.

M. G. Hauser and E. Dwek. The Cosmic Infrared Background: Measurements and Implications. *ARA&A*, 39:249–307, Jan. 2001. doi: 10.1146/annurev.astro.39.1.249.

HAWC Collaboration and IceCube Collaboration. Multimessenger Gamma-Ray and Neutrino Coincidence Alerts Using HAWC and IceCube Subthreshold Data. *ApJ*, 906(1):63, Jan. 2021. doi: 10.3847/1538-4357/abcaa4.

HEGRA Collaboration. Detection of VHE γ-rays from MKN 421 with the HEGRA Cherenkov Telescopes. *A&A*, 311:L13–L16, July 1996. doi: 10.48550/arXiv.astro-ph/9606159.

HEGRA Collaboration. Detection of γ-rays above 1.5TeV from MKN 501. *A&A*, 320:L5–L8, Apr. 1997a. doi: 10.48550/arXiv.astro-ph/9612058.

HEGRA Collaboration. Measurement of the flux, spectrum, and variability of TeV γ-rays from MKN 501 during a state of high activity. *A&A*, 327:L5–L8, Nov. 1997b. doi: 10.48550/arXiv.astro-ph/9706019.

HEGRA Collaboration. Evidence for TeV gamma ray emission from Cassiopeia A. *A&A*, 370:112–120, Apr. 2001. doi: 10.1051/0004-6361:20010243.

HEGRA Collaboration. An unidentified TeV source in the vicinity of Cygnus OB2. *A&A*, 393:L37–L40, Oct. 2002. doi: 10.1051/0004-6361:20021171.

HEGRA Collaboration. Is the giant radio galaxy M 87 a TeV gamma-ray emitter? *A&A*, 403:L1–L5, May 2003a. doi: 10.1051/0004-6361:20030372.

HEGRA Collaboration. The technical performance of the HEGRA system of imaging air Cherenkov telescopes. *Astroparticle Physics*, 20(3):267–291, Dec. 2003b. doi: 10.1016/j.astropartphys.2003.06.001.

HEGRA Collaboration. The unidentified TeV source (TeV J2032+4130) and surrounding field: Final HEGRA IACT-System results. *A&A*, 431:197–202, Feb. 2005. doi: 10.1051/0004-6361:20041552.

W. Hermsen, J. B. G. M. Bloemen, K. Bennett, et al. Further COS-B evidence for gamma-ray emission from 3C273. In *Proceedings of the 17th International Cosmic Ray Conference (ICRC1981)*, volume 1, pages 230–233, Jan. 1981.

L. Herold and D. Malyshev. Hard and bright gamma-ray emission at the base of the Fermi bubbles. *A&A*, 625:A110, May 2019. doi: 10.1051/0004-6361/201834670.

V. F. Hess. Über Beobachtungen der durchdringenden Strahlung bei sieben Freiballonfahrten. *Phys. Z.*, 13:1084–1091, 1912.

HESS Collaboration. The status of the HESS project. *New Astronomy Reviews*, 48(5-6):331–337, Apr 2004. doi: 10.1016/j.newar.2003.12.004.

H.E.S.S. Collaboration. Observations of selected AGN with HESS. *A&A*, 441(2): 465–472, Oct. 2005a. doi: 10.1051/0004-6361:20053478.

H.E.S.S. Collaboration. Discovery of Very High Energy Gamma Rays Associated with an X-ray Binary. *Science*, 309(5735):746–749, July 2005b. doi: 10.1126/science.1113764.

H.E.S.S. Collaboration. H.E.S.S. observations following multi-messenger alerts in real-time. In *Proceedings of the 35th International Cosmic Ray Conference (ICRC2017)*, volume 301, page 653, Jan. 2017a. doi: 10.22323/1.301.0653.

H.E.S.S. Collaboration. TeV Gamma-Ray Observations of the Binary Neutron Star Merger GW170817 with H.E.S.S. *ApJ*, 850(2):L22, Dec. 2017b. doi: 10.3847/2041-8213/aa97d2.

H.E.S.S. Collaboration. Characterising the VHE diffuse emission in the central 200 parsecs of our Galaxy with H.E.S.S. *A&A*, 612:A9, Apr. 2018a. doi: 10.1051/0004-6361/201730824.

H.E.S.S. Collaboration. The starburst galaxy NGC 253 revisited by H.E.S.S. and Fermi-LAT. *A&A*, 617:A73, Sept. 2018b. doi: 10.1051/0004-6361/201833202.

H.E.S.S. Collaboration. The population of TeV pulsar wind nebulae in the H.E.S.S. Galactic Plane Survey. *A&A*, 612:A2, Apr. 2018c. doi: 10.1051/0004-6361/201629377.

H.E.S.S. Collaboration. H.E.S.S. observations of RX J1713.7-3946 with improved angular and spectral resolution: Evidence for gamma-ray emission extending beyond the X-ray emitting shell. *A&A*, 612:A6, Apr. 2018d. doi: 10.1051/0004-6361/201629790.

H.E.S.S. Collaboration. Population study of Galactic supernova remnants at very high γ-ray energies with H.E.S.S. *A&A*, 612:A3, Apr. 2018e. doi: 10.1051/0004-6361/201732125.

H.E.S.S. Collaboration. First ground-based measurement of sub-20 GeV to 100 GeV γ-Rays from the Vela pulsar with H.E.S.S. II. *A&A*, 620:A66, Dec. 2018f. doi: 10.1051/0004-6361/201732153.

H.E.S.S. Collaboration. Constraints on the emission region of 3C 279 during strong flares in 2014 and 2015 through VHE γ-ray observations with H.E.S.S. *A&A*, 627:A159, July 2019a. doi: 10.1051/0004-6361/201935704.

H.E.S.S. Collaboration. A very-high-energy component deep in the γ-ray burst afterglow. *Nature*, 575(7783):464–467, Nov. 2019b. doi: 10.1038/s41586-019-1743-9.

H.E.S.S. Collaboration. The 2014 TeV γ-Ray Flare of Mrk 501 Seen with H.E.S.S.: Temporal and Spectral Constraints on Lorentz Invariance Violation. *ApJ*, 870 (2):93, Jan. 2019c. doi: 10.3847/1538-4357/aaf1c4.

H.E.S.S. Collaboration. H.E.S.S. detection of very high-energy γ-ray emission from the quasar PKS 0736+017. *A&A*, 633:A162, Jan. 2020. doi: 10.1051/0004-6361/201935906.

H.E.S.S. Collaboration and MAGIC Collaboration. H.E.S.S. and MAGIC observations of a sudden cessation of a very-high-energy γ-ray flare in PKS 1510−089 in May 2016. *A&A*, 648:A23, Apr. 2021. doi: 10.1051/0004-6361/202038949.

J. W. Hewitt and M. Lemoine-Goumard. Observations of supernova remnants and pulsar wind nebulae at gamma-ray energies. *Comptes Rendus Physique*, 16(6-7): 674–685, Aug. 2015. doi: 10.1016/j.crhy.2015.08.015.

A. M. Hillas. Cerenkov Light Images of EAS Produced by Primary Gamma Rays and by Nuclei. In *Proceedings of the 19th International Cosmic Ray Conference (ICRC1985)*, volume 3, page 445, Aug. 1985.

K. Hipel. Geophysical model discrimination using the akaike information criterion. *IEEE Transactions on Automatic Control*, 26(2):358–378, 1981. doi: 10.1109/TAC.1981.1102597.

J. Holder. Atmospheric Cherenkov Gamma-ray Telescopes. In D. N. Burrows, editor, *The WSPC Handbook of Astronomical Instrumentation*, volume 5, page 1556, July 2021. doi: 10.48550/arXiv.1510.05675.

D. C. Homan, M. L. Lister, Y. Y. Kovalev, et al. MOJAVE. XII. Acceleration and Collimation of Blazar Jets on Parsec Scales. *ApJ*, 798(2):134, Jan 2015. doi: 10.1088/0004-637X/798/2/134.

D. Horan, V. A. Acciari, S. M. Bradbury, et al. Multiwavelength Observations of Markarian 421 in 2005-2006. *ApJ*, 695(1):596–618, Apr. 2009. doi: 10.1088/0004-637X/695/1/596.

S. Hümmer, M. Rüger, F. Spanier, et al. Simplified Models for Photohadronic Interactions in Cosmic Accelerators. *ApJ*, 721(1):630–652, Sept. 2010. doi: 10.1088/0004-637X/721/1/630.

IceCube Collaboration. Time-integrated Searches for Point-like Sources of Neutrinos with the 40-string IceCube Detector. *ApJ*, 732(1):18, May 2011a. doi: 10.1088/0004-637X/732/1/18.

IceCube Collaboration. Measurement of the atmospheric neutrino energy spectrum from 100 GeV to 400 TeV with IceCube. *Phys. Rev. D*, 83(1):012001, Jan. 2011b. doi: 10.1103/PhysRevD.83.012001.

IceCube Collaboration. Search for Time-independent Neutrino Emission from Astrophysical Sources with 3 yr of IceCube Data. *ApJ*, 779(2):132, Dec. 2013a. doi: 10.1088/0004-637X/779/2/132.

IceCube Collaboration. Evidence for High-Energy Extraterrestrial Neutrinos at the IceCube Detector. *Science*, 342(6161):1242856, Nov. 2013b. doi: 10.1126/science.1242856.

IceCube Collaboration. Search for Time-independent Neutrino Emission from Astrophysical Sources with 3 yr of IceCube Data. *ApJ*, 779(2):132, Dec. 2013c. doi: 10.1088/0004-637X/779/2/132.

IceCube Collaboration. IceTop: The surface component of IceCube. The IceCube Collaboration. *Nuclear Instruments and Methods in Physics Research A*, 700: 188–220, Feb. 2013d. doi: 10.1016/j.nima.2012.10.067.

IceCube Collaboration. Energy reconstruction methods in the IceCube neutrino telescope. *Journal of Instrumentation*, 9(3):P03009, Mar. 2014a. doi: 10.1088/1748-0221/9/03/P03009.

IceCube Collaboration. Observation of High-Energy Astrophysical Neutrinos in Three Years of IceCube Data. *Phys. Rev. Lett.*, 113(10):101101, Sept. 2014b. doi: 10.1103/PhysRevLett.113.101101.

IceCube Collaboration. Measurement of the Atmospheric ν_e Spectrum with IceCube. *Phys. Rev. D*, 91(12):122004, June 2015a. doi: 10.1103/PhysRevD.91.122004.

IceCube Collaboration. Flavor Ratio of Astrophysical Neutrinos above 35 TeV in IceCube. *Phys. Rev. Lett.*, 114(17):171102, May 2015b. doi: 10.1103/PhysRevLett.114.171102.

IceCube Collaboration. All-sky Search for Time-integrated Neutrino Emission from Astrophysical Sources with 7 yr of IceCube Data. *ApJ*, 835(2):151, Feb. 2017a. doi: 10.3847/1538-4357/835/2/151.

IceCube Collaboration. Constraints on Galactic Neutrino Emission with Seven Years of IceCube Data. *ApJ*, 849(1):67, Nov. 2017b. doi: 10.3847/1538-4357/aa8dfb.

IceCube Collaboration. The IceCube realtime alert system. *Astroparticle Physics*, 92:30–41, June 2017c. doi: 10.1016/j.astropartphys.2017.05.002.

IceCube Collaboration. The IceCube Neutrino Observatory: instrumentation and online systems. *Journal of Instrumentation*, 12(3):P03012, Mar. 2017d. doi: 10.1088/1748-0221/12/03/P03012.

IceCube Collaboration. All-sky Search for Time-integrated Neutrino Emission from Astrophysical Sources with 7 yr of IceCube Data. *ApJ*, 835(2):151, Feb. 2017e. doi: 10.3847/1538-4357/835/2/151.

IceCube Collaboration. Neutrino emission from the direction of the blazar TXS 0506+056 prior to the IceCube-170922A alert. *Science*, 361(6398):147–151, July 2018. doi: 10.1126/science.aat2890.

IceCube Collaboration. Search for steady point-like sources in the astrophysical muon neutrino flux with 8 years of IceCube data. *European Physical Journal C*, 79(3):234, Mar. 2019a. doi: 10.1140/epjc/s10052-019-6680-0.

IceCube Collaboration. IceCube-190922A - IceCube observation of a high-energy neutrino candidate event. *Gamma-ray Coordinates Network*, 25802:1, Sept. 2019b.

IceCube Collaboration. IceCube-201114A - IceCube observation of a high-energy neutrino candidate event. *Gamma-ray Coordinates Network*, 28887:1, Nov. 2020a.

IceCube Collaboration. Time-Integrated Neutrino Source Searches with 10 Years of IceCube Data. *Phys. Rev. Lett.*, 124(5):051103, Feb. 2020b. doi: 10.1103/PhysRevLett.124.051103.

IceCube Collaboration, Fermi-LAT Collaboration, and M. others. Multimessenger observations of a flaring blazar coincident with high-energy neutrino IceCube-170922A. *Science*, 361(6398):eaat1378, July 2018. doi: 10.1126/science.aat1378.

J. M. Jauch and F. Rohrlich. *The theory of photons and electrons. The relativistic quantum field theory of charged particles with spin one-half.* Texts and Monographs in Physics. Springer, Berlin, 2nd ed. edition, 1976. doi: 10.1007/978-3-642-80951-4.

J. Jelley and W. Galbraith. Light pulses from the night sky and cherenkov radiation. part ii. *Journal of Atmospheric and Terrestrial Physics*, 6(1-6):304–312, 1955. doi: 10.1016/0021-9169(55)90047-7.

J. V. Jelley. In Days of Yore. In K. E. Turver, editor, *Very High Energy Gamma Ray Astronomy*, volume 199 of *NATO Advanced Study Institute (ASI) Series C*, page 27, Jan. 1987.

S. Johnston, A. G. Lyne, R. N. Manchester, et al. A high-frequency survey of the southern galactic plane for pulsars. *MNRAS*, 255:401–411, Apr. 1992. doi: 10.1093/mnras/255.3.401.

M. Kadler, F. Krauß, K. Mannheim, et al. Coincidence of a high-fluence blazar outburst with a PeV-energy neutrino event. *Nature Physics*, 12(8):807–814, Aug. 2016. doi: 10.1038/nphys3715.

M. Kadler, J. Hessdoerfer, F. Eppel, et al. Contemporary Effelsberg Observations of Two Radio Sources in the Fields of IceCube-201114A and IceCube-201115A. *The Astronomer's Telegram*, 14191:1, Nov. 2020a.

M. Kadler, J. Hessdoerfer, F. Eppel, et al. Correction to ATel #14191 (Contemporary Effelsberg Observations of Two Radio Sources in the Fields of IceCube-201114A and IceCube-201115A). *The Astronomer's Telegram*, 14194:1, Nov. 2020b.

P. Kalaczyński and KM3NeT Collaboration. KM3NeT/ORCA: status and perspectives for neutrino oscillation and mass hierarchy measurements. In *40th International Conference on High Energy Physics*, page 149, Apr. 2021. doi: 10.22323/1.390.0149.

G. Kanbach, D. L. Bertsch, C. E. Fichtel, et al. The project EGRET (energetic gamma-ray experiment telescope) on NASA's Gamma-Ray Observatory CGRO. *SSR*, 49(1-2):69–84, Jan. 1989. doi: 10.1007/BF00173744.

Y. Kaneko, R. D. Preece, M. S. Briggs, et al. The Complete Spectral Catalog of Bright BATSE Gamma-Ray Bursts. *ApJS*, 166(1):298–340, Sept. 2006. doi: 10.1086/505911.

A. Kashlinsky. Cosmic infrared background and early galaxy evolution. *Physics Reports*, 409(6):361–438, Apr. 2005. doi: 10.1016/j.physrep.2004.12.005.

H. Katagiri, S. Sugiyama, M. Ackermann, et al. Fermi/LAT Study of Gamma-Ray Emission in the Direction of the Monoceros Loop Supernova Remnant. *ApJ*, 831 (1):106, Nov. 2016. doi: 10.3847/0004-637X/831/1/106.

K. Katarzyński and K. Walczewska. On the correlation between the X-ray and gamma-ray emission in TeV blazars. *A&A*, 510:A63, Feb. 2010. doi: 10.1051/0004-6361/200913128.

A. Keivani, K. Murase, M. Petropoulou, et al. A Multimessenger Picture of the Flaring Blazar TXS 0506+056: Implications for High-energy Neutrino Emission and Cosmic-Ray Acceleration. *ApJ*, 864(1):84, Sept. 2018. doi: 10.3847/1538-4357/aad59a.

S. R. Kelner and F. A. Aharonian. Energy spectra of gamma rays, electrons, and neutrinos produced at interactions of relativistic protons with low energy radiation. *Phys. Rev. D*, 78(3):034013, Aug. 2008. doi: 10.1103/PhysRevD.78.034013.

R. W. Klebesadel, I. B. Strong, and R. A. Olson. Observations of Gamma-Ray Bursts of Cosmic Origin. *ApJ*, 182:L85, June 1973. doi: 10.1086/181225.

R. W. Klebesadel, W. D. Evans, J. P. Glore, et al. The Pioneer Venus Orbiter Gamma Burst Detector. *IEEE Transactions on Geoscience and Remote Sensing*, 18:76–80, Jan. 1980. doi: 10.1109/TGRS.1980.350285.

KM3NeT Collaboration. Letter of intent for KM3NeT 2.0. *Journal of Physics G Nuclear Physics*, 43(8):084001, Aug. 2016. doi: 10.1088/0954-3899/43/8/084001.

KM3NeT Collaboration. Sensitivity of the KM3NeT/ARCA neutrino telescope to point-like neutrino sources. *Astroparticle Physics*, 111:100–110, Sept. 2019. doi: 10.1016/j.astropartphys.2019.04.002.

T. M. Kneiske and H. Dole. A lower-limit flux for the extragalactic background light. *A&A*, 515:A19, June 2010. doi: 10.1051/0004-6361/200912000.

J. Knödlseder, M. Mayer, C. Deil, et al. GammaLib and ctools. A software framework for the analysis of astronomical gamma-ray data. *A&A*, 593:A1, Aug. 2016. doi: 10.1051/0004-6361/201628822.

A. Kolmogorov. Sulla determinazione empirica di una legge di distribuzione. *Giornale dell' Istituto Italiano degli Attuari*, 4:83–91, 1933.

M. Kowalski. Status of High-Energy Neutrino Astronomy. In *Journal of Physics Conference Series*, volume 632, page 012039, Aug. 2015. doi: 10.1088/1742-6596/632/1/012039.

W. Kraushaar, G. W. Clark, and G. o. Garmire. Explorer XI Experiment on Cosmic Gamma Rays. *ApJ*, 141:845, Apr. 1965. doi: 10.1086/148179.

W. L. Kraushaar and G. W. Clark. Search for Primary Cosmic Gamma Rays with the Satellite Explorer XI. *Phys. Rev. Lett.*, 8(3):106–109, Feb. 1962. doi: 10.1103/PhysRevLett.8.106.

W. L. Kraushaar, G. W. Clark, G. P. Garmire, et al. High-Energy Cosmic Gamma-Ray Observations from the OSO-3 Satellite. *ApJ*, 177:341, Nov. 1972. doi: 10.1086/151713.

F. Krauß, M. Kadler, K. Mannheim, et al. TANAMI blazars in the IceCube PeV-neutrino fields. *A&A*, 566:L7, June 2014. doi: 10.1051/0004-6361/201424219.

H. Krawczynski, S. B. Hughes, D. Horan, et al. Multiwavelength Observations of Strong Flares from the TeV Blazar 1ES 1959+650. *ApJ*, 601(1):151–164, Jan. 2004. doi: 10.1086/380393.

G. F. Krymskii. A regular mechanism for the acceleration of charged particles on the front of a shock wave. *Akademiia Nauk SSSR Doklady*, 234:1306–1308, June 1977.

S. Kullback and R. A. Leibler. On Information and Sufficiency. *The Annals of Mathematical Statistics*, 22(1):79 – 86, 1951. doi: 10.1214/aoms/1177729694.

P. Kumar and B. Zhang. The physics of gamma-ray bursts & relativistic jets. *Physics Reports*, 561:1–109, Feb. 2015. doi: 10.1016/j.physrep.2014.09.008.

L. Kuzmichev. The lake Baikal Neutrino Telescope NT-200 ; First year operation. In *Proceedings of the 26th International Cosmic Ray Conference (ICRC1999)*, volume 2, page 217, Jan. 1999.

A. J. Levan. Swift discoveries of new populations of extremely long duration high energy transient. *Journal of High Energy Astrophysics*, 7:44–55, Sept. 2015. doi: 10.1016/j.jheap.2015.05.004.

F. Lewis, A. Butler, and L. Gilbert. A unified approach to model selection using the likelihood ratio test. *Methods in Ecology and Evolution*, 2(2):155–162, 2011. doi: 10.1111/j.2041-210X.2010.00063.x.

A. Lidvansky. Air cherenkov methods in cosmic rays: Review and some history. *Radiation Physics and Chemistry*, 75:891–898, 08 2006. doi: 10.1016/j.radphyschem.2005.12.019.

LIGO Collaboration, Virgo Collaboration, Fermi-GBM Collaboration, et al. Gravitational Waves and Gamma-Rays from a Binary Neutron Star Merger: GW170817 and GRB 170817A. *ApJ*, 848(2):L13, Oct. 2017. doi: 10.3847/2041-8213/aa920c.

LIGO Scientific Collaboration and Virgo Collaboration. GW170817: Observation of Gravitational Waves from a Binary Neutron Star Inspiral. *Phys. Rev. Lett.*, 119(16):161101, Oct. 2017. doi: 10.1103/PhysRevLett.119.161101.

LIGO Scientific Collaboration, Virgo Collaboration, IceCube Collaboration, et al. Multi-messenger Observations of a Binary Neutron Star Merger. *ApJ*, 848(2):L12, Oct. 2017. doi: 10.3847/2041-8213/aa91c9.

R.-Y. Liu, K. Wang, R. Xue, et al. Hadronuclear interpretation of a high-energy neutrino event coincident with a blazar flare. *Phys. Rev. D*, 99(6):063008, Mar 2019. doi: 10.1103/PhysRevD.99.063008.

M. S. Longair. *High Energy Astrophysics*. Cambridge University Press, 3 edition, 2011. doi: 10.1017/CBO9780511778346.

N. R. MacDonald, A. P. Marscher, S. G. Jorstad, et al. Through the Ring of Fire: Gamma-Ray Variability in Blazars by a Moving Plasmoid Passing a Local Source of Seed Photons. *ApJ*, 804(2):111, May 2015. doi: 10.1088/0004-637X/804/2/111.

P. Madau and M. Dickinson. Cosmic Star-Formation History. *ARA&A*, 52:415–486, Aug 2014. doi: 10.1146/annurev-astro-081811-125615.

MAGIC Collaboration. Variable Very-High-Energy Gamma-Ray Emission from the Microquasar LS I +61 303. *Science*, 312(5781):1771–1773, June 2006a. doi: 10.1126/science.1128177.

MAGIC Collaboration. Variable Very-High-Energy Gamma-Ray Emission from the Microquasar LS I +61 303. *Science*, 312(5781):1771–1773, June 2006b. doi: 10.1126/science.1128177.

MAGIC Collaboration. Variable Very High Energy γ-Ray Emission from Markarian 501. *ApJ*, 669(2):862–883, Nov. 2007. doi: 10.1086/521382.

MAGIC Collaboration. Very-High-Energy gamma rays from a Distant Quasar: How Transparent Is the Universe? *Science*, 320(5884):1752, June 2008a. doi: 10.1126/science.1157087.

MAGIC Collaboration. Observation of Pulsed γ-Rays Above 25 GeV from the Crab Pulsar with MAGIC. *Science*, 322(5905):1221, Nov. 2008b. doi: 10.1126/science.1164718.

MAGIC Collaboration. MAGIC Discovery of Very High Energy Emission from the FSRQ PKS 1222+21. *ApJ*, 730(1):L8, Mar. 2011a. doi: 10.1088/2041-8205/730/1/L8.

MAGIC Collaboration. MAGIC Discovery of Very High Energy Emission from the FSRQ PKS 1222+21. *ApJ*, 730(1):L8, Mar. 2011b. doi: 10.1088/2041-8205/730/1/L8.

MAGIC Collaboration. Performance of the MAGIC stereo system obtained with Crab Nebula data. *Astroparticle Physics*, 35(7):435–448, Feb 2012a. doi: 10.1016/j.astropartphys.2011.11.007.

MAGIC Collaboration. Discovery of VHE γ-rays from the blazar 1ES 1215+303 with the MAGIC telescopes and simultaneous multi-wavelength observations. *A&A*, 544:A142, Aug. 2012b. doi: 10.1051/0004-6361/201219133.

MAGIC Collaboration. MAGIC observations and multifrequency properties of the flat spectrum radio quasar 3C 279 in 2011. *A&A*, 567:A41, July 2014a. doi: 10.1051/0004-6361/201323036.

MAGIC Collaboration. Discovery of very high energy gamma-ray emission from the blazar 1ES 1727+502 with the MAGIC Telescopes. *A&A*, 563:A90, Mar. 2014b. doi: 10.1051/0004-6361/201321360.

MAGIC Collaboration. Discovery of very high energy γ-ray emission from the blazar 1ES 0033+595 by the MAGIC telescopes. *MNRAS*, 446(1):217–225, Jan. 2015. doi: 10.1093/mnras/stu2024.

MAGIC Collaboration. The major upgrade of the MAGIC telescopes, Part I: The hardware improvements and the commissioning of the system. *Astroparticle Physics*, 72:61–75, Jan. 2016a. doi: 10.1016/j.astropartphys.2015.04.004.

MAGIC Collaboration. Long-term multi-wavelength variability and correlation study of Markarian 421 from 2007 to 2009. *A&A*, 593:A91, Sept. 2016b. doi: 10.1051/0004-6361/201628447.

MAGIC Collaboration. Teraelectronvolt pulsed emission from the Crab Pulsar detected by MAGIC. *A&A*, 585:A133, Jan. 2016c. doi: 10.1051/0004-6361/201526853.

MAGIC Collaboration. Limits to dark matter annihilation cross-section from a combined analysis of MAGIC and Fermi-LAT observations of dwarf satellite galaxies. *J. Cosmology Astropart. Phys.*, 2016(2):039, Feb. 2016d. doi: 10.1088/1475-7516/2016/02/039.

MAGIC Collaboration. A cut-off in the TeV gamma-ray spectrum of the SNR Cassiopeia A. *MNRAS*, 472(3):2956–2962, Dec. 2017. doi: 10.1093/mnras/stx2079.

MAGIC Collaboration. Constraining dark matter lifetime with a deep gamma-ray survey of the Perseus galaxy cluster with MAGIC. *Physics of the Dark Universe*, 22:38–47, Dec. 2018. doi: 10.1016/j.dark.2018.08.002.

MAGIC Collaboration. Measurement of the extragalactic background light using MAGIC and Fermi-LAT gamma-ray observations of blazars up to z = 1. *MNRAS*, 486(3):4233–4251, July 2019. doi: 10.1093/mnras/stz943.

MAGIC Collaboration. MAGIC observations of the diffuse γ-ray emission in the vicinity of the Galactic center. *A&A*, 642:A190, Oct. 2020a. doi: 10.1051/0004-6361/201936896.

MAGIC Collaboration. Detection of the Geminga pulsar with MAGIC hints at a power-law tail emission beyond 15 GeV. *A&A*, 643:L14, Nov. 2020b. doi: 10.1051/0004-6361/202039131.

MAGIC Collaboration. Follow-up observations of GW170817 with the MAGIC telescopes. In *Proceedings of the 37th International Cosmic Ray Conference (ICRC2021)*, page 944, Mar. 2022. doi: 10.22323/1.395.0944.

MAGIC Collaboration and Fermi-LAT Collaboration. Very High Energy γ-Rays from the Universe's Middle Age: Detection of the z = 0.940 Blazar PKS 1441+25 with MAGIC. *ApJ*, 815(2):L23, Dec. 2015. doi: 10.1088/2041-8205/815/2/L23.

MAGIC Collaboration and Fermi-LAT Collaboration. Broadband characterisation of the very intense TeV flares of the blazar 1ES 1959+650 in 2016. *A&A*, 638: A14, June 2020. doi: 10.1051/0004-6361/201935450.

MAGIC Collaboration and VERITAS Collaboration. Unprecedented study of the broadband emission of Mrk 421 during flaring activity in March 2010. *A&A*, 578:A22, June 2015a. doi: 10.1051/0004-6361/201424811.

MAGIC Collaboration and VERITAS Collaboration. The 2009 multiwavelength campaign on Mrk 421: Variability and correlation studies. *A&A*, 576:A126, Apr. 2015b. doi: 10.1051/0004-6361/201424216.

MAGIC Collaboration, FACT Collaboration, and MWL partners. An intermittent extreme BL Lac: MWL study of 1ES 2344+514 in an enhanced state. *MNRAS*, 496(3):3912–3928, Aug. 2020. doi: 10.1093/mnras/staa1702.

MAGIC Collaboration, FACT Collaboration, and MWL Collaboration. Multi-wavelength variability and correlation studies of Mrk 421 during historically low X-ray and γ-ray activity in 2015-2016. *MNRAS*, 504(1):1427–1451, June 2021. doi: 10.1093/mnras/staa3727.

G. Maier. Performance of the Cherenkov Telescope Array. In *Proceedings of the 36th International Cosmic Ray Conference (ICRC2019)*, volume 36, page 733, July 2019. doi: 10.22323/1.358.0733.

K. Mannheim. The proton blazar. *A&A*, 269:67–76, Mar. 1993. doi: 10.48550/arXiv.astro-ph/9302006.

K. Mannheim and P. L. Biermann. Gamma-ray flaring of 3C 279: a proton-initiated cascade in the jet? *A&A*, 253:L21–L24, Jan. 1992.

L. Maraschi, G. Ghisellini, and A. Celotti. A jet model for the gamma-ray emitting blazar 3C 279. *ApJ*, 397:L5–L9, Sept. 1992. doi: 10.1086/186531.

M. A. Markov and I. M. Zheleznykh. On high energy neutrino physics in cosmic rays. *Nuclear Physics*, 27(3):385–394, Oct. 1961. doi: 10.1016/0029-5582(61)90331-5.

A. P. Marscher. Turbulent, Extreme Multi-zone Model for Simulating Flux and Polarization Variability in Blazars. *ApJ*, 780(1):87, Jan. 2014. doi: 10.1088/0004-637X/780/1/87.

A. P. Marscher, S. G. Jorstad, F. D. D'Arcangelo, et al. The inner jet of an active galactic nucleus as revealed by a radio-to-γ-ray outburst. *Nature*, 452:966–969, Apr. 2008. doi: 10.1038/nature06895.

A. P. Marscher, S. G. Jorstad, V. M. Larionov, et al. Probing the Inner Jet of the Quasar PKS 1510-089 with Multi-Waveband Monitoring During Strong Gamma-Ray Activity. *ApJ*, 710:L126–L131, Feb. 2010. doi: 10.1088/2041-8205/710/2/L126.

C. Mascaretti and F. Vissani. On the relevance of prompt neutrinos for the interpretation of the IceCube signals. *J. Cosmology Astropart. Phys.*, 2019(8):004, Aug. 2019. doi: 10.1088/1475-7516/2019/08/004.

A. Mastichiadis, M. Petropoulou, and S. Dimitrakoudis. Mrk 421 as a case study for TeV and X-ray variability in leptohadronic models. *MNRAS*, 434(3):2684–2695, Sept. 2013. doi: 10.1093/mnras/stt1210.

M. Mayer, R. Buehler, E. Hays, et al. Rapid Gamma-Ray Flux Variability during the 2013 March Crab Nebula Flare. *ApJ*, 775(2):L37, Oct. 2013. doi: 10.1088/2041-8205/775/2/L37.

H. A. Mayer-Haselwander, K. Bennett, G. F. Bignami, et al. COS-B observation of the milky way in high-energy gamma rays. *Annals of the New York Academy of Sciences*, 336(1):211–222, 1980. doi: 10.1111/j.1749-6632.1980.tb15931.x.

E. P. Mazets and S. V. Golenetskii. Recent Results from the Gamma-Ray Burst Studies in the KONUS Experiment. *Ap&SS*, 75(1):47–81, Mar. 1981. doi: 10.1007/BF00651384.

E. P. Mazets, S. V. Golenetskii, V. N. Ilinskii, et al. Catalog of cosmic gamma-ray bursts from the KONUS experiment data. *Ap&SS*, 80(1):3–83, Nov. 1981. doi: 10.1007/BF00649140.

D. Mazin and M. Raue. New limits on the density of the extragalactic background light in the optical to the far infrared from the spectra of all known TeV blazars. *A&A*, 471(2):439–452, Aug. 2007. doi: 10.1051/0004-6361:20077158.

J. McEnery et al. All-sky Medium Energy Gamma-ray Observatory: Exploring the Extreme Multimessenger Universe. In *Bulletin of the American Astronomical Society*, volume 51, page 245, Sept. 2019. doi: 10.48550/arXiv.1907.07558.

P. Mészáros, D. B. Fox, C. Hanna, et al. Multi-messenger astrophysics. *Nature Reviews Physics*, 1(10):585–599, Oct. 2019. doi: 10.1038/s42254-019-0101-z.

P. F. Michelson, W. B. Atwood, and S. Ritz. Fermi Gamma-ray Space Telescope: high-energy results from the first year. *Reports on Progress in Physics*, 73(7): 074901, July 2010. doi: 10.1088/0034-4885/73/7/074901.

M. Mori. CANGAROO Project for High-Energy Gamma-Ray Astrophysics. *Progress of Theoretical Physics Supplement*, 151:85–94, Jan. 2003. doi: 10.1143/PTPS.151.85.

A. Mücke and R. J. Protheroe. A proton synchrotron blazar model for flaring in Markarian 501. *Astroparticle Physics*, 15(1):121–136, Mar. 2001. doi: 10.1016/S0927-6505(00)00141-9.

A. Mücke, J. P. Rachen, R. Engel, et al. Photohadronic Processes in Astrophysical Environments. *Publ. Astron. Soc. Austral.*, 16(2):160–166, Aug. 1999. doi: 10.1071/AS99160.

A. Mücke, R. Engel, J. P. Rachen, et al. Monte Carlo simulations of photohadronic processes in astrophysics. *Computer Physics Communications*, 124(2-3):290–314, Feb. 2000. doi: 10.1016/S0010-4655(99)00446-4.

A. Mücke, R. J. Protheroe, R. Engel, et al. BL Lac objects in the synchrotron proton blazar model. *Astroparticle Physics*, 18(6):593–613, Mar. 2003. doi: 10.1016/S0927-6505(02)00185-8.

R. Mukherjee. ATel 7516: VERITAS Detection of Very High-Energy Gamma-Ray Emission from S3 1227+25. *The Astronomer's Telegram*, 7516:1, May 2015.

K. Murase and E. Waxman. Constraining high-energy cosmic neutrino sources: Implications and prospects. *Phys. Rev. D*, 94:103006, Nov 2016. doi: 10.1103/PhysRevD.94.103006.

K. Murase, D. Guetta, and M. Ahlers. Hidden Cosmic-Ray Accelerators as an Origin of TeV-PeV Cosmic Neutrinos. *Phys. Rev. Lett.*, 116(7):071101, Feb. 2016. doi: 10.1103/PhysRevLett.116.071101.

A. I. Nikishov. Absorption of high-energy photons in the universe. *Zhurnal Eksperimental'noi i Teoreticheskoi Fiziki*, 41(393):549–550, 8 1961.

S. Ohm. γ-rays from starburst galaxies. In F. A. Aharonian, W. Hofmann, and F. M. Rieger, editors, *High Energy Gamma-Ray Astronomy: 5th International Meeting on High Energy Gamma-Ray Astronomy*, volume 1505 of *American Institute of Physics Conference Series*, pages 64–71, Dec. 2012. doi: 10.1063/1.4772221.

F. Oikonomou, K. Murase, P. Padovani, et al. High-energy neutrino flux from individual blazar flares. *MNRAS*, 489(3):4347–4366, Nov. 2019. doi: 10.1093/mnras/stz2246.

R. A. Ong. Highlights from VERITAS on VHE gamma-ray sources in our Galaxy. *Advances in Space Research*, 53(10):1483–1491, May 2014. doi: 10.1016/j.asr.2013.09.020.

OSSE Collaboration. Operation and performance of the OSSE instrument. In *NASA Conference Publication*, volume 3137 of *NASA Conference Publication*, pages 3–14, Feb. 1992.

OSSE Collaboration. Initial results from OSSE on the Compton Observatory. *A&AS*, 97:21–25, Jan. 1993.

P-ONE Collaboration. The Pacific Ocean Neutrino Experiment. *Nature Astronomy*, 4:913–915, Sept. 2020. doi: 10.1038/s41550-020-1182-4.

W. S. Paciesas. Fermi GBM: Instrument Description and Science Highlights. In V. Florinski, J. Heerikhuisen, G. P. Zank, and D. L. Gallagher, editors, *Partially Ionized Plasmas Throughout the Cosmos-Proceedings of the 2010 Huntsville Workshop*, volume 1366 of *American Institute of Physics Conference Series*, pages 155–162, Sept. 2011. doi: 10.1063/1.3625601.

P. Padovani. Is there a relationship between BL Lacertae objects and flat-spectrum radio quasars? *MNRAS*, 257:404–414, Aug. 1992. doi: 10.1093/mnras/257.3.404.

P. Padovani, E. Resconi, P. Giommi, et al. Extreme blazars as counterparts of IceCube astrophysical neutrinos. *MNRAS*, 457(4):3582–3592, Apr. 2016. doi: 10.1093/mnras/stw228.

P. Padovani, F. Oikonomou, M. Petropoulou, et al. TXS 0506+056, the first cosmic neutrino source, is not a BL Lac. *MNRAS*, 484(1):L104–L108, Mar. 2019. doi: 10.1093/mnrasl/slz011.

S. Paiano. The optical spectrum of 4FGLJ0658.6+0636: a candidate counterpart of the IceCube 201114A neutrino event. *The Astronomer's Telegram*, 14213:1, Nov. 2020.

Particle Data Group. Review of Particle Physics. *Progress of Theoretical and Experimental Physics*, 2020(8):083C01, Aug. 2020. doi: 10.1093/ptep/ptaa104.

D. Pasham, K. Gendreau, Z. Arzoumanian, et al. NICER observations of 4FGL J0658.6+0636, candidate counterpart to the IceCube neutrino event IceCube-201114A. *The Astronomer's Telegram*, 14202:1, Nov. 2020.

G. N. Pendleton, W. S. Paciesas, J. P. Lestrade, et al. Preliminary Burst Location Calibration Results for the BATSE Instrument on CGRO. In W. S. Paciesas and G. J. Fishman, editors, *American Institute of Physics Conference Series*, volume 265 of *American Institute of Physics Conference Series*, page 395, Jan. 1992. doi: 10.1063/1.42770.

A. Pénin, G. Lagache, A. Noriega-Crespo, et al. An accurate measurement of the anisotropies and mean level of the cosmic infrared background at 100 μm and 160 μm. *A&A*, 543:A123, July 2012. doi: 10.1051/0004-6361/201015929.

B. M. Peterson. *An Introduction to Active Galactic Nuclei*. Cambridge University Press, 1997. doi: 10.1017/CBO9781139170901.

M. Petropoulou, K. Murase, M. Santander, et al. Multi-epoch Modeling of TXS 0506+056 and Implications for Long-term High-energy Neutrino Emission. *ApJ*, 891(2):115, Mar. 2020. doi: 10.3847/1538-4357/ab76d0.

A. Pichel. Highlights from the Whipple 10-m Blazar Monitoring Program. In *Proceedings of the 31st International Cosmic Ray Conference (ICRC2009)*, Jul 2009. doi: 10.48550/arXiv.0908.0010.

Pierre Auger Collaboration. Observation of the Suppression of the Flux of Cosmic Rays above $4{\times}10^{19}$eV. *Phys. Rev. Lett.*, 101(6):061101, Aug. 2008. doi: 10.1103/PhysRevLett.101.061101.

T. Piran, O. Bromberg, E. Nakar, et al. The long, the short and the weak: the origin of gamma-ray bursts. *Philosophical Transactions of the Royal Society of London Series A*, 371(1992):20120273–20120273, Apr. 2013. doi: 10.1098/rsta.2012.0273.

F. Piron. Gamma-ray bursts at high and very high energies. *Comptes Rendus Physique*, 17(6):617–631, June 2016. doi: 10.1016/j.crhy.2016.04.005.

Planck Collaboration. Planck 2015 results. XIII. Cosmological parameters. *A&A*, 594:A13, Sept. 2016. doi: 10.1051/0004-6361/201525830.

A. V. Plavin, Y. Y. Kovalev, Y. A. Kovalev, et al. Directional Association of TeV to PeV Astrophysical Neutrinos with Radio Blazars. *ApJ*, 908(2):157, Feb. 2021. doi: 10.3847/1538-4357/abceb8.

M. Punch, C. W. Akerlof, M. F. Cawley, et al. Detection of TeV photons from the active galaxy Markarian 421. *Nature*, 358:477, Aug. 1992. doi: 10.1038/358477a0.

J. P. Rachen. *Interaction Processes and Statistical Properties of the Propagation of Cosmic Rays in Photon Backgrounds*. PhD thesis, Max-Planck-Institute for Radioastronomy, Bonn, Sept. 1996.

J. P. Rachen and P. Mészáros. Photohadronic neutrinos from transients in astrophysical sources. *Phys. Rev. D*, 58(12):123005, Dec. 1998. doi: 10.1103/PhysRevD.58.123005.

B. Rani, B. Lott, T. P. Krichbaum, et al. Constraining the location of rapid gamma-ray flares in the flat spectrum radio quasar 3C 273. *A&A*, 557:A71, Sept. 2013. doi: 10.1051/0004-6361/201321440.

B. C. Raubenheimer. TeV Gamma-Ray Astronomy in South Africa. *Ap&SS*, 230 (1-2):263–277, Aug. 1995. doi: 10.1007/BF00658185.

M. J. Rees. Appearance of Relativistically Expanding Radio Sources. *Nature*, 211 (5048):468–470, July 1966. doi: 10.1038/211468a0.

A. Reimer, M. Böttcher, and S. Buson. Cascading Constraints from Neutrino-emitting Blazars: The Case of TXS 0506+056. *ApJ*, 881(1):46, Aug. 2019. doi: 10.3847/1538-4357/ab2bff.

L. Resvanis, S. Tzamarias, G. Voulgaris, et al. The Haleakala Gamma Observatory. In K. E. Turver, editor, *Very High Energy Gamma Ray Astronomy*, volume 199 of *NATO Advanced Study Institute (ASI) Series C*, page 225, Jan. 1987. doi: 10.1007/978-94-009-3831-1_34.

A. Roberts. The birth of high-energy neutrino astronomy: A personal history of the DUMAND project. *Reviews of Modern Physics*, 64(1):259–312, Jan. 1992. doi: 10.1103/RevModPhys.64.259.

X. Rodrigues, S. Gao, A. Fedynitch, et al. Leptohadronic Blazar Models Applied to the 2014-2015 Flare of TXS 0506+056. *ApJ*, 874(2):L29, Apr 2019. doi: 10.3847/2041-8213/ab1267.

X. Rodrigues, S. Garrappa, S. Gao, et al. Multiwavelength and Neutrino Emission from Blazar PKS 1502 + 106. *ApJ*, 912(1):54, May 2021. doi: 10.3847/1538-4357/abe87b.

G. E. Romero, M. Boettcher, S. Markoff, et al. Relativistic Jets in Active Galactic Nuclei and Microquasars. *SSR*, 207(1-4):5–61, July 2017. doi: 10.1007/s11214-016-0328-2.

A. Rosales de León, A. M. Brown, and P. M. Chadwick. Photohadronic modelling of the 2010 gamma-ray flare from Mrk 421. *MNRAS*, 501(2):2198–2208, Feb. 2021. doi: 10.1093/mnras/staa3839.

A. Rosales de León, A. M. Brown, and P. M. Chadwick. Possible photohadronic origin of the IC-201114A alert. In *Proceedings of the 37th International Cosmic Ray Conference (ICRC2021)*, page 1001, Mar. 2022. doi: 10.22323/1.395.1001.

S. Sahu, B. Zhang, and N. Fraija. Hadronic-origin TeV γ rays and ultrahigh energy cosmic rays from Centaurus A. *Phys. Rev. D*, 85(4):043012, Feb. 2012. doi: 10.1103/PhysRevD.85.043012.

S. Sahu, A. F. O. Oliveros, and J. C. Sanabria. Hadronic-origin orphan TeV flare from 1ES 1959+650. *Phys. Rev. D*, 87(10):103015, May 2013. doi: 10.1103/PhysRevD.87.103015.

S. Sahu, L. S. Miranda, and S. Rajpoot. Multi-TeV flaring from blazars: Markarian 421 as a case study. *Eur. Phys. J. C*, 76:127, Mar. 2016. doi: 10.1140/epjc/s10052-016-3975-2.

S. Sahu, A. Rosales de León, and L. S. Miranda. Photohadronic scenario in interpreting the February-March 2014 flare of 1ES 1011+496. *Eur. Phys. J. C*, 77 (11):741, Nov. 2017. doi: 10.1140/epjc/s10052-017-5335-2.

S. Sahu, A. Rosales de León, S. Nagataki, and V. Gupta. The origin of multi-TeV flares from the nearest blazar Markarian 421. *Eur. Phys. J. C*, 78(7):557, July 2018. doi: 10.1140/epjc/s10052-018-6038-z.

K. Satalecka, A. Brown, A. Rosales de León, et al. Neutrino Target of Opportunity program of the Cherenkov Telescope Array. In *Proceedings of the 36th International Cosmic Ray Conference (ICRC2019)*, volume 36, page 784, July 2019. doi: 10.22323/1.358.0784.

K. Satalecka, E. Bernardini, D. Dorner, et al. Searching for VHE gamma-ray emission associated with IceCube neutrino alerts using FACT, H.E.S.S., MAGIC,

and VERITAS. In *Proceedings of the 37th International Cosmic Ray Conference (ICRC2021)*, page 960, Sept. 2021. doi: 10.22323/1.395.0960.

V. Schoenfelder, K. Bennett, H. Bloemen, et al. COMPTEL overview: Achievements and expectations. *A&AS*, 120:13–21, Nov. 1996.

C. Shang, Z. Haiman, L. Knox, et al. Improved models for cosmic infrared background anisotropies: new constraints on the infrared galaxy population. *MNRAS*, 421(4):2832–2845, Apr. 2012. doi: 10.1111/j.1365-2966.2012.20510.x.

M. Sikora, M. C. Begelman, and M. J. Rees. Comptonization of Diffuse Ambient Radiation by a Relativistic Jet: The Source of Gamma Rays from Blazars? *ApJ*, 421:153, Jan. 1994. doi: 10.1086/173633.

S. Singer. The vela satellite program for detection of high-altitude nuclear detonations. *Proceedings of the IEEE*, 53(12):1935–1948, 1965. doi: 10.1109/PROC.1965.4470.

M. Snipes and D. C. Taylor. Model selection and akaike information criteria: An example from wine ratings and prices. *Wine Economics and Policy*, 3(1):3–9, 2014. ISSN 2212-9774. doi: 10.1016/j.wep.2014.03.001.

C. Spiering. Towards high-energy neutrino astronomy. A historical review. *European Physical Journal H*, 37(3):515–565, Aug. 2012. doi: 10.1140/epjh/e2012-30014-2.

D. Staszak and VERITAS Collaboration. Science Highlights from VERITAS. In *Proceedings of the 34th International Cosmic Ray Conference (ICRC2015)*, volume 34, page 868, July 2015. doi: 10.22323/1.236.0868.

F. W. Stecker. Neutral-Pion Gamma Rays from the Galaxy and the Interstellar Gas Content. *ApJ*, 185:499–504, Oct 1973. doi: 10.1086/152435.

F. W. Stecker, O. C. de Jager, and M. H. Salamon. TeV Gamma Rays from 3C 279: A Possible Probe of Origin and Intergalactic Infrared Radiation Fields. *ApJ*, 390: L49, May 1992. doi: 10.1086/186369.

A. A. Stepanian, V. P. Fomin, and B. M. Vladimirskii. A method of distinguishing Cerenkov gamma-ray flashes from the proton component of cosmic rays. *Izvestiya Ordena Trudovogo Krasnogo Znameni Krymskoj Astrofizicheskoj Observatorii*, 66:234–241, Jan. 1983.

G. M. Stirpe. Broad emission lines in active galactic nuclei. II. Statistical properties of H-alpa and H-beta. *A&A*, 247:3, July 1991.

M. Su and C. van Eldik. Gamma rays from the Galactic Centre region. *Comptes Rendus Physique*, 16(6-7):686–703, Aug. 2015. doi: 10.1016/j.crhy.2015.09.001.

M. Su, T. R. Slatyer, and D. P. Finkbeiner. Giant Gamma-ray Bubbles from Fermi-LAT: Active Galactic Nucleus Activity or Bipolar Galactic Wind? *ApJ*, 724(2): 1044–1082, Dec. 2010. doi: 10.1088/0004-637X/724/2/1044.

B. N. Swanenburg, K. Bennett, G. F. Bignami, et al. Second COS-B catalogue of high-energy gamma-ray sources. *ApJ*, 243:L69–L73, Jan. 1981. doi: 10.1086/183445.

Swift Collaboration. The Swift Gamma-Ray Burst Mission. *ApJ*, 611(2):1005–1020, Aug. 2004. doi: 10.1086/422091.

Swift Collaboration. The Burst Alert Telescope (BAT) on the SWIFT Midex Mission. *SSR*, 120(3-4):143–164, Oct. 2005a. doi: 10.1007/s11214-005-5096-3.

Swift Collaboration. The Swift Ultra-Violet/Optical Telescope. *SSR*, 120(3-4): 95–142, Oct. 2005b. doi: 10.1007/s11214-005-5095-4.

Swift Collaboration. The Swift X-Ray Telescope. *SSR*, 120(3-4):165–195, Oct. 2005c. doi: 10.1007/s11214-005-5097-2.

Swift Collaboration. Gamma-ray bursts: Huge explosion in the early Universe. *Nature*, 440(7081):164, Mar. 2006. doi: 10.1038/440164a.

Swift Collaboration. GRB 080913 at Redshift 6.7. *ApJ*, 693(2):1610–1620, Mar. 2009a. doi: 10.1088/0004-637X/693/2/1610.

Swift Collaboration. A γ-ray burst at a redshift of z$\sim$8.2. *Nature*, 461(7268): 1254–1257, Oct. 2009b. doi: 10.1038/nature08459.

Swift Collaboration. A Photometric Redshift of z$\sim$9.4 for GRB 090429B. *ApJ*, 736 (1):7, July 2011. doi: 10.1088/0004-637X/736/1/7.

Swift Collaboration. Swift and NuSTAR observations of GW170817: Detection of a blue kilonova. *Science*, 358(6370):1565–1570, Dec. 2017. doi: 10.1126/science.aap9580.

I. Tamm and I. Frank. Coherent in-medium fast-electron radiation. *Doklady Akademil Mauk USSR*, 14(109), 1937.

Y. T. Tanaka, S. Buson, and D. Kocevski. Fermi-LAT detection of increased gamma-ray activity of TXS 0506+056, located inside the IceCube-170922A error region. *The Astronomer's Telegram*, 10791:1, Sept. 2017.

TANAMI Collaboration and Fermi-LAT Collaboration. TANAMI counterparts to IceCube high-energy neutrino events. In *5th International Fermi Symposium*, page C141020, Feb. 2015. doi: 10.48550/arXiv.1502.02147.

M. Tavani. Ten years of AGILE: the mission and scientific highlights. *Rendiconti Lincei. Scienze Fisiche e Naturali*, 30:13–50, Dec. 2019. doi: 10.1007/s12210-019-00841-5.

F. Tavecchio, L. Maraschi, and G. Ghisellini. Constraints on the Physical Parameters of TeV Blazars. *ApJ*, 509(2):608–619, Dec. 1998. doi: 10.1086/306526.

F. Tavecchio, G. Ghisellini, G. Ghirlanda, et al. The hard TeV spectrum of 1ES 0229+200: new clues from Swift. *MNRAS*, 399(1):L59–L63, Oct 2009. doi: 10.1111/j.1745-3933.2009.00724.x.

THEMISTOCLE Collaboration. Gamma ray spectrum of the Crab nebula in the multi TeV region k20. *Astroparticle Physics*, 1(4):341–355, Dec. 1993. doi: 10.1016/0927-6505(93)90001-T.

J. I. Trombka, A. E. Metzger, J. R. Arnold, et al. The Cosmic y-RAY Spectrum Between 0.3 and 25 MeV Measured on Apollo 15. *ApJ*, 181:737–746, May 1973. doi: 10.1086/152084.

J. I. Trombka, E. L. Eller, R. L. Schmadebeck, et al. Observation of a Cosmic Gamma-Ray Burst on Apollo 16. II. X-Ray Time Profile and Source Location. *ApJ*, 194:L27, Nov. 1974. doi: 10.1086/181661.

C. Tung, T. Glauch, M. Larson, et al. FIRESONG: A python package to simulate populations of extragalactic neutrino sources. *The Journal of Open Source Software*, 6(61):3194, May 2021. doi: 10.21105/joss.03194.

C. M. Urry and P. Padovani. Unified Schemes for Radio-Loud Active Galactic Nuclei. *PASP*, 107:803, Sept. 1995. doi: 10.1086/133630.

VERITAS Collaboration. A Multiwavelength View of the TeV Blazar Markarian 421: Correlated Variability, Flaring, and Spectral Evolution. *ApJ*, 630:130–141, Sept. 2005. doi: 10.1086/431925.

VERITAS Collaboration. The first VERITAS telescope. *Astroparticle Physics*, 25 (6):391–401, July 2006. doi: 10.1016/j.astropartphys.2006.04.002.

VERITAS Collaboration. VERITAS Telescope 1 Relocation: Details and Improvements. In *2nd International Fermi Symposium*, page C091122, Dec 2009a. doi: 10.48550/arXiv.0912.3841.

VERITAS Collaboration. A connection between star formation activity and cosmic rays in the starburst galaxy M82. *Nature*, 462(7274):770–772, Dec. 2009b. doi: 10.1038/nature08557.

VERITAS Collaboration. Multiwavelength Observations of the Previously Unidentified Blazar RX J0648.7+1516. *ApJ*, 742(2):127, Dec. 2011. doi: 10.1088/0004-637X/742/2/127.

VERITAS Collaboration. Discovery of High-energy and Very High Energy γ-Ray Emission from the Blazar RBS 0413. *ApJ*, 750(2):94, May 2012. doi: 10.1088/0004-637X/750/2/94.

VERITAS Collaboration. Constraints on Very High Energy Emission from GRB 130427A. *ApJ*, 795(1):L3, Nov. 2014a. doi: 10.1088/2041-8205/795/1/L3.

VERITAS Collaboration. A Three-year Multi-wavelength Study of the Very-high-energy γ-Ray Blazar 1ES 0229+200. *ApJ*, 782(1):13, Feb. 2014b. doi: 10.1088/0004-637X/782/1/13.

VERITAS Collaboration. VERITAS Detection of γ-Ray Flaring Activity From the BL Lac Object 1ES 1727+502 During Bright Moonlight Observations. *ApJ*, 808 (2):110, Aug. 2015. doi: 10.1088/0004-637X/808/2/110.

VERITAS Collaboration. Discovery of Very-high-energy Emission from RGB J2243+203 and Derivation of Its Redshift Upper Limit. *ApJS*, 233(1):7, Nov. 2017a. doi: 10.3847/1538-4365/aa8d76.

VERITAS Collaboration. The VERITAS Dark Matter Program. In *Proceedings of the 35th International Cosmic Ray Conference (ICRC2017)*, volume 301, page 904, Jan. 2017b. doi: 10.22323/1.301.0904.

VERITAS Collaboration. Search for Magnetically Broadened Cascade Emission from Blazars with VERITAS. *ApJ*, 835(2):288, Feb. 2017c. doi: 10.3847/1538-4357/835/2/288.

VERITAS Collaboration. VTSCat: The VERITAS Catalog of Gamma-Ray Observations. In *Proceedings of the 37th International Cosmic Ray Conference (ICRC2021)*, page 812, Mar. 2022. doi: 10.22323/1.395.0812.

VERITAS Collaboration and Fermi-LAT Collaboration. Discovery of Very High Energy Gamma Rays from PKS 1424+240 and Multiwavelength Constraints on Its Redshift. *ApJ*, 708(2):L100–L106, Jan. 2010. doi: 10.1088/2041-8205/708/2/L100.

VERITAS Collaboration and Fermi-LAT Collaboration. Deep Broadband Observations of the Distant Gamma-Ray Blazar PKS 1424+240. *ApJ*, 785(1):L16, Apr. 2014. doi: 10.1088/2041-8205/785/1/L16.

VERITAS Collaboration and Icecube Collaboration. Searching for TeV gamma-ray emission associated with IceCube high-energy neutrinos using VERITAS. In *Proceedings of the 34th International Cosmic Ray Conference (ICRC2015)*, volume 34, page 785, July 2015. doi: 10.22323/1.236.0785.

VERITAS Collaboration and MAGIC Collaboration. Periastron Observations of TeV Gamma-Ray Emission from a Binary System with a 50-year Period. *ApJ*, 867(1):L19, Nov. 2018. doi: 10.3847/2041-8213/aae70e.

VERITAS Collaboration, Fermi-LAT Collaboration, Swift Collaboration, et al. Multiwavelength Observations of the AGN 1ES 0414+009 with VERITAS, Fermi-LAT, Swift-XRT, and MDM. *ApJ*, 755(2):118, Aug. 2012. doi: 10.1088/0004-637X/755/2/118.

VERITAS Collaboration, SPOL Collaboration, ASAS-SN Collaboration, et al. Gamma-Rays from the Quasar PKS 1441+25: Story of an Escape. *ApJ*, 815 (2):L22, Dec. 2015. doi: 10.1088/2041-8205/815/2/L22.

VERITAS Collaboration, FACT Collaboration, Icecube Collaboration, et al. Searching for VHE gamma-ray emission associated with IceCube astrophysical neutrinos using FACT, H.E.S.S., MAGIC, and VERITAS. In *Proceedings of the*

35th International Cosmic Ray Conference (ICRC2017), volume 301, page 618, Jan. 2017. doi: 10.22323/1.301.0618.

VERITAS Collaboration, MAGIC Collaboration, and MWL Partners. The Great Markarian 421 Flare of 2010 February: Multiwavelength Variability and Correlation Studies. *ApJ*, 890(2):97, Feb. 2020. doi: 10.3847/1538-4357/ab6612.

P. Virtanen et al. SciPy 1.0: fundamental algorithms for scientific computing in Python. *Nature Methods*, 17:261–272, Feb. 2020. doi: 10.1038/s41592-019-0686-2.

H. J. Völk and K. Bernlöhr. Imaging very high energy gamma-ray telescopes. *Experimental Astronomy*, 25(1-3):173–191, Aug. 2009. doi: 10.1007/s10686-009-9151-z.

S. P. Wakely and D. Horan. TeVCat: An online catalog for Very High Energy Gamma-Ray Astronomy. In *Proceedings of the 21st International Cosmic Ray Conference (ICRC2008)*, volume 3, pages 1341–1344, Jan. 2008.

R. C. Walker, P. E. Hardee, F. Davies, et al. Observations of the Structure and Dynamics of the Inner M87 Jet. *Galaxies*, 4:46, Oct 2016. doi: 10.3390/galaxies4040046.

T. C. Weekes. A Fast Large Aperture Camera for Very High Energy Gamma-Ray Astronomy. In *Proceedings of the 17th International Cosmic Ray Conference (ICRC1981)*, volume 8, page 34, Jan. 1981.

T. C. Weekes and K. E. Turver. Gamma-Ray Astronomy from 10-100 GeV: a New Approach. In R. D. Wills and B. Battrick, editors, *Recent Advances in Gamma-Ray Astronomy*, volume 124 of *ESA Special Publication*, page 279, July 1977.

Whipple Collaboration. Observation of TeV Gamma Rays from the Crab Nebula Using the Atmospheric Cerenkov Imaging Technique. *ApJ*, 342:379, July 1989. doi: 10.1086/167599.

Whipple Collaboration. Observations of Markarian 421 by the Whipple Observatory Collaboration. In *Proceedings of the 24th International Cosmic Ray Conference (ICRC1995)*, volume 2, page 491, Jan. 1995.

Whipple Collaboration. Multiwavelength Observations of a Flare from Markarian 501. *ApJ*, 487(2):L143–L146, Oct. 1997. doi: 10.1086/310899.

Whipple Collaboration. Detection of TeV Gamma Rays from the BL Lacertae Object 1ES 1959+650 with the Whipple 10 Meter Telescope. *ApJ*, 583(1):L9–L12, Jan. 2003. doi: 10.1086/367816.

Whipple Collaboration. The Whipple Observatory 10 m gamma-ray telescope, 1997 2006. *Astroparticle Physics*, 28(2):182–195, Oct. 2007. doi: 10.1016/j.astropartphys.2007.05.004.

S. S. Wilks. The Large-Sample Distribution of the Likelihood Ratio for Testing Composite Hypotheses. *Annals Math. Statist.*, 9(1):60–62, 1938. doi: 10.1214/aoms/1177732360.

H. Y. Yang, M. Ruszkowski, and E. Zweibel. Unveiling the Origin of the Fermi Bubbles. *Galaxies*, 6(1):29, Feb. 2018. doi: 10.3390/galaxies6010029.

G. Zatsepin and A. Chudakov. On the methods for searching local sources of high energy photons. *Zhur. Eksptl'. i Teoret. Fiz.*, 41, 1961.

G. T. Zatsepin and V. A. Kuzmin. Upper Limit of the Spectrum of Cosmic Rays. *Soviet Journal of Experimental and Theoretical Physics Letters*, 4:78, Aug. 1966.

A. Zech, M. Cerruti, and D. Mazin. Expected signatures from hadronic emission processes in the TeV spectra of BL Lacertae objects. *A&A*, 602:A25, Jun 2017. doi: 10.1051/0004-6361/201629997.

L. Zhang, S. Chen, H. Xiao, et al. Doppler Factor Estimation for Fermi Blazars. *ApJ*, 897(1):10, July 2020. doi: 10.3847/1538-4357/ab9180.

Colophon

This thesis has made use of the CTA instrument response functions (version prod3b-v2) provided by the CTA Consortium and Observatory. See `https://www.cta-observatory.org/science/cta-performance/` and CTA Consortium (2016) for more details.

This work has also made use of public *Fermi*-LAT data obtained from the High Energy Astrophysics Science Archive Research Center (HEASARC) website, administrated by NASA Goddard Space Flight Center.

This thesis is based on a template developed by Matthew Townson and Andrew Reeves. It was typeset with LaTeX 2_ε. It was created using the *memoir* package, maintained by Lars Madsen, with the *madsen* chapter style. The font used is Latin Modern, derived from fonts designed by Donald E. Kunith.